Motion from measurement: The role of symmetry of quantum measurements

Luka Antonić, Yariv Kafri ⬤, Daniel Podolsky ⬤,* and Ari M. Turner

Department of Physics, Technion—Israel Institute of Technology, Haifa 3200003, Israel

In quantum mechanics, measurements are dynamical processes and thus they should be capable of inducing currents. The symmetries of the Hamiltonian and measurement operator provide an organizing principle for understanding the conditions for such currents to emerge. The central role is played by the inversion and time-reversal symmetries. We classify the distinct behaviors that emerge from single and repeated measurements, with and without coupling to a dissipative bath. While the breaking of inversion symmetry alone is sufficient to generate currents through measurements, the breaking of time-reversal symmetry by the measurement operator leads to a dramatic increase in the magnitude of the currents. We consider the dependence on the measurement rate and find that the current is nonmonotonic. Furthermore, nondegenerate measurements can lead to current loops within the steady state even in the Zeno limit.

I. INTRODUCTION

One of the most exciting properties of quantum mechanics is the ability to influence the dynamics and steady-state properties of systems through measurement. Notable examples include the Zeno effect, where the dynamics of a system under constant observation can be stalled or severely restricted [1–4], the ability to use quantum measurements to entangle qubits [5–9], control quantum computations [10,11] and dynamics [12–17], and induce currents [18–20]. More recently, the remarkable possibility that measurements in quantum circuits can induce phase transitions in the nature of the entanglement has been pointed out [21–28].

Much of the above body of work relies on quantum measurements disrupting the unitary evolution. However, a salient feature which is typically ignored is the symmetries of the measurement operator and their interplay with those of the Hamiltonian. In this paper, we explore the ramifications of symmetries for the question, "Can quantum measurements induce currents, and, if so, how?" For instance, it is interesting to ask whether a series of measurements of observables with time-reversal symmetry can create currents due to the irreversibility of the measurements or if explicit time-reversal symmetry breaking is necessary.

Throughout the paper, we focus on local projective measurements and consider the current averaged over an ensemble of experiments without postselection. Although we focus on a single particle, results on averaged behavior will also be relevant for many-particle systems provided interactions are negligible. For a many-particle system, it is necessary to carry out multiple single-particle measurements to get a macroscopic current. Then, the resulting current is given by the ensemble average over all possible outcomes of individual measurements.

To address this, we begin by identifying two distinct sources of charge transfer. The first is the standard current operator, which we dub the Hamiltonian current. The second is the measurement charge displacement, which occurs at the instant of measurement and is independent of the Hamiltonian.

Considering first a single measurement applied to a system in equilibrium, we find that a current can be produced only if inversion is broken, either in the Hamiltonian H or the observable A (for a measurement, a symmetry S is preserved if and only if $SAS^{-1} = \pm A$). Given that inversion symmetry is broken, if time reversal is preserved then a current can be generated but it either oscillates or decays after the measurement. In sharp contrast, measurements that break time-reversal symmetry lead to a dc current [29].

We then turn to investigate an isolated system subjected to repeated measurements. In this case, the steady state is an infinite temperature state, which we show not to support currents or measurement charge displacements. This fate is avoided by coupling the system to a thermal bath, which provides dissipation and leads to a nontrivial steady state. Then, currents develop provided that inversion symmetry is broken, and their magnitude is a nonmonotonic function of the measurement rate. Also, here the time-reversal properties of A play a central role. If the measurement preserves time-reversal symmetry, then the current requires strong dissipation to be sizable. By contrast, if A breaks time reversal, a large steady-state current develops, even for weak dissipation.

In the particular case where the measurement preserves inversion, but the Hamiltonian does not, by analogy with classical [30–36] and quantum [37–40] ratchets, we describe the currents as resulting from a quantum-measurement ratchet effect. This is a unique type of ratchet effect, where an inversion-preserving measurement, which acts as an unbiased drive, nonetheless leads to a directed current.

Time-reversal symmetry also plays an important role in the Zeno limit. It is often stated that a watched pot never boils

---

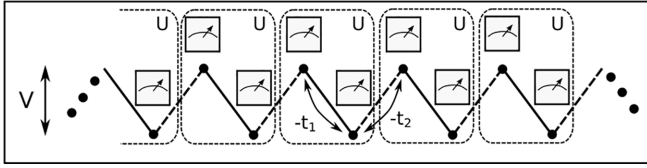*Contact author: podolsky@physics.technion.ac.il

FIG. 1. One-dimensional chain with two sites in a unit cell, with alternating hopping amplitudes t_1 and t_2, and with a staggered potential V, which breaks inversion. A measurement consists of acting with a 2×2 unitary U on all cells simultaneously, measuring the location of the particle, and then acting with the inverse transformation $U^\dagger$.

[41], referring to the fact that nondegenerate measurements lead to frozen dynamics. Here, we interestingly find that local current loops develop when the measurement breaks time-reversal symmetry. In other words, a watched pot can convect.

Our analysis considers both stochastic Poisson measurements and periodic ones. In the latter case, we find resonances when the measurement period matches the natural dynamical scales of the Hamiltonian.

To make the discussion concrete, we restrict our discussion to one-dimensional lattice systems and demonstrate our results on a specific example—a single spinless particle hopping on a dimerized chain with amplitudes $t_1 \neq t_2$ and staggered potential V, with the Rice-Mele Hamiltonian (see Fig. 1)

$$H = \sum_{n=1}^{N} \left[-t_1 c_{2n-1}^\dagger c_{2n} - t_2 c_{2n}^\dagger c_{2n+1} + \text{H.c.} \right.$$
$$\left. + \frac{V}{2}(c_{2n-1}^\dagger c_{2n-1} - c_{2n}^\dagger c_{2n}) \right]. \quad (1)$$

Here, N is the number of unit cells in the chain, and we assume periodic boundary conditions $c_{n+2N}^\dagger = c_n^\dagger$. Inversion symmetry is broken provided $V \neq 0$. The eigenstates of the Hamiltonian are fully specified by the wave vector k and band index $\mu \in \{+, -\}$, with energies $E_{k,\mu} = \mu \sqrt{t_1^2 + t_2^2 + 2t_1 t_2 \cos(2k) + \frac{V^2}{4}}$, where $k = \frac{n\pi}{N}, n \in \{0, 1, ..., N - 1\}$. When appropriate, we will also consider coupling to a thermal bath.

We consider a measurement that determines the unit cell that the particle occupies as well as the value of an operator within the unit cell. This can be written as a single measurement of an operator,

$$A = \bigoplus_{n=1}^{N} \left(2n + \frac{\hat{\mathbf{m}} \cdot \boldsymbol{\sigma} - 1}{2} \right), \quad (2)$$

where $\hat{\mathbf{m}}$ is a unit vector that determines the specific measurement and $\sigma_{x,y,z}$ are the Pauli matrices acting on the two-dimensional Hilbert space within a unit cell. Note that for $\hat{\mathbf{m}} = \hat{\mathbf{e}}_z$, A corresponds to a measurement of the exact location of the particle, where $2n$ distinguishes between different unit cells and $(\sigma_z - 1)/2$ specifies the site within the unit cell. For general $\hat{\mathbf{m}}$, A can be implemented, in practice, through an associated 2×2 unitary transformation U which satisfies $U^\dagger \sigma_z U = \hat{\mathbf{m}} \cdot \boldsymbol{\sigma}$. The unitary U is applied simultaneously on all the unit cells, as sketched in Fig. 1. The measurement of the observable A is then a composite operation, consisting of the

unitary U, a measurement of location, and the inverse unitary $U^\dagger$, performed in rapid succession.

The paper is organized as follows. In Sec. II, we discuss different kinds of charge displacements that can occur in a quantum system with measurements. In Sec. III, we use symmetry arguments to understand the characteristics of the currents that occur when a measurement is performed starting in thermal equilibrium. In Sec. IV, we consider the steady state resulting from repeated measurements on a thermally isolated system. In Sec. V, we couple the system to a thermal bath using the Lindblad formalism and study the case of random Poisson measurements. Finally, in Sec. VI we study the complementary case of Floquet measurements.

II. CHARGE DISPLACEMENT IN A QUANTUM SYSTEM WITH MEASUREMENTS

The current operator on a lattice can be defined from the continuity equation, $\dot{n}(x) = j(x - 1) - j(x)$, where $n(x)$ is the density at site x and $j(x)$ is the current from x to $x + 1$. The center-of-mass velocity is equal to the time derivative of the position operator $\hat{x} = \sum_x x\, n(x)$. This is given by

$$\frac{d\hat{x}}{dt} = \sum_x x\, \dot{n}(x) = \sum_x x[j(x-1) - j(x)] \quad (3)$$

$$= \sum_x j(x) = J, \quad (4)$$

where $J \equiv \sum_x j(x)$ is the current operator summed over all space. The average charge displacement in the time interval (t_i, t_f) is thus

$$\Delta x = \int_{t_i}^{t_f} dt\, \langle J \rangle. \quad (5)$$

Here angular brackets denote an average with respect to the density matrix, $\langle J \rangle = \text{tr}[\rho J]$.

In a closed quantum system with unitary evolution governed by the Hamiltonian H, the velocity operator is given by the Heisenberg equation of motion for $\hat{x}$. Thus,

$$J_H = -i[H, \hat{x}], \quad (6)$$

where we have added the subscript H to indicate that this is the current resulting from the unitary dynamics. We call this type of current the Hamiltonian current.

When quantum measurements are added to the mix, the Hamiltonian current defined above is not enough to capture all particle motion [42,43]. A projective measurement of an observable A leads to a sudden change in the density matrix

$$\rho \mapsto \rho' = \sum_a P_a \rho P_a, \quad (7)$$

where P_a is the operator that projects to the eigenspace of A with eigenvalue a. This represents averaging over all possible outcomes of the measurement.

The sudden nature of projective measurements renders the definition of a current unnatural. Therefore, we consider the average displacement of the position of the particle as a result

of this measurement, which is given by

$$\Delta x_A = \text{tr}[(\rho' - \rho)\hat{x}] = \text{tr}\left[\rho\left(\sum_a P_a \hat{x} P_a - \hat{x}\right)\right]. \quad (8)$$

This is the expectation value of the operator

$$\hat{Q} = \sum_a P_a \hat{x} P_a - \hat{x} \quad (9)$$

in the premeasurement state ρ. We call $\hat{Q}$ the measurement charge displacement. It describes a charge transfer that is sudden to the extent that the measurement is instantaneous. In a system with unitary Hamiltonian dynamics interspersed with measurements, the total charge motion can be obtained from the integral of the Hamiltonian current over the periods of unitary evolution, together with the charge displacement at the instants of measurement.

In systems with periodic boundary conditions, the position operator $\hat{x}$ is ill-defined, rendering the definition of the measurement charge displacement operator problematic. To sidestep this issue, $\hat{Q}$ can be rewritten as

$$\hat{Q} = \frac{1}{2} \sum_a (P_a[\hat{x}, P_a] - [\hat{x}, P_a]P_a). \quad (10)$$

This involves only the commutator of $\hat{x}$ with a local operator, which is well-defined.

Note that the definition of $\hat{Q}$ depends only on the choice of measurement operator A, and is independent of the Hamiltonian. In the special case where the operator A is the position itself, $\hat{Q}$ vanishes exactly, since in that case P_a commutes with $\hat{x}$ in Eq. (9).

We emphasize that we are performing an average over the initial density matrix of the system, over the possible outcomes of the observable A, and over the possible values of the measured displacement.

III. SYMMETRY CONSIDERATIONS FOR A SINGLE MEASUREMENT

In this section, we will consider the creation of currents by a single measurement starting from equilibrium. We will discuss the restrictions that discrete symmetries place on the charge displacements and currents discussed in the previous section. We consider three symmetries: spatial inversion I, time reversal T, and their product IT (more commonly referred to as PT symmetry). The results will play an important role later, when we discuss multiple measurements.

A. Symmetry transformations of the current and displacement operators

Let us first recall the symmetry properties of the Hamiltonian current $J_H = -i[H, \hat{x}]$. This current is odd under time-reversal symmetry T and inversion I, provided that H is invariant under these symmetries:

$$SHS^{-1} = H \Rightarrow \begin{cases} SJ_H S^{-1} = -J_H, & S \in \{I, T\} \\ SJ_H S^{-1} = J_H, & S = IT. \end{cases} \quad (11)$$

Note that if H is not invariant under these symmetries, then J_H will, in general, not have simple transformation rules.

We now turn to the measurement charge displacement $\hat{Q}$. For this, we must consider the transformation properties of the measured observable A under the symmetry operations. Using a common symbol $S \in \{I, T, IT\}$, a special distinction occurs for an observable A that has well-defined parity (either even or odd) under the action of S. For such observables, we will show that $\hat{Q}$ transforms simply under S,

$$SAS^{-1} = \pm A \Rightarrow \begin{cases} S\hat{Q}S^{-1} = -\hat{Q}, & S \in \{I, IT\} \\ S\hat{Q}S^{-1} = \hat{Q}, & S = T, \end{cases} \quad (12)$$

so $\hat{Q}$ is even under time reversal and odd under inversion and IT symmetries. On the other hand, if A does not have well-defined parity under these symmetries, then we cannot make any general claim regarding the symmetry properties of the measurement charge displacement operator.

To demonstrate Eq. (12), we note that, for an eigenstate $|a\rangle$ of A with eigenvalue a, the symmetry-related eigenstate $S|a\rangle$ satisfies

$$AS|a\rangle = \pm SA|a\rangle = \pm aS|a\rangle, \quad (13)$$

so it belongs either to the same eigenspace with eigenvalue a or the eigenspace with the complementary eigenvalue $-a$. Equation (13) implies that the symmetry operator maps projectors onto projectors [44]:

$$SAS^{-1} = \pm A \Rightarrow SP_a S^{-1} = P_{\pm a}. \quad (14)$$

Hence, for an S-even observable, the projector P_a is invariant under the symmetry transformation. For an S-odd observable, the projector P_0 onto the subspace with zero eigenvalue $a = 0$ is invariant, whereas the projectors onto nonzero eigenvalues $a \neq 0$ are mapped onto the complementary projectors P_{-a}.

Since the definition of $\hat{Q}$, Eq. (9), involves a sum over all projectors P_a, this permutation of projectors leaves $\hat{Q}$ unchanged. Hence, the transformation properties of $\hat{Q}$ are determined directly by those of $\hat{x}$, which is odd under inversion and IT symmetries and even under time reversal. This implies Eq. (12).

We comment that for the Rice-Mele model, the observable A as defined in Eq. (2) does not have well-defined parity but can be regarded as a composite operator combining a measurement of the unit cell n and the observable $\hat{\mathbf{m}} \cdot \boldsymbol{\sigma}$ within the unit cell. Hence, the projectors P_a are products of projectors in the two subspaces $P_a = P_n P_\sigma$. The two parts can transform differently under the action of symmetry. The unit cell projectors always satisfy $IP_n I^{-1} = P_{-n}$ and $TP_n T^{-1} = P_n$. Assuming that $S(\hat{\mathbf{m}} \cdot \boldsymbol{\sigma})S^{-1} = \pm\hat{\mathbf{m}} \cdot \boldsymbol{\sigma}$, the projectors P_σ are either left invariant or permuted according to Eq. (14). Hence, $P_a = P_n P_\sigma$ are permuted by the action of the symmetries too, and all the reasoning still holds. Therefore, it is enough to consider the symmetry of $\hat{\mathbf{m}} \cdot \boldsymbol{\sigma}$. In what follows, we will write $SAS^{-1} = \pm A$ as a shorthand for $S(\hat{\mathbf{m}} \cdot \boldsymbol{\sigma})S^{-1} = \pm\hat{\mathbf{m}} \cdot \boldsymbol{\sigma}$.

With the above insights, we now turn to discuss the role of the symmetries in measurement-induced currents.

B. Currents require breaking of inversion symmetry

Inversion symmetry plays an important role in restricting currents. Consider a Hamiltonian that is inversion symmetric, $IHI^{-1} = H$, and suppose that the observable A has well-defined parity under inversion, $IAI^{-1} = \pm A$. If the system

starts in thermal equilibrium, then no currents or measurement charge displacements will develop after a measurement of A, even if multiple measurements of A are carried out in succession at different times.

To see this, note that the equilibrium density matrix $\rho_{\text{eq}} = \frac{e^{-\beta H}}{Z}$ at temperature $T = 1/\beta$ is invariant under inversion, $I\rho_{\text{eq}}I^{-1} = \rho_{\text{eq}}$. The state immediately following a projective measurement of A is

$$\rho_0 = \sum_a P_a \rho_{\text{eq}} P_a. \tag{15}$$

If $IAI^{-1} = \pm A$, then I leads to a permutation of projectors, see Eq. (14), which leaves ρ_0 invariant. Furthermore, unitary evolution by H preserves the inversion symmetry. We conclude that $I\rho(t)I^{-1} = \rho(t)$ at all times. Since the Hamiltonian current is odd under inversion, Eq. (11), this implies that

$$\langle J_H \rangle (t) = \text{tr}(J_H \rho(t)) = \text{tr}(IJ_H I^{-1} I\rho(t) I^{-1})$$
$$= -\text{tr}(J_H \rho(t)) = 0, \tag{16}$$

i.e., the Hamiltonian current vanishes at all times. Similarly, the measurement charge displacement $\hat{Q}$ is also odd under inversion, see Eq. (12), and hence it also vanishes for all measurements.

In the specific case where the observable is nondegenerate, there is a simple intuition behind this result that follows from keeping track of specific measurement outcomes. Inversion-even observables collapse the system to states that do not carry a Hamiltonian current [45]. Inversion-odd observables, on the other hand, collapse the system to current-carrying states. However, we are considering averages over measurement outcomes and this leads to zero average current since the measurement eigenstates come in complementary pairs. These carry opposite currents and are equally likely to occur in thermal equilibrium, leading to a vanishing expectation value for the current.

This result implies that the generation of currents requires the breaking of inversion symmetry, either by A or H. For the former, we mean that A does not have a well-defined parity under inversion. In the next subsection, we will assume that inversion is broken, either by A or H. Finally, we note that the conclusions are unchanged even for initial states that are not thermal, as long as they are invariant under inversion.

C. dc currents require breaking of time-reversal symmetry

Since currents require time-reversal symmetry breaking, one would naively think that T plays an equivalent role to inversion symmetry in preventing currents. In particular, one might expect currents to vanish if $THT^{-1} = H$ and $TAT^{-1} = \pm A$. However, as we show now, time reversal allows currents but constrains their time dependence.

We will first show that time reversal implies the vanishing of the current immediately after a measurement starting from an equilibrium state. Recall that $THT^{-1} = H$ and assume that $TAT^{-1} = \pm A$. Then, the equilibrium density matrix is time-reversal invariant, $T\rho_{\text{eq}}T^{-1} = \rho_{\text{eq}}$. Immediately after a measurement, the density matrix remains time-reversal invariant, since according to Eq. (14) T only permutes the projectors in the sum in Eq. (15). This implies that the Hamiltonian

current *immediately* postmeasurement vanishes. The intuition for this result is similar to that leading to the lack of currents for observables with a well-defined inversion parity. This would not be the case if $TAT^{-1} \neq \pm A$.

However, the current does not remain zero because the evolution of the state after the measurement breaks time reversal, as will be seen. This produces currents, but we now show that they are either oscillating or decaying in nature, so the net displacement after a long time is finite. To see this, we write the density matrix as

$$\rho(t) = \sum_{k,\alpha,\beta} c_k^{\alpha\beta}(t) |k,\alpha\rangle \langle k,\beta|, \tag{17}$$

where $|k,\alpha\rangle$ is an eigenstate of the Hamiltonian with energy $\epsilon_{k,\alpha}$. Here k is a crystal momentum and α is a band index arising from orbital degrees of freedom, so it is not changed upon time reversal. Here, we have assumed translational symmetry, which ensures that $\rho(t)$ is diagonal in k. Immediately following a measurement at $t = 0$, $T\rho(0)T^{-1} = \rho(0)$ implies that the coefficients satisfy

$$c_k^{\alpha\beta}(0) = \left(c_{-k}^{\alpha\beta}(0)\right)^* = c_{-k}^{\beta\alpha}(0), \tag{18}$$

where the second equality follows from Hermiticity of ρ. This condition represents time-reversal symmetry for the density matrix at $t = 0$. Time evolution leads to $c_k^{\alpha\beta}(t) = c_k^{\alpha\beta}(0)e^{-i\omega_{k,\alpha\beta}t}$, where $\omega_{k,\alpha\beta} = \epsilon_{k,\alpha} - \epsilon_{k,\beta}$, which disrupts this condition.

The Hamiltonian current $\langle J_H \rangle (t) = \text{tr}[\rho(t)J_H]$ is then

$$\langle J_H \rangle (t) = \sum_{k,\alpha,\beta} c_k^{\alpha\beta}(0)e^{-i\omega_{k,\alpha\beta}t} \langle k,\beta| J_H |k,\alpha\rangle. \tag{19}$$

To proceed, we distinguish between intraband ($\alpha = \beta$) and interband ($\alpha \neq \beta$) terms in Eq. (19). The intraband terms are time independent since $\omega_{k,\alpha\alpha} = 0$. They equal

$$\langle J_H \rangle_{\text{intra}} = \frac{1}{2} \sum_{k,\alpha} \left[c_k^{\alpha\alpha}(0) - c_{-k}^{\alpha\alpha}(0) \right] \langle k,\alpha| J_H |k,\alpha\rangle, \tag{20}$$

where $TJ_H T^{-1} = -J_H$ has been used to combine terms with opposite momenta together. This is zero due to the balance of the k and $-k$ populations, as follows from the time-reversal invariance, Eq. (18).

Turning our attention to the interband terms, $\alpha \neq \beta$, we obtain

$$\langle J_H \rangle_{\text{inter}} (t) = -i \sum_{k,\alpha\neq\beta} c_k^{\alpha\beta}(0) \sin[\omega_{k,\alpha\beta}t] \langle k,\beta| J_H |k,\alpha\rangle, \tag{21}$$

where we used Eq. (18) and $\langle k,\beta| J_H |k,\alpha\rangle = -\langle -k,\alpha| J_H |-k,\beta\rangle$, as follows from time-reversal symmetry. These terms are oscillating in nature. Hence, for $TAT^{-1} = \pm A$, currents are allowed, but they are either oscillating in time or decaying, due to destructive interference between different frequencies.

To elucidate the role of time-reversal symmetry in preventing dc currents, consider the transition probability for the system in state $|\psi\rangle$ to evolve unitarily for time t, be measured, evolve for time t', and become $|\phi\rangle$:

$$T_{t,t'}^{\psi\to\phi} = \sum_a |\langle\phi| e^{-iHt'} P_a e^{-iHt} |\psi\rangle|^2. \tag{22}$$

TABLE I. Constraints on currents arising from spatial inversion and time-reversal symmetries, following a measurement starting from the equilibrium state. The symbols $\checkmark$ and $\times$ indicate whether the conditions on the leftmost column are satisfied. A value of 0 indicates that a given quantity vanishes by symmetry, while # means it is symmetry allowed. $\langle J_H \rangle (0^+)$ is the Hamiltonian current immediately after a measurement. The measurement charge displacement $\langle \hat Q \rangle$ is permitted by symmetry if inversion symmetry is disrupted, either by H or A. However, two exceptions are observed: ($*$) an observable that is not an eigenoperator of I or T but has IT symmetry will lead to $\langle \hat Q \rangle = 0$. In addition, $\langle \hat Q \rangle = 0$ always for measurements of position ($\dagger$).

$IHI^{-1} = H$	$\checkmark$	$\checkmark$	$\checkmark$	$\times$	$\times$
$IAI^{-1} = \pm A$	$\checkmark$	$\times$	$\times$	$\checkmark$	$\checkmark$
$TAT^{-1} = \pm A$	any	$\checkmark$	$\times$	$\checkmark$	$\times$
$\langle J_H \rangle (0^+)$	0	0	#	0	#
$\langle J_H \rangle (t)$	0	#	#	#	#
$\langle J_H \rangle_{\mathrm{dc}}$	0	0	#	0	#
$\langle \hat Q \rangle$	0	#	#*	#†	#

If $THT^{-1} = H$ and $TAT^{-1} = \pm A$, this is equal to the probability of the time-reversed process,

$$T_{t',t}^{\tilde\phi \to \tilde\psi} = \sum_a | \langle \tilde\psi | e^{-iHt} P_a e^{-iHt'} | \tilde\phi \rangle |^2, \qquad (23)$$

where $|\tilde\psi\rangle$ and $|\tilde\phi\rangle$ are time-reversed partners of states $|\psi\rangle$ and $|\phi\rangle$. Hermiticity of the projectors $P_a^\dagger = P_a$ implies that, for $t = t' = 0$, $T_{0,0}^{\psi \to \phi} = T_{0,0}^{\phi \to \psi}$. This, combined with $T_{0,0}^{\psi \to \phi} = T_{0,0}^{\tilde\phi \to \tilde\psi}$ implies that

$$T_{0,0}^{\tilde\phi \to \tilde\psi} = T_{0,0}^{\phi \to \psi}. \qquad (24)$$

As a consequence, if there is a balance of populations between two time-reversed states before a measurement, the balance will remain after the measurement. This implies the absence of dc currents, see Eq. (20). If $TAT^{-1} \neq \pm A$, then in general the rates in Eq. (24) would differ.

In sum, measurements of observables that are T eigenoperators cause oscillating or decaying currents when the initial state is time-reversal even. On the other hand, measurements that are not T eigenoperators can lead to dc currents.

Turning our attention to $\hat Q$, time-reversal symmetry does not prevent a measurement charge transfer since $\hat Q$ is even under T. On the other hand, IT symmetry does prevent it; see Eq. (12). Below, this will be illustrated in the Rice-Mele model.

As in the previous section, the limitations on the existence of currents are unchanged even if the initial state is not thermal, as long as it is time-reversal symmetric and translationally invariant. In Appendix A, we show that in the special case when A is time even and nondegenerate, the conclusions remain valid regardless of the initial state.

D. Summary and numerical illustration

Table I summarizes the conclusions of the symmetry analysis for the current after a single measurement. Starting from an equilibrium state, if the Hamiltonian is inversion symmet-
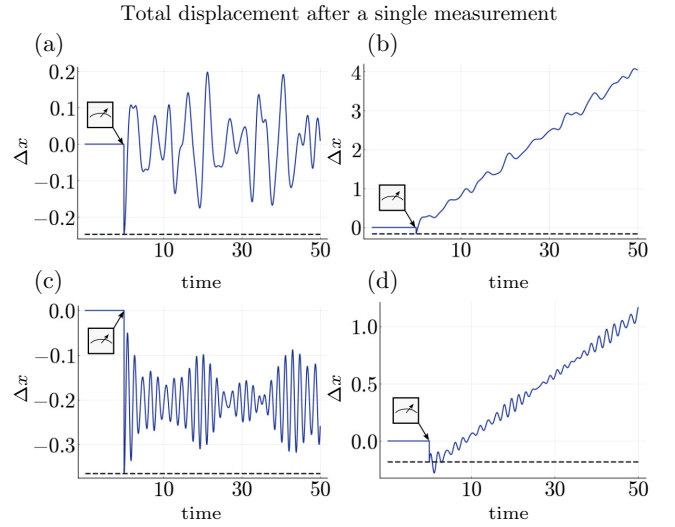

Total displacement after a single measurement

FIG. 2. Total displacement Δx as a function of time. The measured observables and staggered potential for the graphs are (a) $m_y = 0$, $m_x = m_z = \frac{1}{\sqrt{2}}$; $V = 0$; (b) $m_x = m_y = m_z = \frac{1}{\sqrt{3}}$, $V = 0$; (c) $m_x = 1$, $V = 3$; and (d) $m_x = 0$, $m_y = -m_z = \frac{1}{\sqrt{2}}$, $V = 3$. The dashed line shows the charge displacement at the instant of measurement. In (a) and (b), the Hamiltonian has spatial inversion, but the measured observable breaks it. The oscillating part of the current is always present, while there is also a dc component in (b) when time reversal is broken by the measured observable. In (c) and (d), the Hamiltonian doesn't have spatial inversion symmetry, but observables do. If a time-reversal symmetric observable is measured [as in (c)], there is no dc component, while if it is broken as in (d) it is present.

ric and the observable A is an inversion eigenoperator, then no currents or measurement charge displacements develop. Therefore, currents require breaking of inversion symmetry in either H or A. When one of these occurs, then the time-reversal properties of A determine whether there are dc currents or not, and also whether the Hamiltonian current immediately following a measurement vanishes or not.

We illustrate the role of symmetries in constraining the currents using the Rice-Mele model. Figure 2 shows the total displacement

$$\Delta x(t) = \langle \hat Q \rangle + \int_{0^+}^t dt' \langle J_H(t') \rangle \qquad (25)$$

as a function of time for a measurement starting from equilibrium. The first contribution, $\langle \hat Q \rangle$, describes the measurement displacement, i.e., the average particle displacement at the instant of the projective measurement, computed as the expectation value of the operator $\hat Q$ with respect to the density matrix immediately prior to the measurement. The second contribution describes the integral of the average Hamiltonian current for times following the measurement and is averaged with respect to the projected density matrix after the measurement.

Four different cases are considered. In Figs. 2(a) and 2(b), the Hamiltonian is inversion invariant, $IHI^{-1} = H$, while $IAI^{-1} \neq \pm A$. Conversely, in Figs. 2(c) and 2(d), $IHI^{-1} \neq H$ while $IAI^{-1} = \pm A$. In Figs. 2(a) and 2(c), $TAT^{-1} = \pm A$, whereas in Figs. 2(b) and 2(d), $TAT^{-1} \neq \pm A$. It is important

Hamiltonian current after the measurement $\langle J_H \rangle (0^+)$

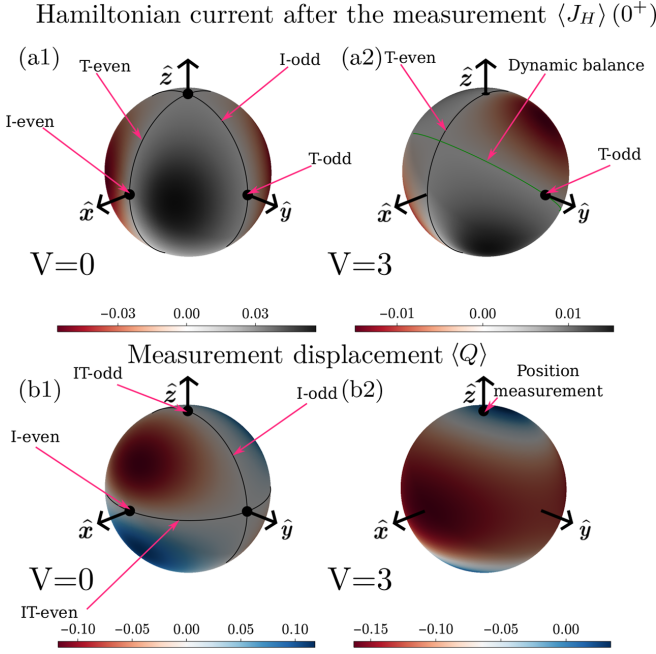Measurement displacement $\langle Q \rangle$

FIG. 3. Transferred charge for every bond observable represented on the Bloch sphere. The parameters of all plots are $t_1 = 1$, $t_2 = 0.5$, while the spatial inversion is controlled by a staggered potential V. For a Hamiltonian current immediately after the measurement, the measurement of T and I eigenoperators leads to the vanishing of the current [shown in (a1)] if the Hamiltonian has spatial inversion. In (a2), the nonzero staggered potential breaks spatial inversion. Then, only time-reversal symmetry gives a simple condition for zero current. The zero-current line shown in green is a result of dynamic balance rather than symmetry. In (b1) and (b2), we show similar results for the measurement displacement. If the Hamiltonian has a center of symmetry as in (b1), the symmetries to consider are spatial inversion and IT symmetry. If the Hamiltonian breaks this symmetry as in (b2), the only point at which displacement is guaranteed to vanish corresponds to the measurement of position, for which the displacement operator is identically zero.

to note that in all scenarios, a measurement displacement occurs ($\langle \hat{Q} \rangle \neq 0$), which is succeeded by oscillatory currents. These features are present despite having averaged over measurement outcomes of the observable A. Furthermore, the disruption of inversion symmetry by either H or A results in similar behavior. However, a qualitative distinction exists between measurements that are not eigenoperators of T and those that are: only measurements that are not T-eigenoperators permit dc currents.

To see the dependence of current on the parameters, Fig. 3 shows the currents for a measurement starting from equilibrium, as a function of $\hat{\mathbf{m}}$ on the Bloch sphere. Figure 3(a1) displays the Hamiltonian current immediately following the measurement, $\langle J_H \rangle (0^+)$, while Fig. 3(b1) shows the measurement displacement, $\langle \hat{Q} \rangle$, both in the case where no staggered potential is present, $V = 0$. Then, the Hamiltonian has time-reversal and inversion symmetries, as does the equilibrium state. As a consequence, currents are only expected for $IAI^{-1} \neq \pm A$. Time reversal T corresponds to complex conjugation in the position basis, thus changing the sign of σ_y while leaving the other two matrices unchanged since they only have

real elements. On the other hand, inversion I exchanges the left and right sites within a cell and is hence represented by σ_x. IT symmetry is a combination of these two symmetries and therefore can be represented as $\sigma_x K$, where K is a complex conjugation operator. The current and measurement displacement vanish along the planes and axes of these symmetries.

Figures 3(a2) and 3(b2) show $\langle J_H \rangle (0^+)$ and $\langle \hat{Q} \rangle$ for $V \neq 0$, when the equilibrium state is not inversion invariant. The locus of points that are T even or T odd still have vanishing Hamiltonian currents $\langle J_H \rangle (0^+)$ as shown in Fig. 3(a2). However, inversion is no longer a useful guide to determine the locations of zero current. In this case, the current vanishes when the inversion breaking of the observable and that of the staggered potential counteract each other. For the measurement displacement in Fig. 3(b2), when inversion is broken, IT symmetry is also broken as default. Then, the only point at which the measurement displacement is guaranteed to vanish is the position measurement $m_z = 1$, for which the displacement is identically zero.

IV. STEADY STATES OF A THERMALLY ISOLATED SYSTEM

We now turn our attention to systems that are measured repeatedly. We consider multiple measurements of the same observable A that occur at a series of arbitrary times. If this is continued for a sufficiently long time, then under fairly generic conditions, the system reaches an infinite-temperature steady state [22,46–49]. We show that currents vanish in this state irrespective of symmetry considerations.

To see that the steady state of a measured quantum system is an infinite-temperature state, we recall that a projective measurement when averaged over all possible outcomes causes the von Neumann entropy of a system $S(\rho) = -\text{tr}[\rho \ln \rho]$ to increase (or stay the same) [47,50]. The infinite-temperature density matrix, being proportional to the identity matrix, is a steady state of both unitary evolution ($U\mathbb{1}U^\dagger = \mathbb{1}$) and of projective measurements ($\sum_a P_a \mathbb{1} P_a = \mathbb{1}$). Therefore, to the extent that the dynamics is ergodic, the steady state under repeated measurements has infinite temperature. This fate can be avoided by two different mechanisms for nonergodicity. First, if there exists a combination of eigenvectors of A and a combination of eigenvectors of H that span the same proper subspace, then the system can be trapped in this subspace [51]. (see Ref. [52] for an experimental demonstration). This occurs, for example, when the observable A commutes with the Hamiltonian. Then, states with different eigenvalues of A are prevented from mixing during the evolution. Second, when measurements are performed infinitely fast, they effectively freeze the unitary evolution between measurements, leading to the quantum Zeno effect [53].

The tendency of measurements to lead the system toward infinite temperature can be further clarified by looking at the transition rates that are induced by it. For two energy eigenstates $|E_1\rangle$ and $|E_2\rangle$, the transition probabilities caused by the measurement of an observable A are identical:

$$\sum_a |\langle E_1|P_a|E_2 \rangle|^2 = \sum_a |\langle E_2|P_a|E_1 \rangle|^2. \qquad (26)$$

This implies that the steady state has equal occupation of energy eigenstates, independent of their energy.

Absence of currents in infinite temperature

Given that the steady state is generically an infinite-temperature state, we now show that currents vanish in this state. There are well-known statistical mechanics systems, such as the asymmetric simple exclusion process [54], which support steady-state currents even with a uniform probability distribution. In this case, the currents arise due to asymmetry in the hopping amplitudes, and one may expect that inversion-breaking measurements could also generate currents through a similar mechanism. We now show that measurements cannot lead to such currents.

We first consider the Hamiltonian current. Writing the infinite-temperature density matrix as $\rho_\infty = \frac{1}{\mathcal{N}}\mathbb{1}$ (here, $\mathcal{N}$ is the dimensionality of the Hilbert space), the expectation value of the Hamiltonian current is

$$\langle J_H \rangle_\infty = \frac{1}{\mathcal{N}}\mathrm{tr}(-i[H, \hat{x}]) = 0, \tag{27}$$

as follows from the cyclic property of the trace.

We turn our attention to the measurement charge displacement. In the infinite-temperature state, $\rho = \mathbb{1}/\mathcal{N}$,

$$\langle \hat{Q} \rangle_\infty = \frac{1}{\mathcal{N}}\mathrm{tr}\left(\hat{x}\sum_a P_a P_a\right) - \frac{1}{\mathcal{N}}\mathrm{tr}(\hat{x}), \tag{28}$$

where we used the cyclic property of the trace. This is seen to vanish identically, since $\sum_a P_a^2 = \sum_a P_a = \mathbb{1}$. Hence, projective measurement cannot result in charge transfer at an infinite temperature [55].

A natural way to avoid the infinite-temperature state is to couple the system to a heat bath. This allows the system to reach a nontrivial steady state that emerges as a consequence of a balance between the bath that cools the system and the measurement apparatus that heats it up. We consider this in the next section.

V. COUPLING TO A THERMAL BATH

We model the dissipative dynamics through the Markovian quantum master equation (Lindblad equation), where the dynamics of an open quantum system is generated by the Lindbladian $\mathcal{L}_0$,

$$\mathcal{L}_{\mathrm{HD}}[\rho] = -i[H, \rho] + \mathcal{D}[\rho], \tag{29}$$

where $\mathcal{D}$ is the dissipator which accounts for the coupling to a thermal bath:

$$\mathcal{D}[\rho] = \sum_\alpha \left(L_\alpha \rho L_\alpha^\dagger - \frac{1}{2}\{L_\alpha^\dagger L_\alpha, \rho\}\right). \tag{30}$$

We choose jump operators L_α so, in the absence of measurements, they thermalize the system at a temperature T. This means that the steady state of this Lindbladian is a Gibbs state $\rho_{\mathrm{eq}} = e^{-\frac{H}{T}}/Z$.

We now imagine that the system is being measured. We start by considering measurements that occur at random uncorrelated times (a Poisson process) with a measurement rate $1/\tau$ [56–58]. Later, in Sec. VI, we will consider time-periodic measurements. In this case, the measurement process can be described by introducing an additional term in the Lindbladian

(see Appendix B),

$$\mathcal{L} = \mathcal{L}_{\mathrm{HD}} + \frac{1}{\tau}\mathcal{L}_{\mathrm{m}}, \tag{31}$$

where $\mathcal{L}_{\mathrm{m}}$ acts on the density matrix as

$$\mathcal{L}_{\mathrm{m}}[\rho] = \sum_a (P_a \rho P_a) - \rho. \tag{32}$$

We observe that the Kraus map $\mathcal{P}_A[\rho] = \sum_a P_a \rho P_a$, corresponding to measurements is a superprojector. We can define the complementary projector $\mathcal{Q}_A = 1 - \mathcal{P}_A$, so $\mathcal{P}_A \mathcal{Q}_A = 0$. The measurement term in the Lindbladian [Eq. (31)] is $\frac{1}{\tau}\mathcal{L}_{\mathrm{m}}\rho = -\frac{1}{\tau}\mathcal{Q}_A\rho$ which causes any elements that are off-diagonal in the measurement basis to decay with a characteristic decay time τ.

It is interesting to note that the same Lindbladian can be obtained for a system under continuous weak measurement of an observable A, see Ref. [57]. There, the measurement strength takes on the role of the measurement rate $1/\tau$ in our analysis. Therefore, our discussion of currents in the Poisson measurement scheme is also relevant to such systems.

The steady state can be determined from the condition $\mathcal{L}[\rho_{\mathrm{st}}] = 0$, or

$$(\mathcal{L}_{\mathrm{m}} + \tau\mathcal{L}_{\mathrm{HD}})[\rho_{\mathrm{st}}] = 0. \tag{33}$$

It is interesting to see how the Lindblad equation predicts an infinite temperature state in the absence of dissipation. Then, Eq. (33) becomes

$$-\mathcal{Q}_A\rho_{\mathrm{st}} - i\tau[H, \rho_{\mathrm{st}}] = 0. \tag{34}$$

Multiplying this by ρ_{st} and computing the trace gives $0 = -i\tau\ \mathrm{tr}[\rho_{\mathrm{st}}[H, \rho_{\mathrm{st}}]] = \mathrm{tr}[\rho_{\mathrm{st}}\mathcal{Q}_A\rho_{\mathrm{st}}] = \mathrm{tr}[(\mathcal{Q}_A\rho_{\mathrm{st}})^2]$, where we used $\mathrm{tr}[(\mathcal{P}_A\rho_{\mathrm{st}})(\mathcal{Q}_A\rho_{\mathrm{st}})] = 0$. This implies $\mathcal{Q}_A\rho_{\mathrm{st}} = 0$, i.e., ρ_{st} commutes with A. If $\mathcal{Q}_A\rho_{\mathrm{st}} = 0$, then Eq. (34) implies that ρ_{st} commutes with H as well. For generic A and H, ρ_{st} must therefore be the infinite temperature state.

We now turn to define and study the steady-state currents.

A. Currents in measured open quantum systems

In an open quantum system undergoing Lindblad dynamics, the Hamiltonian current does not satisfy the continuity equation. The presence of measurements and dissipation in the master equation forces us to consider additional types of currents that do not exist in closed quantum systems measurement currents and dissipative currents. Only the total current, which is the sum of all three, is conserved. As we will show below, the measurement current is directly related to the measurement charge displacement $\hat{Q}$.

We use the generalized definition of current between sites x and y for a quantum master equation [43],

$$j^{x\to y} = \frac{1}{2}\left\{P_x, \frac{dP_y}{dt}\right\} - \frac{1}{2}\left\{P_y, \frac{dP_x}{dt}\right\}, \tag{35}$$

where P_x and P_y are projectors onto x and y and $\{,\}$ is the anticommutator. The current is defined so it explicitly satisfies the continuity equation. The current, integrated over all space, is then

$$J = \sum_{x<y}(y - x)j^{x\to y}, \tag{36}$$

where the factor of $(y - x)$ takes into account the distance traveled by a particle in the transition from x to y [59]. Equation (35) is a Heisenberg picture expression, written in terms of the time derivatives of the projectors P_x. A more explicit expression for the current can be obtained using [43]

$$\frac{d}{dt} P_x = \mathcal{L}^\dagger [P_x], \tag{37}$$

where $\mathcal{L}^\dagger$ is the adjoint Lindbladian:

$$\mathcal{L}^\dagger[\Theta] = i[H, \Theta] + \frac{1}{\tau} \left(\sum_a (P_a \Theta P_a) - \Theta \right)$$
$$+ \sum_\alpha \left(L_\alpha^\dagger \Theta L_\alpha - \frac{1}{2} \{ L_\alpha^\dagger L_\alpha, \Theta \} \right). \tag{38}$$

Replacing $\frac{dP_x}{dt}$ by $\mathcal{L}^\dagger[P_x]$ (and similarly for P_y) in Eq. (35) gives the expressions for the Hamiltonian, measurement, and dissipative currents, depending on which term of the adjoint Lindbladian is used.

The Hamiltonian part of the evolution leads to the Hamiltonian current discussed in Sec. II. The space-integrated current takes the form

$$J_H = -i \sum_{x,y} P_y H P_x (y - x) = -i[\hat{x}, H]. \tag{39}$$

The measurement part of the Lindbladian $\mathcal{L}_m$ gives the measurement current:

$$j_{\text{meas}}^{x \to y} = \frac{1}{2\tau} \sum_a (\{ P_x, P_a P_y P_a \} - (x \leftrightarrow y)). \tag{40}$$

Integrating over space gives

$$J_{\text{meas}} = \frac{1}{\tau} \left(\sum_a P_a \hat{x} P_a - \hat{x} \right) = \frac{\hat{Q}}{\tau}, \tag{41}$$

where $\hat{Q}$ is defined in Eq. (9). This relation describes the fact that charge displacements occur, on average, at a rate $1/\tau$.

Finally, the last term in Eq. (38) is a source of a dissipative current that comes from thermal bath jump operators [43]. This gives

$$J_{\text{dis}} = \frac{1}{2} \sum_{n,m} j_{\text{dis}}^{n \to m} (m - n)$$
$$= \sum_\alpha \left[L_\alpha^\dagger \hat{x} L_\alpha - \frac{1}{2} \{ \hat{x}, L_\alpha^\dagger L_\alpha \} \right]. \tag{42}$$

The second equality relies on the locality of $j_{\text{dis}}^{n \to m}$. For the Hamiltonian and measurement currents, locality is guaranteed by the short-range interactions and local measurements. By contrast, to ensure equilibration it is often convenient to work with a bath that spans the whole system, rendering the definition of dissipative currents problematic. For this reason, we focus on a sufficiently weak dissipation rate, compared to the Hamiltonian scale and to the measurement rate $1/\tau$. Then, the dissipative current can be neglected. We comment that the use of a Lindblad master equation to describe the coupling to a thermal bath is only justified in this limit [60].

B. Measurement-induced steady-state currents in the Rice-Mele model

We will demonstrate the existence and properties of steady-state currents on the Rice-Mele model defined in the Introduction. As will become clear, much of the intuition comes from the single-measurement results. We model the thermal bath by choosing jump operators that connect energy eigenstates,

$$L_\alpha = L_{k,\mu;q,\nu} = \sqrt{\gamma_{k,\mu;q,\nu}} c_{k,\mu}^\dagger c_{q,\nu}, \tag{43}$$

with the decay rates chosen to satisfy detailed balance at temperature T:

$$\gamma_{k,\mu;q,\nu} = \begin{cases} \frac{\gamma_0}{\mathcal{N}} & \text{for } E_{k,\mu} < E_{q,\nu} \\ \frac{\gamma_0}{\mathcal{N}} e^{-\frac{E_{k,\mu} - E_{q,\nu}}{T}} & \text{for } E_{k,\mu} \geqslant E_{q,\nu}, \end{cases} \tag{44}$$

where k and q are wave vectors, μ and ν band indices, and γ_0 sets the overall timescale of relaxation. The factor $1/\mathcal{N}$ is added since we allow transitions between all pairs of energy levels. This ensures that the relaxation rate of the system remains finite as $\mathcal{N} \to \infty$. The dissipation is inversion symmetric if the Hamiltonian is, so we do not have to consider its symmetry properties independently.

The steady state of the Lindbladian—consisting of the Hamiltonian dynamics together with dissipation and measurements—is found numerically. Throughout, we assume a weak dissipation rate compared to the Hamiltonian scale, $\gamma_0 \ll ||H||$.

Figure 4(a) shows the total (Hamiltonian plus measurement) current for an inversion-odd observable, as a function of τ. The current is obtained from the expectation value of the corresponding operators with respect to the steady-state density matrix. The presence of steady-state currents is a demonstration of the quantum-measurement ratchet effect, where the combination of an inversion-invariant measurement and an inversion-breaking Hamiltonian give rise to currents. The ratchet effect occurs only for $V \neq 0$ since a non-zero staggered potential (ratchet potential) is necessary to break the inversion symmetry. In addition, changing the sign of the potential reverses the direction of the current.

By contrast, Fig. 4(b) shows the total current for an observable that is not an inversion eigenoperator, $m_x = m_y = -m_z = 1/\sqrt{3}$. Here, a current is created even in the absence of a staggered potential, and the current is not odd in V.

The currents in Fig. 4 display a pronounced peak at $\tau \approx 1/\gamma_0$, which is the typical equilibration time of the bath. To understand the origin of this peak, we begin from the rare measurement limit $\tau \gg 1/\gamma_0$. There, the current is expected to approach zero, since the system is only rarely perturbed from equilibrium. Then, the currents are given by the cumulative displacement following a single measurement before returning to equilibrium, divided by the time between measurements τ.

In this context, it is important to distinguish between measurements that are time-reversal eigenoperators, $TAT^{-1} = \pm A$, and those that are not. In the latter case, measurements starting from equilibrium give rise to dc currents, J_{dc}. Due to dissipation, such currents decay on a timescale of order $1/\gamma_0$. Hence, the cumulative displacement per measurement is $\approx J_{dc}/\gamma_0$, and the average current in the rare-measurement limit
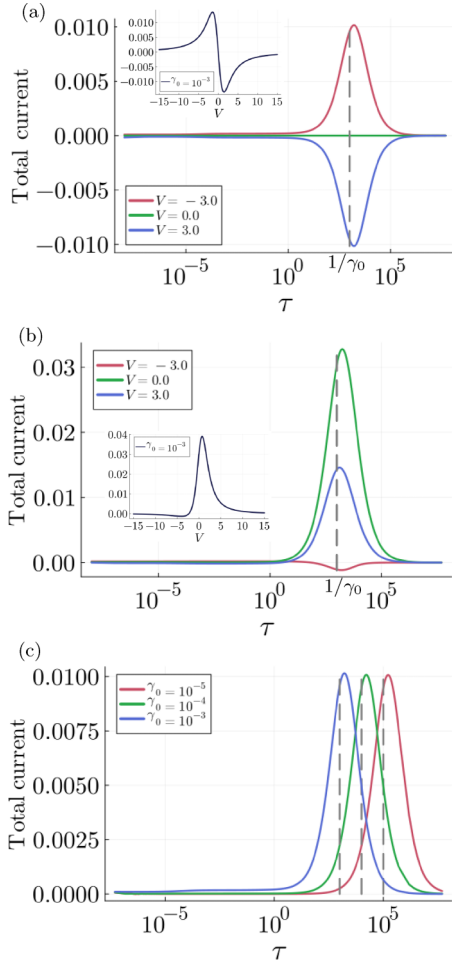
FIG. 4. Steady-state currents as a function of average measurement time. In (a), the measured observable is inversion-odd and is given by $m_y = m_z = 1/\sqrt{2}$, and $m_x = 0$. Note that the τ axis is logarithmic in all plots. The total current dependence is shown for three values of the staggered potential as the staggered potential V is varied. The relaxation scale, $\tau \approx 1/\gamma_0$, is marked by dashed lines, where $\gamma_0 = 10^{-3}$. The current changes direction when the staggered potential is tilted in the opposite direction ($V \rightarrow -V$). This is clearly not the case when the measured observable is not an inversion eigenoperator, as seen in (b), where the measured observable is given by $m_x = m_y = -m_z = 1/\sqrt{3}$. In the insets, we plot the dependence of total current on staggered potential for $\tau = 1/\gamma_0$. In (c), we show how the location of the peaks matches the relaxation timescale $1/\gamma_0$ where the total current is plotted for different values of γ_0 and $V = -3.0$. The plot is given for the same inversion-odd observable as the one in (a). The parameters of all the plots are $t_1 = 1.0$, $t_2 = 0.5$, $T = 0.1$, and $N = 3$.

is $\approx J_{dc}/(\gamma_0 \tau)$. As τ is decreased from the rare measurement limit, significant heating occurs as a result of the measurements, as will be shown below. This heating suppresses the currents, an effect that becomes important when measurements are closer together than the relaxation time $\tau_r = 1/\gamma_0$. The net effect is that a peak in the current is obtained at $\tau \approx \tau_r$, whose height is $\approx J_{dc}/(\gamma_0 \tau_r) = J$, which is independent of γ_0, as seen in Fig. 4(c).

By contrast, for $TAT^{-1} = \pm A$, no dc currents are created starting from equilibrium. This implies that, in the rare measurement limit, the charge displacement between each pair of measurements is of order 1, and that the average current is of order $1/\tau$. Then, the current for $\tau = \tau_r$ is of order $1/\tau_r = \gamma_0$, which is negligible for weak dissipation. Furthermore, as τ is decreased below τ_r, the heating is found to prevent currents from developing. For this reason, to induce sizable steady-state currents in the weak dissipation limit, measurements must not be time-reversal eigenoperators.

Irrespective of the heating, the current is also expected to approach zero in the Zeno limit, $\tau \ll \tau_Z$, where $\tau_Z = \gamma_0/||H||^2$ is the Zeno onset scale, derived in Appendix C. Here, $||H||$ is the characteristic energy scale of the system. The emergence of the Zeno onset scale can also be understood intuitively. When A is measured twice in close succession, the system is with high probability determined to remain in the same state. The Zeno effect comes about since the Born rule implies a quadratic timescaling of the effective evolution—which is of order $||H||^2\tau^2$ [53]. The dissipation, on the other hand, evolves the density matrix according to classical probability, which means that it has a usual linear scaling $\gamma_0\tau$. For sufficiently small τ, the dissipation always wins in this competition, and the Hamiltonian evolution is irrelevant. The turnaround point is at τ_Z which is the mean measurement time at which the two scales become comparable. For larger times, the evolution is dominated by the Hamiltonian, which together with the measurements drive the system toward the infinite-temperature state since the dissipation can be neglected. Then the conclusions of Sec. IV apply.

In the Zeno limit, currents are small because rapid local measurements tend to freeze particle motion, as will be analyzed in detail in the following section.

To further understand the suppression of currents below the peak at $\tau \approx 1/\gamma_0$, it is useful to study the von Neumann entropy S of the steady-state density matrix as a function of τ; see Fig. 5(a). For rare measurements, $\tau \gg 1/\gamma_0$, the system has time to equilibrate to the bath temperature, which is low in our simulation. Hence, the entropy becomes small. As τ is decreased, when the measurement time becomes comparable to the relaxation time $1/\gamma_0$, S rises rapidly. For $\tau_Z \ll \tau \ll 1/\gamma_0$, the bath struggles to remove the entropy created by the measurements, and therefore the entropy plateaus close to the infinite temperature value $\ln(2N)$. This is the origin of the current suppression, since the current is guaranteed to vanish in the infinite-temperature state; see Sec. IV. Finally, for $\tau \ll \tau_Z$, the system enters the Zeno limit, in which the Hamiltonian has no effect and the steady state is determined by the interplay between measurements and dissipation. Then, the entropy saturates below the infinite temperature entropy at a value that is independent of γ_0.

Note that as the dissipation is made weaker, the high-entropy plateau in Fig. 5(a) becomes broader. This is consistent with the fact that, in the absence of dissipation, the steady state is an infinite temperature state, as discussed in Sec. IV. At a finite value of γ_0, the range of the plateau extends from τ_Z to $1/\gamma_0$, as argued above. The distance to the infinite temperature state can be seen more clearly from the normalized difference between the von Neumann entropy of
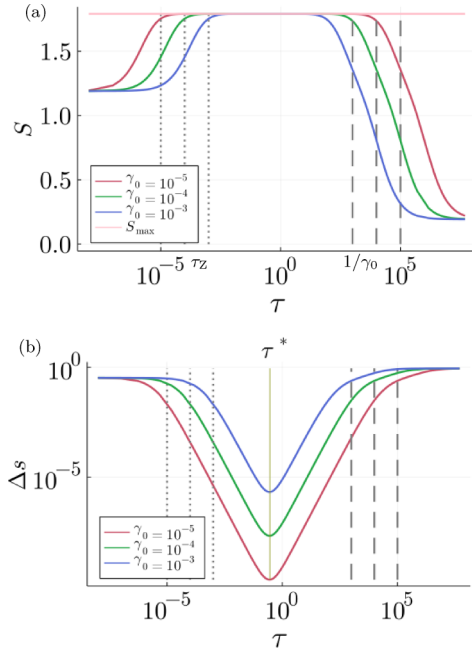
FIG. 5. The von Neumann entropy as a function of average measurement time. The measured observable is given by $m_y = m_z = 1/\sqrt{2}$, and $m_x = 0$. In (a), we show the entropy as a function of measurement time τ. The maximal entropy S_{max} of an infinite-temperature state is almost saturated near the middle of the plot. In (b), the relative distance of the entropy from the maximal entropy [Eq. (45)] is plotted on the log-log scale. The parameters of the plots are the same as in Fig. 4.

the system S and the maximum entropy $S_{max} = \ln(2N)$. The normalized difference,

$$\Delta s = \frac{S_{max} - S}{S_{max}}, \qquad (45)$$

is plotted as a function of measurement time τ on a log-log scale in Fig. 5(b). We see that the steady-state entropy reaches a maximum at τ^*, which is of order $1/||H||$ and independent of γ_0. On either side of τ^*, the maximum entropy displays a power-law behavior over a large window, with $\Delta s \propto \tau^{-2}$ for $\tau_Z \ll \tau \ll \tau^*$ and $\Delta s \propto \tau^{+2}$ for $\tau^* \ll \tau \ll 1/\gamma_0$. An analytic derivation for this behavior is given in Appendix C.

C. The Zeno limit and local current loops

In the Zeno limit, measurements are fast relative to the Hamiltonian and dissipative timescales [61]. Then the system stays very close to the measurement subspace (the space of density matrices that are block-diagonal in the measurement basis). Therefore, if measurements are local and nonoverlapping in space, charge cannot escape the measurement subspace, thus forbidding global currents. Interestingly, we will show that the Hamiltonian and measurement charge displacements do not individually vanish but their sum does. Furthermore, despite the absence of charge displacements, we will show that in the Zeno limit steady-state currents can form loops within each measurement subspace, even when the measurement subspace is nondegenerate. These current loops show that motion can occur when a system is continually

observed, in a counterpoint to the Zeno effect. While the Zeno effect implies only that transitions between states are very slow, a current of order one is still found.

For simplicity, throughout we assume that the measurement operator A is nondegenerate. When this is not the case, one may expect interesting dynamics within the degenerate Zeno subspaces [3,12–14,53,62], which we do not consider here.

In the Zeno limit, the density matrix will be nearly diagonal in the basis of measurement outcomes. The probabilities of the outcomes are determined by balancing transitions between them by the coupling to the bath. To represent this analytically, we treat the measurements as the dominant part of the Lindbladian and the unitary evolution and the coupling to the bath as perturbations. Then, using the perturbation theory derived in Appendix C and in Ref. [63], we find that to zeroth order in τ,

$$\rho_{st}^{(0)} = \sum_a w_a^{(0)} |a\rangle \langle a|, \qquad (46)$$

where $w_a^{(0)}$ is the occupation of the eigenstate $|a\rangle$. This is given by the balance equation

$$\sum_{a' \neq a} w_{a'}^{(0)} T^{a' \to a} = w_a^{(0)} \sum_{a' \neq a} T^{a \to a'}, \qquad (47)$$

where $T^{a \to a'} = \sum_\alpha |\langle a'|L_\alpha|a\rangle|^2$ is the transition rate from state $|a\rangle$ to state $|a'\rangle$, and L_α are the quantum jump operators; see Eq. (30). Note that even though the dissipation is weak, it determines the steady state in the strict Zeno limit, whereas the Hamiltonian appears only at higher orders in τ.

1. Hamiltonian and measurement currents in the Zeno limit

Since the density matrix in Eq. (46) is diagonal in the measurement basis, it is unaffected by measurements. Therefore, the expectation value of the measurement current with respect to the zeroth order density matrix vanishes, $\langle J_{meas} \rangle_{\rho_{st}^{(0)}} = 0$. The first contribution to $\langle J_{meas} \rangle$ then arises from $\rho_{st}^{(1)}$, which is linear in τ, and is given by [see Appendix C, Eq. (C24)]

$$\langle J_{meas} \rangle_{\rho_{st}^{(1)}} = \text{tr}(-i[H, \rho_{st}^{(0)}] J_{meas}) \tau, \qquad (48)$$

up to corrections of order $\gamma_0/||H||$ which can be neglected for weak dissipation. The measurement current operator, Eq. (40), has an overall factor of $1/\tau$ in its definition, making this contribution of the same order as the Hamiltonian current at zeroth order, $\langle J_H \rangle_{\rho_{st}^{(0)}} = \text{tr}(\rho_{st}^{(0)} J_H)$. For a generic observable, we find that both currents are nonzero individually. However, their sum cancels

$$\langle J_{meas} \rangle_{\rho_{st}^{(1)}} + \langle J_H \rangle_{\rho_{st}^{(0)}} = 0 \qquad (49)$$

up to corrections of order $\gamma_0/||H||$, as proven in Appendix D. This follows intuitively since we perform measurements that are local and nonoverlapping in space. Then, in the strict Zeno limit, particles cannot leave the domain over which the local measurements act, e.g., one of the unit cells in the Rice-Mele model, and therefore the total current must be zero. This cancellation is born out by numerical results in the Rice-Mele model, as seen in Fig. 6. This cancellation is discussed in more detail in Appendix E.
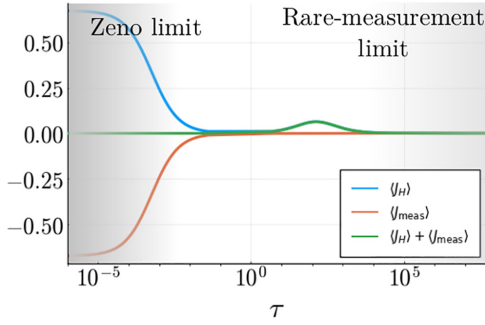
FIG. 6. Hamiltonian, measurement, and total current dependence on measurement time τ. The τ axis is logarithmic. The parameters of the plot are $t_1 = 1.5$, $t_2 = 1.0$, $V = 3.0$, $\gamma_0 = 0.01$, $T = 0.1$, $N = 3$, and the measured observable is specified by $m_x = m_y = -m_z$. When τ is very small, we are in the Zeno limit, and the measurement current compensates for the Hamiltonian current.

2. Local current loops in the Zeno limit

Thus far, we have focused on dimerized Hamiltonians with bond measurements. It is also interesting to consider Hamiltonians with a three-site unit cell acted on by three-site measurements. Here we consider

$$H = \sum_{n=1}^{N} \left[\left(-t_1 c_{3n-2}^{\dagger} c_{3n-1} - t_2 c_{3n-1}^{\dagger} c_{3n} - t_3 c_{3n}^{\dagger} c_{3n+1} + \text{H.c.} \right) + \frac{V}{2} \left(c_{3n-2}^{\dagger} c_{3n-2} - c_{3n}^{\dagger} c_{3n} \right) \right].$$ (50)

The model is pictorially represented in Fig. 7(a). Each unit cell contains two bonds with hopping integrals t_1 and t_2 and the bond connecting two cells has hopping integral t_3. We choose the measured observable as a nondegenerate operator whose eigenstates are restricted within the unit cell. Following the argument for the Rice-Mele model, the net charge transfer has to vanish in the Zeno limit. However, this does not prohibit current loops within each unit cell, as shown in Fig. 7(b).

To show that loop currents can emerge we choose, for concreteness, a measurement operator whose eigenstates within the unit cell are

$$|\Psi_1(\alpha)\rangle = \frac{1}{\sqrt{3}} (|1\rangle + e^{i\alpha} |2\rangle + |3\rangle),$$ (51)
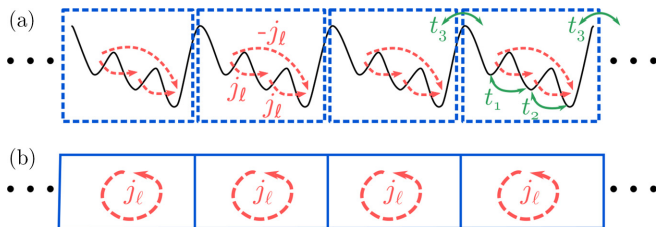

FIG. 7. Illustration of the three-site model. The measurements of an observable are performed on three-site unit cells, shown as dashed boxes in (a). Particles hop between sites with amplitudes $t_{1,2,3}$. In the Zeno limit, measurements prohibit charge transfer between the unit cells. This implies that the net current vanishes. However, as illustrated in (b), this does not prohibit the existence of loop currents within the unit cell (drawn in red).

$$|\Psi_2(\alpha)\rangle = \frac{1}{\sqrt{2}} (|1\rangle - e^{i\alpha} |2\rangle),$$ (52)

$$|\Psi_3(\alpha)\rangle = \frac{1}{\sqrt{6}} (|1\rangle + e^{i\alpha} |2\rangle - 2|3\rangle).$$ (53)

If the parameter α is not an integer multiple of π, complex phases are present. Then, the measured observable is not even under time reversal, and currents are not prohibited by symmetry.

The steady-state currents are computed in Appendix E. There, it is found that the currents between sites satisfy $j^{1\to2} = j^{2\to3} = -j^{1\to3} = j_\ell$, where

$$j_\ell = \frac{1}{54} [-(t_1 + 2t_2)(3u^{(0)}(\alpha) - 2) + 3(t_1 - t_2)\Delta u^{(0)}(\alpha)] \sin(\alpha).$$ (54)

Here $u^{(0)}$ and $\Delta u^{(0)}$ are population parameters determined by solving the balance equation, Eq. (47), and which depend on α. Hence, the integrated total current vanishes for any value of α, $j^{1\to2} + j^{2\to3} + 2j^{1\to3} = 0$, as expected. However, the nonvanishing of j_ℓ signals the presence of loop currents in the Zeno limit, as advertised.

VI. FLOQUET MEASUREMENTS

We now consider a Floquet measurement scheme in which measurements are performed periodically in time with a fixed period τ [12,13]. In contrast to the Poisson measurement scheme, the system now lacks a true steady state. Instead, the steady state is stroboscopic, with a time-periodic density matrix with period τ. As we now show, this allows Floquet measurements to probe the dynamics of the current following a measurement.

Figure 8 shows the total current for Floquet measurements of an inversion-preserving and time-reversal breaking observable in a system with broken inversion symmetry ($V \neq 0$). The results were calculated by numerically evolving the density matrix and evaluating the expectation value of the Hamiltonian current once the system reaches a stroboscopic steady state. Figure 8(a) shows the current in the rare-measurement limit $\tau_m \gg 1/\gamma_0$. In this limit, the system has time to relax to equilibrium between measurements. Then, the evolution of the current created by the measurement is revealed to oscillate on a timescale controlled by the Hamiltonian parameters and to decay with a rate of order γ_0. There is a net charge transfer which we show by integrating the current over time, as seen in the inset of the figure. This indicates a nonzero average current, $\bar{J}_H$, defined as the integrated charge transfer divided by the measurement period τ:

$$\bar{J}_H = \frac{1}{\tau} \int_0^\tau dt \, \text{tr}[\rho(t) J_H].$$ (55)

Figure 8(b) shows the Hamiltonian current near the Zeno limit. Similar to the Poisson case, in the Zeno limit, the Hamiltonian current is compensated by the measurement charge displacement to give net zero displacement.

Figure 9(a) shows the current as a function of τ and compares it to the Poisson measurement protocol. In both the Zeno and rare measurement limits, the two protocols converge to each other. Both schemes display a broad peak at
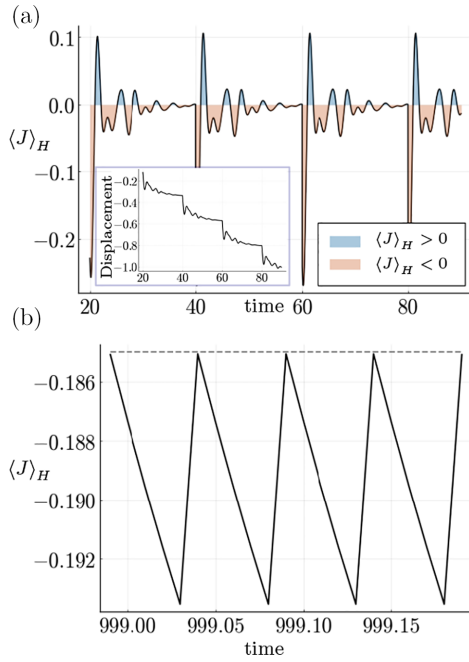
FIG. 8. Expectation value of the Hamiltonian current as a function of time in the Floquet measurement scheme. The measured observable is given by $m_y = m_z = 1/\sqrt{2}$, and $m_x = 0$. The parameters of the plot are $t_1 = 1.0$, $t_2 = 0.5$, $V = 1.5$, $T = 0.2$, $N = 4$, and $\gamma_0 = 0.5$. In (a), the time between measurements is $\tau = 20$, which is large compared to the relaxation time of the system and the system has enough time to relax until close to thermal equilibrium between measurements. In the inset, we show that for the given parameters, the particle moves to the left, on average, by time integrating the Hamiltonian current and adding the measurement displacement. In (b), $\tau = 0.05$ and the evolution time dependence of the Hamiltonian current can be well approximated by taking low orders of expansion in τ. Near the Zeno limit, the measurement charge displacement, not shown, is roughly compensated by the Hamiltonian current.

$\tau \approx 1/\gamma_0$. However, the Floquet measurement scheme reveals a series of narrow resonances which, as shown in Fig. 9(b), are almost periodic in τ. The origin of these resonances is the current oscillations induced by measurements, as seen in Fig. 8. This suggests that Floquet measurements might be used as a method for probing the dynamics of quantum systems.

VII. DISCUSSION

Our paper provides a framework for analyzing currents in monitored quantum systems. We showed that, beyond the usual Hamiltonian current, there is a measurement current, which can be comparable in magnitude. The central topic has been the interplay of the symmetries of the Hamiltonian and the measurement observable, which dictates whether currents can exist, and their magnitude. In particular, currents can be generated whether the measurement operators are time-reversal symmetric or not, due to the irreversibility of the system. However, time-reversal breaking observables give rise to enhanced currents. It would be interesting to investigate to what extent these differences based on symmetry survive in more general systems, such as ones including interactions for example. Similar considerations about symmetry may influ-
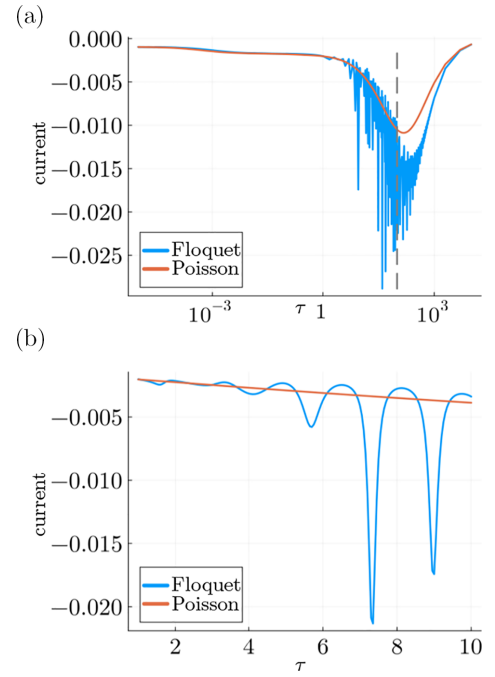

FIG. 9. Dependence of current on measurement timescale τ. Floquet and Poisson measurement schemes are compared. The plot parameters are $t_1 = 1.0$, $t_2 = 0.5$, $V = 3.0$, $T = 0.1$, $N = 3$, and $\gamma_0 = 0.01$. For Floquet measurements, $\bar{J}_H$ is shown. Measurements are of $m_y = m_z = 1/\sqrt{2}$, and $m_x = 0$. Note that the Floquet measurement scheme displays resonances when the measurement period matches some of the internal system frequencies, as shown in (b), which focuses on a small window of (a) but on a linear scale.

ence other properties of monitored quantum systems, beyond currents. In particular, monitoring a particle in this way could be an interesting way of generating quantum active matter [64–67].

APPENDIX A: NONDEGENERATE T-EVEN OBSERVABLES

In Sec. III C, we showed that a measurement operator A that is either even or odd under the action of time reversal ($TAT^{-1} = \pm A$) does not give rise to dc currents, provided the measurement is done on a state that is time-reversal symmetric. In this Appendix, we show that, in the special case that A is nondegenerate and time-reversal even, $TAT^{-1} = A$, then there are no dc currents after the measurement, regardless of the initial state.

When these conditions are satisfied, then each measurement induces a state that is time-reversal invariant, thereby precluding the occurrence of dc currents. To see this, observe that, in this scenario, the eigenstates of A are also eigenstates of T, $T |a\rangle = |a\rangle$. These eigenstates therefore have no current initially, and as in Sec. III C, they also do not carry any dc

currents because they have balanced occupation numbers at k and $-k$. Thus, even if the system starts out in a state that is carrying a current, the measurement switches off the current by forcing the system into a time-reversal symmetric state. The current vanishes in this case for every measurement of A, without the need to average over outcomes.

APPENDIX B: DERIVATION OF THE MEASUREMENT LINDBLADIAN

We derive the Lindbladian for a system that undergoes repeated measurements of an observable A at random and uncorrelated times with a rate $1/\tau$.

We begin by discretizing time into short intervals Δt and consider how the density matrix changes between t_n and $t_{n+1} = t_n + \Delta t$. In the small time Δt, the density matrix evolves with the Lindbladian $\mathcal{L}_{\mathrm{HD}}$ [defined in Eq. (29)] into $e^{\mathcal{L}_{\mathrm{HD}}\Delta t}[\rho(t_n)]$. At the end of the interval, it is measured with probability $\frac{\Delta t}{\tau}$ causing it to change as in (7), or not measured, with probability $1 - \frac{\Delta t}{\tau}$. (The measurement may be regarded as occurring at the end of the interval since the order in which the measurement and the rest of the evolution occurs does not matter for a short interval of time, since they both involve infinitesimal changes to ρ, so they commute to first order.) The density matrix at $t_{n+1} = t_n + \Delta t$ is

$$\rho(t_{n+1}) = \left(1 - \frac{\Delta t}{\tau}\right) e^{\mathcal{L}_{\mathrm{HD}}\Delta t}[\rho(t_n)]$$
$$+ \frac{\Delta t}{\tau} \mathcal{P}_A[e^{\mathcal{L}_{\mathrm{HD}}\Delta t}[\rho(t_n)]] + \mathcal{O}(\Delta t^2). \quad \text{(B1)}$$

In the limit $\Delta t \to 0$, one finds

$$\frac{d\rho(t)}{dt} = \mathcal{L}_{\mathrm{HD}}[\rho(t)] + \frac{1}{\tau}[\mathcal{P}_A[\rho(t)] - \rho(t)]. \quad \text{(B2)}$$

This equation describes the evolution of the density matrix averaged over all measurement histories. It retains the canonical Lindblad form with additional jump operators that are projectors P_a onto eigenstates of the measured observable A. When the measured observable acts on a two-site unit cell, the projectors for the specific cell can be written as $P_\pm = \frac{1}{2}(1 \pm U\sigma_z U^\dagger)$. The term in the measurement part of the Linbladian for this cell is then $\frac{1}{2\tau}(U\sigma_z U^\dagger \rho(t) U\sigma_z U^\dagger - \rho(t))$. This has the form of a decohering bath with the decoherence rate $1/2\tau$. In this sense, the measurement apparatus is an engineered bath that picks a preferred basis and eliminates the coherences within it.

APPENDIX C: PERTURBATION THEORY FOR THE STEADY STATE

In this Appendix, we develop a perturbation theory to compute the steady state for the Lindbladian

$$\mathcal{L} = \mathcal{L}_0 + \mathcal{V}, \quad \text{(C1)}$$

where $\mathcal{V}$ is a small perturbation relative to $\mathcal{L}_0$. The perturbation theory presented here is an application to Lindbladians of Brillouin-Wigner perturbation theory of quantum mechanics [68]. The reason for using this approach rather than more straightforward perturbation theory is that the unperturbed $\mathcal{L}_0$ that we will choose has more than one steady state. The steady

state of the Lindbladian $\mathcal{L}$, which is unique, will be obtained approximately from an effective Lindbladian acting within the space of steady states of $\mathcal{L}_0$ that lifts the degeneracy.

The choice of $\mathcal{L}_0$ and $\mathcal{V}$ depends on the regime under consideration. The full Lindbladian in our system is

$$\mathcal{L} = \mathcal{H} + \mathcal{L}_{\mathrm{m}} + \mathcal{D}. \quad \text{(C2)}$$

Here $\mathcal{H}[\rho] = -i[H, \rho]$ generates the unitary evolution, $\mathcal{D}$ is the coupling to the bath, and $\mathcal{L}_{\mathrm{m}}$ is the measurement, $\mathcal{L}_{\mathrm{m}} = -\frac{1}{\tau}\mathcal{Q}_A$, where $\mathcal{Q}_A[\rho] = \rho - \sum_a P_a \rho P_a$ is a projector onto density matrices that have vanishing diagonal elements in the basis of the measurement observable A. We denote the characteristic scale of the Hamiltonian by $||H||$, which is also the scale of $\mathcal{H}$. The scale of $\mathcal{D}$ is the dissipation rate γ_0, which is assumed to be weak, $\gamma_0 \ll ||H||$. In the limit of slow measurements ($\tau ||H|| \gg 1$), we take $\mathcal{L}_0 = \mathcal{H}$ and $\mathcal{V} = -\frac{1}{\tau}\mathcal{Q}_A + \mathcal{D}$. For fast measurements ($\frac{1}{\tau} \gg ||H||$), we take $\mathcal{L}_0 = -\frac{1}{\tau}\mathcal{Q}_A$ and $\mathcal{V} = \mathcal{H} + \mathcal{D}$. Similar approaches have been used previously to study strongly monitored quantum systems, where classical Markov dynamics are found to emerge beyond the strict Zeno limit [63,69].

To develop the perturbation theory, it is useful to think about $\mathcal{L}$ as a superoperator that acts on the vector space of operators, including the density matrix ρ. The steady-state condition is then written as $\mathcal{L}\rho_{\mathrm{st}} = 0$. Define $\mathcal{P}$ as a projector that fixes any steady state of $\mathcal{L}_0$, while taking any eigenvector of $\mathcal{L}_0$ with a nonzero eigenvalue to 0, so

$$\mathcal{P}\mathcal{L}_0 = \mathcal{L}_0 \mathcal{P} = 0. \quad \text{(C3)}$$

Let $\mathcal{Q} = 1 - \mathcal{P}$ be the complementary projector. We will split the steady state of the full Lindbladian into components in the two complementary spaces, $\rho_{\mathrm{st}} = \rho_P + \rho_Q$, where $\rho_P = \mathcal{P}\rho_{\mathrm{st}}$ and $\rho_Q = \mathcal{Q}\rho_{\mathrm{st}}$. Then, the steady state condition is

$$0 = \mathcal{L}\rho_{\mathrm{st}} = (\mathcal{L}_0 + \mathcal{V})(\rho_P + \rho_Q) = \mathcal{V}\rho_P + (\mathcal{L}_0 + \mathcal{V})\rho_Q, \quad \text{(C4)}$$

using Eq. (C3). This can be divided into two conditions by projecting it with $\mathcal{P}$ and $\mathcal{Q}$. The latter gives

$$\mathcal{Q}(\mathcal{L}_0 + \mathcal{V})\mathcal{Q}\rho_Q = -\mathcal{Q}\mathcal{V}\rho_P \quad \text{(C5)}$$

and can be used to determine ρ_Q in terms of ρ_P:

$$\rho_Q = -\mathcal{Q}[\mathcal{Q}(\mathcal{L}_0 + \mathcal{V})\mathcal{Q}]^{-1}\mathcal{Q}\mathcal{V}\rho_P. \quad \text{(C6)}$$

While $\mathcal{Q}[\mathcal{L}_0 + \mathcal{V}]\mathcal{Q}$ is noninvertible, as it has the same kernel as $\mathcal{Q}$; the notation $\mathcal{Q}[\mathcal{Q}(\mathcal{L}_0 + \mathcal{V})\mathcal{Q}]^{-1}\mathcal{Q}$ indicates that the inverse is computed only within the complementary space. Projecting Eq. (C4) with $\mathcal{P}$ gives $\mathcal{P}\mathcal{V}\rho_P + \mathcal{P}\mathcal{V}\rho_Q = 0$ which, combined with Eq. (C6), becomes

$$\mathcal{P}\mathcal{V}\rho_P - \mathcal{P}\mathcal{V}\mathcal{Q}[\mathcal{Q}(\mathcal{L}_0 + \mathcal{V})\mathcal{Q}]^{-1}\mathcal{Q}\mathcal{V}\rho_P = 0. \quad \text{(C7)}$$

Hence, ρ_P is a steady state of the effective Lindbladian:

$$\mathcal{L}_{\mathrm{eff}} = \mathcal{P}\mathcal{V}\mathcal{P} - \mathcal{P}\mathcal{V}\mathcal{Q}[\mathcal{Q}(\mathcal{L}_0 + \mathcal{V})\mathcal{Q}]^{-1}\mathcal{Q}\mathcal{V}\mathcal{P}. \quad \text{(C8)}$$

Once ρ_P is known (based on this effective Lindbladian), ρ_Q can be obtained from it using Eq. (C6) to obtain $\rho_{\mathrm{st}} = \rho_P + \rho_Q$. To second order in $\mathcal{V}$, the effective Lindblad operator is

$$\mathcal{L}_{\mathrm{eff}} \approx \mathcal{P}\mathcal{V}\mathcal{P} - \mathcal{P}\mathcal{V}\mathcal{Q}(\mathcal{L}_0)^{-1}\mathcal{Q}\mathcal{V}\mathcal{P}. \quad \text{(C9)}$$
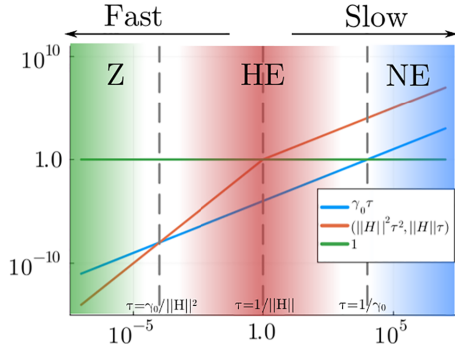
FIG. 10. Schematic depiction of the different dynamical regimes. Different dynamical scales are shown as a function of measurement time τ. They are the Hamiltonian scale ($||H||\tau$ or $||H||^2\tau^2$ depending on whether measurements are fast or slow), the dissipative scale ($\gamma_0\tau$), and the measurement scale (constant in τ), all normalized by the measurement rate. Both axes are logarithmic. In the Zeno (Z) regime, the Hamiltonian dynamics is negligible and the steady state is determined by the interplay of measurements and dissipation. In the near-equilibrium (NE) regime, the dissipation has enough time to equilibrate the system between measurements. In the high entropy (HE) regime, the dissipation is the weakest scale and the system approaches an infinite temperature state. The parameters in the plot are $||H|| = 1$, $\gamma_0 = 10^{-4}$.

Perturbation theory is justified provided that there is a gap from the zero eigenvalues of $\mathcal{L}_0$ to the nonzero eigenvalues.

We will next apply this formalism in the limits of fast and slow measurements, in turn. We will find various dynamical regimes as the measurement time is varied, which are summarized in Fig. 10.

1. Fast measurement limit $||H||\tau \ll 1$

When measurements are fast relative to the Hamiltonian timescale, $||H||\tau \ll 1$, we take $\mathcal{L}_0 = -\frac{1}{\tau}\mathcal{Q}_A$ as the dominant term in the Lindbladian, and $\mathcal{V} = \mathcal{H} + \mathcal{D}$ as the perturbation. In this case, the projector onto the steady states of $\mathcal{L}_0$ is $\mathcal{P}_A = 1 - \mathcal{Q}_A$, whose action on ρ is $\mathcal{P}_A[\rho] = \sum_a P_a\rho P_a$. This is highly degenerate, as any density matrix that is diagonal in the measurement basis,

$$\rho = \sum_a w_a |a\rangle \langle a|, \tag{C10}$$

is a steady state of $\mathcal{L}_0$, regardless of the value of the occupations w_a. The perturbation $\mathcal{V}$ lifts this degeneracy. Equation (C9) gives

$$\mathcal{L}_{\text{eff}} = \mathcal{P}_A\mathcal{V}\mathcal{P}_A + \tau\mathcal{P}_A\mathcal{V}\mathcal{Q}_A\mathcal{V}\mathcal{P}_A. \tag{C11}$$

The unitary evolution vanishes at leading order, $\mathcal{P}_A\mathcal{H}\mathcal{P}_A = 0$, as can be seen by acting on a general density matrix ρ,

$$\mathcal{P}_A\mathcal{H}\mathcal{P}_A[\rho] = \sum_a P_a\left(-i\left[H, \sum_b P_b\rho P_b\right]\right)P_a \tag{C12}$$

$$= -i\sum_a [P_aHP_a, P_a\rho P_a] = 0, \tag{C13}$$

which vanishes for a nondegenerate observable A. Therefore, $\mathcal{H}$ contributes to $\mathcal{L}_{\text{eff}}$ starting at second order. To leading

nonvanishing order in γ_0 and $||H||$:

$$\mathcal{L}_{\text{eff}} = \mathcal{P}_A(\mathcal{D} + \tau\mathcal{H}^2)\mathcal{P}_A. \tag{C14}$$

The condition $\mathcal{L}_{\text{eff}}\rho_P = 0$ next fixes the steady-state occupations w_a in the measurement basis, ρ_P. The off-diagonal elements of ρ_{st} in the measurement basis, ρ_Q, are then given by Eq. (C6). They are subdominant in $\tau\mathcal{V}$ relative to the diagonal elements.

The form of ρ_{st} depends on which of the terms in Eq. (C14) is larger. There is thus a crossover as a function of τ at $\tau_Z \equiv \gamma_0/||H||^2$. For ultrafast measurements, $\tau \ll \tau_Z$, the steady-state occupations are determined by the condition $\mathcal{P}_A\mathcal{D}\mathcal{P}_A\rho_{\text{st}}^{(0)} = 0$, which yields the balance equation

$$\sum_{a'\neq a} w_{a'}^{(0)}T^{a'\to a} = w_a^{(0)}\sum_{a'\neq a} T^{a\to a'}, \tag{C15}$$

where $T^{a\to a'} = \sum_\alpha |\langle a'|L_\alpha|a\rangle|^2$ is the transition rate from state a to a'. The subscript (0) indicates that these are the occupations to zeroth order in τ. The von Neumann entropy in this case saturates to a value that is independent of both γ_0 and τ. This is what we refer to as the Zeno limit.

On the other hand, for $\tau_Z \ll \tau \ll 1/||H||$, the Hamiltonian plays a dominant role over the dissipation in Eq. (C14). If the dissipation is fully neglected, then according to the arguments in Sec. V, the steady state will be an infinite temperature state, $\rho_\infty = \frac{1}{\mathcal{N}}$. Adding the dissipation $\mathcal{D}$ prevents the system from reaching this state. Let

$$\rho_P = \rho_\infty + \delta\rho_P, \tag{C16}$$

where $\delta\rho_P$ is proportional to γ_0. The correction can be found by solving $\mathcal{L}_{\text{eff}}\rho_P = 0$ to first order in γ_0 for $\delta\rho_P$. This gives

$$\delta\rho_P = -\frac{1}{\tau}\mathcal{P}_A(\mathcal{P}_A\mathcal{H}^2\mathcal{P}_A)^{-1}\mathcal{P}_A\mathcal{D}\rho_\infty, \tag{C17}$$

which is of order $\gamma_0/(\tau||H||^2)$. The complementary part of the density matrix, $\rho_Q = \mathcal{Q}_A\rho_{\text{st}}$, is found to be smaller:

$$\rho_Q = \tau\mathcal{Q}_A(\mathcal{H} + \mathcal{D})(\rho_\infty + \delta\rho_P) \tag{C18}$$

$$\approx \mathcal{Q}_A\mathcal{D}\tau\rho_\infty - \mathcal{Q}_A\mathcal{H}\mathcal{P}_A(\mathcal{P}_A\mathcal{H}^2\mathcal{P}_A)^{-1}\mathcal{P}_A\mathcal{D}\rho_\infty.$$

These terms are smaller than $\delta\rho_P$ by factors of $(\tau||H||)^2$ and $(\tau||H||)$, respectively, so they can be neglected in the fast measurement limit.

We turn our attention to the von Neumann entropy:

$$S[\rho_{\text{st}}] = -\text{tr}[(\rho_\infty + \delta\rho)\ln(\rho_\infty + \delta\rho)]. \tag{C19}$$

Expanding $\ln(\rho_\infty + \delta\rho) = \ln((1 + \mathcal{N}\delta\rho)/\mathcal{N}) = -\ln\mathcal{N} + \mathcal{N}\delta\rho - \frac{\mathcal{N}^2}{2}\delta\rho^2 + \mathcal{O}(\gamma_0^3)$ then, since $\delta\rho$ is traceless, the entropy is to order γ_0^2:

$$S[\rho_{\text{st}}] = \ln\mathcal{N} - \frac{\mathcal{N}}{2}\text{tr}[\delta\rho^2]. \tag{C20}$$

The relative entropy as defined in Eq. (45) is then

$$\Delta s = \frac{\mathcal{N}}{2\ln(\mathcal{N})}\text{tr}[\delta\rho^2]. \tag{C21}$$

Since $\delta\rho$ is of order $\gamma_0/(\tau||H||^2)$, Δs scales with τ as

$$\Delta s \propto \frac{\gamma_0^2}{||H||^4\tau^2} \tag{C22}$$

in the regime $\gamma_0/||H||^2 \ll \tau \ll 1/||H||$, explaining the scaling seen numerically in Sec. V B.

In Appendix D, we compute currents in the Zeno limit. The measurement current is nonzero only in the complement of the measurement subspace:

$$\langle J_{\text{meas}} \rangle_{\mathcal{P}_A[\rho]} = 0. \tag{C23}$$

Therefore, we need the off-diagonal entries of the density matrix when $\tau \ll \frac{1}{\gamma_0}$. Using Eq. (C6), we find

$$\mathcal{Q}_A \rho_{\text{st}}^{(1)} = \tau \mathcal{Q}_A \mathcal{H} \mathcal{P}_A \rho_{\text{st}}^{(0)}$$
$$= -i\tau[H, \rho_{\text{st}}^{(0)}], \tag{C24}$$

where we have neglected terms of order $\tau\gamma_0$, and where the superscript (1) indicates linear order in τ. In the second line, we used $\mathcal{Q}_A = 1 - \mathcal{P}_A$, $\mathcal{P}_A \mathcal{H} \mathcal{P}_A = 0$ and the expression for $\mathcal{H}$ as the commutator with H.

2. Slow measurement limit $\tau||H|| \gg 1$

In the opposite limit, when measurements are slow relative to the Hamiltonian timescale, we take $\mathcal{L}_0 = \mathcal{H}$ and $\mathcal{V} = \mathcal{L}_{\text{m}} + \mathcal{D} = -\frac{1}{\tau}\mathcal{Q}_A + \mathcal{D}$. Any diagonal density matrix in the Hamiltonian basis is a steady state of $\mathcal{L}_0$. The projector onto the space of steady states is $\mathcal{P}_H$, whose action on density matrices is $\mathcal{P}_H[\rho] = \sum_E P_E \rho P_E$. Here, P_E is a projector into the subspace of states with energy E. Equation (C9) then gives

$$\mathcal{L}_{\text{eff}} = \mathcal{P}_H \left(-\frac{1}{\tau}\mathcal{Q}_A + \mathcal{D} \right) \mathcal{P}_H, \tag{C25}$$

where the terms above are nonvanishing and hence the leading order contributions in $\mathcal{V}$. The condition $\mathcal{L}_{\text{eff}}\rho_{\text{st}} = 0$ fixes the steady-state occupations in the Hamiltonian basis. There is a crossover as a function of τ at $\tau_R \equiv 1/\gamma_0$. For $\tau \gg \tau_R$, the steady-state occupations are given by $\mathcal{P}_H \mathcal{D} \mathcal{P}_H \rho_{\text{st}} = 0$, which yields the equilibrium state at the temperature of the bath.

On the other hand, for $1/||H|| \ll \tau \ll \tau_R$, $\mathcal{L}_{\text{eff}} \approx -\frac{1}{\tau}\mathcal{P}_H \mathcal{Q}_A \mathcal{P}_H$, whose steady state is the infinite temperature state (since it is simultaneously diagonal in the Hamiltonian and measurement bases). The dissipation $\mathcal{D}$ prevents the system from reaching infinite temperature. Writing $\rho_{\text{st}} = \rho_\infty + \delta\rho$ for the steady state of Eq. (C25), we find that $\delta\rho$ is of order $\gamma_0\tau$. Plugging this into Eq. (C22) yields

$$\Delta s \propto \gamma_0^2 \tau^2, \tag{C26}$$

which is the scaling of the relative entropy with τ in the regime $1/||H|| \ll \tau \ll \tau_R$.

APPENDIX D: NO CHARGE TRANSFER IN THE ZENO LIMIT

Using the results from Appendix C, we show that the total current vanishes in the Zeno limit. By Eq. (39), the total Hamiltonian current is $-i[\hat{x}, H]$ and its expectation value for the density matrix of the Zeno limit, Eq. (46), is

$$\langle J_H \rangle_{\rho_{\text{st}}^{(0)}} = i \sum_a w_a^{(0)} \text{tr}([H, \hat{x}] P_a). \tag{D1}$$

The measurement current is nonzero only in the complement of the measurement subspace, $\langle J_{\text{meas}} \rangle_{\mathcal{P}_A[\rho]} = 0$ [see

Eq. (41)]. Therefore, we evaluate the expectation value with respect to ρ_Q. This part of the density matrix is smaller by a factor of $\tau||H||$. However, its contribution to the total current is of the same order as the Hamiltonian current at leading order, since the measurement current has an overall factor of $1/\tau$ in its definition; see Eq. (40). By Eq. (C24):

$$\mathcal{Q}_A \rho_{\text{st}}^{(1)} = -i[H, \rho_{\text{st}}^{(0)}]\tau + \mathcal{O}(\gamma_0)$$
$$= -i \sum_a [H, P_a] w_a^{(0)} \tau + \mathcal{O}(\gamma_0). \tag{D2}$$

The expectation value of the integrated measurement current for this density matrix is

$$\langle J_{\text{meas}} \rangle_{\rho_{\text{st}}^{(1)}} = i \sum_{a,a'} w_a^{(0)} \text{tr}([H, P_a](\hat{x} - P_{a'}\hat{x}P_{a'})). \tag{D3}$$

The first term cancels the Hamiltonian current since $\text{tr}[H, P_a]\hat{x} = -\text{tr}[H, \hat{x}]P_a$. Thus, the current will vanish if the last term is zero. The last term is

$$-i \sum_{a,a'} w_a^{(0)} \text{tr}([H, P_a]P_{a'}\hat{x}P_{a'})$$
$$= -i \sum_{a,a'} w_a^{(0)} \text{tr}(HP_a P_{a'}\hat{x}P_{a'} - P_a H P_{a'}\hat{x}P_{a'})$$
$$= -i \sum_a w_a^{(0)} \text{tr}(HP_a\hat{x}P_a - P_a H P_a\hat{x}P_a) = 0 \tag{D4}$$

from the projector identity $P_a P_{a'} = \delta_{a,a'} P_a$ and the cyclic property of the trace.

APPENDIX E: TWO-SITE AND THREE-SITE MEASUREMENTS IN THE ZENO LIMIT

We will now consider local currents in the Zeno limit. In this limit, for the dynamics we consider (see Fig. 1), measurements destroy coherence between unit cells. The lack of coherence between unit cells prevents Hamiltonian currents from developing between unit cells. Since measurements do not connect unit cells, no measurement currents will develop either. Therefore, in what follows, we study the dynamics within a unit cell.

To ease notation, given an operator O, we define the operator O^c,

$$O^c = NP_n O P_n, \tag{E1}$$

where P_n is the projector onto a specific unit cell n. The factor N takes into account the fact that the particle can be in any of the N unit cells and ensures proper normalization. In particular, the density matrix in the Zeno limit is a sum over unit cells, so no information is lost by considering ρ^c for a specific cell. Consequently, in the calculation of the currents, e.g., the Hamiltonian current $\langle J_H \rangle = i \text{ tr } \rho_{\text{st}}[H, \hat{x}]$, the Hamiltonian may also be replaced by H^c.

1. Two-site measurements

If the measurement subspace is two-dimensional, as in Sec. V B, the density matrix projected onto a unit cell can be written as

$$\rho_{\text{st}}^c = \frac{1}{2}[1 + (2w_L^{(0)} - 1)\hat{\mathbf{m}} \cdot \boldsymbol{\sigma}], \tag{E2}$$

where $w_{\text{L}}^{(0)}$ is the occupation probability of the left site after the control U is applied. It is determined by Eq. (C15),

$$w_{\text{L}}^{(0)} = \frac{1}{1 + \frac{T^{1\to2}}{T^{2\to1}}}, \tag{E3}$$

where $T^{1\to2} = \sum_\alpha |\langle 2|UL_\alpha U^\dagger|1\rangle|^2$ is the transition probability between state $U^\dagger|1\rangle$ and $U^\dagger|2\rangle$, where $|1\rangle$ and $|2\rangle$ are the position eigenstates. Consider a general form for the Hamiltonian projected into the two-site unit cell:

$$H^{\text{c}} = h_0\sigma_0 + \mathbf{h}\cdot\boldsymbol{\sigma}, \tag{E4}$$

where σ_0 is the identity matrix and the vector $\mathbf{h}$ specifies the subspace Hamiltonian. Then the operator for the Hamiltonian current, $i[H^c, \hat{x}] = i[H^c, -\frac{\sigma_z}{2}]$, can be written as

$$J_H^{\text{c}} = (\mathbf{h}\times\hat{z})\cdot\boldsymbol{\sigma}. \tag{E5}$$

The expectation value of the Hamiltonian current is then

$$\langle J_H^{\text{c}}\rangle = \left(w_{\text{L}}^{(0)} - \frac{1}{2}\right)\text{tr}[(\mathbf{h}\times\hat{z})\cdot\boldsymbol{\sigma}(\hat{\mathbf{m}}\cdot\boldsymbol{\sigma})]$$
$$= -2\left(w_{\text{L}}^{(0)} - \frac{1}{2}\right)(\mathbf{h}\times\hat{\mathbf{m}})_z. \tag{E6}$$

The effective two-site measurement current operator can be found by inserting the projectors onto the measured states $P_\pm = \frac{1}{2}(1\pm\hat{\mathbf{m}}\cdot\boldsymbol{\sigma})$ into the general measurement current expression [Eq. (41)]. We find

$$J_{\text{meas}}^{\text{c}} = \frac{1}{2\tau}(\sigma_z - m_z(\hat{\mathbf{m}}\cdot\boldsymbol{\sigma})). \tag{E7}$$

The measurement current expectation value is zero within the measurement subspace, and the dominant contribution comes from $\mathcal{Q}_A\rho_{\text{st}}^{(1)}$ [Eq. (C24)]. By projecting to the measurement subspace, we get that the expectation value of the measurement current is

$$\langle J_{\text{meas}}^{\text{c}}\rangle = -\frac{i}{2}\text{tr}\big[(\sigma_z - m_z(\hat{\mathbf{m}}\cdot\boldsymbol{\sigma}))\big([H, \rho_{\text{st}}^{(0)}]^{\text{c}}\big)\big]$$
$$= \left(w_{\text{L}}^{(0)} - \frac{1}{2}\right)\text{tr}[(\sigma_z - m_z(\hat{\mathbf{m}}\cdot\boldsymbol{\sigma}))(\mathbf{h}\times\hat{\mathbf{m}})\cdot\boldsymbol{\sigma}]$$
$$= 2\left(w_{\text{L}}^{(0)} - \frac{1}{2}\right)(\mathbf{h}\times\hat{\mathbf{m}})_z, \tag{E8}$$

where in the last line we used $(\mathbf{h}\times\hat{\mathbf{m}})\cdot\hat{\mathbf{m}} = 0$ and $\text{tr}(\sigma_i) = 0$. Note that the Hamiltonian current is exactly compensated by the measurement current.

Despite the cancellation, it is interesting to look at the Hamiltonian and measurement currents separately. In the Zeno limit, the steady-state currents for the Rice-Mele model ($\mathbf{h} = -t_1\hat{\mathbf{e}}_x + \frac{V}{2}\hat{\mathbf{e}}_z$) are

$$\langle J_H\rangle_{\rho_{\text{st}}^{(0)}} = -\langle J_{\text{meas}}\rangle_{\rho_{\text{st}}^{(1)}} = 2t_1(w_L^{(0)} - 1/2)m_y. \tag{E9}$$

Figure 11 illustrates these currents. Note that each current vanishes separately on the great circle $m_y = 0$, corresponding to T-even observables. It also vanishes for measurements of the bond current itself, $m_y = \pm1$, when $w_{\text{L}}^{(0)} = \frac{1}{2}$.
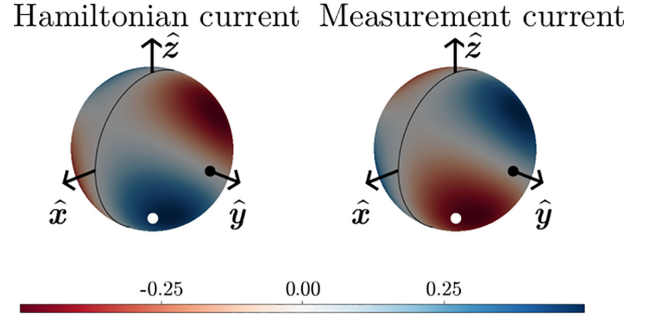

FIG. 11. Hamiltonian and measurement currents are plotted on the Bloch sphere in the Zeno limit. The observable that is measured in Fig. 6 is marked by the white dot. In that figure, it can be seen that these two currents cancel out in the Zeno limit and that this cancellation doesn't persist to larger measurement times. The parameters are the same as in Fig. 6.

2. Three-site measurements and loop currents

In analogy to the Rice-Mele Hamiltonian, we use a similar Hamiltonian, but with three sites in the unit cell instead of two:

$$H = \sum_{n=1}^{N}\bigg[(-t_1c_{3n-2}^\dagger c_{3n-1} - t_2c_{3n-1}^\dagger c_{3n}$$
$$- t_3c_{3n}^\dagger c_{3n+1} + \text{H.c.}) + \frac{V}{2}(c_{3n-2}^\dagger c_{3n-2} - c_{3n}^\dagger c_{3n})\bigg]. \tag{E10}$$

We perform measurements within the three-dimensional unit cell. The measurement subspace Hamiltonian can be written in the Gell-Mann basis as

$$H^{\text{c}} = -t_1\lambda_1 - t_2\lambda_6 + \frac{V}{2}\left(\frac{1}{2}\lambda_3 + \frac{\sqrt{3}}{2}\lambda_8\right), \tag{E11}$$

where λ_i-s are Gell-Mann matrices. Similarly, we write the expression for the Hamiltonian current:

$$J_H^{\text{c}} = t_1\lambda_2 + t_2\lambda_7. \tag{E12}$$

To obtain nonzero currents, the measurements should act on the three sites of the unit cell. This allows the density matrix to have coherences between all three sites in the unit cell, allowing for currents between all pairs of sites so a circular current can form. Moreover, for the current to be nonzero, the measured eigenstates should not have a well-defined parity under time reversal, indicating that complex amplitudes must be involved. An example of a vector that satisfies these requirements is

$$|\Psi_1(\alpha)\rangle = \frac{1}{\sqrt{3}}(|1\rangle + e^{i\alpha}|2\rangle + |3\rangle), \tag{E13}$$

where α is a phase that is not an integer multiple of π. We choose the two other eigenvectors to be

$$|\Psi_2(\alpha)\rangle = \frac{1}{\sqrt{2}}(|1\rangle - e^{i\alpha}|2\rangle), \tag{E14}$$

$$|\Psi_3(\alpha)\rangle = \frac{1}{\sqrt{6}}(|1\rangle + e^{i\alpha}|2\rangle - 2|3\rangle). \tag{E15}$$

Measurement of the nondegenerate observable $A^c(\alpha) = \sum_{i=1}^{3} a_i |\Psi_i(\alpha)\rangle \langle\Psi_i(\alpha)|$, where each a_i is unique, will yield these eigenvectors. For instance, if $\alpha = \frac{\pi}{2}$ the projectors onto these three eigenstates, $P_i(\alpha) = |\Psi_i(\alpha)\rangle \langle\Psi(\alpha)|$, are

$$P_1\left(\frac{\pi}{2}\right) = \frac{1}{3}(1 + \lambda_4 + \lambda_2 - \lambda_7), \qquad (E16)$$

$$P_2\left(\frac{\pi}{2}\right) = \frac{1}{3}\left(1 + \frac{\sqrt{3}}{2}\lambda_8 - \frac{3}{2}\lambda_2\right), \qquad (E17)$$

$$P_3\left(\frac{\pi}{2}\right) = \frac{1}{3}\left(1 - \lambda_4 - \frac{\sqrt{3}}{2}\lambda_8 + \frac{\lambda_2}{2} + \lambda_7\right). \qquad (E18)$$

Using the discrete translational symmetry of the problem, we write the steady-state density matrix as

$$\rho_{st}^c(\alpha) = \frac{1}{3}\Bigg[1 - \frac{u^{(0)} + \Delta u^{(0)}}{2}P_1(\alpha)$$
$$- \frac{u^{(0)} - \Delta u^{(0)}}{2}P_2(\alpha) + u^{(0)}P_3(\alpha)\Bigg], \qquad (E19)$$

where $u^{(0)}$ and $\Delta u^{(0)}$ are parameters that can be determined by solving the balance equation, Eq. (47).

The expectation value of the Hamiltonian current is

$$\langle J_H^c\rangle(\alpha) = \frac{1}{18}[3(2t_2 + t_1)u^{(0)} - (5t_1 - 2t_2)\Delta u^{(0)}]\sin(\alpha). \qquad (E20)$$

On the other hand, the expectation values of the measurement currents between any of three possible pairs of sites come out to be [after calculating the traces of the products of matrices in Eq. (40)]

$$\langle j_{meas}^c\rangle_{1\to2}(\alpha) = \frac{1}{18}[-2(t_1 - t_2)u^{(0)} + (4t_1 + t_2)\Delta u^{(0)}]\sin(\alpha), \qquad (E21)$$

$$\langle j_{meas}^c\rangle_{2\to3}(\alpha) = \frac{1}{18}[(t_1 - 4t_2)u^{(0)} - (t_1 + t_2)\Delta u^{(0)}]\sin(\alpha), \qquad (E22)$$

$$\langle j_{meas}^c\rangle_{1\to3}(\alpha) = \frac{1}{18}[-(t_1 + 2t_2)u^{(0)} + (t_1 - t_2)\Delta u^{(0)}]\sin(\alpha). \qquad (E23)$$

If we calculate the total measurement current $\langle j_{meas}^c\rangle_{1\to2} + \langle j_{meas}^c\rangle_{2\to3} + 2\langle j_{meas}^c\rangle_{1\to3}$, we see that the charge transferred by measurement is exactly compensated by the charge transferred via the Hamiltonian current:

$$\langle J_{meas}^c + J_H^c\rangle = 0. \qquad (E24)$$

However, the current between pairs of sites does not vanish. The Hamiltonian contains only nearest-neighbor couplings, which means that $\langle j_H^c\rangle_{1\to3}$ is zero. This is evidently not the case for the measurement current between these two sites, as seen in Eq. (E23). This indicates that a steady-state current flows in a loop that encompasses the three sites. In fact, if the Hamiltonian current is divided into currents between pairs of sites, one finds that $\langle j_{meas}^c + j_H^c\rangle_{1\to2} = \langle j_{meas}^c + j_H^c\rangle_{2\to3} = \langle j_{meas}^c + j_H^c\rangle_{3\to1} \neq 0$. This is seen using the expression for the Hamiltonian current $j_H^{x\to y} = i(P_x H P_y - P_y H P_x)$ between pairs of sites.

---

[1] B. Misra and E. C. G. Sudarshan, The Zeno's paradox in quantum theory, J. Math. Phys. **18**, 756 (1977).

[2] S. Hacohen-Gourgy, L. P. García-Pintos, L. S. Martin, J. Dressel, and I. Siddiqi, Incoherent qubit control using the quantum Zeno effect, Phys. Rev. Lett. **120**, 020505 (2018).

[3] E. Blumenthal, C. Mor, A. A. Diringer, L. S. Martin, P. Lewalle, D. Burgarth, K. B. Whaley, and S. Hacohen-Gourgy, Demonstration of universal control between non-interacting qubits using the quantum Zeno effect, npj Quantum Inf. **8**, 88 (2022).

[4] D. Herman, R. Shaydulin, Y. Sun, S. Chakrabarti, S. Hu, P. Minssen, A. Rattew, R. Yalovetzky, and M. Pistoia, Constrained optimization via quantum Zeno dynamics, Commun. Phys. **6**, 219 (2023).

[5] R. Raussendorf and H. J. Briegel, A one-way quantum computer, Phys. Rev. Lett. **86**, 5188 (2001).

[6] M. A. Nielsen, Cluster-state quantum computation, Rep. Math. Phys. **57**, 147 (2006).

[7] D. K. Burgarth, P. Facchi, V. Giovannetti, H. Nakazato, S. Pascazio, and K. Yuasa, Exponential rise of dynamical complexity in quantum computing through projections, Nat. Commun. **5**, 5173 (2014).

[8] D. Cogan, Z.-E. Su, O. Kenneth, and D. Gershoni, Deterministic generation of indistinguishable photons in a cluster state, Nat. Photon. **17**, 324 (2023).

[9] E. Bairey, I. Arad, and N. H. Lindner, Learning a local Hamiltonian from local measurements, Phys. Rev. Lett. **122**, 020504 (2019).

[10] N. Tantivasadakarn, R. Thorngren, A. Vishwanath, and R. Verresen, Long-range entanglement from measuring symmetry-protected topological phases, Phys. Rev. X **14**, 021040 (2024).

[11] G.-Y. Zhu, N. Tantivasadakarn, A. Vishwanath, S. Trebst, and R. Verresen, Nishimori's cat: Stable long-range entanglement from finite-depth unitaries and weak measurements, Phys. Rev. Lett. **131**, 200201 (2023).

[12] F. A. Grünbaum, L. Velázquez, A. H. Werner, and R. F. Werner, Recurrence for discrete time unitary evolutions, Commun. Math. Phys. **320**, 543 (2013).

[13] R. Yin, Q. Wang, S. Tornow, and E. Barkai, Restart uncertainty relation for monitored quantum dynamics, Proc. Natl. Acad. Sci. USA **122**, e2402912121 (2025).

[14] S. Dhar, S. Dasgupta, and A. Dhar, Quantum time of arrival distribution in a simple lattice model, J. Phys. A: Math. Theor. **48**, 115304 (2015).

[15] H. Friedman, D. A. Kessler, and E. Barkai, Quantum walks: The first detected passage time problem, Phys. Rev. E **95**, 032141 (2017).

[16] P. Pöpperl, I. V. Gornyi, and Y. Gefen, Measurements on an Anderson chain, Phys. Rev. B **107**, 174203 (2023).

[17] P. Pöpperl, I. V. Gornyi, D. B. Saakian, and O. M. Yevtushenko, Localization, fractality, and ergodicity in a monitored qubit, Phys. Rev. Res. **6**, 013313 (2024).

[18] M. Wampler, B. J. J. Khor, G. Refael, and I. Klich, Stirring by staring: Measurement-induced chirality, Phys. Rev. X **12**, 031031 (2022).

[19] B. J. J. Khor, M. Wampler, G. Refael, and I. Klich, Measurement-induced chirality: Diffusion and disorder, Phys. Rev. B **108**, 214305 (2023).

[20] J. Ferreira, T. Jin, J. Mannhart, T. Giamarchi, and M. Filippone, Transport and nonreciprocity in monitored quantum devices: An exact study, Phys. Rev. Lett. **132**, 136301 (2024).

[21] Y. Li, X. Chen, and M. P. A. Fisher, Quantum Zeno effect and the many-body entanglement transition, Phys. Rev. B **98**, 205136 (2018).

[22] B. Skinner, J. Ruhman, and A. Nahum, Measurement-induced phase transitions in the dynamics of entanglement, Phys. Rev. X **9**, 031009 (2019).

[23] A. Chan, R. M. Nandkishore, M. Pretko, and G. Smith, Unitary-projective entanglement dynamics, Phys. Rev. B **99**, 224307 (2019).

[24] M. Buchhold, Y. Minoguchi, A. Altland, and S. Diehl, Effective theory for the measurement-induced phase transition of Dirac fermions, Phys. Rev. X **11**, 041004 (2021).

[25] C. Noel, P. Niroula, D. Zhu, A. Risinger, L. Egan, D. Biswas, M. Cetina, A. V. Gorshkov, M. J. Gullans, D. A. Huse *et al.*, Measurement-induced quantum phases realized in a trapped-ion quantum computer, Nat. Phys. **18**, 760 (2022).

[26] B. Ladewig, S. Diehl, and M. Buchhold, Monitored open fermion dynamics: Exploring the interplay of measurement, decoherence, and free hamiltonian evolution, Phys. Rev. Res. **4**, 033001 (2022).

[27] I. Poboiko, P. Pöpperl, I. V. Gornyi, and A. D. Mirlin, Theory of free fermions under random projective measurements, Phys. Rev. X **13**, 041046 (2023).

[28] I. Poboiko, I. V. Gornyi, and A. D. Mirlin, Measurement-induced phase transition for free fermions above one dimension, Phys. Rev. Lett. **132**, 110403 (2024).

[29] A Hamiltonian that breaks time reversal and inversion generically leads to currents, even in equilibrium, at least for finite systems (Bloch's theorem states that these currents vanish in the thermodynamic limit [70]). We therefore restrict our attention to time-reversal symmetric Hamiltonians that may or may not have an inversion symmetry.

[30] M. von Smoluchowski, Experimentell nachweisbare, der üblichten Thermodynamik widersprechende Molekularphänomene, Phys. Zeitchrift **13**, 1069 (1912).

[31] R. P. Feynman, R. B. Leighton, and M. Sands, *The Feynman Lectures on Physics* (Addison-Wesley, New York, 1963), Vol. 1.

[32] P. Hänggi and F. Marchesoni, Artificial Brownian motors: Controlling transport on the nanoscale, Rev. Mod. Phys. **81**, 387 (2009).

[33] M. O. Magnasco, Forced thermal ratchets, Phys. Rev. Lett. **71**, 1477 (1993).

[34] C. Peskin, G. Odell, and G. Oster, Cellular motions and thermal fluctuations: The Brownian ratchet, Biophys. J. **65**, 316 (1993).

[35] J. Rousselet, L. Salome, A. Ajdari, and J. Prost, Directional motion of Brownian particles induced by a periodic asymmetric potential, Nature (London) **370**, 446 (1994).

[36] F. Jülicher, A. Ajdari, and J. Prost, Modeling molecular motors, Rev. Mod. Phys. **69**, 1269 (1997).

[37] P. Reimann and P. Hänggi, Quantum features of Brownian motors and stochastic resonance, Chaos **8**, 629 (1998).

[38] P. Reimann, M. Grifoni, and P. Hänggi, Quantum ratchets, Phys. Rev. Lett. **79**, 10 (1997).

[39] S. Scheidl and V. M. Vinokur, Quantum Brownian motion in ratchet potentials, Phys. Rev. B **65**, 195305 (2002).

[40] T. Salger, S. Kling, T. Hecking, C. Geckeler, L. Morales-Molina, and M. Weitz, Directed transport of atoms in a hamiltonian quantum ratchet, Science **326**, 1241 (2009).

[41] A. Peres, Zeno paradox in quantum theory, Am. J. Phys. **48**, 931 (1980).

[42] J. E. Avron, M. Fraas, and G. M. Graf, Adiabatic response for Lindblad dynamics, J. Stat. Phys. **148**, 800 (2012).

[43] K. V. Hovhannisyan and A. Imparato, Quantum current in dissipative systems, New J. Phys. **21**, 052001 (2019).

[44] Considering that time reversal is antiunitary, Eq. (14) requires attention. If we write $P_a = \sum_\lambda |a, \lambda\rangle \langle a, \lambda|$, where λ is an index that labels states spanning a-eigenspace, and $|\bar{a}\rangle = T |a\rangle$, we need to show that TP_aT^{-1} equals $P_{\bar{a}} = \sum_\lambda |\bar{a}, \lambda\rangle \langle \bar{a}, \lambda|$. A generic state can be written in the eigenbasis of time-reversed states, $|\Psi\rangle = \sum_{\lambda'} c_{\bar{a}, \lambda'} |\bar{a}, \lambda'\rangle + |\Psi^\perp\rangle$. Then, $TP_aT^{-1} |\Psi\rangle = \sum_{\lambda, \lambda'} T |a, \lambda\rangle \langle a, \lambda| T^{-1} c_{\bar{a}, \lambda'} |\bar{a}, \lambda'\rangle = \sum_{\lambda, \lambda'} c_{\bar{a}, \lambda'} |\bar{a}, \lambda'\rangle \langle a, \lambda|a, \lambda'\rangle = \sum_\lambda c_{\bar{a}, \lambda} |\bar{a}, \lambda\rangle$, which is seen to equal $P_{\bar{a}} |\Psi\rangle = \sum_\lambda c_{\bar{a}, \lambda} |\bar{a}, \lambda\rangle$.

[45] This argument relies on the observable being non-degenerate. However, the proof is more general.

[46] V. J. Neumann, *Mathematical Foundations of Quantum Mechanics* (Princeton University Press, Princeton, 1996).

[47] G. Lindblad, An entropy inequality for quantum measurements, Commun. Math. Phys. **28**, 245 (1972).

[48] G. Lindblad, Entropy, information and quantum measurements, Commun. Math. Phys. **33**, 305 (1973).

[49] J. Yi, P. Talkner, and G.-L. Ingold, Approaching infinite temperature upon repeated measurements of a quantum system, Phys. Rev. A **84**, 032121 (2011).

[50] D. Ruelle, *Statistical Mechanics: Rigorous Results* (Imperial College Press, London, 1999).

[51] This relies on the result that if A and H are a generic pair of Hermitian matrices, there is no Hermitian matrix besides a scalar matrix that commutes with both of them. Let M commute with both, and let λ one of its eigenvalues. Let V be the span of all eigenvectors of M with this eigenvalue, which will be a proper subspace if M is not a scalar matrix. A maps V into itself, since it commutes with M. This implies that A can be diagonalized within the space V, so V is the span of a set of A's eigenvectors. This is also true for H. So, there is a combination of eigenvectors of A and a combination of eigenvectors of H that span the same space, which is not a generic situation.

[52] Q. Wang, S. Ren, R. Yin, K. Ziegler, E. Barkai, and S. Tornow, First hitting times on a quantum computer: Tracking vs. local monitoring, topological effects, and dark states, arXiv:2402.15843.

[53] P. Facchi and S. Pascazio, Quantum Zeno dynamics: Mathematical and physical aspects, J. Phys. A: Math. Theor. **41**, 493001 (2008).

[54] F. Spitzer, Interaction of Markov processes, Adv. Math. **5**, 246 (1970).

[55] It is straightforward to check that this argument can be generalized to any Kraus operator $\rho \mapsto \rho' = \sum_a K_a \rho K_a^\dagger$ that is normal, $[K_a, K_a^\dagger] = 0$.

[56] R. Dum, P. Zoller, and H. Ritsch, Monte Carlo simulation of the atomic master equation for spontaneous emission, Phys. Rev. A **45**, 4879 (1992).

[57] K. Jacobs and D. A. Steck, A straightforward introduction to continuous quantum measurement, Contemp. Phys. **47**, 279 (2006).

[58] K. Jacobs, *Quantum Measurement Theory and its Applications* (Cambridge University Press, Cambridge, 2014).

[59] For periodic boundary conditions, $(y - x)$ is the shortest displacement on the ring.

[60] H. Spohn and J. L. Lebowitz, Irreversible thermodynamics for quantum systems weakly coupled to thermal reservoirs, Adv. Chem. Phys. 109 (1978).

[61] Note that the choice of dissipator introduced in Eq. (30) is physically not well-justified in the Zeno limit, when measurements are performed faster than the characteristic timescale of the Hamiltonian. However, we expect the qualitative behavior not to be affected by the exact model of dissipation.

[62] V. Popkov, S. Essink, C. Presilla, and G. Schütz, Effective quantum Zeno dynamics in dissipative quantum systems, Phys. Rev. A **98**, 052110 (2018).

[63] D. Bernard, T. Jin, and O. Shpielberg, Transport in quantum chains under strong monitoring, Europhys. Lett. **121**, 60006 (2018).

[64] K. Adachi, K. Takasan, and K. Kawaguchi, Activity-induced phase transition in a quantum many-body system, Phys. Rev. Res. **4**, 013194 (2022).

[65] Y. Zheng, A. P. Antonov, B. Liebchen, and H. Löwen, Engineering active motion in quantum matter, arXiv:2305.16131.

[66] R. Khasseh, S. Wald, R. Moessner, C. A. Weber, and M. Heyl, Active quantum flocks, arXiv:2308.01603.

[67] M. Yamagishi, N. Hatano, and H. Obuse, Proposal of a quantum version of active particles via a nonunitary quantum walk, Sci. Rep. **14**, 28648 (2024).

[68] J. E. Lennard-Jones, Perturbation problems in quantum mechanics, Proc. R. Soc. London, Ser. A **129**, 598 (1930).

[69] M. Bauer, D. Bernard, and A. Tilloy, Computing the rates of measurement-induced quantum jumps, J. Phys. A: Math. Theor. **48**, 25FT02 (2015).

[70] H. Watanabe, A proof of the Bloch theorem for lattice models, J. Stat. Phys. **177**, 717 (2019).

Paired states at 5/2: Particle-hole Pfaffian and particle-hole symmetry breaking

L. Antonić,[1] J. Vučičević,[2] and M. V. Milovanović[2]

[1]*Faculty of Physics, University of Belgrade, 11001 Belgrade, Serbia*

[2]*Scientific Computing Laboratory, Center for the Study of Complex Systems, Institute of Physics Belgrade, University of Belgrade, Pregrevica 118, 11080 Belgrade, Serbia*

We study Cooper pairing in the Dirac composite fermion (CF) system. The presence of the mass term in the Dirac CF description (which may simulate Landau level mixing), i.e., breaking of particle-hole (PH) symmetry in this system, is a necessary condition for the existence of a PH Pfaffian-like topological state. In the scope of the random-phase approximation (RPA) and hydrodynamic approach, we find some signatures of pairing at finite frequencies. Motivated by this insight, we extend our analysis to the case of a different but still Dirac quasiparticle (CF) representation, appropriate in the presence of a mass term, and discuss the likelihood of PH Pfaffian and Pfaffian pairings in general. On the basis of gauge field effects, we find for a small Dirac mass, an anti-Pfaffian or Pfaffian instability depending on the sign of mass, while for large mass (Landau level mixing), irrespective of its sign, we find a PH Pfaffian-like instability.

I. INTRODUCTION

The fractional quantum Hall effect (FQHE) [1] is a remarkable effect of electrons confined to two dimensions. In the presence of a strong, perpendicular to the plane magnetic field, the phase space of the strongly correlated system is further confined into Landau levels (LLs) and quantized. At special fillings of LLs, when the system is described by special ratios of the number of electrons per number of flux quanta, highly entangled states of FQHE are established. In experiments, the effect is seen by measuring the fractionally quantized Hall conductance, which stays constant, at the particular value of fractional filling factor, as the magnetic field or density is varied.

The Laughlin state [2] with its generalizations describes the effect at odd denominator filling factors. A surprise came with the experimental detection of FQHE at filling factor 5/2, i.e., half-filling of the second LL (SLL) [3]. The Cooper pairing was invoked to explain the effect. Assuming spinless (frozen spin) electrons, at half-filling of active (second) LL, in the regime of experiments, the most natural BCS pairing function in the real space, which can be associated with an antisymmetric matrix, is a Pfaffian wave function [4]. Thus we expect Cooper pairing due to phase-space constraints—gauge field effects in a field theory description, in the presence of the repulsive Coulomb interaction.

However, the realization of the pairing correlations even for spinless fermions is not unique. We may envision a theoretical construct, an isolated half-filled LL with the exact particle-hole symmetry that can be explored in numerical experiments. The early pairing proposal—Pfaffian or Moore-Read state [4]—does not possess the particle-hole symmetry, and, under particle-hole exchange the Pfaffian transforms into an anti-Pfaffian state [5,6]. The Pfaffian and anti-Pfaffian equally participate in the ground state of the half-filled SLL with Coulomb interaction [7]. The system with the particle-hole symmetry requires for its field-theoretical description a special Dirac composite fermion (DCF) representation of constitutive classical electrons and their strong correlations [8]. On the basis of this representation a proposal was made for a special Pfaffian that respects the particle-hole symmetry, the so-called PH Pfaffian [8].

Arguments were given in Refs. [9–13] that the PH Pfaffian in the particle-hole symmetric setting, i.e., half-filled LL is an unstable, critical state. Arguments based on numerics were first given in Ref. [12]. Nevertheless, the PH Pfaffian type of pairing seems relevant from the experimental point of view, as argued in Ref. [14], despite LL mixing (absence of the particle-hole symmetry) and disorder effects.

Inspired by the recent experiment described in Ref. [15] that measured the thermal Hall conductance of the paired state at filling 5/2, and found that the measured value is consistent with the conductance of PH Pfaffian, we would like to check if a PH Pfaffian-like state may be realized in the absence of the PH symmetry, i.e., in the presence of LL mixing, but without disorder. The possibility for PH Pfaffian physics due to disorder effects is considered in Refs. [14,16–18], see also Ref. [19], while in Ref. [20], a proposal is made that the result of the experiment may be still consistent with the anti-Pfaffian state, due to an insufficient equilibration of edge modes. Very recently, this proposal is criticized in Ref. [21].

In this work we discuss the effective Cooper pairing channel of the system at half-filling in the scope of the DCF theory with a mass term. The mass term of the DCF theory represents a term that breaks the particle-hole symmetry of electrons confined in an LL and represents an LL mixing.

The paper is organized as follows. In Sec. II, we review arguments for the criticality of the PH Pfaffian in a particle-hole symmetric setting, and argue why a symmetry-breaking mass in the DCF theory is necessary to stabilize the PH Pfaffian. In Sec. III, we discuss the effective Cooper pairing

channel in the DCF theory in the presence of a mass term, and recover only some finite frequency pairing correlations. This is followed by a discussion in Sec. IV, which uses a different form of the DCF theory to analyze the Cooper pairing of modified CFs, in which a usual BCS problem emerges from a gauge field description of constraints. The Pfaffian family solutions of the problem are described and conclusions can be found in Sec. V.

II. PH PFAFFIAN AS A CRITICAL STATE IN A HALF-FILLED LANDAU LEVEL

A. PH Pfaffian as a critical state in a (particle-hole symmetric) half-filled Landau level

In this section, we will review arguments given in Ref. [11] for the critical nature of the PH Pfaffian state, and, in addition, relate the PH Pfaffian physics in a half-filled Landau level to the critical behavior and transition between Pfaffian and anti-Pfaffian [5], and discuss how general the arguments for the critical nature of PH Pfaffian are.

In the following, we will denote by a PH Pfaffian state, a FQHE state, at filling factor $1/2$ (half-filled Landau level) with Pfaffian (p-wave pairing) correlations that is invariant under particle-hole (PH) transformation. The correlations are expected to be in the opposite sense of rotation with respect to the one set by external magnetic field. [This is corroborated by available constructions based (a) on the Laughlin-Jastrow ansatz, Eqs. (1) and (2) below, at the PH symmetric filling factor on sphere, and (b) on the DCF theory.] On the other hand, we will denote by $P\tilde{H}$ Pfaffian, a state with Pfaffian correlations in the opposite sense of rotation with respect to the one set by an external magnetic field that may or may not have the PH symmetry. The $P\tilde{H}$ Pfaffian is a generalization of PH Pfaffian. A Pfaffian state with the PH symmetry was mathematically defined as an s-wave pairing instability of an effective description by Dirac composite fermions at half-filling. That is known in the literature as the Son's proposal for the PH (symmetric) Pfaffian [8].

Based on a mean-field analysis, we will argue that the PH Pfaffian and its $P\tilde{H}$ Pfaffian extensions, in the presence of the PH symmetry (i.e., in a system with PH symmetric Hamiltonian), describe *critical* states and thus they can not describe gapped topological phase(s) in half-filled LLs.

First, we will examine the underlying physics behind the states with the so-called negative flux insertion, either macroscopically (the number of the inserted negative flux quanta is of the order of the size of the system) as in Ref. [22], or microscopically (the number of the inserted negative flux quanta is of the order of one) as in Ref. [14], that induces p-wave pairing in the opposite sense of the rotation with respect to the one set by the external field. These states can be described as $P\tilde{H}$ Pfaffian states. As long as we are not sure of the fate of the PH symmetry in these constructions we will consider them as $P\tilde{H}$ Pfaffians. Here we should note that for the states in Eqs. (1) and (2) below, which we classify as the $P\tilde{H}$ Pfaffian constructions, recent numerical investigations demonstrate high degrees of the PH symmetry [12,13].

A negative flux Pfaffian (a $P\tilde{H}$ Pfaffian), which is also a lowest LL (LLL) wave function, was introduced in Ref. [22] as

$$\Psi_{TJ} = P_{\text{LLL}}\Big[\mathcal{S}\Big\{\prod(z_{i1}^* - z_{j1}^*)^2 \times \prod(z_{i2}^* - z_{j2}^*)^2\Big\} \\ \times \prod(z_k - z_l)^3\Big], \qquad (1)$$

where $\{z_i = x_i + iy_i, i = 1, \ldots, N_e\}$ are the electron coordinates, we omitted the Gaussian factors, P_{LLL} projects to the lowest LL, and the symmetrizer $\mathcal{S}$ symmetrizes between two groups, 1 and 2, in which the particles are equally distributed. This is a state with the number of flux quanta equal to $N_\phi = 3N_e - 3 - 2(N_e/2 - 1) = 2N_e - 1$, i.e., with a PH symmetric shift. An algebraic procedure introduced in Ref. [23] may be followed to generate possible edge states, i.e., a sector, if the system is incompressible. Namely, the proposition applied in the procedure is that if we consider bulk quasihole coherent state constructions, we can use them to generate edge states of an incompressible state. The method proved successful in the Pfaffian case especially so because, in that case, the edge states can be defined as those that make energy zero subspace of a model interaction for which the ground state—Pfaffian model wave function—is also a zero-energy state. In the case of the state in (1), we are not aware of the existence of a model interaction, and, furthermore, we do not know if the state is incompressible. Nevertheless, we may examine which states well-known, well-motivated quasiparticle bulk constructions can generate as low-momentum states. If the state is incompressible, these states we expect will make the edge sector. The analysis was done in Ref. [24], and the states recovered in this way, under the assumption of the incompressibility, would make a counterpropagating Majorana edge branch, together with the charged boson edge branch. The analysis missed a neutral copropagating neutral boson, whose states can be described as insertions in the antiholomorphic part of the wave function, of holomorphic differences of symmetric polynomials belonging to two groups of particles under a symmetrizer. (The antiholomorphic differences, i.e., their linearly independent combinations under symmetrization, make the states of the counterpropagating Majorana edge branch.)

Next to the construction in (1) we can consider a $P\tilde{H}$ Pfaffian state:

$$\Psi_{ZF} = P_{\text{LLL}}\Big[Pf\Big\{\frac{1}{(z_i^* - z_j^*)}\Big\}\prod(z_k - z_l)^2\Big], \qquad (2)$$

which was introduced in Ref. [14]. Here,

$$Pf\Big\{\frac{1}{(z_i^* - z_j^*)}\Big\} \sim \sum_P \text{sgn}\,P \prod_{i=1}^{N/2} \frac{1}{(z_{P(2i-1)}^* - z_{P(2i)}^*)}. \qquad (3)$$

In this case, an analysis of the edge states can include only antiholomorphic Majorana (neutral fermion) constructions described in the Moore-Read (holomorphic Pfaffian) case in Ref. [23]. Thus next to the charged boson we have only a single counterpropagating Majorana.

At this stage, it is interesting to note that in one of the papers that introduced the anti-Pfaffian physics, in Ref. [5], two out of three states that may appear at the transition

between Pfaffian and anti-Pfaffian, have the same edge physics as described here for the states in (1) and (2).

In the following, we will demonstrate that the states in (1) and (2), which may describe electrons in half-filled LLs, are in fact critical states, i.e., gapless and unstable states. For that we will consider a simplified (mean field) version of the Son's theory—the DCF theory [8]—that describes the Fermi-liquid-like state of Dirac CFs, in a half-filled, i.e., PH symmetric, Landau level. Thus we consider a massless Dirac fermion, at finite density, with s-wave pairing among spinor components, and neglect the presence of the gauge field, i.e., its fluctuations around zero value. In the chirality basis, i.e., in the basis of Dirac eigenstates without pairing, see Ref. [11] for details, we can express the pairing term. which pairs spinor components a and b as

$$\Psi_a(\mathbf{k})\Psi_b(-\mathbf{k})$$
$$= -\frac{1}{2}\frac{k_+}{k}[\Psi_+(\mathbf{k})\Psi_+(-\mathbf{k}) + \Psi_-(\mathbf{k})\Psi_-(-\mathbf{k})], \quad (4)$$

where $k \equiv |\mathbf{k}|$ and $k_+ = k_x + ik_y$. The fermion fields Ψ_+ and Ψ_- represent definite chirality (eigenstates of $\frac{\vec{\sigma}\cdot\vec{k}}{k}$) particle (positive energy) and hole (negative energy) states. As the relevant low-energy physics is around a finite chemical potential, for the description of the pairing physics we may use the following low-energy, decoupled from higher modes, BCS Hamiltonian,

$$H_{\rm BCS} = \sum_{\mathbf{k}}(k - \mu)\Psi_+^\dagger(\mathbf{k})\Psi_+(\mathbf{k})$$
$$+ \sum_{\mathbf{k}}\left\{\frac{1}{2}\frac{k_+}{k}\Delta_s\Psi_+(\mathbf{k})\Psi_+(-\mathbf{k}) + \text{H.c.}\right\}. \quad (5)$$

We arrived to the usual form of the p-wave spinless fermion pairing Hamiltonian as can be found in Ref. [25] except that here we have linearly dispersing fermions, and not a fully specified Δ_s function in the pairing part. With respect to the notation of Ref. [25], the pairing function can be identified as

$$\Delta_{\mathbf{k}}^* = -\frac{k_+}{k}\Delta_s. \quad (6)$$

The algebra of the Bogoliubov problem (Ref. [25]) leads to the following expression for the Cooper pair wave function:

$$g_{\mathbf{r}} = \frac{1}{V}\int d\mathbf{k}\exp(i\mathbf{k}\mathbf{r})\frac{-(E_{\mathbf{k}} - \xi_{\mathbf{k}})}{\Delta_{\mathbf{k}}^*}, \quad (7)$$

where $\xi_{\mathbf{k}} = k - \mu$, and $E_{\mathbf{k}}^2 = \xi_{\mathbf{k}}^2 + |\Delta_{\mathbf{k}}|^2$. We are interested in the long-distance behavior, and thus the behavior of $\Delta_{\mathbf{k}}$ for small momenta around $k = 0$. For $\mu > 0$, finite chemical potential and density of the system that we consider here, the long distance behavior is determined by the behavior of $\Delta_{\mathbf{k}}$, i.e., Δ_s [see Eq. (6)] for small $\mathbf{k}$. In the small k limit, we are motivated to consider two cases:

$$(a)\lim_{k\to 0}\Delta_s \to \text{const.}, \quad \text{when } g_{\mathbf{r}} \sim \frac{1}{z|z|} \quad (8)$$

and

$$(b)\lim_{k\to 0}\Delta_s \sim k \equiv |\mathbf{k}|, \quad \text{when } g_{\mathbf{r}} \sim \frac{1}{z}. \quad (9)$$

For the usual choice of the direction of the magnetic field $\vec{B} = B\,\hat{e}_z$, $B < 0$ (instead of $B > 0$ as is implicit in the DCF theory because the density of Dirac CFs is proportional to B) we would have in (49) and (9), instead of z, in fact z^*. Thus, in the long-distance limit, when we can neglect the projection to a definite LL, the case (9) corresponds to wave functions in (1) and (2), because [26]

$$\mathcal{S}\left\{\prod(z_{i1}^* - z_{j1}^*)^2 \times \prod(z_{i2}^* - z_{j2}^*)^2\right\}$$
$$= Pf\left\{\frac{1}{(z_i^* - z_j^*)}\right\} \times \prod(z_k^* - z_l^*), \quad (10)$$

and thus the pairing with the Cooper pair wave function, $g_{\mathbf{r}} \sim \frac{1}{z^*}$, is present in both wave functions. Thus we can conclude that in order to reproduce the pairing encoded in the wave functions (1) and (2) we need nonanalytic behavior in the small k limit, $\lim_{k\to 0}\Delta_s \sim k \equiv |\mathbf{k}|$.

Thus, for the states in Eqs. (1) and (2), we cannot have a Landau-Ginzburg type of description (together with the fermionic part, see below), as we would expect to have for a well-defined, stable pairing phase. A question may be raised, whether in this argument for the critical nature of these states, we are allowed to use the region around $|\mathbf{k}| = 0$ to describe the pairing instabilities of Dirac CFs, with the understanding that the Dirac description is only well-defined near $|\mathbf{k}| = k_F$. However, a complete theory (description) of a pairing instability involves both regions; the one around $|\mathbf{k}| = k_F$ and the one around $|\mathbf{k}| = 0$, associated with the long-wavelength, low-energy description with a bosonic variable (an order parameter $\Delta_{\mathbf{k}}$ in the mean-field description) associated with the pairing.

On the other hand, the introduction of an analytical s-wave pairing in the DCF theory would lead to the following Lagrangian density:

$$\mathcal{L} = i\bar{\chi}\gamma^\mu(\partial_\mu + ia_\mu)\chi + (ig\tilde{\Delta}_s(\mathbf{r})\chi\sigma_y\chi + \text{H.c.})$$
$$+ |(\partial_\mu - 2ia_\mu)\tilde{\Delta}_s|^2 - u|\tilde{\Delta}_s|^2 - \frac{v}{2}|\tilde{\Delta}_s|^4. \quad (11)$$

The theory is invariant under CP (charge conjugation + parity) transformation

$$CP\chi(\mathbf{r})(CP)^{-1} = \sigma_x\chi(\mathbf{r}'), \quad (12)$$

where $\mathbf{r} = (x, y)$ and $\mathbf{r}' = (x, -y)$, though the pairing term up to a gauge transformation. This invariance corresponds to the invariance under the PH transformation of real electrons [8]; the introduced s-wave pairing constitutes the Son's proposal for the PH Pfaffian. With the usual s-wave pairing behavior, $\lim_{k\to 0}\Delta_s \to \text{Const.}$, and neglecting the influence of gauge field, as before, we can arrive to the following characteristic long-distance behavior:

$$g_{\mathbf{r}} \sim \frac{1}{z|z|}\left(\text{i.e., }\frac{1}{z^*|z|}\right), \quad (13)$$

which should enter the Pfaffian part of the PH Pfaffian,

$$\Psi_{\rm PH} = P_{\rm LLL}\left[Pf\left\{\frac{1}{(z_i^* - z_j^*)|z_i - z_j|}\right\}\prod(z_k - z_l)^2\right]. \quad (14)$$

We will list two reasons why this state can be considered only as a gapless (critical) state. (a) If we attempt to generate an edge Majorana sector using Ψ_{PH}, and the method of Ref. [23], we will not be able to separate (bulk) charge modes from the usual Majorana counterpropagating edge modes, because this is possible only for the peculiar form of the Cooper pair wave function with $g_{\mathbf{r}} \sim \frac{1}{z^*}$. (b) The universal, long-distance behavior $g_{\mathbf{r}} \sim \frac{1}{z^*|z|}$ is also a characteristic behavior of the critical system of classical (nonrelativistic) fermions at the transition from weak to strong coupling as described in Ref. [25].

Though we commented in the beginning that we are applying the mean-field approach and neglect gauge field fluctuations, our approach is in fact quite general, and can reach conclusions that are not biased. Namely, once we assume PH Pfaffian pairing instabilities, by the very assumption of the pairing order parameters of the underlying Dirac composite fermions, we expect, due to the Anderson-Higgs mechanism, that the gauge field (that couples to the fermions) will be expelled from the low-energy physics, and therefore our assumption and approach concerning the nature of PH Pfaffian is justified. The arguments, in this section, are given in the long-distance limit, when the magnetic length can be neglected with respect to distances considered and thus the projection to the LLL in Eqs. (1), (2), and (14) can be omitted. The limit characterizes the universal, low-energy physics, which we argue is gapless, and this should be valid even when the projection is included and the system is characterized as a whole in a half-filled LL.

Thus the state with a manifest PH symmetry, the PH Pfaffian in the half-filled LL, can be only a critical state. This state may correspond to the (third) state that characterizes the transition between Pfaffian and anti-Pfaffian state in Ref. [5]. According to the analysis of Ref. [5] we may expect that this state is the lowest energy state at the transition between Pfaffian and anti-Pfaffian state, i.e., a "real" critical state, while other two states, in (1) and (2), may represent excited states at the point of the transition with an exact particle-hole symmetry. [The two states in (1) and (2), correspond to the other two states of the same reference, due to their edge spectrum.]

B. Particle-hole symmetry breaking and the criticality of PH Pfaffian

It is interesting to introduce a mass, i.e., a particle-hole symmetry breaking term in the previously discussed description of the pairing instabilities in a fixed Landau level. We will assume the analytic ($\lim_{k\to 0} \Delta_s \sim$ const) description, discussed in the previous section. At the particle-hole symmetric point, m(mass) $= 0$. Away from this point, for $\Delta_s = 0$, we have a simple Dirac description of the Hamiltonian with the following 2×2 matrix,

$$H = \begin{bmatrix} m & k_- \\ k_+ & -m \end{bmatrix}, \quad (15)$$

for the following choice for gamma matrices $\gamma^0 = \sigma_3$, $\gamma^1 = i\sigma_2$, and $\gamma^2 = -i\sigma_1$, and we set the Dirac velocity, $v_F = 1$. In

this case,

$$\Psi_+(\mathbf{k}) = \frac{1}{\sqrt{2E(E+m)}}[(m+E)\Psi_a(\mathbf{k}) + k_-\Psi_b(\mathbf{k})] \quad (16)$$

and

$$\Psi_-(\mathbf{k}) = \frac{1}{\sqrt{2E(E-m)}}[(m-E)\Psi_a(\mathbf{k}) + k_-\Psi_b(\mathbf{k})], \quad (17)$$

where $E \equiv \sqrt{|\mathbf{k}|^2 + m^2}$. We find that

$$\Psi_a(\mathbf{k})\Psi_b(-\mathbf{k}) = -\frac{k_+}{2E}\Psi_+(\mathbf{k})\Psi_+(-\mathbf{k})$$
$$-\frac{m}{E}\frac{k_+}{|\mathbf{k}|}\Psi_+(\mathbf{k})\Psi_-(-\mathbf{k})$$
$$+\frac{k_+}{2E}\Psi_-(\mathbf{k})\Psi_-(-\mathbf{k}). \quad (18)$$

We immediately see that in this case, with respect to the Eq. (4), we do not have nonanaliticity for $\mathbf{k} = 0$ (if Δ_s is a constant in that limit). Thus, for $m \neq 0$, we have a description similar to the ordinary p wave in Ref. [25], that reproduces Pfaffian pairing in the opposite direction with respect to the one set by the external magnetic field, as discussed in the previous section, but with a mixing term $\sim \Psi_+(\mathbf{k})\Psi_-(-\mathbf{k})$.

A straightforward solution of the Bogoliubov (BCS) problem gives a BCS ground state, where Ψ_+ degrees of freedom pair as $g_{\mathbf{r}} \sim \frac{1}{z}$, while interband correlations are described with $g_{\mathbf{r}} \sim \frac{1}{z|z|}$. Thus the implied ground-state wave function in the effective long-wavelength description is

$$\Psi_{PHL} = Pf\left\{\frac{1}{(z_i^* - z_j^*)}\right\} \prod (z_k - z_l)^2. \quad (19)$$

This leads to the conclusion that the particle-hole symmetry breaking mass term may stabilize the PH Pfaffian -like state in (19). This is a very interesting, counterintuitive conclusion, which was originally suggested in Ref. [11], in the context of singlet and triplet pairings of spinor components, in the presence of a mass term. Here we showed that the same conclusion can be reached by considering only the s-wave (singlet) pairing [Eq. (18)] in the presence of a mass term.

Although this simple scenario seems quite plausible, the numerical investigations of the second Landau level (SLL) (for which we expect that is dominated by the Pfaffian physics) imply that the physics around the particle-hole symmetric point is dominated by a nonuniversal influence of the short-range part of the Coulomb interaction, which is hard to capture by field theoretical means. Namely, the investigation in Ref. [7] clearly shows the (Schroedinger cat) mixing of Pfaffian and anti-Pfaffian at the particle-hole symmetric point, and their relevance for the nearby physics. The most recent investigations in Refs. [12,13] point out that the state in Eq. (2) is likely an excited state in the half-filled SLL (compare with our identification above), and has very high overlap with the composite Fermi liquid (CFL) wave function [27,28]. Thus, although the DCF theory seems a very good description of the half-filled LLL, it has to be modified to capture the nonuniversal physics in the SLL. But, by modifying the Coulomb interaction in the SLL, one may increase the overlap of the exact ground state with the state in (2) or stabilize the CFL

state [13]. Thus a relevant question may be whether a mass term in the DCF theory may induce pairing irrespective of the details of the projected to an LL Coulomb interaction. Therefore we are motivated to study the DCF theory in the presence of a mass term in order to see if this may induce pairing correlations and a pairing instability of the PH Pfaffian kind [Eq. (19)].

III. THE DIRAC COMPOSITE FERMION THEORY WITH A PARTICLE-HOLE SYMMETRY BREAKING TERM

In this section, we will consider the usual formulation of the DCF theory, with a mass term, in the RPA approximation in order to find the effective Cooper channel and examine pairing correlations. A different formulation of the same theory we will discuss in the next section.

A. The Dirac composite fermion theory with a particle-hole symmetry breaking term: an introduction

We start by examining the DCF theory in the presence of PH symmetry breaking mass term. The generalized Lagrangian can be found in Ref. [29] and is given by the following expression,

$$\mathcal{L} = i\bar{\psi}\gamma^{\mu}(\partial_{\mu} + ia_{\mu})\psi + \frac{1}{4\pi}adA + \frac{1}{8\pi}AdA - m\bar{\psi}\psi, \tag{20}$$

where χ is the Dirac CF field, a_{μ} is an emergent $U(1)$ gauge field, the Chern-Simons terms are abbreviated as $\epsilon^{\mu\nu\lambda}A_{\mu}\partial_{\nu}A_{\lambda} \equiv AdA$, $\mu = 0, x, y$, and we have omitted the Coulomb interaction and higher order terms. As a consequence, we have the following equations, by differentiating with resect to A_{μ},

$$J_e = \frac{dA}{4\pi} + \frac{da}{4\pi}, \tag{21}$$

where J_e is the electron density current, and, by differentiating with resect to a_{μ},

$$J_{\psi} = \frac{dA}{4\pi}, \tag{22}$$

where J_{ψ} is the Dirac composite fermion density current. As discussed in Ref. [29], transport coefficients like the Hall conductance can be found from the implied form of currents,

$$\mathbf{j}_e = \frac{1}{4\pi}\hat{\epsilon}(\mathbf{E} - \mathbf{e}) \tag{23}$$

and

$$\mathbf{j}_{\psi} = \frac{1}{4\pi}\hat{\epsilon}\mathbf{E}, \tag{24}$$

where $\hat{\epsilon}$ is the unit antisymmetric tensor with components $\epsilon^{ii} = 0, \epsilon^{xy} = -\epsilon^{yx} = 1$, together with the relationship that we have to extract from the theory,

$$\mathbf{j}_{\psi} = \frac{1}{4\pi}\hat{\sigma}_D\mathbf{e}, \tag{25}$$

where $\hat{\sigma}_D$ represents the Dirac composite fermion conductance tensor. To find $\hat{\sigma}_D$, we need to find the polarization

tensor $\Pi_{\mu\nu}$,

$$j_{\mu}^{\psi} = \Pi_{\mu\nu}\, a^{\nu}, \tag{26}$$

which may be identified in the RPA treatment of the theory: the expansion of the effective action to second order in a^{ν}, after the integration of fermion fields in the functional formalism, or directly calculating

$$\Pi^{\mu\nu} = -itr[\gamma^{\mu}S_F(x, y)\gamma^{\nu}S_F(y, x)], \tag{27}$$

where

$$iS_F(x, y) = \langle T[\psi(x)\bar{\psi}(y)]\rangle, \tag{28}$$

i.e., the composite fermion propagator (T is the time ordering and the expectation value is with respect to the ground state of noninteracting fermions). In calculating (27), we encounter (ultraviolet) divergences, which come from the presence of the infinite sea of negative energy solutions. There are two ways to regularize the theory: (a) dimensional and (b) Pauli-Villars regularization. The physical meaning of these two possibilities, when considering Berry curvature contributions of the positive and negative energy band to the Hall conductance, is that in the dimensional regularization we combine (add) the contributions, while in the Pauli-Villars regularization we consider the contribution only from the positive band. (For the Berry curvature contributions of the two bands see Ref. [29].) The dimensional regularization at the neutrality point [μ(chemical potential) $= 0$], and in the presence of a mass gives an unphysical prediction for the Hall conductance ($=\frac{1}{2}\frac{e^2}{h}$), i.e., a half integral quantum Hall effect of noninteracting fermions. But at a finite chemical potential, and in the absence of mass the Hall conductance is zero. This result or consequence is at the basis of the DCF theory (that is defined at a finite chemical potential), which results in the precise value of the Hall conductance of electrons $= \frac{1}{2}\frac{e^2}{h}$, dictated by the particle-hole symmetry, even in the presence of disorder. Thus the dimensional regularization is the assumed regularization in the DCF theory. On the other hand, the Pauli-Villars regularization gives a so-called parity anomaly, a half of the unit of the Hall conductance even in the absence of a mass. Later, we will explore the role of the Pauli-Villars regularization, when we consider a smooth connection between the DCF theory and the HLR theory [30]. Thus this type of regularization is important when we switch the quasiparticle representation from the one based on the Read's construction [31] (the DCF theory) to the one based on the usual Chern-Simons construction [32] (the HLR theory [33]).

We obtained the polarization tensor $\Pi^{\mu\nu}(\mathbf{k}, \omega)$, in the hydrodynamic approximation, i.e., when $|\mathbf{k}| \ll k_F$, in the presence of the mass term. The results can be found in Appendix A.

B. The Cooper channel in the Dirac composite fermion theory with a particle-hole symmetry breaking term

In this section, we will extend the approach applied in Refs. [9,10] to the case with the particle-hole symmetry breaking mass term. Namely, in Ref. [9], in order to study the possibilities for pairing within the DCF theory, the Coulomb interaction was considered as an additional term in the theory

described by Eq. (20) with $m = 0$. An effective Coulomb interaction was found by a projection of fermion operators to the low-energy sector around $|\mathbf{k}| = k_F$ of positive energy solutions. The BCS interaction or Cooper channel of the effective interaction for the p-wave (PH Pfaffian) pairing was found to be repulsive and in no way conducive for the pairing. The investigations in Refs. [9,10] included, at the RPA level, modifications of the effective interaction due to the fluctuations of the gauge field (a_μ), but the conclusion was the same. In this section, we would like to find out the effective Cooper channel, within the RPA approach, in the presence of a mass term.

To investigate the possibility for a stable pairing phase, we will look for the expression of the effective interaction in the imaginary time formalism, but fix T (temperature) $= 0$. In the Euclidean space-time, we have

$$\mathcal{L}_E = \bar{\psi}_E \gamma^0 (\partial_\tau + a_E^0) \psi_E + \bar{\psi}_E (-i\gamma)(\nabla + i\mathbf{a}_E)\psi_E$$
$$- \mu \bar{\psi}_E \gamma^0 \psi_E + m \bar{\psi}_E \psi_E, \quad (29)$$

where we consider the situation with a constant magnetic field and, thus, the Fermi system at a finite chemical potential μ. We can get (29) from (20) by a naive analytical continuation $\tau = it$. We may introduce Euclidean gamma matrices $\gamma_E = \gamma_0$ and $\vec{\gamma}_E = (-i)\vec{\gamma}$, but to make an easier contact with previous calculations and literature, we will keep a Minkowski set: $\gamma_0 = \sigma_3$ and $\vec{\gamma} = i\vec{\sigma}$. We introduce the gauge field propagator by the functional integration over fermionic degrees of freedom,

$$\int \mathcal{D}\bar{\psi}_E \mathcal{D}\psi_E \exp\left\{ -\int d\tau d\mathbf{x}[\mathcal{L}_E] \right\}$$
$$= \exp\left\{ -\int dx \int dy \frac{\bar{\mathcal{D}}_{\mu\nu}^{-1}}{2}(x-y)a^\mu(x)a^\nu(y) \right\}. \quad (30)$$

Therefore

$$\bar{\mathcal{D}}_{\mu\nu}^{-1}(x-y) = \mathrm{tr}[\gamma_\mu G_E(x,y)\gamma_\nu G_E(y,x)], \quad (31)$$

where

$$G_E(x,y) = -\langle T_\tau[\psi_E(x)\bar{\psi}_E(y)]\rangle, \quad (32)$$

and x and y are points in the Euclidean space-time. We present explicit expressions for $\bar{\mathcal{D}}_{\mu\nu}^{-1}$, in the hydrodynamic approximation, in Appendix B.

With the addition of the Coulomb interaction to $\mathcal{L}_E$ [Eq. (29)], its contribution to the propagator of the vector potential a_i, $i = x, y$ can be found by considering

$$\delta\mathcal{L}_E = \frac{\int d\mathbf{q} \int d\omega}{(2\pi)^3} \frac{1}{2}\left(\frac{\mathbf{q} \times \mathbf{a}(-\mathbf{q})}{4\pi}\right) \frac{2\pi e^2}{\epsilon_r q}\left(\frac{\mathbf{q} \times \mathbf{a}(\mathbf{q})}{4\pi}\right). \quad (33)$$

To get the effective interaction among fermions, at the RPA level, we integrate out gauge fields in the transverse gauge ($\vec{\nabla} \cdot \vec{a} = 0$). If we define the fermion density-current as

$$\frac{\delta\mathcal{L}_E}{\delta a_E^\mu} = \mathcal{J}^\mu, \quad (34)$$

for the effective four-fermion interaction, we get

$$V_{\mathrm{int}}(x-y) = -\frac{1}{2}\mathcal{D}_{\mu\nu}(x-y)\mathcal{J}^\mu(x)\mathcal{J}^\mu(y), \quad (35)$$

where by $\mathcal{D}_{\mu\nu}$ we denoted the gauge-field propagator with the Coulomb interaction contribution. The propagator $\mathcal{D}_{\mu\nu}$ can be found in Appendix B.

To find the second quantized expressions for the currents and the interaction, we use the following expansion for the fermionic operator,

$$\Psi_E(\mathbf{x}) = \sum_{\mathbf{k}} \begin{bmatrix} ik_- \\ E-m \end{bmatrix} \frac{1}{\sqrt{2E(E-m)}} \exp\{i\mathbf{k}\mathbf{x}\} c_{\mathbf{k}} + \cdots, \quad (36)$$

where we did not write the negative energy contribution. To describe the Cooper channel we project all momenta to the Fermi circle, i.e., $k_\pm = k_x \pm ik_y = k_F \exp\{\pm i\theta\}$. Starting from the defining expression

$$\mathcal{J}_0(x) = \bar{\Psi}_E(x)\gamma_0 \Psi_E(x) = \Psi_E^\dagger(x)\Psi_E(x), \quad (37)$$

we find an effective expression for the density operator,

$$\mathcal{J}_0(\mathbf{k}_1 - \mathbf{k}_2) = \exp\left\{ i\frac{(\theta_2 - \theta_1)}{2} \right\}\left[\cos\left\{ \frac{(\theta_2 - \theta_1)}{2} \right\} \right.$$
$$\left. + i\frac{m}{\mu}\sin\left\{ \frac{(\theta_2 - \theta_1)}{2} \right\} \right]c_{\mathbf{k}_2}^\dagger c_{\mathbf{k}_1}. \quad (38)$$

Defining the transverse part of the current operator by

$$\mathcal{J}_T(\mathbf{k}_1 - \mathbf{k}_2) = i\hat{q} \times \bar{\Psi}_E(\mathbf{k}_1)\vec{\gamma}\Psi_E(\mathbf{k}_2), \quad (39)$$

where $\mathbf{q} = \mathbf{k}_1 - \mathbf{k}_2$ $\hat{q} = \frac{\mathbf{q}}{|\mathbf{q}|}$, we find the effective expression to be

$$\mathcal{J}_T(\mathbf{k}_1 - \mathbf{k}_2) = i\frac{k_F}{\mu}\exp\left\{ i\frac{(\theta_2 - \theta_1)}{2} \right\} \times \frac{\sin\left\{ \frac{(\theta_2 - \theta_1)}{2} \right\}}{\left|\sin\left\{ \frac{(\theta_2 - \theta_1)}{2} \right\}\right|}c_{\mathbf{k}_2}^\dagger c_{\mathbf{k}_1}. \quad (40)$$

Note the presence of the sine function which ensures the hermiticity of the operator [$\mathcal{J}_T^\dagger(\mathbf{q}) = \mathcal{J}_T(-\mathbf{q})$]. This part is missing in Ref. [9].

If we denote the components of $\mathcal{D}^{-1}$ by

$$\mathcal{D}^{-1}(\mathbf{q}, \omega) = \begin{bmatrix} \hat{\Pi}_{00} & \hat{\Pi}_{0T} \\ \hat{\Pi}_{0T} & \hat{\Pi}_{TT} \end{bmatrix}, \quad (41)$$

the effective interaction potential is

$$V_{\mathrm{int}}(\mathbf{q}, \omega)$$
$$= -\frac{1}{[\hat{\Pi}_{00}\hat{\Pi}_{TT} - (\hat{\Pi}_{0T})^2]}[\hat{\Pi}_{TT}\mathcal{J}_0(-\mathbf{q})\mathcal{J}_0(\mathbf{q})$$
$$+ \hat{\Pi}_{00}\mathcal{J}_T(-\mathbf{q})\mathcal{J}_T(\mathbf{q}) - 2\hat{\Pi}_{0T}\mathcal{J}_0(-\mathbf{q})\mathcal{J}_T(\mathbf{q})]. \quad (42)$$

We can find the effective Cooper channel, by taking expressions for the components of the gauge field propagator (B3)–(B5) with $k_0 = i\omega$, where ω is real, inserting the components in the expression for the effective interaction in (42), and choosing momenta to describe a Cooper pair scattering.

Before a closer look at the effective Cooper channel, we may note that always $\hat{\Pi}_{00}(i\omega, \mathbf{k}) < 0$ and $\hat{\Pi}_{TT}(i\omega, \mathbf{k}) > 0$. In the static limit ($\omega = 0$), we have $\hat{\Pi}_{00}(0, \mathbf{k}) = -\frac{\mu}{2\pi}$, $\hat{\Pi}_{TT}(0, \mathbf{k}) = \alpha\frac{|\mathbf{k}|}{(4\pi)^2}$, and $\hat{\Pi}_{0T}(0, \mathbf{k}) = 0$. In this case, the

Cooper channel is

$$
\begin{aligned}
&V_{\text{int}}^{\text{Cooper}}(\mathbf{q} = \mathbf{p} - \mathbf{k}, \omega = 0) \\
&= \Bigg\{ -\frac{1}{\hat{\Pi}_{00}(0, \mathbf{q})} \left[\cos \frac{(\theta_{\mathbf{k}} - \theta_{\mathbf{p}})}{2} + i \frac{m}{\mu} \sin \frac{(\theta_{\mathbf{k}} - \theta_{\mathbf{p}})}{2} \right]^2 \\
&\quad + \frac{1}{\hat{\Pi}_{TT}(0, \mathbf{q})} \left(\frac{k_F}{\mu} \right)^2 \Bigg\} \exp\{i(\theta_{\mathbf{k}} - \theta_{\mathbf{p}})\} c_{\mathbf{k}}^\dagger c_{\mathbf{p}} c_{-\mathbf{k}}^\dagger c_{-\mathbf{p}}.
\end{aligned}
$$

(43)

In the scope of the hydrodynamic approximation, i.e., $\theta_{\mathbf{k}} \approx \theta_{\mathbf{p}}$, we find repulsive behavior and no cause for a Cooper instability even in the massive case.

The second limit we want to consider is a finite frequency limit $\omega \gg \alpha_F |\mathbf{k}|$. We have $\hat{\Pi}_{00}(\omega, \mathbf{k}) \approx -\frac{\mu}{4\pi} \frac{(\alpha_F |\mathbf{k}|)^2}{\omega^2} \sim 0$, $\hat{\Pi}_{TT}(\omega, \mathbf{k}) \approx \frac{\mu}{4\pi} + \alpha \frac{|\mathbf{k}|}{(4\pi)^2}$, and $\hat{\Pi}_{0T}(\omega, \mathbf{k}) \approx -\frac{1}{4\pi} \frac{m}{\mu} |\mathbf{k}|$. The effective Cooper channel can be described with two terms: (a) density-current part,

$$
\begin{aligned}
&V_{\rho J}^{\text{Cooper}}(\mathbf{q} = \mathbf{p} - \mathbf{k}, \omega) \\
&= \frac{4\pi}{m} i \frac{\sin \frac{(\theta_{\mathbf{k}} - \theta_{\mathbf{p}})}{2}}{\left| \sin \frac{(\theta_{\mathbf{k}} - \theta_{\mathbf{p}})}{2} \right|^2} \left[\cos \frac{(\theta_{\mathbf{k}} - \theta_{\mathbf{p}})}{2} + i \frac{m}{\mu} \sin \frac{(\theta_{\mathbf{k}} - \theta_{\mathbf{p}})}{2} \right] \\
&\quad \times \exp\{i(\theta_{\mathbf{k}} - \theta_{\mathbf{p}})\} c_{\mathbf{k}}^\dagger c_{\mathbf{p}} c_{-\mathbf{k}}^\dagger c_{-\mathbf{p}};
\end{aligned}
$$

(44)

(b) density-density part,

$$
\begin{aligned}
&V_{\rho\rho}^{\text{Cooper}}(\mathbf{q} = \mathbf{p} - \mathbf{k}, \omega) \\
&= \left(\frac{4\pi\mu}{m} \right)^2 \frac{\frac{k_F^2}{4\pi\mu} + \frac{\alpha}{(4\pi)^2} (2k_F) \left| \sin \frac{(\theta_{\mathbf{k}} - \theta_{\mathbf{p}})}{2} \right|}{(2k_F)^2 \left| \sin \frac{(\theta_{\mathbf{k}} - \theta_{\mathbf{p}})}{2} \right|^2} \\
&\quad \times \left[\cos \frac{(\theta_{\mathbf{k}} - \theta_{\mathbf{p}})}{2} + i \frac{m}{\mu} \sin \frac{(\theta_{\mathbf{k}} - \theta_{\mathbf{p}})}{2} \right]^2 \\
&\quad \times \exp\{i(\theta_{\mathbf{k}} - \theta_{\mathbf{p}})\} c_{\mathbf{k}}^\dagger c_{\mathbf{p}} c_{-\mathbf{k}}^\dagger c_{-\mathbf{p}}.
\end{aligned}
$$

(45)

In the density-density part, we have extremely singular repulsive interaction present at finite frequencies, i.e., a repulsive singular interaction that describes the physics of excited states. We do not see any cause for a real Cooper instability, except that in the density-current part we can recognize some pairing correlations. This motivates a search for a different quasiparticle representation in which the pairing correlations may be better captured and exposed.

IV. PAIRING CORRELATIONS WITHIN A DIFFERENT QUASIPARTICLE REPRESENTATION

In this section, we will consider a different formulation of the DCF theory with a mass term. This will enable us, on the level of equations of motion, to deduce the effective Cooper channel of different Dirac quasiparticles from the ones discussed in the preceding section. The channel, derived from purely gauge field effects, supports the Pfaffian family of instabilities, and we will examine the ensuing phase diagram as a function of the Dirac mass.

We may also consider the addition of the mass term to the Dirac composite fermion theory by adopting the following

form of the Lagrangian [30]:

$$
\begin{aligned}
\mathcal{L} &= i \bar{\chi} \gamma^\mu (\partial_\mu + i a_\mu) \chi + \frac{1}{4\pi} a dA + \frac{1}{8\pi} A dA \\
&\quad - \frac{m}{|m|} \frac{1}{8\pi} a da - m \bar{\chi} \chi.
\end{aligned}
$$

(46)

Note the presence of the Chern-Simons term for gauge field a^μ. In this case (to recover the identical results for the response with respect to the previous formulation), we have to adopt the Pauli-Villars way of regularizing the theory. Why we discuss this, to say, a redundant formulation? It is important to notice that with a simple redefinition of the gauge field in (46), and in the large mass limit, we can recover the HLR or anti-HLR [35] theory depending on the sign of mass [30]. See Appendix D for details.

By differentiating with resect to A_μ the Lagrangian density in (46), we get

$$
J_e = \frac{dA}{4\pi} + \frac{da}{4\pi},
$$

(47)

where J_e is the electron density-current, and, by differentiating with resect to a_μ,

$$
J_\chi = \frac{dA}{4\pi} - \frac{m}{|m|} \frac{da}{4\pi},
$$

(48)

where J_χ is the Dirac composite fermion density-current. Thus the Dirac composite fermion density-current in this case is determined, on the classical level, by the fluctuations of the gauge field, just as in usual Chern-Simons theories [32,33]. These theories are based on the quasiparticle (composite fermion) constructions via "flux tube"—unitary transformations of the original electrons, and not with "vortex"—Laughlin quasihole constructions [31] of quasiparticles. The usual Chern-Simons theories (at the RPA level) can recover the Jastrow-Laughlin correlations [32] as a part of magnetoplasmon (cyclotron energy) dynamics, while in the "vortex" constructions they are, in a way, frozen and built in quasiparticles. This distinction may be important when discussing the presence of pairing correlations. In the DCF limit, at the RPA level, both formulations give the same response, because they describe the response of "vortex" construction, using different regularization schemes. However, at the classical level [Eqs. (22) and (48)], their predictions may differ, because the distinction between the quasiparticle perspectives is preserved. Thus, although, at the RPA level, we find the absence of pairing correlations for "vortex" constructions (Sec. III), the fact that some pairing correlations are present in the high-energy, i.e., the high-frequency sector in the density-current part of the interaction, gives us an expectation that by adopting different quasiparticle representation, we may recover the pairing correlations in the low-frequency or static limit.

The problem, as described by Eq. (48), is formally identical to the problem discussed in Ref. [34] in the context of the graphene Dirac electrons in FQHE regime. Following the analysis of Ref. [34], for a fixed valley, definite spin, Dirac electrons, of the gauge field a^μ induced interaction between current and density of Dirac particles in the presence of a mass term, we can arrive at the effective form of the pairing channel, Eq. (25) in Ref. [34].

Let us discuss the details that lead to the p-wave pairing channel or attractive interaction for a definite, negative sign of the mass, $m < 0$. The equality in Eq. (48) will lead to the following integral expression for the gauge field a^μ, $a = a_x + i a_y$,

$$a(\mathbf{r}) = 2 \int d\mathbf{r}' i \frac{z - z'}{|\mathbf{r} - \mathbf{r}'|^2} \delta\rho_\chi(\mathbf{r}'), \tag{49}$$

where $\delta\rho_\chi(\mathbf{r}')$ represents the fermion density with respect to the constant value given by the fixed strength of the external magnetic field that we assume. In the following, we will analyze the statistical interaction defined as the one between the current of Dirac fermions and the field $a_i; i = x, y$:

$$V_{st} = \bar{\chi} \gamma^i a_i \chi. \tag{50}$$

We work in the following representation of γ matrices:

$$\gamma^0 = \sigma_3, \quad \gamma^1 = i\sigma_2, \quad \gamma^2 = -i\sigma_1. \tag{51}$$

In this representation, we have the following expression for the statistical interaction:

$$V_{st} = -i2 \int d\mathbf{r}' \delta\rho_\chi(\mathbf{r}') \chi^\dagger(\mathbf{r}) \begin{bmatrix} 0 & \frac{\bar{z} - \bar{z}'}{|\mathbf{r} - \mathbf{r}'|^2} \\ -\frac{z - z'}{|\mathbf{r} - \mathbf{r}'|^2} & 0 \end{bmatrix} \chi(\mathbf{r}), \tag{52}$$

and $\delta\rho_\chi(\mathbf{r}') = \chi^\dagger(\mathbf{r}')\chi(\mathbf{r}') - \bar{\rho}$, where $\bar{\rho}$ is a constant (external flux density). The constant part gives no contribution to V_{st}.

On the other hand, the presence of the mass term in the Dirac system leads to the following eigenproblem,

$$\begin{bmatrix} m - \epsilon & k_- \\ k_+ & -m - \epsilon \end{bmatrix} \chi(\mathbf{k}) = 0, \tag{53}$$

where a positive eigenvalue $\epsilon = \sqrt{|\mathbf{k}|^2 + m^2} \equiv E_\mathbf{k}$, corresponds to the following eigenstate:

$$\chi_E = \begin{bmatrix} m + E_\mathbf{k} \\ k_+ \end{bmatrix} \frac{1}{\sqrt{2E_\mathbf{k}(E_\mathbf{k} + m)}}. \tag{54}$$

As we consider relevant only (positive energy) states around k_F, we will keep only these states in the expansion over $\mathbf{k}$ eigenstates of field $\chi(\mathbf{r})$, and, further, only consider the BCS pairing channel in V_{st}. Thus

$$\chi(\mathbf{r}) = \frac{1}{\sqrt{2V}} \sum_\mathbf{k} \exp\{i\mathbf{k}\mathbf{r}\} \chi_E(\mathbf{k}) a_\mathbf{k} + \cdots, \tag{55}$$

and

$$V_{st}^{\text{BCS}} = \frac{2\pi}{8V} \sum_{\mathbf{k},\mathbf{p}} a_\mathbf{k}^\dagger a_\mathbf{p} a_{-\mathbf{k}}^\dagger a_{-\mathbf{p}} \frac{1}{E_\mathbf{k} E_\mathbf{p} (m + E_\mathbf{k})(m + E_\mathbf{p})}$$

$$\times [m + E_k \quad k_-] \begin{bmatrix} 0 & \frac{1}{k_+ - p_+} \\ -\frac{1}{k_- - p_-} & 0 \end{bmatrix} \begin{bmatrix} m + E_p \\ p_+ \end{bmatrix}$$

$$\times [(m + E_k)(m + E_p) + k_- p_+]. \tag{56}$$

We used $\int d\mathbf{r} \frac{1}{z} \exp\{i\mathbf{k}\mathbf{r}\} = i\frac{2\pi}{k_+}$. The terms with the coefficient $k_- p_+$ give a p-wave channel contribution (for spinless fermions),

$$\frac{k_- p_+}{|\mathbf{k} - \mathbf{p}|^2} \{(2m + E_k + E_p)(m + E_k)(m + E_p)$$

$$- |p|^2(m + E_k) - |k|^2(m + E_p)\}. \tag{57}$$

These terms give the following contribution:

$$V_p^{\text{BCS}} = m \frac{2\pi}{2V} \sum_{\mathbf{k},\mathbf{p}} a_\mathbf{k}^\dagger a_\mathbf{p} a_{-\mathbf{k}}^\dagger a_{-\mathbf{p}}$$

$$\times \exp\{-i(\theta_k - \theta_p)\} \frac{|k||p|}{E_\mathbf{k} \cdot E_\mathbf{p} |\mathbf{k} - \mathbf{p}|^2}, \tag{58}$$

where we see that because of the assumed sign of the mass, $m < 0$, we have an attractive pairing channel. We will discuss in more detail the effective interaction and possible pairing solutions below, but in the following we will make a few general comments. We see from Eq. (58) that only for nonzero mass we can have pairing. Also the chirality of the induced p-wave pairing can be identified. Notice the different phase factors in V_p^{BCS} with respect to Ref. [34]. That comes from a different overall phase in eigenstates that we used in the fermion field expansion in Eq. (55) and the one used in Ref. [34]. Both representations lead to a special chirality pairing function $g(\mathbf{r})$:

$$\lim_{|r| \to \infty} g(\mathbf{r}) \sim f(|\mathbf{r}|) \frac{|z|}{z}. \tag{59}$$

The function $f(|\mathbf{r}|)$ depends on the details of the small $\mathbf{k}$ behavior of the order parameter. The self-consistent equation for the pairing function, $\Delta_\mathbf{k}^* = 2\mathcal{E}_\mathbf{k} \langle a_\mathbf{k}^\dagger a_{-\mathbf{k}}^\dagger \rangle$, where $\mathcal{E}_\mathbf{k}^2 = (E_\mathbf{k} - \mu)^2 + |\Delta_\mathbf{k}|^2$, implied by Eq. (58), with the assumption that $|\Delta_k|$ is the largest around $|\mathbf{k}| = k_F$, gives us the small $\mathbf{k}$ behavior, $\Delta_\mathbf{k}^* \sim k_+$, and thus $g(\mathbf{r}) \sim \frac{1}{z}$. However, again we have to take into account that the assumed direction of the external magnetic field in the Son's formalism is $\vec{B} = B \vec{e}_z$, $B > 0$, because the uniform Dirac composite fermion density is $\bar{\rho}_\chi = \vec{\nabla} \times \vec{A} = B > 0$. For the usual setup, with $B < 0$, the analysis implies $g(\mathbf{r}) \sim \frac{1}{z^*}$, i.e., Pfaffian pairing of the opposite chirality with respect to the one given by the external field. The same conclusions, i.e., an attractive pairing channel with special PH Pfaffian chirality pairing hold true for $m > 0$ as can be easily checked. Thus, for large enough mass, we may expect that the interaction term due to the gauge field [Eq. (58)] can lead to the PH Pfaffian-like pairing instability, but for very large m, the pairing interaction is suppressed. [For large m, in the scope of the HLR theories as shown in Appendix D, any pairing (Pfaffian and anti-Pfaffian) correlations that come from the current-density interaction are obstructed by a three-body interaction, and do not give a clear scenario that comes from the constrained dynamics of the system.]

A more careful examination of the Cooper channel interaction in Eq. (58), which we may begin by angular integration in a BCS self-consistent equation, shows that the pairing interaction is extremely singular and would overcome any repulsive, short-range or Coulomb, interaction. Also the interaction in Eq. (58) does not correspond exactly to the statistical interaction that is usually connected with the Pfaffian physics as described in Ref. [36]. Thus we need to examine more carefully all the terms that follow from Eq. (56). A complete discussion can be found in Appendix C. The picture that emerges from the detailed analysis in Appendix C is very simple: for large $|m|$, irrespective of the sign of mass, we may expect a PH Pfaffian-like state, but for small $|m|$, depending on its sign,

we have anti-Pfaffian, for $m > 0$, and Pfaffian state for $m < 0$. Due to considerable numerical support for anti-Pfaffian under LL mixing in the SLL [37], we may identify the case with the positive mass to the one of the SLL. Furthermore, the identification of Pfaffian and anti-Pfaffian for opposite sign of m, i.e., particle-hole symmetry breaking that is not large is consistent with the numerics (in the SLL) [7].

However, we should be aware of the absence of pairing in the LLL, and that our analysis based on the gauge field description only, is not sufficient for the explanation of the physics in the LLL. We need to include Coulomb repulsive interactions among electrons. This inclusion in the Chern-Simons theories, especially the DCF theory is not an easy task, because a part of the influence of the interactions is built in the gauge dynamics. We may try to include a bare Coulomb interaction with densities that correspond to those of the Dirac quasiparticles [of the theory in the Eq. (46)] as a consequence of Eqs. (47) and (48). The singular behavior of the Coulomb law can suppress any pairing correlations that follow from the gauge field description and constraints. Thus we need to include the interactions in a way that reflects the physics of a fixed LL to explain the dichotomy of the physics in the LLL and SLL, i.e., a Fermi-liquid-like state, and topological paired state, respectively, i.e., to include more intra-Landau level physics in the DCF theory. The way to achieve that is to include a term that represents the interaction of the effective dipoles of the Read's construction with an electric field as discussed in Refs. [38,39]. As explained in Ref. [39], the inclusion of this physics amounts to a change in the expression of the Coulomb interaction of the form

$$\frac{\alpha}{|\mathbf{q}|} \to \frac{\alpha}{|\mathbf{q}| + \frac{m^*}{2B}\alpha|\mathbf{q}|^2}, \tag{60}$$

where we assumed a static case, i.e., no external fields except for the uniform, constant magnetic field B, and m^* represents an effective parameter (mass) in the long distance limit. In the following, we briefly recapitulate how we can reach the modified interaction in (60). First, we note that in a functional formulation we can introduce a scalar field ϕ that decouples the Coulomb term in the inverse space as

$$\delta\mathcal{L}_c = -\frac{2\pi\alpha}{|\mathbf{q}|}\delta\rho(-\mathbf{q})\delta\rho(\mathbf{q})$$
$$\to \phi(-\mathbf{q})\delta\rho(\mathbf{q}) + \frac{|\mathbf{q}|}{2\pi\alpha}\phi(-\mathbf{q})\phi(\mathbf{q}). \tag{61}$$

The scalar represents a potential that a particle experiences due to other particles. On the other hand, Galilean invariance allows an extra term in the kinetic part of the DCF theory [38],

$$\delta\mathcal{L}_u = iu_i\chi^\dagger\partial_i\chi, \tag{62}$$

where u_i is the local drift velocity, $u_i = \epsilon_{ij}\frac{\partial_i\phi}{B}$, $i = x, y$. This term represents an interaction between the (local) electric field and dipoles of the DCF theory, which are propotional to quasiparticle momenta [38]. If we introduce a mass parameter, m^*, to relate the momenta of quasiparticles to their (local) velocity $\mathbf{u}$, we may represent (62), in the inverse space, as

$$\delta\mathcal{L}_u = \frac{m^*|\mathbf{u}|^2\bar{\rho}}{2} = m^*\frac{\bar{\rho}}{2B^2}|\mathbf{q}|^2\phi(-\mathbf{q})\phi(\mathbf{q}), \tag{63}$$

where $\bar{\rho} = \frac{1}{2\pi l_B^2}$ with $l_B = 1/k_F$, the magnetic length, is the density of the system. Integrating field ϕ in the functional representation of the theory, with $\delta\mathcal{L}_u$ and $\delta\mathcal{L}_c$ included, we reach (60). Thus the BCS channel in Eq. (C3) with a modified Coulomb interaction in Eq. (60) may represent a good starting point for the investigation of the pairing instabilities at half-filling in the presence of the PH symmetry breaking mass m.

The role of the modified Coulomb interaction is crucial for the existence of paired states. For m^* finite, we have to deal with a singular repulsive interaction at this level of approximation, which will preclude any pairing as is the case in the LLL. For m^* infinite, the effects of the interaction will be obliterated, and we will have the pairing scenario as is the case in the SLL. Moreover, in this case, for $|m|$ (LL mixing) large, we may expect the PH Pfaffian-like state, which is stabilized with $|m|$ in a uniform system and a consequence of the constrained gauge field description. Nevertheless, we should note that the PH Pfaffian effective (attractive) interaction scales as $\sim \frac{k_F}{|m|}$ (with respect to those of Pfaffian and anti-Pfaffian for small $|m|$), and thus it is suppressed in magnitude with large $|m|$.

We may ask ourselves what is the physical meaning of the m^* infinite limit in the SLL. In this case, the local drift velocity should go to zero and thus the potential that other particles make for a given one is flat, i.e., the correlation hole does not exist and particles are free to pair. That this indeed may be the case in the SLL, we have indications from numerical experiments that find larger size of hole excitations in the SLL than in the LLL in the FQHE regime at filling factors 1/3 and 7/3 [40,41].

The numerical solutions of the BCS self-consistent equation:

$$\Delta_\mathbf{p}^* = -\sum_\mathbf{k} V_{\mathbf{k}\mathbf{p}}\frac{\Delta_\mathbf{k}^*}{\mathcal{E}_\mathbf{k}}, \tag{64}$$

for channels $l = 1, 3, -1$, with $\Delta_\mathbf{k}^* = |\Delta_\mathbf{k}|e^{il\theta_\mathbf{k}}$, are described in Fig. 1. Details concerning Eq. (64) and its solutions can be found in Appendix E. The parameter m in Fig. 1 is measured in units of energy, $(\hbar v_F)k_F$, and this dimensionless quantity along x axis on the right-hand side of Fig. 1, can be described in the following way. First, we rewrite the quantity with the Fermi velocity and explicit physical constants:

$$m \to \frac{m_D v_F^2}{\hbar v_F k_F} = \frac{m_D v_F}{\hbar}l_B = \sqrt{\frac{c}{\hbar e}}v_F\frac{m_D}{\sqrt{B}}, \tag{65}$$

where m_D is the mass of DCFs, $l_B = \sqrt{\frac{\hbar c}{eB}}$ is the magnetic length, and $k_F = \frac{1}{l_B}$. On the other hand, the coefficient of the LL mixing is the ratio of the characteristic Coulomb energy and cyclotron energy:

$$\frac{V_c}{\hbar\omega_c} = \frac{e^2}{l_B}\frac{m_e c}{eB} = \frac{e\sqrt{ec}}{\hbar\sqrt{\hbar}}\frac{m_e}{\sqrt{B}}, \tag{66}$$

where m_e is the mass of electron. Thus the plotted (dimensionless) parameter m may be identified with LL mixing if $m_D = \frac{e^2}{\hbar v_F}m_e$, i.e., the mass of DCF is the electron mass multiplied with a "fine-structure constant" of DCFs, $\frac{e^2}{\hbar v_F}$, characterizing the relative strength of the Coulomb interaction. The
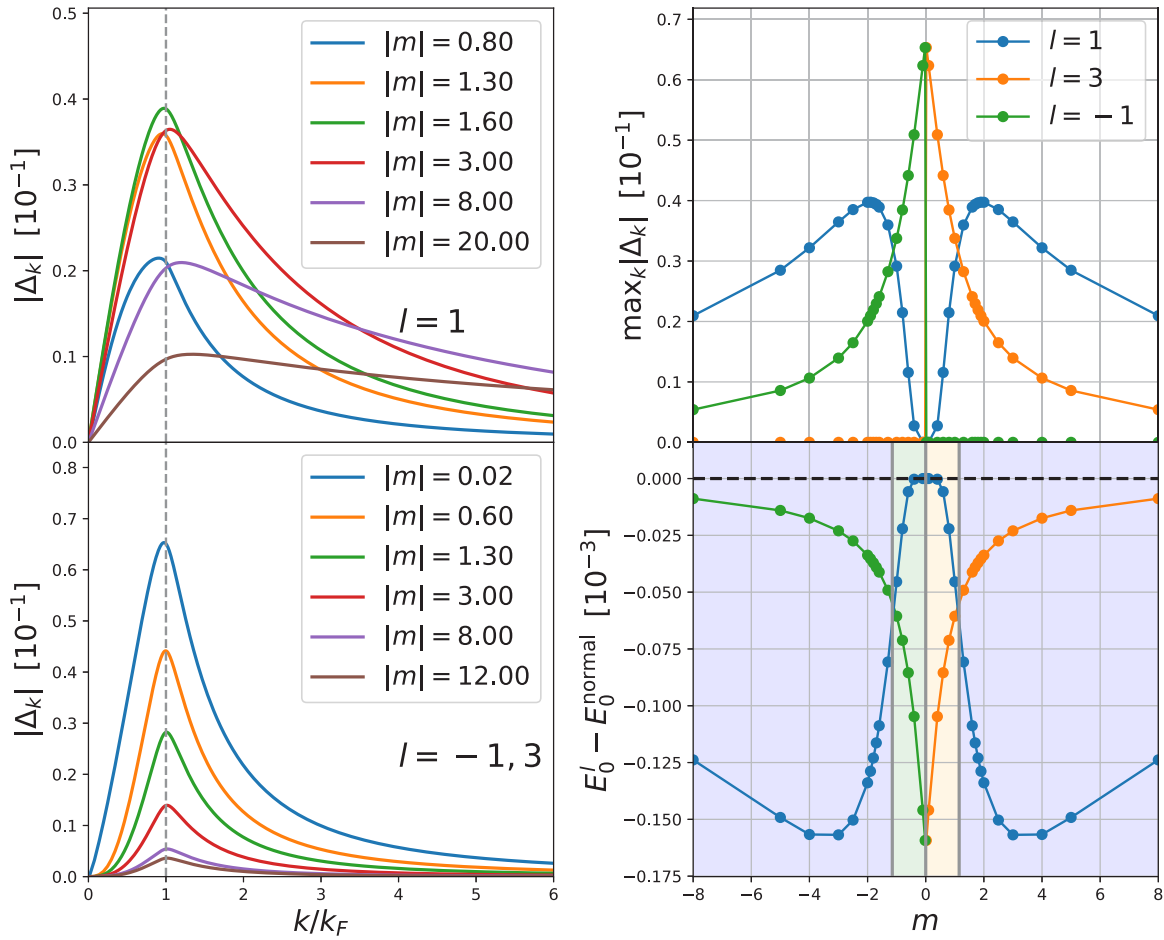
FIG. 1. The solutions of the self-consistent BCS problem. (Left column) Radial direction k-dependent pairing amplitude for various values of m. Channel $l = 1$ solution only depends on $|m|$, while $l = 3$ and $l = -1$ channel solutions are symmetric with the sign flip of m (see Appendix E 3). (Upper right) Dependence of the maximum of the pairing amplitude on m (always found at the Fermi level k_F). (Lower right) Total energy of the different pairing solutions compared to the normal state energy. Gray vertical lines denote the transition between different l channels. Color in the background corresponds to the energetically favorable channel at the given m. We identify $l = 3$ and -1 channels with an anti-Pfaffian and Pfaffian state, respectively, and $l = 1$ channel with a PH Pfaffian-like state.

identification seems plausible, although we do not have an explicit proof; we expect that the prediction of the phase diagram that follows from the theory, up to physical constants, depends solely on the unique parameter of the system, $l_B = \frac{1}{k_F}$, and thus the dimensionless parameter in Fig. 1 should represent LL mixing.

The LL mixing in experiments is of order 1, although it can be large as 4–8 [42,43], and with the above identification we may expect the anti-Pfaffian ($l = 3$) to be the dominant instability in the SLL from the phase diagram in Fig. 1, though the critical m [for the transition into the PH Pfaffian-like state ($l = 1$)], may be estimated to be $m_c = 1.2$, and thus the role and possibility for the development of a PH Pfaffian-like state, at sufficiently large LL mixing in a uniform system should not be underestimated or excluded.

We have confidence in our predictions, because the global features of the phase diagram in Fig. 1 are in agreement with numerical experiments in the SLL. (a) At $m = 0$, a Schrödinger cat superposition of Pfaffian and anti-Pfaffian is present as in Ref. [7], and depending on the sign of the mass for $m \neq 0$ we have Pfaffian or anti-Pfaffian. (b) The

PH Pfaffian-like state is continuously connected to the excited composite FL state at $m = 0$ in an agreement with Ref. [13]. However, this does not mean that with an absolute certainty we can expect a PH Pfaffian-like state at large enough LL mixing in the SLL. This is because we do not possess the precise knowledge of the phenomenological parameter m^* as a function of the Dirac mass, m. The parameter m^* enters Eq. (60) and controls the effectiveness of the pair breaking due to the repulsive Coulomb interaction. We expect that for smaller values of Dirac mass, the parameter m^* is infinite and pairing is present, but, for some large m, the parameter m^* will become finite and an HLR-type of CFL will be established. As we do not know the precise value of m for which this drastic change will occur, we can not say beyond which large enough m the pairing scenario of Fig. 1 will not be realized.

V. DISCUSSION AND CONCLUSIONS

We showed that a complete DCF theory (introduced in Refs. [38,39]) may describe both the paired and FL state of the SLL and LLL, respectively, if we treat the parameter

m^* in (60) as a phenomenological long-distance parameter, which (in the scope of our treatment) is necessarily infinite in the paired states. The m^* is necessarily finite in the limit of large Dirac mass, m, (HLR theory) and in that region we should expect known results (no pairing). For small m, in the SLL, m^* must be infinite to allow for pairing of the (anti-)Pfaffian type consistent with numerics (see Fig. 1). But interestingly enough, we reveal (Fig. 1) a strong competition between an anti-Pfaffian and a PH Pfaffian-like state for intermediate Dirac mass m although we can not claim the absolute relevance of the PH Pfaffian-like state because we do not know the behavior of m^* in that region. However, it seems likely and the results of Fig. 1 are suggestive that a PH Pfaffian-like state [Eq. (19)] may play a role in experiments.

In this work, we discussed the effective Cooper pairing channel of the system at half-filling in the scope of the DCF theory with a mass term. The mass term of the DCF theory represents a term that breaks the particle-hole symmetry of electrons confined in an LL and represents an LL mixing. Solely on the basis of a gauge field description, we find for small Dirac mass an anti-Pfaffian or Pfaffian instability

depending on the sign of the mass, consistent with numerical investigations of the SLL [7], while for large mass (LL mixing), irrespective of the mass sign, we find a PH Pfaffian-like instability.

APPENDIX A: THE POLARIZATION TENSOR

The derivation of the polarization tensor $\Pi(\mathbf{k}, k_0)$ in the massive case, in the hydrodynamic approximation, can be done following and generalizing the procedure described in the massless case in Ref. [44]. We start from the fermion propagator in Eq. (28) as described in Ref. [45],

$$iS_F(x, y) = \theta(x^0 - y^0)\int \frac{d^2p}{(2\pi)^2}\frac{1}{2p_0}(\gamma p + m)\theta(p^0 - \mu)\exp\{-ip(x-y)\} - \theta(y^0 - x^0)\int \frac{d^2p}{(2\pi)^2}\frac{1}{2p_0}$$

$$\times (\gamma p + m)\theta(\mu - p_0)\exp\{-ip(x-y)\} - \theta(y^0 - x^0)\int \frac{d^2p}{(2\pi)^2}\frac{1}{2p_0}(\gamma p - m)\exp\{ip(x-y)\}, \quad \text{(A1)}$$

where $p_0 = \sqrt{\mathbf{p}^2 + m^2}$, $px = p_0 x^0 - \mathbf{px}$, and $\gamma p = \gamma^0 p_0 - \gamma \mathbf{p}$. Using the theta function representation,

$$\theta(x^0 - y^0) = -\int \frac{d\omega}{2\pi i}\frac{\exp\{-i\omega(x^0 - y^0)\}}{\omega + i\eta}, \quad \text{(A2)}$$

we arrive at

$$iS_F(x - y) = \int \frac{d\omega}{2\pi}\int \frac{d^2p}{(2\pi)^2}\exp\{-i\omega(x^0 - y^0) + i\mathbf{p}(\mathbf{x} - \mathbf{y})\}$$

$$\times \left[i\gamma^0\frac{1}{\omega - p_0 + i\eta(\theta(p_0 - \mu) - \theta(\mu - p_0))}\Omega_{\mathbf{p}}^- + i\gamma^0\frac{1}{\omega + p_0 - i\eta}\Omega_{\mathbf{p}}^+\right], \quad \text{(A3)}$$

where

$$\Omega_{\mathbf{p}}^- = \frac{1}{2}\left(1 + \frac{\gamma^0 m}{p_0} - \frac{\gamma^0 \gamma \mathbf{p}}{p_0}\right), \quad \text{(A4)}$$

and

$$\Omega_{\mathbf{p}}^+ = \frac{1}{2}\left(1 - \frac{\gamma^0 m}{p_0} + \frac{\gamma^0 \gamma \mathbf{p}}{p_0}\right). \quad \text{(A5)}$$

To get the form of the fermion operator in Ref. [44], we can shift the frequency variable ω as $\omega \to \omega + \mu$. To find

$$\Pi^{\mu\nu} = -i\mathrm{tr}[\gamma^\mu S_F(x, y)\gamma^\nu S_F(y, x)], \quad \text{(A6)}$$

we need to generalize the trace calculations, frequency, and momentum integrals. The main approximation in the momentum integrals for the external momentum $\mathbf{k}$, $|\mathbf{k}| \ll k_F$, μ, and internal momentum $\mathbf{q}$, $|\mathbf{q}| \sim k_F$ (constrained by the Fermi

statistics inside integrals for $|\mathbf{k}| \ll k_F$) is

$$\theta(\sqrt{|\mathbf{q} + \mathbf{k}|^2 + m^2} - \mu)$$

$$\approx \theta\left(\sqrt{|\mathbf{q}|^2 + m^2} - \mu + |\mathbf{k}|\frac{|\mathbf{q}|}{\sqrt{|\mathbf{q}|^2 + m^2}}\cos\phi\right)$$

$$\approx \theta(\sqrt{|\mathbf{q}|^2 + m^2} - \mu)$$

$$+ |\mathbf{k}|\frac{k_F}{\sqrt{k_F^2 + m^2}}\delta(\sqrt{|\mathbf{q}|^2 + m^2} - \mu)\cos\phi, \quad \text{(A7)}$$

where $k_F = \sqrt{\mu^2 - m^2}$, and ϕ is the angle between vectors $\mathbf{k}$ and $\mathbf{q}$. Here an important difference with respect to the massless case is the appearance of the factor $\frac{k_F}{\sqrt{k_F^2 + m^2}}$. A detailed analysis leads to a conclusion that to get $\Pi^{\mu\nu}$ in the massive case we have to rescale the external momenta $\mathbf{k}$ in the

massless case with a factor $\alpha_F = \frac{k_F}{\sqrt{k_F^2 + m^2}}$, i.e., $\mathbf{k} \to \alpha_F \mathbf{k}$. In particular,

$$\Pi^{00}(k_0, \mathbf{k}) = \tilde{\Pi}^{00}(k_0, \alpha_F \mathbf{k}), \tag{A8}$$

$$\Pi^{0i}(k_0, \mathbf{k}) = \alpha_F \tilde{\Pi}^{0i}(k_0, \alpha_F \mathbf{k})$$
$$+ \epsilon_{ji} \left(-\frac{ik_j m}{4\pi} - i\frac{k_j m}{2\mu^2} \tilde{\Pi}^{00}(k_0, \alpha_F \mathbf{k}) \right), \tag{A9}$$

$$\Pi^{ij}(k_0, \mathbf{k}) = \alpha_F^2 \tilde{\Pi}^{ij}(k_0, \alpha_F \mathbf{k}), \tag{A10}$$

where by $\tilde{\Pi}^{\mu\nu}; \mu, \nu = 0, i, j$ we denoted the components of the polarization tensor in the massless case, and, furthermore, we can see the antisymmetric (Hall conductance) contribution in Π^{0i}, due to the presence of the mass term.

The components of the polarization tensor in the massless case, $\tilde{\Pi}^{\mu\nu}(k_0, \mathbf{k})$, can be found in Ref. [44], and they are

$$\tilde{\Pi}^{00}(k_0, \mathbf{k}) = \Pi_l(k_0, \mathbf{k}),$$

$$\tilde{\Pi}^{0i}(k_0, \mathbf{k}) = k_0 \frac{k^i}{|\mathbf{k}|^2} \Pi_l(k_0, \mathbf{k}),$$

$$\tilde{\Pi}^{ij}(k_0, \mathbf{k}) = \left(\delta^{ij} - \frac{k^i k^j}{|\mathbf{k}|^2} \right) \Pi_t(k_0, \mathbf{k}) + \frac{k^i k^j}{|\mathbf{k}|^2} \frac{k_0^2}{|\mathbf{k}|^2} \Pi_l(k_0, \mathbf{k}), \tag{A11}$$

where

$$\Pi_l(k_0, \mathbf{k}) = \frac{\mu}{2\pi} \left(\theta(k^2) \sqrt{\frac{k_0^2}{k^2} - 1} - i\theta(-k^2) \sqrt{\frac{k_0^2}{-k^2}} \right), \tag{A12}$$

$$\Pi_t(k_0, \mathbf{k}) = \frac{\mu}{2\pi} - \frac{k^2}{|\mathbf{k}|^2} \Pi_l(k_0, \mathbf{k}), \tag{A13}$$

and $k^2 = k_0^2 - |\mathbf{k}|^2$.

The antisymmetric contribution in Eq. (A9) is expected from the Berry curvature contributions in the scope of the relativistic quantum mechanics [29], and here the Hall conductance can be recovered to be $\sigma_H = -\frac{1}{4\pi} \frac{m}{\sqrt{k_F^2 + m^2}}$.

It is important to comment that due to the infinite Dirac sea, we have divergent contributions to the polarization tensor (when doing the calculation according to the definition). As discussed in the main text, the DCF theory as defined in Eq. (20) requires dimensional regularization in order to recover finite $\Pi^{\mu\nu}$. We used the version of the DCF theory given

in Eq. (46) and the associated Pauli-Villars regularization to recover $\Pi^{\mu\nu}$.

APPENDIX B: THE PROPAGATOR OF THE GAUGE FIELD

To find $\bar{\mathcal{D}}_{\mu\nu}^{-1}$ defined in Eq. (31), we need to switch from Minkowski to Euclidean space-time. According to the definition of $\bar{\mathcal{D}}_{\mu\nu}^{-1}$, we need only to take into account the change in the fermion propagator, which amounts to taking $i\omega$ instead of ω at T (temperature) $= 0$ in the Fourier transform of the fermion propagator described in Eqs. (A3)–(A5). Thus we have to repeat the steps that we took to calculate $\Pi^{\mu\nu}$ taking into account this change. The components of $\bar{\mathcal{D}}_{\mu\nu}^{-1}$ are formally equal to the expressions in Eqs. (A8)–(A11) and (A13), i.e., $\bar{\mathcal{D}}_{\mu\nu}^{-1}(k_0, \mathbf{k}) = \Pi_{\mu\nu}(k_0, \mathbf{k})$, with $\Pi_l(k_0, \mathbf{k})$ equal to

$$\hat{\Pi}_l(k_0, \mathbf{k}) = \frac{\mu}{2\pi} \left(-1 + \frac{1}{\sqrt{1 - \frac{|\mathbf{k}|^2}{k_0^2}}} \right), \tag{B1}$$

where k_0 is purely imaginary.

In the transverse gauge, $\vec{\nabla} \mathbf{a} = 0$, and if we denote by $\alpha = \frac{2\pi e^2}{\epsilon_r}$, the Coulomb coupling constant, the inverse of the gauge field propagator is

$$\mathcal{D}^{-1}(k_0, \mathbf{k}) = \begin{bmatrix} \hat{\Pi}_{00} & \hat{\Pi}_{0T} \\ \hat{\Pi}_{0T} & \hat{\Pi}_{TT} \end{bmatrix}, \tag{B2}$$

where

$$\hat{\Pi}_{00} = \hat{\Pi}_l(k_0, \alpha_F \mathbf{k}), \tag{B3}$$

$$\hat{\Pi}_{0T} = -\frac{1}{4\pi} \frac{m}{\mu} |\mathbf{k}| - \frac{m}{2\mu^2} |\mathbf{k}| \hat{\Pi}_l(k_0, \alpha_F \mathbf{k}), \tag{B4}$$

$$\hat{\Pi}_{TT} = \frac{k_F^2}{2\pi\mu} - \frac{k_0^2 - \alpha_F^2 |\mathbf{k}|^2}{|\mathbf{k}|^2} \hat{\Pi}_l(k_0, \alpha_F \mathbf{k}) + \alpha |\mathbf{k}| \frac{1}{(4\pi)^2}. \tag{B5}$$

Here we defined the transverse component of the gauge field to be $a_T = i\mathbf{k} \times \mathbf{a}(\mathbf{k})$ and it is understood that k_0 is purely imaginary.

APPENDIX C: THE EFFECTIVE COOPER CHANNEL AND POSSIBLE PAIRINGS

We can rewrite the Cooper channel interaction in Eq. (56), taking into account both possibilities for the sign of mass,

$$V_{st}^{\text{BCS}} = -\frac{m}{|m|} \frac{2\pi}{8V} \sum_{\mathbf{k}, \mathbf{p}} a_{\mathbf{k}}^\dagger a_{\mathbf{p}} a_{-\mathbf{k}}^\dagger a_{-\mathbf{p}} \frac{1}{E_{\mathbf{k}} \cdot E_{\mathbf{p}} |\mathbf{k} - \mathbf{p}|^2}$$

$$\times \left\{ -|\mathbf{p}|^2 (m + E_k) - |\mathbf{k}|^2 (m + E_p) + 4mk_- p_+ + \frac{(k_- p_+)^2}{|\mathbf{p}|^2 |\mathbf{k}|^2} (E_k + E_p + 2m)(E_k - m)(E_p - m) \right\}. \tag{C1}$$

We expect that in a self-consistent BCS equation the most important contribution will come from the region in which $\mathbf{k} \approx \mathbf{p}$, due to the denominator in the equation above. To explore this limiting behavior, we can divide terms in curly brackets as follows:

$$\left[-|\mathbf{p}|^2 (m + E_k) - |\mathbf{k}|^2 (m + E_p) + 2m(k_- p_+ + k_+ p_-) + \frac{(E_k + E_p + 2m)(E_k - m)(E_p - m)}{2|\mathbf{p}|^2 |\mathbf{k}|^2} ((k_- p_+)^2 + (k_+ p_-)^2) \right]$$

$$+ \left[2m(k_- p_+ - k_+ p_-) + \frac{(E_k + E_p + 2m)(E_k - m)(E_p - m)}{2|\mathbf{p}|^2 |\mathbf{k}|^2} ((k_- p_+)^2 - (k_+ p_-)^2) \right]. \tag{C2}$$

The first part in the square brackets is an even function of $(\theta_p - \theta_k)$ and as $\mathbf{k} \to \mathbf{p}$ the part is of the order of $(\theta_p - \theta_k)^2$. The second part is leading and dominant because in the same limit it is of the order of $(\theta_p - \theta_k)$. The Cooper channel can be cast in the following form:

$$V_{st}^{\mathrm{BCS}} = \frac{2\pi}{8V} \sum_{\mathbf{k},\mathbf{p}} a_{\mathbf{k}}^{\dagger} a_{\mathbf{p}} a_{-\mathbf{k}}^{\dagger} a_{-\mathbf{p}} \frac{1}{E_{\mathbf{k}} \cdot E_{\mathbf{p}}} \left\{ -4|m||\mathbf{k}||\mathbf{p}| \frac{i\sin(\theta_p - \theta_k)}{|\mathbf{k}-\mathbf{p}|^2} - \frac{m}{|m|}(E_k + E_p + 2m)(E_k - m)(E_p - m) \frac{i\sin 2(\theta_p - \theta_k)}{|\mathbf{k}-\mathbf{p}|^2} \right.$$
$$\left. + 4|m||\mathbf{k}||\mathbf{p}| \frac{(\lambda - 1)}{|\mathbf{k}-\mathbf{p}|^2} - 4|m||\mathbf{k}||\mathbf{p}| \frac{\cos(\theta_p - \theta_k) - 1}{|\mathbf{k}-\mathbf{p}|^2} - \frac{m}{|m|}(E_k + E_p + 2m)(E_k - m)(E_p - m) \frac{\cos 2(\theta_p - \theta_k) - 1}{|\mathbf{k}-\mathbf{p}|^2} \right\},$$

$$\tag{C3}$$

where $\lambda = \frac{|\mathbf{k}|^2 + |\mathbf{p}|^2}{2|\mathbf{k}||\mathbf{p}|}$. The following analysis of the effective Cooper channel in Eq. (C3) is based on considerations similar to those described in the case of classical composite fermions Pfaffian pairing in Ref. [36].

For $m > 0$ and m large, the Cooper channel can be approximated as

$$V_{st}^{\mathrm{BCS}} \approx \frac{2\pi}{8V} \sum_{\mathbf{k},\mathbf{p}} a_{\mathbf{k}}^{\dagger} a_{\mathbf{p}} a_{-\mathbf{k}}^{\dagger} a_{-\mathbf{p}} \frac{1}{E_{\mathbf{k}} \cdot E_{\mathbf{p}}} - 2|m| \left\{ \frac{i\sin(\theta_p - \theta_k)}{\lambda - \cos(\theta_p - \theta_k)} - 1 \right\}. \tag{C4}$$

Thus, as previously discussed, the implied angular momentum pairing is $\Delta_{\mathbf{k}}^{*} \sim \langle a_{\mathbf{k}}^{\dagger} a_{-\mathbf{k}}^{\dagger} \rangle \sim e^{i\theta_{\mathbf{k}}}$, i.e., a PH Pfaffian-like pairing. For $m > 0$ and m small, the Cooper channel can be approximated as

$$V_{st}^{\mathrm{BCS}} \approx \frac{2\pi}{8V} \sum_{\mathbf{k},\mathbf{p}} a_{\mathbf{k}}^{\dagger} a_{\mathbf{p}} a_{-\mathbf{k}}^{\dagger} a_{-\mathbf{p}} \frac{1}{E_{\mathbf{k}} \cdot E_{\mathbf{p}}} - \frac{m}{|m|}(E_k + E_p + 2m)(E_k - m)(E_p - m) \frac{\exp i2(\theta_p - \theta_k) - 1}{|\mathbf{k}-\mathbf{p}|^2}. \tag{C5}$$

By doing the angular integration first in the implied BCS self-consistent equation, we find that the pairing $\Delta_{\mathbf{k}}^{*} \sim e^{i\theta_{\mathbf{k}}}$ is suppressed, and that $\Delta_{\mathbf{k}}^{*} \sim e^{i3\theta_{\mathbf{k}}}$ is the dominant pairing. The pairing in the same direction of PH Pfaffian, with angular momentum equal to 3, can be identified as an anti-Pfaffian instability. For $m < 0$ and $|m|$ small, the sign of the effective Cooper channel in Eq. (C5) is switched. This changes the chirality of the implied pairing, and we find that now $\Delta_{\mathbf{k}}^{*} \sim e^{-i\theta_{\mathbf{k}}}$ is the dominant pairing, which we can identify with a Pfaffian instability. For $m < 0$ and $|m|$ large, the effective channel is

$$V_{st}^{\mathrm{BCS}} \approx \frac{2\pi}{8V} \sum_{\mathbf{k},\mathbf{p}} a_{\mathbf{k}}^{\dagger} a_{\mathbf{p}} a_{-\mathbf{k}}^{\dagger} a_{-\mathbf{p}} \frac{1}{E_{\mathbf{k}} \cdot E_{\mathbf{p}}} - 2|m| \left\{ \frac{i\sin(\theta_p - \theta_k)}{\lambda - \cos(\theta_p - \theta_k)} - \lambda \frac{(\exp i2(\theta_p - \theta_k) - 1)}{\lambda - \cos(\theta_p - \theta_k)} \right\}, \tag{C6}$$

and we recover again a PH Pfaffian-like instability, $\Delta_{\mathbf{k}}^{*} \sim e^{i\theta_{\mathbf{k}}}$.

APPENDIX D: CLASSICAL HLR FERMIONS AT HALF-FILLING AND PAIRING INSTABILITIES

It is interesting to probe the large $|m|$ limit of the Lagrangian given by Eq. (46). In this limit and after redefinitions $a_\mu \to a_\mu + \frac{m}{|m|} A_\mu$, the Lagrangian becomes

$$\mathcal{L}_{\mathrm{ccf}} = \frac{m}{|m|} \frac{1}{8\pi} ada + \psi^{\dagger} \left(i\partial_0 + a_0 + \frac{m}{|m|} A_0 \right) \psi$$
$$- \sum_{i=x,y} \frac{1}{2|m|} \psi^{\dagger} \left(i\partial_i + a_i + \frac{m}{|m|} A_i \right)^2 \psi$$
$$+ \frac{\left(1 - \frac{m}{|m|} \right)}{2} \frac{1}{4\pi} AdA. \tag{D1}$$

If $m > 0$, we have the usual Lagrangian of HLR (up to a Coulomb interaction term that we omitted), which, based on the mean-field approximation, leads to the description of composite fermion liquid (CFL). On the other hand, for $m < 0$, we have exactly the Lagrangian of Ref. [35], which in the same approximation describes anti-CFL, i.e., a Fermi liquid of composite holes.

The HLR theory ($m > 0$ case) is described by the following kinetic term of the Hamiltonian density:

$$\mathcal{K} = \frac{1}{2|m|} (-i\nabla + \mathbf{c})\psi^{\dagger}(i\nabla + \mathbf{c})\psi, \tag{D2}$$

where $\vec{c}$ represents the deviation from the uniform magnetic field configuration of the CS gauge field a_μ: $c_\mu = a_\mu + A_\mu$ such that

$$-\delta\rho_\psi = \frac{1}{4\pi} \nabla \times \mathbf{c}. \tag{D3}$$

In this nonrelativistic case, the effective statistical density-current interaction is given by

$$\tilde{V}_{\mathrm{st}} = -\frac{1}{2|m|} \mathbf{c}[\psi^{\dagger}(i\nabla\psi) - (i\nabla\psi^{\dagger})\psi] \equiv \frac{\mathbf{cj}}{2|m|}. \tag{D4}$$

Using Eq. (D3), in parallel to Eqs. (48) and (8) in the relativistic case, we can express the interaction as

$$\tilde{V}_{\mathrm{st}} = \frac{1}{2|m|} \int d\mathbf{r}' \left[\frac{y - y'}{|\mathbf{r} - \mathbf{r}'|^2} j_x - \frac{x - x'}{|\mathbf{r} - \mathbf{r}'|^2} j_y \right] \delta\rho(\mathbf{r}'). \tag{D5}$$

If we introduce momentum space states,

$$\psi(\mathbf{r}) = \frac{1}{\sqrt{V}} \sum_{\mathbf{k}} \exp\{i\mathbf{k}\mathbf{r}\} c_{\mathbf{k}}, \tag{D6}$$

$$\mathbf{j}(\mathbf{k}) = \frac{1}{\sqrt{V}} \int d\mathbf{r} \exp\{-i\mathbf{k}\mathbf{r}\} \mathbf{j}(\mathbf{r})$$
$$= \frac{1}{\sqrt{V}} \sum_{\mathbf{q}} (2\mathbf{q} - \mathbf{k}) c_{\mathbf{q}}^{\dagger} c_{\mathbf{k}+\mathbf{q}}. \tag{D7}$$

Thus

$$\int d\mathbf{r}\,\tilde{V}_{\mathrm{st}}(\mathbf{r}) = \frac{i\,V}{|m|}\sum_{\mathbf{q},\mathbf{p},\mathbf{l}}\frac{\mathbf{q}\times\mathbf{p}}{|\mathbf{q}|^2}\,c^{\dagger}_{\mathbf{p}}\,c_{\mathbf{p}-\mathbf{q}}\,c^{\dagger}_{\mathbf{l}}\,c_{\mathbf{l}+\mathbf{q}}. \quad (D8)$$

We get the BCS channel by taking $\mathbf{l} = -\mathbf{p}$. If we let $\mathbf{p}\to\mathbf{k}$ and $\mathbf{q}\to\mathbf{k}-\mathbf{p}$, we have

$$\sum_{\mathbf{k}}\tilde{V}_{\mathrm{st}}(\mathbf{k}) = \frac{-i\,V}{|m|}\sum_{\mathbf{k},\mathbf{p}}\frac{\mathbf{p}\times\mathbf{k}}{|\mathbf{p}-\mathbf{k}|^2}\,c^{\dagger}_{\mathbf{k}}\,c_{\mathbf{p}}\,c^{\dagger}_{-\mathbf{k}}\,c_{-\mathbf{p}}. \quad (D9)$$

Now we should note that

$$\mathbf{p}\times\mathbf{k} = \frac{p_+k_- - p_-k_+}{-2i}. \quad (D10)$$

Direct comparison of Eq. (D9) with Eq. (58) shows that a p wave of opposite chirality with respect to the one of PH Pfaffian, i.e., a Pfaffian p wave, is the statistical interaction implied BCS pairing instability of classical HLR CFs.

The diamagnetic term in Eq. (D2), i.e., the term $\sim\mathbf{c}^2\,\psi^{\dagger}\psi$ makes an interesting three-body interaction in the real space:

$$\int d\mathbf{r}_3\,\tilde{V}_{\mathrm{st}}(\mathbf{r}_3) \sim \int d\mathbf{r}_1\int d\mathbf{r}_2\int d\mathbf{r}_3\,\frac{\mathbf{r}_1-\mathbf{r}_3}{|\mathbf{r}_1-\mathbf{r}_3|^2}\frac{\mathbf{r}_2-\mathbf{r}_3}{|\mathbf{r}_2-\mathbf{r}_3|^2}$$
$$\times\,\delta\rho(\mathbf{r}_1)\delta\rho(\mathbf{r}_2)\delta\rho(\mathbf{r}_3), \quad (D11)$$

whose sign is fluctuating and this interaction represents a disordering factor.

We can easily repeat the analysis in the anti-CFL case and find that the current-density statistical interaction favors opposite chirality pairing with respect to the Pfaffian but of composite holes. This special pairing state of composite holes can be identified with an anti-Pfaffian [35]. However, again the additional, fluctuating sign three-body interaction, next to the attractive channel exists.

APPENDIX E: BCS SELF-CONSISTENT PROBLEM AND ITS SOLUTIONS

We start with the relevant parts of BCS mean-field theory and follow the notation of Ref. [25]. The effective Hamiltonian is

$$K_{\mathrm{eff}} = \sum_{\mathbf{k}}\left\{\xi_k c^{\dagger}_{\mathbf{k}}c_{\mathbf{k}} + \frac{1}{2}\left(\Delta^* c_{-\mathbf{k}}c_{\mathbf{k}} + \Delta c^{\dagger}_{\mathbf{k}}c^{\dagger}_{-\mathbf{k}}\right)\right\}, \quad (E1)$$

and in our case $\xi_k = E_k - \mu$, with $E_k = \sqrt{|\mathbf{k}|^2+m^2}$. The Bogoliubov transformation is

$$\alpha_{\mathbf{k}} = u_{\mathbf{k}}c_{\mathbf{k}} - v_{\mathbf{k}}c^{\dagger}_{-\mathbf{k}}, \quad (E2)$$

with

$$\frac{v_{\mathbf{k}}}{u_{\mathbf{k}}} = \frac{-(\mathcal{E}_k - \xi_k)}{\Delta^*_{\mathbf{k}}},$$

$$|u_{\mathbf{k}}|^2 = \frac{1}{2}\left(1 + \frac{\xi_k}{\mathcal{E}_k}\right), \quad (E3)$$

$$|v_{\mathbf{k}}|^2 = \frac{1}{2}\left(1 - \frac{\xi_k}{\mathcal{E}_k}\right),$$

and $\mathcal{E}_k = \sqrt{\xi_k^2 + |\Delta_{\mathbf{k}}|^2}$.

On the other hand, if we start with a Cooper channel interaction and do the BCS mean-field decomposition with $b^{\dagger}_{\mathbf{k}} = c^{\dagger}_{\mathbf{k}}c^{\dagger}_{-\mathbf{k}}$,

$$\sum_{\mathbf{k},\mathbf{p}}V_{\mathbf{k}\mathbf{p}}\,b^{\dagger}_{\mathbf{k}}\,b_{\mathbf{p}} = \sum_{\mathbf{k},\mathbf{p}}V_{\mathbf{k}\mathbf{p}}\langle b^{\dagger}_{\mathbf{k}}\rangle b_{\mathbf{p}} + \sum_{\mathbf{k},\mathbf{p}}V_{\mathbf{k}\mathbf{p}}b^{\dagger}_{\mathbf{k}}\langle b_{\mathbf{p}}\rangle$$
$$- \sum_{\mathbf{k},\mathbf{p}}V_{\mathbf{k}\mathbf{p}}\langle b^{\dagger}_{\mathbf{k}}\rangle\langle b_{\mathbf{p}}\rangle, \quad (E4)$$

and specify $u_{-\mathbf{k}} = u_{\mathbf{k}} = u^*_{\mathbf{k}}$ and $v_{-\mathbf{k}} = -v_{\mathbf{k}}$, then

$$\frac{\Delta^*_{\mathbf{p}}}{2} = \sum_{\mathbf{k}}V_{\mathbf{k}\mathbf{p}}\langle c^{\dagger}_{\mathbf{k}}c^{\dagger}_{-\mathbf{k}}\rangle$$
$$= \sum_{\mathbf{k}}V_{\mathbf{k}\mathbf{p}}\langle(u_{\mathbf{k}}\alpha^{\dagger}_{\mathbf{k}} + v^*_{\mathbf{k}}\alpha_{-\mathbf{k}})(-v^*_{\mathbf{k}}\alpha_{\mathbf{k}} + u_{\mathbf{k}}\alpha^{\dagger}_{-\mathbf{k}})\rangle, \quad (E5)$$

i.e.,

$$\frac{\Delta^*_{\mathbf{p}}}{2} = \sum_{\mathbf{k}}V_{\mathbf{k}\mathbf{p}}v^*_k u_k = \sum_{\mathbf{k}}V_{\mathbf{k}\mathbf{p}}(-)\frac{\Delta^*_{\mathbf{k}}}{2\,\mathcal{E}_k}, \quad (E6)$$

and thus Eq. (64) in the main text.

1. BCS equation in polar coordinates $\mathbf{k}\to(k,\theta_k)$

We simplify the expression in Eq. (C3) to obtain

$$V_{\mathbf{k}\mathbf{p}} = \frac{2\pi}{8V}\frac{1}{E_k\cdot E_p}\left[-4|m|kp\frac{i\sin(\theta_p-\theta_k)}{|\mathbf{k}-\mathbf{p}|^2}\right.$$
$$-\frac{m}{|m|}(E_k + E_p + 2m)(E_k - m)(E_p - m)$$
$$\left.\times\frac{\exp\{i2(\theta_p-\theta_k)\}-1}{|\mathbf{k}-\mathbf{p}|^2}\right]. \quad (E7)$$

For a fixed angular momentum channel, $\Delta^*_{\mathbf{k}} = |\Delta_{\mathbf{k}}|e^{il\theta_k}$, we do first the integration over the angular variable, $\theta_k - \theta_p$, in Eq. (64) [or Eq. (E6) and after the change from sum to integral: $\sum_{\mathbf{k}}\to\frac{V}{(2\pi)^2}\int d\mathbf{k}$]. We use

$$I_m = \int_0^{2\pi}d\theta\,\frac{\sin m\theta\sin\theta}{\lambda-\cos\theta} = 2\pi(\lambda-\sqrt{\lambda^2-1})^m, \quad (E8)$$

$m = 1,\,2,\,3$, with $\lambda = \frac{k^2+p^2}{2kp}$, to get

$$V^l_{kp} = \frac{1}{2\pi}\int_0^{2\pi}d(\theta_k-\theta_p)e^{il(\theta_k-\theta_p)}V_{\mathbf{k}\mathbf{p}}, \quad (E9)$$

for $l = 1,\,3,\,-1$.

In particular, for $l = 1$ in (E9), we use (E8) to express the following integral:

$$\int_0^{2\pi}d(\theta_k-\theta_p)e^{i(\theta_k-\theta_p)}\frac{-i\sin(\theta_k-\theta_p)}{\lambda-\cos(\theta_k-\theta_p)} = I_1 \quad (E10)$$

and

$$\int_0^{2\pi} d(\theta_k - \theta_p) e^{i(\theta_k - \theta_p)} \frac{e^{-i2(\theta_k - \theta_p)} - 1}{\lambda - \cos(\theta_k - \theta_p)} = \int_0^{2\pi} d(\theta_k - \theta_p) \frac{e^{-i(\theta_k - \theta_p)} - e^{i(\theta_k - \theta_p)}}{\lambda - \cos(\theta_k - \theta_p)} = 0,$$

(E11)

for $l = 3$ in (E9), we have

$$\int_0^{2\pi} d(\theta_k - \theta_p) e^{i3(\theta_k - \theta_p)} \frac{-i \sin(\theta_k - \theta_p)}{\lambda - \cos(\theta_k - \theta_p)} = I_3$$

(E12)

and

$$\int_0^{2\pi} d(\theta_k - \theta_p) e^{i3(\theta_k - \theta_p)} \frac{e^{-i2(\theta_k - \theta_p)} - 1}{\lambda - \cos(\theta_k - \theta_p)} = \int_0^{2\pi} d(\theta_k - \theta_p) e^{i2(\theta_k - \theta_p)} \frac{e^{-i(\theta_k - \theta_p)} - e^{i(\theta_k - \theta_p)}}{\lambda - \cos(\theta_k - \theta_p)} = 2I_2,$$

(E13)

and similarly for $l = -1$. In this way, we can get the following expressions for V_{kp}^l, $l = 1, 3, -1$:

$$V_{kp}^1 = \frac{2\pi}{8 \, E_p \, E_k} [-2|m|(\lambda - \sqrt{\lambda^2 - 1})],$$

(E14)

$$V_{kp}^3 = \frac{2\pi}{8 E_p \, E_k} \left[-2|m|(\lambda - \sqrt{\lambda^2 - 1})^3 - \frac{m}{|m|} \frac{(E_p - m)(E_k - m)(E_p + E_k + 2m)}{p \, k} (\lambda - \sqrt{\lambda^2 - 1})^2 \right],$$

(E15)

and

$$V_{kp}^{-1} = \frac{2\pi}{8 E_p \, E_k} \left[2|m|(\lambda - \sqrt{\lambda^2 - 1}) + \frac{m}{|m|} \frac{(E_p - m)(E_k - m)(E_p + E_k + 2m)}{p \, k} (\lambda - \sqrt{\lambda^2 - 1})^2 \right].$$

(E16)

Note that we take

$$\lambda - \sqrt{\lambda^2 - 1} = \begin{cases} \frac{k}{p}, & k < p \\ \frac{p}{k}, & p < k \end{cases} \equiv r_{pk}$$

(E17)

as $\sqrt{\lambda^2 - 1} = \sqrt{\frac{k^4 + p^4 + 2k^2 p^2}{4k^2 p^2} - 1} = \sqrt{\frac{k^4 + p^4 - 2k^2 p^2}{4k^2 p^2}} = \frac{\sqrt{(k^2 - p^2)^2}}{2kp}$. At this point, we choose $\sqrt{(k^2 - p^2)^2} = |k^2 - p^2|$, which then leads to Eq. (E17). Other choices lead to an unphysical V that does not decay to zero with large k and p and diverges at $k = 0$ or $p = 0$. The general expression for V in the three cases of interest $l = 1, 3, -1$ is given by

$$V_{kp}^l = \frac{2\pi}{8 E_p \, E_k} \left[-2 \, \text{sgn}(l) \, |m| \, r_{kp}^{|l|} - (1 - \delta_{l,1}) \text{sgn}(l) \text{sgn}(m) \frac{(E_p - m)(E_k - m)(E_p + E_k + 2m)}{p \, k} r_{kp}^2 \right].$$

(E18)

where $\delta_{x,y}$ is the Kronecker delta, equal 1 when $x = y$ and otherwise 0. Finally, we need to solve

$$|\Delta_{\mathbf{k}}| = -\frac{1}{2\pi} \int_0^\infty dp \, p \, V_{kp}^l \frac{|\Delta_{\mathbf{p}}|}{\mathcal{E}_p},$$

(E19)

with V_{kp}^l defined in Eq. (E18). Note that $|\Delta_{\mathbf{k}}|$ only depends on k.

2. Ground-state energy

For the BCS ground state $|\Omega\rangle$ for which $\alpha_{\mathbf{k}} |\Omega\rangle = 0$, after a simple algebra, we have

$$\langle \Omega | K_{\text{eff}} | \Omega \rangle = -\sum_{\mathbf{k}} \frac{\mathcal{E}_k - \xi_k}{2}.$$

(E20)

To make assessment of the implied ground-state energies we first note that

$$\langle b_{\mathbf{k}}^\dagger \rangle = -\frac{\Delta_{\mathbf{k}}^*}{2 \, \mathcal{E}_k},$$

(E21)

and thus

$$E_0 = \langle \Omega | K_{\text{eff}} | \Omega \rangle - \sum_{\mathbf{k}, \mathbf{p}} V_{\mathbf{kp}} \langle b_{\mathbf{k}}^\dagger \rangle \langle b_{\mathbf{k}} \rangle$$

$$= -\sum_{\mathbf{k}} \frac{\mathcal{E}_k - (E_k - \mu)}{2} - \sum_{\mathbf{k}, \mathbf{p}} V_{\mathbf{kp}} \frac{\Delta_{\mathbf{k}}^*}{2 \, \mathcal{E}_k} \frac{\Delta_{\mathbf{p}}}{2 \, \mathcal{E}_p}.$$

(E22)

In the second term (after the infinite volume limit), we need to integrate over θ_k and θ_p. Because $\Delta_{\mathbf{k}}^* \Delta_{\mathbf{p}} = |\Delta_{\mathbf{k}}| |\Delta_{\mathbf{p}}| e^{il(\theta_k - \theta_p)}$, a change of variables, $\theta_+ = \theta_k + \theta_p$ and $\theta_- = \theta_k - \theta_p$, is appropriate to apply. The function under integral $f(\theta_k, \theta_p) \sim e^{il(\theta_k - \theta_p)} V_{\mathbf{kp}}$ has a periodicity under translations for (multiples of) 2π of θ_k and of θ_p. After a short analysis of mappings, we can conclude

$$\int_0^{2\pi} d\theta_k \int_0^{2\pi} d\theta_p f(\theta_k, \theta_p)$$

$$= \frac{1}{2} \int_0^{4\pi} d\theta_+ \int_0^{2\pi} d\theta_- f(\theta_-)$$

$$= 2\pi \int_0^{2\pi} d\theta_- f(\theta_-).$$

(E23)

Therefore the ground-state energy density for a fixed angular momentum l instability, $\Delta_{\mathbf{k}}^{*} = |\Delta_{\mathbf{k}}|e^{il\theta_k}$, is

$$E_0^l = -\frac{1}{(2\pi)} \int dk \, k \frac{\mathcal{E}_k - (E_k - \mu)}{2} - \frac{1}{(2\pi)^2} \int_0^\infty dp \, p$$

$$\times \int_0^\infty dk \, k \, V_{kp}^l \frac{|\Delta_{\mathbf{k}}|}{2 \, \mathcal{E}_k} \frac{|\Delta_{\mathbf{p}}|}{2 \, \mathcal{E}_p}, \tag{E24}$$

3. Proof of symmetry between $l = -1$ and 3 channels

The two pairing channels corresponding to $l = -1$ and 3 satisfy a symmetry relation

$$V_{kp}^{l=3}(m) = V_{kp}^{l=-1}(-m) \tag{E25}$$

and therefore the solutions for these two channels are equal up to a sign-flip of m. Here we present the proof of Eq. (E25).

First, we note that $E_k(m) = E_k(-m)$, as $E_k = \sqrt{k^2 + m^2}$. Therefore E_k is an implicit function of $|m|$. For the sake of clarity, we introduce $A_{kp}(m) \equiv \frac{2\pi}{8E_k E_p}$ and $A_{kp}(m) = A_{kp}(-m)$. We also introduce $a \equiv E_k$ and $b \equiv E_p$. We focus here on the case $k < p$ but an analogous proof can be easily given for the case $k > p$,

$$V_{kp,k<p}^{l=3}(m) = A_{kp}(m)\left[-2|m|\frac{k^3}{p^3}\right.$$

$$\left. - \operatorname{sgn}(m)\frac{(a-m)(b-m)(a+b+2m)}{pk}\frac{k^2}{p^2}\right]. \tag{E26}$$

We now separate the second term into parts which are even and odd with respect to m:

$$(a-m)(b-m)(a+b+2m) = (ab - am - bm + m^2)(a+b+2m)$$

$$= a^2b + b^2a + 2mab - ma^2 - mab - 2m^2a - mab - mb^2 - 2m^2b + m^2a + m^2b + 2m^3$$

$$= a^2b + b^2a - m^2(a+b) - m(a^2 + b^2 - 2m^2). \tag{E27}$$

Now we perform a change of variables $\tilde{m} = -m$:

$$(a-m)(b-m)(a+b+2m) = a^2b + b^2a - \tilde{m}^2(a+b) + \tilde{m}(a^2 + b^2 - 2\tilde{m}^2)$$

$$= (a-\tilde{m})(b-\tilde{m})(a+b+2\tilde{m}) + 2\tilde{m}(a^2 + b^2 - 2\tilde{m}^2). \tag{E28}$$

We now use $\operatorname{sgn}(x) = -\operatorname{sgn}(-x)$, and $\operatorname{sgn}(x)x = |x|$ to obtain

$$V_{kp,k<p}^{l=3}(-\tilde{m}) = A_{kp}(\tilde{m})\left[-2|\tilde{m}|\frac{k^3}{p^3} + \operatorname{sgn}(\tilde{m})\frac{(a-\tilde{m})(b-\tilde{m})(a+b+2\tilde{m})}{pk}\frac{k^2}{p^2} + 2|\tilde{m}|\frac{a^2 + b^2 - 2\tilde{m}^2}{kp}\frac{k^2}{p^2}\right]. \tag{E29}$$

We rewrite the additional term using k, p, and $\tilde{m}$:

$$a^2 + b^2 - 2\tilde{m}^2 = k^2 + \tilde{m}^2 + p^2 + \tilde{m}^2 - 2\tilde{m}^2 = k^2 + p^2 \tag{E30}$$

and

$$\frac{k^2 + p^2}{kp}\frac{k^2}{p^2} = (k^2 + p^2)\frac{k}{p^3} = \frac{k^3}{p^3} + \frac{k}{p}. \tag{E31}$$

The $\frac{k^3}{p^3}$ terms cancel and we finally obtain

$$V_{kp,k<p}^{l=3}(-\tilde{m}) = A_{kp}(\tilde{m})\left[2|\tilde{m}|\frac{k}{p} + \operatorname{sgn}(\tilde{m})\frac{(a-\tilde{m})(b-\tilde{m})(a+b+2\tilde{m})}{pk}\frac{k^2}{p^2}\right] = V_{kp,k<p}^{l=-1}(\tilde{m}). \tag{E32}$$

4. Numerical solution

We solve Eq. (E19) numerically, using the forward-substitution algorithm. We start from an initial guess for $|\Delta_k|$ (in practice $|\Delta_k| = 10^{-5}$, $\forall k$) and then recalculate it from the RHS of Eq. (E19) iteratively until it converges. We take as the criterion for convergence

$$\frac{\max_k |\Delta_k^{\text{new}} - \Delta_k^{\text{old}}|}{\max_k |\Delta_k^{\text{new}}|} < 10^{-3} k_F. \tag{E33}$$

It takes 30–130 iterations to satisfy the convergence criterion. We keep $k_F = 1$ to set the unit.

We perform the integration on the RHS of Eq. (E19) using the trapezoid rule. The integrand function on the RHS is very sharply peaked around k_F. To properly resolve the integrand function, we discretize k using a logarithmic grid,

$$\tilde{k}_j = e^{a_{\min} + \frac{j}{N_k}(a_{\max} - a_{\min})}, \quad j \in [0, N_k) \tag{E34}$$

with $N_k = 500$, $a_{\min} = -30$, and $a_{\max} = 4$. The logarithmic grid is placed on both sides of k_F, to include all points given by

$$1 \pm \tilde{k}_j > 0.$$

We add the $k = 1$ point by hand. Therefore our grid can resolve peaks at k_F that have a width $\gtrsim e^{-30}$, which is near the limitation of double precision numeric type. The logarithmic grid is particularly important for the $l = 1$ case
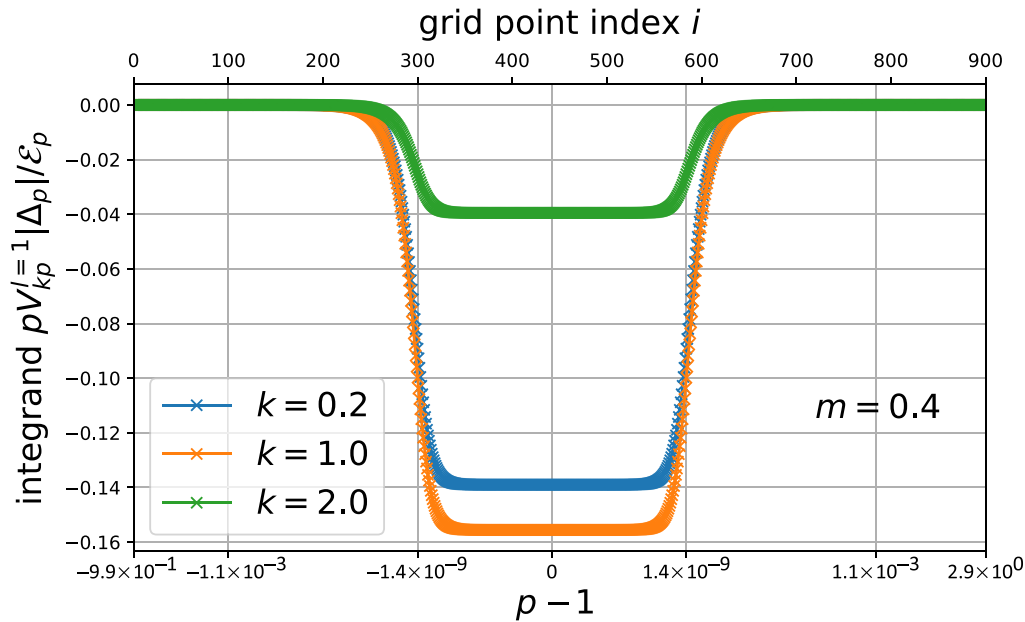
FIG. 2. Integrand function in the final iteration for $l = 1$, $m = 0.4$, and $k_F = 1$. Examples are given for three different k. The sharp peak at k_F has a width $\sim 10^{-9}$ and is properly resolved using a logarithmic grid.

at low m, where the integrand is most sharply peaked. We illustrate our grid and the integrand function in Fig. 2. We have checked that the results do not depend on the numerical parameters.

[1] D. C. Tsui, H. L. Störmer, and A. C. Gossard, Phys. Rev. Lett. **48**, 1559 (1982).

[2] R. B. Laughlin, Phys. Rev. Lett. **50**, 1395 (1983).

[3] R. Willett, J. P. Eisenstein, H. L. Stormer, D. C. Tsui, A. C. Gossard, and J. H. English, Phys. Rev. Lett. **59**, 1776 (1987).

[4] G. Moore and N. Read, Nucl. Phys. B **360**, 362 (1991).

[5] S.-S. Lee, S. Ryu, C. Nayak, and M. P. A. Fisher, Phys. Rev. Lett. **99**, 236807 (2007).

[6] M. Levin, B. I. Halperin, and B. Rosenow, Phys. Rev. Lett. **99**, 236806 (2007).

[7] H. Wang, D. N. Sheng, and F. D. M. Haldane, Phys. Rev. B **80**, 241311(R) (2009).

[8] D. T. Son, Phys. Rev. X **5**, 031027 (2015).

[9] S. Kachru, M. Mulligan, G. Torroba, and H. Wang, Phys. Rev. B **92**, 235105 (2015).

[10] Z. Wang and S. Chakravarty, Phys. Rev. B **94**, 165138 (2016).

[11] M. V. Milovanović, Phys. Rev. B **95**, 235304 (2017).

[12] A. C. Balram, M. Barkeshli, and M. S. Rudner, Phys. Rev. B **98**, 035127 (2018).

[13] R. V. Mishmash, D. F. Mross, J. Alicea, and O. I. Motrunich, Phys. Rev. B **98**, 081107 (2018).

[14] P. T. Zucker and D. E. Feldman, Phys. Rev. Lett. **117**, 096802 (2016).

[15] M. Banerjee, M. Heiblum, V. Umansky, D. E. Feldman, Y. Oreg, and A. Stern, Nature **559**, 205 (2018).

[16] C. Wang, A. Vishwanath, and B. I. Halperin, Phys. Rev. B **98**, 045112 (2018).

[17] D. F. Mross, Y. Oreg, A. Stern, G. Margalit, and M. Heiblum, Phys. Rev. Lett. **121**, 026801 (2018).

[18] B. Lian and J. Wang, Phys. Rev. B **97**, 165124 (2018).

[19] B. I. Halperin, Journal Club for Condensed Matter Physics, December, 2017, https://www.condmatjclub.org.

[20] S. H. Simon, Phys. Rev. B **97**, 121406 (2018).

[21] D. E. Feldman, arXiv:1805.03204.

[22] T. Jolicoeur, Phys. Rev. Lett. **99**, 036805 (2007).

[23] M. Milovanovic and N. Read, Phys. Rev. B **53**, 13559 (1996).

[24] M. V. Milovanovic and T. Jolicoeur, Int. J. Mod. Phys. B **24**, 549 (2010).

[25] N. Read and D. Green, Phys. Rev. B **61**, 10267 (2000).

[26] A. Cappelli, L. S. Georgiev, and I. T. Todorov, Nucl. Phys. B **599**, 499 (2009).

[27] E. H. Rezayi and N. Read, Phys. Rev. Lett. **72**, 900 (1994).

[28] E. H. Rezayi and F. D. M. Haldane, Phys. Rev. Lett. **84**, 4685 (2000).

[29] A. C. Potter, M. Serbyn, and A. Vishwanath, Phys. Rev. X **6**, 031026 (2016).

[30] C. Wang, N. R. Cooper, B. I. Halperin, and A. Stern, Phys. Rev. X **7**, 031029 (2017).

[31] N. Read, Phys. Rev. Lett. **62**, 86 (1989).

[32] S.-C. Zhang, Int. J. Mod. Phys. B **6**, 25 (1992).

[33] B. I. Halperin, P. A. Lee, and N. Read, Phys. Rev. B **47**, 7312 (1993).

[34] F. Cai, Y. Yu, and Z. Wang, J. Phys.: Cond. Mat. **25**, 305601 (2013).

[35] M. Barkeshli, M. Mulligan, and M. P. A. Fisher, Phys. Rev. B **92**, 165125 (2015).

[36] M. Greiter, X. G. Wen, and F. Wilczek, Nucl. Phys. B **374**, 567 (1992).

[37] M. P. Zaletel, R. S. K. Mong, F. Pollmann, and E. H. Rezayi, Phys. Rev. B **91**, 045115 (2015).

[38] K. Prabhu and M. M. Roberts, arXiv:1709.02814.

[39] D. X. Nguyen, S. Golkar, M. M. Roberts, and D. T. Son, Phys. Rev. B **97**, 195314 (2018).

[40] A. C. Balram, Y.-H. Wu, G. J. Sreejith, A. Wojs, and J. K. Jain, Phys. Rev. Lett. **110**, 186801 (2013).

[41] S. Johri, Z. Papic, R. N. Bhatt, and P. Schmitteckert, Phys. Rev. B **89**, 115124 (2014).

[42] I. Sodemann and A. H. MacDonald, Phys. Rev. B **87**, 245425 (2013).

[43] S. Pu, M. Fremling, and J. K. Jain, Phys. Rev. B **98**, 075304 (2018).

[44] V. A. Miransky, G. W. Semenoff, I. A. Shovkovy, and L. C. R. Wijewardhana, Phys. Rev. D **64**, 025005 (2001).

[45] C. Manuel, Phys. Rev. D **53**, 5866 (1996).

World Scientific
www.worldscientific.com

Pfaffian paired states for half-integer fractional quantum Hall effect

M. V. Milovanović*,‡, S. Djurdjević†,§ and J. Vučičević*,¶

*Scientific Computing Laboratory,
Center for the Study of Complex Systems,
Institute of Physics Belgrade, University of Belgrade,
Pregrevica 118, Belgrade 11080, Serbia
†Faculty of Natural Sciences and Mathematics,
University of Montenegro, Džordža Vašingtona bb,
Podgorica 81000, Montenegro
‡milica.milovanovic@ipb.ac.rs
§stevandj@ucg.ac.me
¶jaksa.vucicevic@ipb.ac.rs

L. Antonić

Department of Physics, Technion, Haifa 32000, Israel
luka.antonic@campus.technion.ac.il

In this review, the physics of Pfaffian paired states, in the context of fractional quantum Hall effect, is discussed using field-theoretical approaches. The Pfaffian states are prime examples of topological (p-wave) Cooper pairing and are characterized by non-Abelian statistics of their quasiparticles. Here we focus on conditions for their realization and competition among them at half-integer filling factors. Using the Dirac composite fermion description, in the presence of a mass term, we study the influence of Landau level mixing in selecting a particular Pfaffian state. While Pfaffian and anti-Pfaffian are selected when Landau level mixing is not strong, and can be taken into account perturbatively, the particle–hole (PH) Pfaffian state requires non-perturbative inclusion of at least two Landau levels. Our findings, for small Landau level mixing, are in accordance with numerical investigations in the literature, and call for a non-perturbative approach in the search for PH Pfaffian correlations. We demonstrated that a method based on the Chern–Simons field-theoretical approach can be used to generate characteristic interaction pseudo-potentials for Pfaffian paired states.

Keywords: Fractional quantum Hall effect; half-integer filling factor; Pfaffian paired states.

‡Corresponding author.

1. Introduction

The fractional quantum Hall effect (FQHE)[1] is a strongly correlated phenomenon of electrons that is observed when they are confined to two dimensions and subjected to a strong magnetic field perpendicular to the two-dimensional plane, in which electrons live and interact. At special filling factors, i.e. ratios between the number of electrons and the number of flux quanta piercing the two-dimensional plane, experiments reveal highly entangled topological states of electrons with fractionally quantized Hall conductance, for intervals of magnetic field (or density). Almost exclusively the denominator of these fractions is an odd number, which can be traced and connected to the fermionic statistics of electrons. A surprise came when an even-denominator FQHE, at filling factor $5/2$, was discovered.[2] This introduced a new paradigm in our understanding of (even-denominator) FQHE states: they may be Bardeen–Cooper–Schrieffer (BCS) paired states of underlying quasiparticles. If we neglect the role of spin in high magnetic fields, the most natural choice for a pairing in a fixed Landau level (LL) is the unconventional, p-wave pairing of spinless quasiparticles proposed in Ref. 3. The resulting state, Moore–Read state is also called Pfaffian due to the necessary antisymmetrization of a collection of pairs of quasiparticles — identical fermions, which do not possess any additional characteristic like spin.

The underlying quasiparticles at even-denominator fractions beside the possibility of having the BCS pairing correlations in a paired state, may in principle exist in its parent, Fermi-liquid-like (FLL) state.[4] Indeed such a state was probed and detected at filling factor $1/2$,[5] and firstly theoretically described in Ref. 6. The theoretical assessment of even-denominator FLL state(s) may lead also to further understanding of the physics of the BCS pairing of underlying quasiparticles. An important direction in this effort is the understanding of the FLL state that occurs at a half-integer (denominator 2) filling of the system, and, at the same time, in an artificial circumstance of a precisely half-filled LL. Namely, a LL is singled out and half-filled. This mathematical limit of the physical system is highly relevant for the understanding of the real system. Our understanding of FQHE phenomena and real circumstances of FQHE experiments call for the concept of the projection to a single LL. Very often the physics of FQHE is confined to a single LL, and we can neglect the LL mixing — the influence of other LLs. Thus if the system is at half(-integer) filling, it nearly possesses the particle–hole (PH) symmetry — the symmetry under exchange of electrons and holes that a half-filled LL has. The Halperin–Lee–Read (HLR) theory[6] of the FLL state at half-filling does not possess this symmetry (because it is a theory that does not include a projection to a fixed LL), but a phenomenological, effective theory with Dirac quasiparticles, proposed in Ref. 7 is manifestly invariant under exchange of electrons and holes, and describes the artificial system of electrons that is confined to a single LL.

On the other hand, the Pfaffian paired state is not invariant under exchange of electrons and holes. When the PH symmetry operation is applied to the

Pfaffian, a new topological state is generated, Pfaffian's conjugated partner, known as anti-Pfaffian.[8,9] Here we may ask whether a state exists, that is a collection of p-wave Cooper pairs and respects the PH symmetry. Indeed one may argue that the Dirac theory of the half-filled LL offers a distinct possibility[7] known as PH Pfaffian (PH symmetric Pfaffian). Before the proposal of the Dirac theory, studies that were examining possibilities of additional, negative-flux pairing, in which angular momentum of p-wave has opposite sign with respect to the one in Pfaffian, also proposed the PH Pfaffian.[10,11]

While the relevance of Pfaffian and especially anti-Pfaffian for the explanation of the FQHE at 5/2 is firmly established in numerical experiments confined to a fixed LL with LL mixing (perturbatively) included via additional, three-body interactions,[12] we do not have a support for PH Pfaffian when numerical experiments are confined to a fixed LL.[13] But a recent experiment[14] on thermal Hall conductance is consistent with a PH Pfaffian scenario at 5/2. That the PH Pfaffian correlations and topological order may be relevant even in the absence of the PH symmetry (as is the case in experiments) may be shown by careful examination of various experimental probes as discussed in Ref. 15.

Thus the question is whether for sufficiently strong LL mixing, that cannot be treated perturbatively (as it is done in all numerical experiments confined to a single LL), we can reach a regime in a uniform system when PH Pfaffian correlations prevail. Or, is disorder needed to install the effective PH Pfaffian correlations?[16,17] In any case LL mixing may play decisive role in selecting a specific kind of Pfaffian state in experiments. In the following sections, Secs. 3 and 4, we will review our work[18,19] that used Dirac and Chern–Simons (CS) field-theoretical description to examine the role of LL mixing and explore pairing at half-integer fillings, in general.

In Sec. 2, we will review the Dirac theory of the FLL state of underlying quasiparticles — composite fermions at a half-filled LL, and select and describe a version of the theory that is best fitted for a description of Pfaffian paired states. The mass term in this theory mimics LL mixing (for small LL mixing has the role of those additional (three-body) interactions in the electron representation), and the limiting behavior of large mass may be identified with the usual HLR picture of the FLL state of FQHE at half-filling.

In Sec. 3, within this version of the Dirac theory, we will probe the question of topological pairing instabilities in a mean-field approximation (as usual in topological explorations when we assume that topological characterization is immune to the neglect of fluctuations). Instabilities will originate from the minimal coupling term, i.e. the coupling with the CS gauge field, and we will be disregarding the remaining influence of the Coulomb interaction, which has a pair-breaking effect. Our interest will be to find which kind of Pfaffian will prevail at certain LL mixing, if we assume a pairing instability.

In Sec. 4, we will discuss which model Hamiltonians for electrons, i.e. effective interaction pseudo-potentials (PPs) in fixed LLs lead to Pfaffian states. Using CS field-theoretical description we recover dominant, already known PPs for

Pfaffian and anti-Pfaffian in a fixed LL, and discuss the necessity to include non-perturbatively at least one more LL to establish PH Pfaffian correlations, and list pertinent PPs.[19] Section 5 is reserved for a discussion and conclusions.

2. Theoretical Approaches to the Physics at a Half-Integer Filling

2.1. *Wave-function approach*

The basic explanation of the FQHE rests on the Laughlin wave function — the ground state wave function for the most prominent effect at filling $1/3$.[20] The wave function captures the basic correlations of electrons in a constrained space of an isolated LL. To introduce the Laughlin wave function, we start with the single-particle Hamiltonian,

$$H = \frac{(\mathbf{p} - \mathbf{A})^2}{2m_e} \, , \tag{1}$$

of a particle in a constant magnetic field, $\mathbf{B} = B\mathbf{z}$, with $A_x = -(B/2)y$ and $A_y = (B/2)x$, in a rotationally symmetric gauge. We fixed $c = 1$, $e = 1$, and $\hbar = 1$. The physics of FQHE is largely confined to a fixed LL and in the case of filling factor $1/3$, to the lowest LL (LLL). In the rotationally symmetric gauge and in the LLL, the appropriate basis is given by the following single particle wave functions,

$$\Psi_n(\mathbf{r}) = \frac{1}{\sqrt{2\pi l_B^{2+2n} 2^n n!}} z^n \exp\left\{ -\left(\frac{1}{4l_B^2}\right) |z|^2 \right\} \, , \tag{2}$$

where $l_B = \sqrt{\frac{\hbar c}{eB}}$, and $n = 0, 1, 2 \ldots$ is the guiding center angular momentum number. Apart from the exponential factor, these wave functions depend only on the coordinate $z = x + iy$, i.e. they make a holomorphic description, when we neglect the factor which is the same for each $\Psi_n(\mathbf{r})$. Thus many-body wave functions of frozen spin electrons become polynomials in the z coordinate(s) in the LLL, as in the following expression,

$$\Psi(\mathbf{r}_1, \mathbf{r}_2, \ldots, \mathbf{r}_{N_e}) = P(z_1, z_2, \ldots, z_N) \exp\left\{ -\left(\frac{1}{4l_B^2}\right) \sum_{i=1}^{N_e} |z_i|^2 \right\} \, . \tag{3}$$

The Laughlin wave function at filling factor $1/3$ is specified by the Laughlin–Jastrow choice for P,

$$P_{L-J}(z_1, z_2, \ldots, z_{N_e}) = \prod_{i<j} (z_i - z_j)^m \, , \tag{4}$$

with $m = 3$. In this polynomial, the highest power of any z_i; $i = 1, 2, \ldots, N_e$ is $N_m = m(N_e - 1)$ and this number also specifies the number of (single-particle) states available to the system, i.e. the number of flux-quanta piercing the system, $N_\phi = N_m + 1$. Thus the ratio N_e/N_ϕ becomes $1/3$ in the thermodynamic limit when $m = 3$.

For monotonically decreasing with distance repulsive interactions like Coulomb, we may expect an extreme capacity of the wave-function to minimize the interaction energy. Namely, as a function of a fixed electron coordinate, the wave function has all (N_m) zeros on the other electrons, $m = 3$ per electron, though only one zero is required by Fermi statistics. Equivalently, we may say that the zero on any other electron is of the mth order as we study the limiting behavior when a fixed electron approaches any other in (4).

Following the same logic, we may attempt the same construction at filling factor $1/2$, but, because $m = 2$ in (4), in this case, we need additional factors that will ensure that the wave function is antisymmetric. These additional factors should not contribute or change the value of N_m in the thermodynamic limit (mN), and thus, as additional factors in the total wave function, may be considered as its "neutral part" — the part that does not see the macroscopic flux. (The Laughlin–Jastrow part (4) would represent the charged part.) The neutral part may describe a collection of fermionic quasiparticles (that do not see any macroscopic flux, i.e. external magnetic field), and they may be in the first approximation non-interacting (make a FLL state), or they may come in BCS pairs (make a bosonic condensate and possibly a gapped state). Indeed experiment and theory are equivocal that the state at filling factor $1/2$ (in GaAs structures) is a FLL state of underlying quasiparticles, and the state at filling factor $5/2$ (in GaAs²) is effectively a gapped state of half-filled second LL of frozen-spin (spinless) electrons, in which quasiparticles may pair. The exact topological nature of the paired state at filling factor $5/2$ is still under debate.

But we may say that the most theoretically appealing (the most simple and natural BCS pairing) guess for the gapped state at the half-integer filling factors (in various experimental set-ups) is proposed in Ref. 3, and goes under name Moore–Read state or Pfaffian (state). The Pfaffian wave function in the LLL is

$$\Psi_{\text{Pf}} = \sum_{\sigma} \text{sgn}\,\sigma \left\{ \frac{1}{(z_{\sigma(1)} - z_{\sigma(2)})} \cdots \frac{1}{(z_{\sigma(N_e-1)} - z_{\sigma(N_e)})} \right\} \prod_{k<l} (z_k - z_l)^2 , \quad (5)$$

where the sum is over all permutations of N_e objects where N_e is an even number. We omitted the exponential factors and the expression is unnormalized. In mathematics, if $A = \{a_{ij}\}$ is $N \times N$ antisymmetric matrix, and N is even, its Pfaffian is

$$\text{pf}(a_{ij}) = \text{pf}(A) = \frac{1}{2^{N/2}(N/2)!} \sum_{\sigma \in S_N} \text{sgn}\,\sigma \prod_{i=1}^{N/2} a_{\sigma(2i-1)\sigma(2i)} , \quad (6)$$

and $\text{pf}(A)^2 = \det(A)$. In more physical terms, we see that the sum in the Moore–Read wave function describes the antisymmetrization of a collection of Cooper pairs, where each pair wave function, $g(\mathbf{r})$, where $\mathbf{r}$ is the relative coordinate of a pair, can be described as

$$g(\mathbf{r}) \sim \frac{1}{z} . \quad (7)$$

This special algebraic decay is the hallmark of the Pfaffian (Moore–Read) wave function, and expresses a special kind of topological, long-range entanglement in this function that represents a p-wave pairing. The construction is given in the LLL, but can be easily generalized and considered in the second LL, i.e. in any isolated LL.

The highest power of any z_i in the Pfaffian wave function is $N_m = 2N_e - 3$, i.e. $N_m = 2N_e - \mathcal{S}$, where $\mathcal{S} = 3$ is so-called shift — a topological number that characterizes a state of a FQHE system on a curved background, such as a sphere. If a state is PH symmetric, the shift should be invariant under the PH exchange. We require $N_e + N_h = N_m + 1$, i.e. the number of electrons, N_e, plus the number of holes, N_h, should be equal to the number of available single-particle states. Thus the state that we get by applying the PH transformation on Pfaffian, is a distinct state, anti-Pfaffian, with shift equal to -1. This anti-Pfaffian state, that has distinct topological features with respect to Pfaffian, was firstly described in Refs. 8 and 9.

We may wonder whether we may still have a p-wave pairing (the smallest angular momentum pairing of spinless electrons) in a many-body wave function that is invariant under PH exchange. It is not hard to see that in this case we must have $N_m = 2N_e - 1$, and this implies some kind of a microscopic negative flux or simply reversed p-wave pairing as in

$$g_{\mathrm{ph}}(\mathbf{r}) \sim \frac{1}{z^*} \,. \tag{8}$$

The naive guess would be that by doing the projection to the LLL, in the first approximation, we have

$$g_{\mathrm{ph}}(\mathbf{r}) \sim z \,. \tag{9}$$

But, because for any set of complex numbers z_i, $i = 1, 2, \ldots, N,; N$ even, and $N > 2$,

$$\mathrm{pf}(z_i - z_j) = 0 \,, \tag{10}$$

this does not lead to a non-trivial state in the LLL. Thus the question is whether a half-filled isolated LL with special interactions can support a gapped state with PH symmetry, i.e. PH (symmetric) Pfaffian. In the case of Pfaffian and anti-Pfaffian, special interactions exist in an isolated LL[21] (and they do not respect the PH symmetry). Furthermore, the negative flux pairing expression in (8) calls for inclusion of other LLs, and maybe only with significant LL mixing, when the PH symmetry is broken, we can stabilize the pairing correlations in (8). Even in this case, we will call this exotic state PH Pfaffian.

2.2. *Field-theoretical approach*

2.2.1. *Quasiparticles in the FQHE and the HLR theory at half-filling*

We may separate the phase part from the rest of the Laughlin wave function at filling factor $1/m$, where $m = 3$, or from the Laughlin–Jastrow part of a ground

state wave function at half-filling, when $m = 2$, and, then, define a decomposition into two parts of any many-electron wave-function, Ψ_e, as

$$\Psi_e(\mathbf{r}_1, \mathbf{r}_2, \ldots, \mathbf{r}_{N_e}) = \prod_{i<j} \frac{(z_i - z_j)^m}{|z_i - z_j|^m} \Psi_{qp}(\mathbf{r}_1, \mathbf{r}_2, \ldots, \mathbf{r}_{N_e}) \,. \tag{11}$$

The wave function $\Psi_{qp}(\mathbf{r}_1, \mathbf{r}_2, \ldots, \mathbf{r}_{N_e})$ represents a wave function of quasiparticles after the unitary transformation defined by the phase factor: in the Laughlin ($m = 3$) case quasiparticles are bosons, and at half-filling ($m = 2$) they are fermions. This defines a CS transformation, or what we will refer to as a Zhang's construction of quasiparticles.[22] In the field-theoretical terms, quasiparticles induce field $\mathbf{a}$ — they are the sources of an artificial (internal) magnetic field b that also acts as an additional field on quasiparticles,

$$\rho_{qp} = -\frac{1}{m} \frac{\nabla \times \mathbf{a}}{2\pi} = -\frac{1}{m} b \,. \tag{12}$$

In (12) ρ_{qp} is the quasiparticle density. We will discuss the CS field-theoretical approach to the system at half-filling, i.e. the HLR theory with more mathematical details below. Here we will note that in a mean-field picture the internal field will cancel the external field. As a first approximation to the half-filling problem, we will find that the ground state in the quasiparticle representation is simply a Slater-determinant of free waves that are filling a Fermi sphere in the inverse space in two dimensions, i.e. it represents a gas of fermionic quasiparticles. (The amplitude part of the Laughlin–Jastrow factor can be recovered in the field-theoretical approach by the random phase approximation (RPA) treatment of the density harmonic fluctuations.)

Therefore, in the Zhang's quasiparticle construction to each electron at position w is attached the following phase factor:

$$\prod_i \frac{|z_i - w|^m}{(z_i - w)^m} \,, \tag{13}$$

a flux tube. The ensuing quasiparticle sees two gauge fields: external and internal — it is a quasiparticle that possesses charge, and the density of quasiparticles is equal to the density of electrons.

On the other hand in the Read's construction[23] of quasiparticles, we start with the notion of fluxes (flux quanta or vortices) that can be introduced by external field in the system, and can be described by the following construction,

$$\prod_i (z_i - w)^m \,, \tag{14}$$

i.e. by insertion of m Laughlin quasiholes. We can make this object neutral by adding a unit of charge, more precisely an electron, to it, and in this way define the Read's quasiparticles as neutral objects, number of which is proportional to the number of external field flux quanta piercing the system. This view is in a way a dual approach (equivalent description of the same theory from a different

point of view) that was initially applied to bosonic systems where the description in terms of elementary particles — bosons was traded for the description in terms of excitations — vortices.[24]

In any case both approaches take into account the precise commensuration between the number of electrons and the number of flux quanta in a system at a fixed filling factor, in our case 1/2.

The CS approach at 1/2, based on the Zhang's construction of quasiparticles, begins with the following Lagrangian (density),

$$\mathcal{L} = \Psi_{\mathrm{cf}}^*(i\partial_t - A_0 - a_0)\Psi_{\mathrm{cf}} - \frac{\Psi_{\mathrm{cf}}^*(\mathbf{p} - \mathbf{A} - \mathbf{a})^2\Psi_{\mathrm{cf}}}{2m} - \frac{1}{2}\frac{1}{4\pi}a\partial a\,. \tag{15}$$

In (15), Ψ_{cf} represents a fermionic (Grassmann quasiparticle) field, and the CS term is defined by $a\partial a \equiv \epsilon^{\mu\nu\lambda}a_\mu\partial_\nu a_\lambda$, $\mu,\nu,\lambda = 0,1,2$ (denote one time and two spatial coordinates), the summation over repeated indices is understood, and $a_\mu = (a_0, \mathbf{a})$ is a three-vector. The cf stands for composite fermions, a general name for underlying quasiparticles.

Considering the classical equations of motion, from $\frac{\delta\mathcal{L}}{\delta a_0} = 0$, we get

$$-\Psi_{\mathrm{cf}}^*\Psi_{\mathrm{cf}} - \frac{1}{2}\frac{\nabla \times \mathbf{a}}{2\pi} = 0\,. \tag{16}$$

(Above $\nabla \times \mathbf{a}$ denotes the z component of the vector, and can be considered as a scalar in this two-dimensional theory.) In the mean-field, when we assume that the density of quasiparticles is uniform, the internal field, $\frac{\nabla\times\mathbf{a}}{2\pi}$, exactly cancels the uniform external field at half-filling,

$$\frac{\nabla \times \mathbf{A}}{2\pi} = 2\overline{\Psi_{\mathrm{e}}^*\Psi_{\mathrm{e}}} = 2\overline{\Psi_{\mathrm{cf}}^*\Psi_{\mathrm{cf}}}\,, \tag{17}$$

where $\overline{\Psi_{\mathrm{e}}^*\Psi_{\mathrm{e}}}$ stands for the uniform electron density.

The Lagrangian in (15) is the basis or starting point for the HLR theory, which describes the physics at 1/2 as a FLL state of (fermionic) quasiparticles. We may notice, from the form of the Lagrangian, that the electron density–current vector is equal to the one of quasiparticles,

$$-\frac{\delta\mathcal{L}}{\delta A^\mu} = j_{\mathrm{e}}^\mu = j_{\mathrm{cf}}^\mu\,. \tag{18}$$

2.2.2. *Dirac quasiparticle description of half-filled LL and at half-filling*

In this section, we will first review the Dirac theory for a half-filled LL proposed in Ref. 7 and then consider its extension in the presence of a mass term that is relevant for the general case (with LL mixing) at half-filling.

We start with an isolated LL (of classical electrons) that is half-filled. It has the PH symmetry — the symmetry under exchange of electrons and holes. The low-energy physics of a zeroth LL of Dirac electrons in the weak coupling limit should correspond to the low-energy physics of isolated LL (of classical electrons).[7]

Thus we consider the Dirac problem in an external (magnetic) field, which is a background field (no dynamics):

$$\mathcal{L}_D = i\overline{\Psi}\gamma^\mu D_\mu^A \Psi + \text{interactions} = i\overline{\Psi}(\gamma^0 D_t + \boldsymbol{\gamma}\cdot\mathbf{D})\Psi + \text{interactions} \qquad (19)$$

where $D_t = \frac{\partial}{\partial t} + iA_0$ and $\mathbf{D} = \boldsymbol{\nabla} - i\mathbf{A}$, and γ^μ, $\mu = 0, 1, 2$ are 2×2 gamma matrices for the Dirac description in two spacial dimensions, and Ψ is a two-component Grassmann field.

The Dirac system is a neutral system and there is no Hall conductance. To make up for this, i.e. to continue to discuss an isolated LL (of classical electrons), which has $1/(4\pi)$ of the units $(e^2/\hbar)$ of Hall conductance, we consider

$$\mathcal{L}_A = i\overline{\Psi}\gamma^\mu D_\mu^A \Psi - \frac{A\partial A}{8\pi} + \text{interactions}. \qquad (20)$$

If we define the density–current of electrons as

$$j_{\text{el}}^\mu = -\frac{\delta\mathcal{L}}{\delta A^\mu}, \qquad (21)$$

it follows that for densities,

$$\rho_{\text{el}} = \rho_{\text{D}} + \frac{\boldsymbol{\nabla}\times\mathbf{A}}{4\pi}. \qquad (22)$$

Because, $\overline{\rho}_{\text{D}}$ (average density of the Dirac system) $= 0$, we have a non-zero density of electrons

$$\frac{\overline{\rho}_{\text{el}}}{B} = \frac{1}{2}, \qquad (23)$$

where $B = \frac{\boldsymbol{\nabla}\times\mathbf{A}}{2\pi}$ is the uniform external magnetic field. Also

$$\mathbf{j}_{\text{el}} = \mathbf{j}_{\text{D}} + \hat{\epsilon}\frac{\mathbf{E}}{4\pi}, \qquad (24)$$

where $\hat{\epsilon}$ is a 2×2 matrix, $\epsilon_{xy} = -\epsilon_{yx} = 1$, $\epsilon_{xx} = \epsilon_{yy} = 0$. Thus, with $\overline{\rho}_{\text{D}} = 0$ and $\mathbf{j}_{\text{D}} = 0$, we are at half-filling, and the Hall conductance is equal to $\frac{1}{4\pi}(\frac{e^2}{\hbar})$.

Following Ref. 7, in a dual picture, we postulate a new Lagrangian, $\mathcal{L}$, with new dual Dirac field χ:

$$\mathcal{L} = i\overline{\chi}\gamma^\mu D_\mu^a \chi + a\frac{\partial A}{4\pi} - \frac{A\partial A}{8\pi} + \cdots \qquad (25)$$

where $\cdots$ denotes higher order terms. (We will ignore these higher order terms below and consider classical equations of motion in the framework of the linear response theory.) Why would we expect this Lagrangian in a dual picture? We provide an analysis with more details below, but here we may note that the Dirac (two-component) formalism is expected also in a dual picture, because it makes possible that the PH symmetry is manifestly included as demonstrated in Ref. 7. Also note that the dual fermion is not directly coupled to the external field, and, as we show below, the Lagrangian describes a Dirac system at a finite density, in agreement with our expectation that the system is in a FLL state of quasiparticles. For further details on the dual approach see Refs. 25 and 26.

(i) It seems that χ's represent Read's quasiparticles. Indeed, if we consider the following equation of motion,

$$0 = \frac{\delta \mathcal{L}}{\delta a_0} = -\rho_\chi + \frac{\nabla \times \mathbf{A}}{4\pi} \,, \qquad (26)$$

we can conclude that the density of χ depends on the number of flux quanta. On the other hand,

$$\rho_{\text{el}} = -\frac{\delta \mathcal{L}}{\delta A_0} = -\frac{\boldsymbol{\nabla} \times \mathbf{a}}{4\pi} + \frac{\boldsymbol{\nabla} \times \mathbf{A}}{4\pi} \,, \qquad (27)$$

and, at half-filling, in the mean-field approximation, $\boldsymbol{\nabla} \times \mathbf{a} = 0$. Thus, χ's do not experience any uniform, non-zero gauge field, $b = \frac{\boldsymbol{\nabla} \times \mathbf{a}}{2\pi}$, that couples χ's indirectly to the external field. Therefore, χ's are, in the first approximation, neutral objects, but with the Dirac's singularity in the inverse space at $\mathbf{k} = 0$. In this way, they have a non-analytical feature that we do not expect from a description that is based on Read's quasiparticles. We find that the effective theories based on the description with the Dirac's quasiparticle are very useful when considering the pairing physics, as they capture the time-reversal and parity breaking (that is essential for the pairing physics) as we will explain later in this section.

(ii) We expect that the effective theory of a half-filled LL should describe a Fermi-liquid of quasiparticles (if we do not consider the BCS instability). Indeed, in the mean-field approximation, in the first approximation, the internal field (b) is zero, and the theory describes a Dirac Fermi-liquid.

(iii) If we vary $\mathbf{a}$ in $\mathcal{L}$ we find

$$\mathbf{j}_{\text{D}} = \hat{\epsilon} \frac{\mathbf{E}}{4\pi} \,. \qquad (28)$$

Also,

$$\mathbf{j}_{\text{el}} = -\frac{\delta \mathcal{L}}{\delta \mathbf{A}} = \hat{\epsilon} \frac{\mathbf{E} - \mathbf{e}}{4\pi} \,, \qquad (29)$$

where $\mathbf{e}$ is the electric field due to the potential a^μ. Next, we assume that even in the presence of disorder, the PH symmetry is respected, and in the linear response we have,

$$\mathbf{j}_{\text{D}} = \hat{\sigma}^{\text{D}} \mathbf{e} \,, \qquad (30)$$

where $\sigma_{xx}^{\text{D}} = \sigma_{yy}^{\text{D}} \neq 0$ represents a longitudinal conductance, and $\sigma_{xy}^{\text{D}} = \sigma_{yx}^{\text{D}} = 0$ (the Hall conductance is zero). The zero Hall conductance is an expression of the PH symmetry and a property of Dirac fermions. These three equations, (28), (29), and (30), combined lead to the conclusion that the Hall conductance of electrons is $\frac{1}{2}(\frac{e^2}{h})$, which we expect to be the case in the theory of the system with classical electrons that respects the PH symmetry.[27]

It is important to notice that $\sigma_{xy}^{\mathrm{D}} = \sigma_{yx}^{\mathrm{D}} = 0$ is not an only natural "choice" for the response of the non-interacting Dirac system (conus) to a perturbation due to a gauge (internal a^μ) field. To get the Hall conductance, we assume the presence of the mass term in the non-interacting Dirac description,

$$\mathcal{L}_{\mathrm{D}} = i\overline{\chi}\gamma^\mu D_\mu^a \chi - m\overline{\chi}\chi \,. \tag{31}$$

The σ_{xy}^{D} can be found by integration of Berry curvature in the inverse ($\mathbf{k}$) space,[27,28] by choosing a specific gauge for eigenstates, and integrating over occupied states. In this way, we can get contributions (in units $e^2/\hbar$):

$$\mathrm{sgn}(m)\frac{1}{4\pi}\left(1 - \frac{|m|}{\sqrt{k_F^2 + m^2}}\right), \tag{32}$$

from the positive-energy states that are filled for $0 \leq |\mathbf{k}| < k_F$, and

$$-\mathrm{sgn}(m)\frac{1}{4\pi} \,, \tag{33}$$

from the negative-energy states. There are two natural ways to take into account these two contributions: (1) to add them,

$$\sigma_{xy}^{\mathrm{D}} = -\frac{m}{\sqrt{k_F^2 + m^2}} \,, \tag{34}$$

i.e. adopt a "dimensional regularization," or (2) to consider only the contribution from the positive energy solutions:

$$\sigma_{xy}^{\mathrm{D}} = \mathrm{sgn}(m)\frac{1}{4\pi}\left(1 - \frac{|m|}{\sqrt{k_F^2 + m^2}}\right) \,, \tag{35}$$

i.e. adopt a "Pauli–Villars regularization." It is obvious that in order to get an appropriate response in the Dirac theory (of the half-filled LL) we need to assume and apply the dimensional regularization in the field-theoretical treatment.

We can also conclude that by choosing an appropriate singular gauge (phase) transformation on the negative energy eigenstates, we can switch from the dimensional regularization to the Pauli–Villars regularization (and vice versa). This transformation can be understood as an adoption of a new quasiparticle picture and a new Lagrangian (here without higher order terms):

$$\mathcal{L} = i\overline{\chi}^{\mathrm{qp}}\gamma^\mu D_\mu^a \chi^{\mathrm{qp}} - \frac{a\partial a}{8\pi} + a\frac{\partial A}{4\pi} - \frac{A\partial A}{8\pi} \,. \tag{36}$$

To find the same response as before, we have to adopt Pauli–Villars regularization (when integrating out fermions and generating quadratic terms in a) with a positive mass to cancel the second term in $\mathcal{L}$. Physically we indeed switched to a new quasiparticle picture of Zhang's type. To see that let's consider the full theory with a positive ($m > 0$) mass term:

$$\mathcal{L} = i\overline{\chi}^{\mathrm{qp}}D_a\chi^{\mathrm{qp}} - m\overline{\chi}^{\mathrm{qp}}\chi^{\mathrm{qp}} - \frac{a\partial a}{8\pi} + a\frac{\partial A}{4\pi} - \frac{A\partial A}{8\pi} \,. \tag{37}$$

(i) From the equations of motion,

$$0 = \frac{\delta \mathcal{L}}{\delta a^\mu} = -j_\chi^{\text{qp},\mu} - \frac{\partial a}{4\pi} + \frac{\partial A}{4\pi} \,, \tag{38}$$

and

$$j_{\text{el}}^\mu = -\frac{\delta \mathcal{L}}{\delta A^\mu} = \frac{\partial A}{4\pi} - \frac{\partial a}{4\pi} \,, \tag{39}$$

it follows that, $j_{\text{el}}^\mu = j_\chi^{\text{qp},\mu}$, as usual in the CS theory, i.e. the theory directly relates to the Zhang's quasiparticle construction.

(ii) If we let $m \to \infty$ the effective Lagrangian becomes the HLR after the shift $a^\mu \to a^\mu + A^\mu$.[29]

We can conclude that the Lagrangian in (37), with $m = 0$, describes the physics of an isolated (PH symmetric) LL using the Zhang's quasiparticle picture. The introduction of non-zero m represents LL mixing, i.e. a measure of the inclusion of other LLs, so that for large m we can recover the HLR theory that does not reduce the effective physics of the electron system to a single LL.

3. Pfaffian Paired States at Half-Integer Filling

In this section, we will adopt the Dirac quasiparticle picture that is given by the Lagrangian in (37) for a FQHE system at a half-integer filling factor. Thus, the starting Lagrangian is

$$\mathcal{L} = i\overline{\chi}\gamma^\mu D_\mu^a \chi - m\overline{\chi}\chi - \frac{m}{|m|}\frac{a\partial a}{8\pi} + a\frac{\partial A}{4\pi} - \frac{A\partial A}{8\pi} \,, \tag{40}$$

where for simplicity we omitted qp letters when writing χ fields with respect to (37), but we should be aware that for any probes (perturbative expansions) the Pauli–Villars regularization is understood. We generalized the Lagrangian in (37) for both signs of mass m (to cancel the additional contribution due to the assumed Pauli–Villars regularization, the first term in (35)). It follows that

$$j_\chi^\mu = -\frac{m}{|m|}\frac{\partial a}{4\pi} + \frac{\partial A}{4\pi} \,, \tag{41}$$

and

$$j_{\text{el}}^\mu = -\frac{\partial a}{4\pi} + \frac{\partial A}{4\pi} \,, \tag{42}$$

as a generalization of (38) and (39) to both signs of mass. Exactly at half-filling, i.e. when in a uniform, constant magnetic field we have on average one electron per two flux quanta, we may solve (41) in the Coulomb gauge, $\boldsymbol{\nabla} \cdot \mathbf{a} = 0$. The solutions are[22]

$$a_x(\mathbf{r}) = 2\frac{m}{|m|} \int d\mathbf{r}' i \frac{y - y'}{|\mathbf{r} - \mathbf{r}'|^2} \delta\rho_\chi(\mathbf{r}') \,, \tag{43}$$

and

$$a_y(\mathbf{r}) = -2\frac{m}{|m|}\int d\mathbf{r}' i\frac{x-x'}{|\mathbf{r}-\mathbf{r}'|^2}\delta\rho_\chi(\mathbf{r}')\,, \tag{44}$$

and $\delta\rho_\chi(\mathbf{r}') = \chi^\dagger(\mathbf{r}')\chi(\mathbf{r}') - \bar{\rho}$, where $\bar{\rho}$ is a constant (external flux density). We would like to analyze the effect on pairing of the interaction term,

$$V_{\text{int}} = -\mathbf{a}\bar{\chi}\boldsymbol{\gamma}\chi\,. \tag{45}$$

In the following, representation of γ matrices,

$$\gamma^0 = \sigma_3, \quad \gamma^1 = i\sigma_2, \quad \gamma^2 = -i\sigma_1\,, \tag{46}$$

where $\sigma_i, i = 1, 2, 3$ are Pauli matrices, we have

$$V_{\text{int}} = -\mathbf{a}\chi^+\boldsymbol{\sigma}\chi\,. \tag{47}$$

In this representation, we have the following expression for the interaction:

$$V_{\text{int}} = -i2\frac{m}{|m|}\int d\mathbf{r}'\delta\rho_\chi(\mathbf{r}')\chi^\dagger(\mathbf{r})\begin{bmatrix} 0 & \dfrac{\bar{z}-\bar{z}'}{|\mathbf{r}-\mathbf{r}'|^2} \\ -\dfrac{z-z'}{|\mathbf{r}-\mathbf{r}'|^2} & 0 \end{bmatrix}\chi(\mathbf{r})\,. \tag{48}$$

On the other hand, the presence of the mass term in the Dirac system leads to the following eigenproblem,

$$\begin{bmatrix} m-\epsilon & k_- \\ k_+ & -m-\epsilon \end{bmatrix}\chi(\mathbf{k}) = 0\,, \tag{49}$$

where $k_- = k_x - ik_y$ and $k_+ = k_x + ik_y$. The positive eigenvalue, $\epsilon = \sqrt{|\mathbf{k}|^2 + m^2} \equiv E_\mathbf{k}$, corresponds to the following eigenstate,

$$\chi_E = \begin{bmatrix} m+E_\mathbf{k} \\ k_+ \end{bmatrix}\frac{1}{\sqrt{2E_\mathbf{k}(E_\mathbf{k}+m)}}\,. \tag{50}$$

As we consider relevant only (positive energy) states around k_F, we will keep only these states in the expansion over $\mathbf{k}$-eigenstates of field $\chi(\mathbf{r})$, and, further, only consider the BCS pairing channel in V_{int}. Thus (in the second-quantized notation)

$$\chi(\mathbf{r}) = \frac{1}{\sqrt{2V}}\sum_\mathbf{k}\exp\{i\mathbf{k}\cdot\mathbf{r}\}\chi_E(\mathbf{k})a_\mathbf{k} + \cdots\,, \tag{51}$$

and

$$V_{\text{int}}^{\text{BCS}} = \frac{m}{|m|}\frac{2\pi}{8V}\sum_{\mathbf{k},\mathbf{p}} a_\mathbf{k}^\dagger a_\mathbf{p} a_{-\mathbf{k}}^\dagger a_{-\mathbf{p}} \times \frac{1}{E_\mathbf{k}E_\mathbf{p}(m+E_\mathbf{k})(m+E_\mathbf{p})}$$

$$\times \{(m+E_k)(m+E_p) + k_-p_+\}$$

$$\times \begin{bmatrix} m+E_k, & -k_- \end{bmatrix}\begin{bmatrix} 0 & \dfrac{1}{k_+ - p_+} \\ -\dfrac{1}{k_- - p_-} & 0 \end{bmatrix}\begin{bmatrix} m+E_p \\ -p_+ \end{bmatrix}\,. \tag{52}$$

We used: $\int d\mathbf{r} \frac{1}{z} \exp\{i\mathbf{k}\mathbf{r}\} = i\frac{2\pi}{k_+}$. We may rewrite this expression (taking into account the antisymmetry of the fermionic operators) as

$$V_{\text{int}}^{\text{BCS}} = \sum_{\mathbf{k},\mathbf{p}} V_{\mathbf{k}\mathbf{p}} a_{\mathbf{k}}^{\dagger} a_{\mathbf{p}} a_{-\mathbf{k}}^{\dagger} a_{-\mathbf{p}} \,, \tag{53}$$

where

$$V_{\mathbf{k}\mathbf{p}} = \frac{2\pi}{8V} \frac{1}{E_k \cdot E_p}$$
$$\times \left[-4|m|kp\frac{i\sin(\theta_p - \theta_k)}{|\mathbf{k} - \mathbf{p}|^2} - \frac{m}{|m|}(E_k + E_p + 2m)(E_k - m)(E_p - m) \right.$$
$$\left. \times \frac{\exp\{i2(\theta_p - \theta_k)\} - 1}{|\mathbf{k} - \mathbf{p}|^2} \right]. \tag{54}$$

Now we will adopt the mean-field BCS approximation, in an expectation that the topological characterization of pairing instabilities, will stay unchanged under this approximation. In the following, we will review the relevant parts of the BCS mean-field theory. We will follow the notation of Ref. 30. The effective Hamiltonian is

$$K_{\text{eff}} = \sum_{\mathbf{k}} \left\{ \xi_k a_{\mathbf{k}}^{\dagger} a_{\mathbf{k}} + \frac{1}{2}(\Delta_{\mathbf{k}}^{*} a_{-\mathbf{k}} a_{\mathbf{k}} + \Delta_{\mathbf{k}} a_{\mathbf{k}}^{\dagger} a_{-\mathbf{k}}^{\dagger}) \right\} \,, \tag{55}$$

and in our case $\xi_k = E_k - \mu$, with $E_k = \sqrt{|\mathbf{k}|^2 + m^2}$. The Bogoliubov transformation is

$$\alpha_{\mathbf{k}} = u_{\mathbf{k}} a_{\mathbf{k}} - v_{\mathbf{k}} a_{-\mathbf{k}}^{\dagger} \,, \tag{56}$$

with

$$\frac{v_{\mathbf{k}}}{u_{\mathbf{k}}} = \frac{-(\mathcal{E}_k - \xi_k)}{\Delta_{\mathbf{k}}^{*}}, \quad |u_{\mathbf{k}}|^2 = \frac{1}{2}\left(1 + \frac{\xi_k}{\mathcal{E}_k}\right) \,,$$
$$|v_{\mathbf{k}}|^2 = \frac{1}{2}\left(1 - \frac{\xi_k}{\mathcal{E}_k}\right) \,, \tag{57}$$

and $\mathcal{E}_k = \sqrt{\xi_k^2 + |\Delta_{\mathbf{k}}|^2}$.

On the other hand, if we start with a Cooper channel interaction and do the BCS mean-field decomposition with $b_{\mathbf{k}}^{\dagger} = a_{\mathbf{k}}^{\dagger} a_{-\mathbf{k}}^{\dagger}$

$$\sum_{\mathbf{k},\mathbf{p}} V_{\mathbf{k}\mathbf{p}} \, b_{\mathbf{k}}^{\dagger} \, b_{\mathbf{p}} = \sum_{\mathbf{k},\mathbf{p}} V_{\mathbf{k}\mathbf{p}} \langle b_{\mathbf{k}}^{\dagger} \rangle b_{\mathbf{p}} + \sum_{\mathbf{k},\mathbf{p}} V_{\mathbf{k}\mathbf{p}} b_{\mathbf{k}}^{\dagger} \langle b_{\mathbf{p}} \rangle - \sum_{\mathbf{k},\mathbf{p}} V_{\mathbf{k}\mathbf{p}} \langle b_{\mathbf{k}}^{\dagger} \rangle \langle b_{\mathbf{p}} \rangle \,, \tag{58}$$

and specify $u_{-\mathbf{k}} = u_{\mathbf{k}} = u_{\mathbf{k}}^{*}$ and $v_{-\mathbf{k}} = -v_{\mathbf{k}}$, then

$$\frac{\Delta_{\mathbf{p}}^{*}}{2} = \sum_{\mathbf{k}} V_{\mathbf{k}\mathbf{p}} \langle a_{\mathbf{k}}^{\dagger} a_{-\mathbf{k}}^{\dagger} \rangle$$
$$= \sum_{\mathbf{k}} V_{\mathbf{k}\mathbf{p}} \langle (u_{\mathbf{k}} \alpha_{\mathbf{k}}^{\dagger} + v_{\mathbf{k}}^{*} \alpha_{-\mathbf{k}})(-v_{\mathbf{k}}^{*} \alpha_{\mathbf{k}} + u_{\mathbf{k}} \alpha_{-\mathbf{k}}^{\dagger}) \rangle \,, \tag{59}$$

i.e.

$$\frac{\Delta_{\mathbf{p}}^*}{2} = \sum_{\mathbf{k}} V_{\mathbf{k}\mathbf{p}} v_k^* u_k = \sum_{\mathbf{k}} V_{\mathbf{k}\mathbf{p}}(-)\frac{\Delta_{\mathbf{k}}^*}{2\,\mathcal{E}_k}\,. \tag{60}$$

In our case $V_{\mathbf{k}\mathbf{p}}$ is given in (54). The numerical solutions of the BCS self-consistent equation, when the parameter k_F is kept fixed, but mass m is varied, for channels $l = 1, 3, -1$, with $\Delta_{\mathbf{k}}^* = |\Delta_{\mathbf{k}}| \exp\{il\theta_{\mathbf{k}}\}$ are described in Fig. 1. We find that $\Delta_{\mathbf{k}}^* = |\Delta_{\mathbf{k}}| \exp\{-il\theta_{\mathbf{k}}\}$, $l = 1, 3, -1$ are solutions if we switch gauge for the eigenstates of the Dirac equation, i.e. instead of (50) we take

$$\chi_E = \begin{bmatrix} k_- \\ E_{\mathbf{k}} - m \end{bmatrix} \frac{1}{\sqrt{2E_{\mathbf{k}}(E_{\mathbf{k}} - m)}}\,. \tag{61}$$
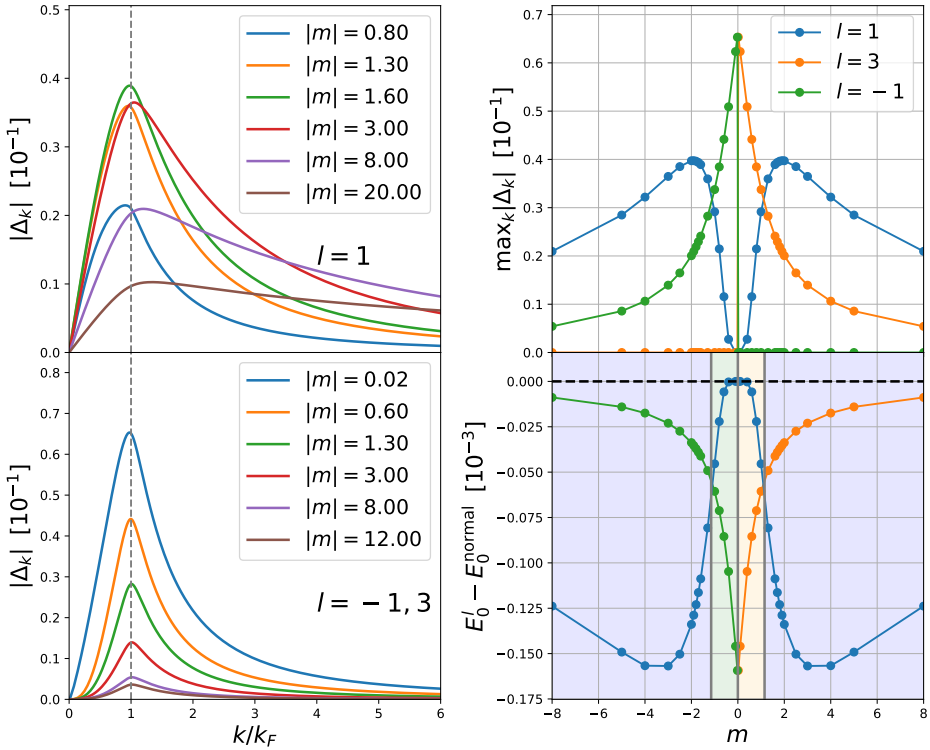
Fig. 1. (Color online) The solution of the self-consistent BCS problem. Left column: radial direction k-dependent pairing amplitude for various values of m. Channel $l = 1$ solution (PH Pfaffian) only depends on $|m|$, while $l = 3$ (anti-Pfaffian) and $l = -1$ (Pfaffian) channel solutions are symmetric with the sign-flip of m. Upper right panel: dependence of the maximum of the pairing amplitude on m (always found at the Fermi level k_F). Lower right panel: total energy of the different pairing solutions compared to the normal state energy. Gray vertical lines denote the transition between different channels. Color in the background corresponds to the energetically favorable channel at the given m: a measure of LL mixing. The color of lines: Pfaffian: green, anti-Pfaffian: orange, PH Pfaffian: blue. Reprinted with permission from Ref. 18 © the American Physical Society.

Thus we get two sets of solutions, because the effective theory does not possess the knowledge of the direction of the external magnetic field. Despite this, we have a clear prediction that for small m, LL mixing, depending on the sign of m we have Pfaffian or anti-Pfaffian, and for large m the PH Pfaffian solution is possible. Thus, in principle, the PH Pfaffian is possible in this effective theory of quasiparticle pairing. The nature of this state, whether it is gapped or gapless state of electrons, needs further investigations (though we see that the Bogoliubov quasiparticle spectrum is gapped).

These predictions on topological pairing, when the LL mixing (mass m) is small, are in accordance with numerical experiments (a) in the second LL, because for $m = 0$ there is a Schrodinger cat superposition of Pfaffian and anti-Pfaffian,[31,32] and depending on the LL mixing (sign of PH breaking mass) we have Pfaffian or anti-Pfaffian, and (b) in the LLL, where a PH Pfaffian wave function has a large overlap with the composite fermion Fermi-liquid wave function,[13,33] in accordance with Fig. 1 where the PH Pfaffian-like state is continuously connected to the excited composite fermion Fermi-liquid state at $m = 0$ and cannot represent a gapped state in an isolated LL.

The dimensionless m in the theory is a measure of the PH symmetry breaking and LL mixing, although the precise relation between m and

$$\kappa = \frac{\frac{e^2}{\epsilon_r l_B}}{\hbar \omega_c},$$ (62)

i.e. the ratio between the characteristic interaction energy and cyclotron energy, known as a LL mixing coefficient, we do not know. In (62), ϵ_r is the dielectric constant of the background material, $\hbar \omega_c = \frac{\hbar e B}{m_b c}$, and m_b is the electron band mass. As we keep the density, $\rho = \frac{\nu}{2\pi l_B^2} = \frac{1}{2} \frac{1}{2\pi l_B^2}$, i.e. k_F fixed, from the mathematical limit of the PH symmetric case when $m = 0$, we reach various systems (experimental settings) by changing the interaction strength (dielectric constant ϵ_r). Thus m, in principle, can be connected with κ, which can be considerable in experiments. (According to Ref. 41 the parameter κ is given by $2.6/\sqrt{B}$, $14.6/\sqrt{B}$, $16.7/\sqrt{B}$, $22.5/\sqrt{B}$, in n-doped GaAs, p-doped GaAs, n-doped ZnO, and n-doped AlAs, with B measured in Tesla.)

4. Model Interactions for Pfaffian Paired States

It is important to know model interactions for model wave functions in order to probe their stability and nature. In the case of bosons, the Pfaffian state at filling factor 1 is

$$\Psi_{\text{Pf}}^b = \sum_\sigma \text{sgn}\, \sigma \left\{ \frac{1}{(z_{\sigma(1)} - z_{\sigma(2)})} \cdots \frac{1}{(z_{\sigma(N_e-1)} - z_{\sigma(N_e)})} \right\}$$
$$\times \prod_{k<l} (z_k - z_l).$$ (63)

The model interaction for which this state is an exact, densest state of zero energy[34] is

$$H = v \sum_{\langle ijk \rangle} \delta^2(z_i - z_j)\delta^2(z_i - z_k) , \tag{64}$$

where $v > 0$ and the sum is over all distinct triples of particles. Thus if three bosons meet (come as close as possible) this will cost repulsive energy. In the case of fermions at filling factor $1/2$, the Pfaffian model interaction is a generalization of the boson interaction to the one that, if three fermions come as close as possible, again, only this will cost energy. The lowest angular momentum wave function of three electrons in the LLL can be described as

$$\Psi(\mathbf{r}_1, \mathbf{r}_2, \mathbf{r}_3) \sim \sum_{\sigma} \operatorname{sgn} \sigma z_{\sigma(1)}^2 z_{\sigma(2)}^1 z_{\sigma(3)}^0 \exp\left\{ -\frac{1}{4l_B}(|z_1|^2 + |z_2|^2 + |z_3|^2) \right\} . \tag{65}$$

We may conclude that if $M(\text{angular momentum}) = 3$ for three electrons this will cost interaction energy. Indeed, it can be argued, just as in the case of the Laughlin state and two-body PPs,[35] that in the case of Pfaffian we need to specify only a truncated series of three-body PPs with definite three-body angular momenta. At filling factor $1/2$, only non-zero three-body PP is the one for $M = 3$. (For bosons, at filling factor 1, the only non-zero three-body PP is for $M = 0$.)

These model interactions are highly artificial if we want to model and probe real physical systems. In the FQHE, we can always specify the base LL from which most of correlations originate, but should also consider the effects of LL mixing. Beside the Coulomb (two-body) interaction at a half-integer filling factor, we may take into account perturbatively the effects of LL mixing, by considering special three-body interactions.[37–41] In this way we may find a characteristic series of three-body PPs for Pfaffian state, when considering the specific problem of the second LL and associated LL mixing contribution. A PP is a certain characteristic energy, V_M, associated with a three-body state at total angular momentum M. (The dimension of the subspace of a fixed angular momentum for three particles may be larger than one for higher M, and V_M may be a matrix.) In the case of Pfaffian, the dominant, first three values of three-body PPs, for $M = 3, 5, 6$ are negative and $\frac{V_{M=5}}{V_{M=3}} \sim 0.4$ and $\frac{V_{M=6}}{V_{M=3}} \sim 0.7$.[41] We may ask what would be a characteristic series for PH Pfaffian, if we assume that the PH Pfaffian state or phase exists, and expect that some kind of three-body interaction will be relevant also in this case.

To answer this question we may consider again the CS formalism, not directly connected with considerations in Sec. 3. We will recall[34] the effective derivation of the Pfaffian physics, by a part of the kinetic term in the non-relativistic CS description. (Thus these considerations will not relate to the solution in Sec. 3, in the large m limit, when we take into account the complete kinetic term.) We will use this formal derivation to propose a method for recovering model interactions for Pfaffian and PH Pfaffian. (By using the PH exchange we can reach a model interaction also for anti-Pfaffian.)

To get (formally) the Pfaffian pairing solution we may consider the kinetic energy part of the (non-relativistic) CS approach in (15), i.e. the part of the Hamiltonian given by

$$\mathcal{H} = \frac{\Psi_{\text{cf}}^{+}(\mathbf{p} - \mathbf{A} - \mathbf{a})^2 \Psi_{\text{cf}}}{2m}, \tag{66}$$

with $\mathbf{B} = B\mathbf{z}$, with $A_x = -(B/2)y$ and $A_y = (B/2)x$, as before, and

$$a_x(\mathbf{r}) = 2\int d\mathbf{r}'i\frac{y - y'}{|\mathbf{r} - \mathbf{r}'|^2}\delta\rho_{\text{cf}}(\mathbf{r}'), \tag{67}$$

and

$$a_y(\mathbf{r}) = -2\int d\mathbf{r}'i\frac{x - x'}{|\mathbf{r} - \mathbf{r}'|^2}\delta\rho_{\text{cf}}(\mathbf{r}'), \tag{68}$$

as before, in the Coulomb gauge $\boldsymbol{\nabla} \cdot \mathbf{a} = 0$, and $\delta\rho_{\text{cf}} = \Psi_{\text{cf}}^{+}\Psi_{\text{cf}} - \overline{\rho}$, where $\overline{\rho}$ is the average density. We consider the following part of the implied interaction,

$$V_{\text{a}} = -\mathbf{a}\mathbf{j}_{\text{cf}}, \tag{69}$$

with

$$\mathbf{j}_{\text{cf}} = \frac{1}{2m}[\Psi_{\text{cf}}^{+}(\mathbf{p}\Psi_{\text{cf}}) - (\mathbf{p}\Psi_{\text{cf}}^{+})\Psi_{\text{cf}}], \tag{70}$$

more specifically its Cooper channel part.

After simple steps,[19] we arrive at the Cooper channel part,

$$V_{\text{int}}^{\text{C}} = \frac{4\pi}{m}\frac{1}{V}\sum_{\mathbf{k},\mathbf{p}}|\mathbf{k}||\mathbf{p}|\frac{i\sin(\theta_k - \theta_p)}{|\mathbf{p} - \mathbf{k}|^2}a_{\mathbf{k}}^{\dagger}a_{\mathbf{p}}a_{-\mathbf{k}}^{\dagger}a_{-\mathbf{p}}. \tag{71}$$

Note that in this case (following the mean-field equations and derivation in Ref. 30, or in Ref. 19) we find that the Cooper pair wave function behaves as,

$$\lim_{|\mathbf{r}|\to\infty} g(\mathbf{r}) \sim \frac{1}{z}. \tag{72}$$

This implies the Pfaffian construction (after the unitary CS transformation into the electron representation), if we recall that the choice of $\mathbf{A}$ in (66) implies a holomorphic Laughlin–Jastrow factor (more precisely a phase factor after the unitary CS transformation) that is associated with the usual description of the Pfaffian state in (5). If we had an extra minus sign in (71), this would lead to the antiholomorphic pairing, i.e. the PH Pfaffian pairing.

To derive the model interactions for Pfaffian and PH Pfaffian, we assume that we can use an effective non-relativistic CS description to describe the pairing of underlying quasiparticles (composite fermions). On the basis of the previous consideration ((69) and (71)), we consider an effective Hamiltonian,

$$H_{\text{BCS}}^{\text{ef}} = \frac{1}{2m}\Psi_{\text{cf}}^{\dagger}(\mathbf{p})^2\Psi_{\text{cf}} + \lambda\delta\mathbf{a}\mathbf{j}_{\text{cf}}, \tag{73}$$

where $\delta\mathbf{a} = \mathbf{A} + \mathbf{a}$, and the coupling λ is negative in the Pfaffian case and positive in the PH Pfaffian case. Thus we assumed that a complete (non-relativistic) CS

description that includes all effects of interactions can be reduced to the effective form if a pairing occurs. By using the non-relativistic CS description we take into account PH symmetry breaking necessary to stabilize these pairing states.

If we apply the CS transformation in reverse,[19] going from the composite fermion representation to an electron one, we arrive at the following effective Hamiltonian for electrons,

$$H_{\text{BCS}}^{\text{el}} = \frac{1}{2m}\Psi^{\dagger}(\mathbf{p} - \mathbf{A})^2\Psi - \frac{1}{2m}(\delta\mathbf{a})^2\Psi^{\dagger}\Psi + (1 + \lambda)\delta\mathbf{a}\mathbf{J}_{\text{el}} + (1 + \lambda)\frac{1}{m}(\delta\mathbf{a})^2\Psi^{\dagger}\Psi\,,$$

(74)

where

$$\mathbf{J}_{\text{el}} = \frac{-i}{2m}\Psi^{\dagger}(\nabla + i\mathbf{A})\Psi - [(\nabla + i\mathbf{A})\Psi]^{\dagger}\Psi\,,$$

(75)

is the (gauge invariant) electron current.

We concentrate on the effective three-body (electron) interaction that is present in the Hamiltonian,

$$V_{\text{BCS}}^3(\lambda) = (1/2 + \lambda)\frac{1}{m} : (\mathbf{a})^2\Psi^{\dagger}\Psi : \,.$$

(76)

The three-body interaction in coordinate representation is

$$V(\mathbf{r}_1, \mathbf{r}_2, \mathbf{r}_3) = (1/2 + \lambda)\frac{4}{m}\frac{(\mathbf{r}_3 - \mathbf{r}_1)(\mathbf{r}_3 - \mathbf{r}_2)}{|\mathbf{r}_3 - \mathbf{r}_1|^2|\mathbf{r}_3 - \mathbf{r}_2|^2}\,.$$

(77)

To describe the relevant matrix elements for LL(s), we will choose our base LL to be the LLL, which is the most natural choice when we consider a CS description; the very CS transformation is based on the Laughlin–Jastrow correlations in the LLL. Thus, for example, we will relate the effective PPs that we know for the Pfaffian state, based on the perturbation theory, in the second LL, with here calculated PPs, based on the CS description, in the LLL.

To describe relevant three-body PPs (V_M) in the LLL, we introduce rescaled matrix elements, $\Delta_{M=2k+3l}$,

$$V_M = \int d\mathbf{r}_1 \int d\mathbf{r}_2 \int d\mathbf{r}_3 V(\mathbf{r}_1, \mathbf{r}_2, \mathbf{r}_3)|\Psi_{k,l}(\mathbf{r}_1, \mathbf{r}_2, \mathbf{r}_3)|^2 = (1/2 + \lambda) \cdot 4/m \cdot \Delta_{M=2k+3l}\,,$$

where $\Psi_{k,l}$ are normalized, fully antisymmetric wave functions for three electrons,[42] classified by integers $k \geq 0; l \geq 1$, and the total angular momentum of the state is $M = (2k + 3l)$. The calculated Δ_M are shown in the Table 1.

The matrix elements are illustrated by their rescaled values $\frac{m}{4}V_M = (1/2 + \lambda) \cdot \Delta_{M=2k+3l}$, in the cases when $\lambda = -1$ and $\lambda = 0$ in Fig. 2. What is remarkable is that according to the Table 1, $\frac{V_{M=5}}{V_{M=3}} = 0.5$, and $\frac{V_{M=6}}{V_{M=3}} = 0.7$, and are quite close to the ratios of the relevant matrix elements from the perturbation theory in the second LL, ~ 0.4, and ~ 0.7, respectively, that favor the Pfaffian physics.[43]

Thus the CS description is able to capture the sign — a negative one of necessary PPs when $\lambda < -1/2$, and their relative magnitude for relevant, those first three PPs in the Pfaffian case. Therefore, we are encouraged to probe the PH Pfaffian case

Table 1. Matrix elements in the LLL. Reprinted with permission from Ref. 19 © the American Physical Society.

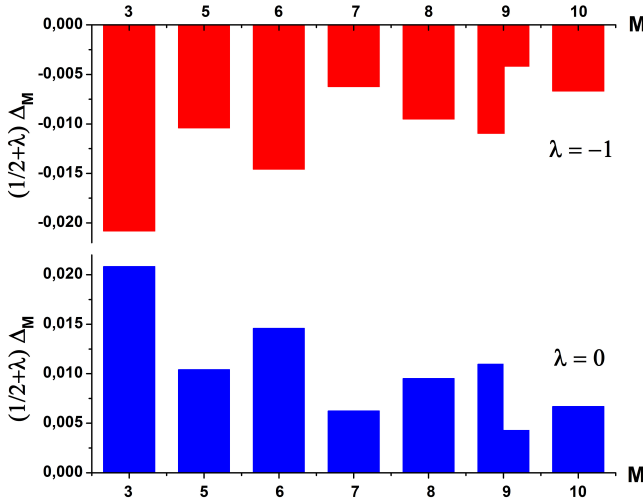| M	3	5	6	7	8	9	
Δ_M	1/24	1/48	7/240	1/80	2/105	$\dfrac{221/10080}{1/(240\sqrt{21})}$	$\dfrac{1/(240\sqrt{21})}{1/120}$
$\dfrac{\Delta_M}{\Delta_{M=3}}$	1	0.5	0.7	0.3	~ 0.475	$\dfrac{\sim 0.526}{\sim 0.022}$	$\dfrac{\sim 0.022}{0.2}$

Fig. 2. (Color online) Matrix elements of three body PPs in the LLL for $\lambda = -1$ (above) and $\lambda = 0$ (bottom). (We plotted two values, diagonal matrix elements in the two-dimensional subspace, in the case when $M = 9$.) Reprinted with permission from Ref. 19 © the American Physical Society.

for certainly $\lambda > 0$. (We can identify the $\lambda = 0$ case with composite fermion Fermi liquid case.) But we have to be aware that in the effective description by $H_{\text{BCS}}^{\text{el}}$, the estimate that we can make for LL mixing parameter (in general the ratio of characteristic interaction energy and cyclotron energy) is $|\lambda + 1/2|$, and that for any considerable $\lambda \gtrsim 1/2$ for which PH Pfaffian correlations are relevant, we have to include higher LL(s) (i.e. not only the base LL — the LLL in the CS description). Thus in the PH Pfaffian case, we have to include (three-body) PPs for at least one more LL. The calculated PPs (more precisely their rescaled $(m/4)V_M$ values) for two LLs when $\lambda = 1$ are illustrated in Fig. 3. While calculating these PPs, we had to include the natural cut-off l_B in the field-theoretical description, to suppress divergences in the second LL. We can conclude from Fig. 3 that in the case of PH Pfaffian, there is an abrupt decrease in the positive values of three-body PPs at $M = 7$ in the base (LLL) level and also at $M = 5$, when two of three electrons are in the higher (second) LL. This can be compared with the usual (truncated) model for Pfaffian with only non-zero, positive potential $V_{M=3}$; there is no three fermion state
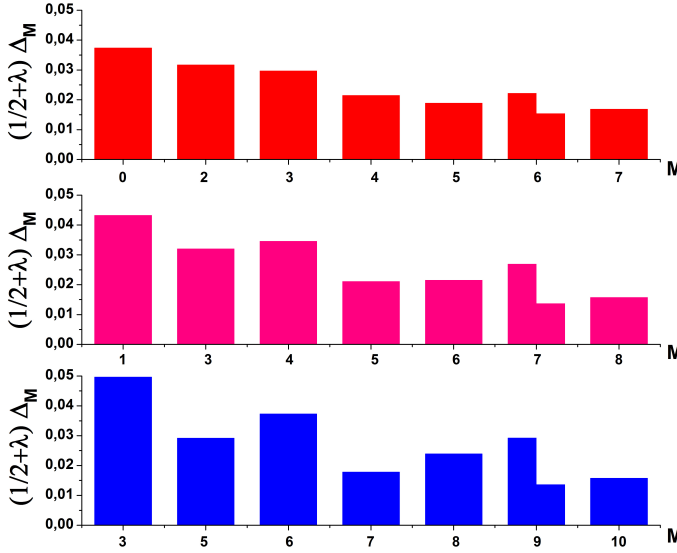
Fig. 3. (Color online) Three-body PP matrix elements for $\lambda = 1$ (PH Pfaffian case) in the second LL (top), for states with two particles in the second LL and one in the LLL (middle), and (all three) in the LLL (bottom). Reprinted with permission from Ref. 19 © the American Physical Society.

with $M = 4$, and the V_5 PP that is connected with the characteristic three-body angular momentum for Pfaffian in the LLL, $M = 5$, is zero.[36] In the case of the PH Pfaffian, the characteristic angular momentum is $M = 7$ in the LLL, and thus the abrupt decrease(s) in the values of three-body PPs that we may associate with the PH Pfaffian pairing correlations. The (almost) monotonic decrease of PPs when all three particles are in the second LL suggests that the space of two LLs may be necessary, but also sufficient for the realization of the PH Pfaffian correlations. The important question, which needs further investigation, is whether these correlations are associated with a gapped state. The most recent suggestion for the realization of PH Pfaffian is in Ref. 44.

5. Conclusions and Outlook

In this review, we have demonstrated that the CS field-theoretical approach can be useful and informative in the description of Pfaffian and anti-Pfaffian states — well-established candidate states for the explanation of gapped states at half-integer filling factors in the FQHE. It can capture the pairing nature of these states, when the basic gauge-field constraints are taken into account in a generalized Dirac effective description of the problem. The effective Dirac description originates from the physics inside a base LL, which, when isolated (in the case of the Coulomb problem) possesses PH symmetry. To stabilize Pfaffian or anti-Pfaffian, we have to break this symmetry by a mass (of definite sign) term in the Dirac theory.

The physics of an isolated base LL in the Dirac effective description suggests a possible existence of a PH symmetric Pfaffian state.[7] We find that this solution is relevant only when a significant PH breaking (mass) is included in the Dirac description. Considering a non-relativistic limit of the description we find that interaction parameters that describe the influence from the higher (second) LL must be non-perturbatively included in a model interaction for PH Pfaffian (beside the ones from the base (lowest) LL). This may be helpful in the effort to stabilize and detect PH Pfaffian correlations in numerical experiments.

Acknowledgments

References

1. D. C. Tsui, H. L. Stormer and A. C. Gossard, *Phys. Rev. Lett.* **59** (1987) 1776.
2. R. Willett, J. P. Eisenstein, H. L. Stormer, D. C. Tsui, A. C. Gossard and J. H. English, *Phys. Rev. Lett.* **59** (1987) 1776.
3. G. Moore and N. Read, *Nucl. Phys. B* **360** (1991) 362.
4. S. H. Simon, in *Composite Fermions*, ed. O. Heinonen (World Scientific, Singapore, 1998), p. 91.
5. R. L. Willett, R. R. Ruel, K. W. West and L. N. Pfeiffer, *Phys. Rev. Lett.* **71** (1993) 3846.
6. B. I. Halperin, P. A. Lee and N. Read, *Phys. Rev. B* **47** (1993) 7312.
7. D. T. Son, *Phys. Rev. X* **5** (2015) 031027.
8. S.-S. Lee, S. Ryu, C. Nayak and M. P. A. Fisher, *Phys. Rev. Lett.* **99** (2007) 236807.
9. M. Levin, B. I. Halperin and B. Rosenow, *Phys. Rev. Lett.* **99** (2007) 236806.
10. T. Jolicoeur, *Phys. Rev. Lett.* **99** (2007) 036805.
11. P. T. Zucker and D. E. Feldman, *Phys. Rev. Lett.* **117** (2016) 096802.
12. E. H. Rezayi, *Phys. Rev. Lett.* **119** (2017) 026801.
13. R. V. Mishmash, D. F. Mross, J. Alicea and O. I. Motrunich, *Phys. Rev. B* **98** (2018) 081107(R).
14. M. Banerjee, M. Heiblum, V. Umansky, D. E. Feldman, Y. Oreg and A. Stern, *Nature* **559** (2018) 205.
15. K. K. W. Ma and D. E. Feldman, *Phys. Rev. B* **100** (2019) 035302.
16. D. F. Mross, Y. Oreg, A. Stern, G. Margalit and M. Heiblum, *Phys. Rev. Lett.* **121** (2018) 026801.
17. C. Wang, A. Vishwanath and B. I. Halperin, *Phys. Rev. B* **98** (2018) 045112.
18. L. Antonić, J. Vučičević and M. V. Milovanović, *Phys. Rev. B* **98** (2018) 115107.
19. S. Djurdjević and M. V. Milovanović, *Phys. Rev. B* **100** (2019) 195303.
20. R. B. Laughlin, *Phys. Rev. Lett.* **50** (1983) 1395.
21. E. H. Rezayi and F. D. M. Haldane, *Phys. Rev. Lett.* **84** (2000) 4685.
22. S.-C. Zhang, *Int. J. Mod. Phys. B* **6** (1992) 25.
23. N. Read, *Semicond. Sci. Technol.* **9** (1994) 1859; N. Read, *Surf. Sci.* **361** (1996) 7.
24. D. H. Lee and M. P. A. Fisher, *Phys. Rev. Lett.* **63** (1989) 903.
25. N. Seiberg, T. Senthil, C. Wang and E. Witten, *Ann. Phys.* **374** (2016) 395.

26. T. Senthil, D.T. Son, C. Wang and C. Xu, *Phys. Rep.* **827** (2019) 1.
27. A. C. Potter, M. Serbyn and A. Vishwanath, *Phys. Rev. X* **6** (2016) 031026.
28. D. Xiao, M.-C. Chang and Q. Niu, *Rev. Mod. Phys.* **82** (2010) 1959.
29. C. Wang, N. R. Cooper, B. I. Halperin and A. Stern, *Phys. Rev. X* **7** (2017) 031029.
30. N. Read and D. Green, *Phys. Rev. B* **61** (2000) 10267.
31. M. R. Peterson, K. Park and S. Das Sarma, *Phys. Rev. Lett.* **101** (2008) 156803.
32. H. Wang, D. N. Sheng and F. D. M. Haldane, *Phys. Rev. B* **80** (2004) 241311(R).
33. A. C. Balram, M. Barkeshli and M. S. Rudner, *Phys. Rev. B* **98** (2018) 035127.
34. M. Greiter, X. G. Wen and F. Wilczek, *Nucl. Phys. B* **374** (1982) 567.
35. F. D. Haldane, in *The Quantum Hall Effect*, eds. R. Prange and S. M. Girvin (Springer-Verlag, New York, 1987), p. 303; F. D. M. Haldane, *Phys. Rev. Lett.* **51** (1983) 605.
36. S. H. Simon, E. H. Rezayi and N. R. Cooper, *Phys. Rev. B* **75** (2007) 195306.
37. W. Bishara and C. Nayak, *Phys. Rev. B* **80** (2009) 121302(R).
38. M. R. Peterson and C. Nayak, *Phys. Rev. B* **87** (2013) 245129.
39. S. H. Simon and E. H. Rezayi, *Phys. Rev. B* **87** (2013) 155426.
40. R. E. Wooten, J. H. Macek and J. J. Quinn, *Phys. Rev. B* **88** (2013) 155421.
41. I. Sodemann and A. H. MacDonald, *Phys. Rev. B* **87** (2013) 245425.
42. R. B. Laughlin, *Phys. Rev. B* **27** (1983) 3383.
43. K. Pakrouski, M. R. Peterson, T. Jolicoeur, V. W. Scarola, C. Nayak and M. Troyer, *Phys. Rev.* **X5** (2015) 021004.
44. C. Sun, K. K. W. Ma and D. Feldman, arXiv:2003.14227 (2020).

Sideband Spectroscopy in the Strong Driving Regime:
Volcano Transparency and Sideband Anomaly

Luka Antonić and Daniel Podolsky

Physics Department, Technion, Haifa 32000, Israel[*]

Sergey Hazanov, Sergei Masis, and Eyal Buks

Andrew and Erna Viterbi Department of Electrical Engineering, Technion, Haifa 32000, Israel

(Dated: August 17, 2025)

We study the response of a spin to two crossed magnetic fields: a strong and fast transverse field, and a weak and slow longitudinal field. We characterize the sideband response at the sum and the difference of driving frequencies over a broad range of parameters. In the strong transverse driving regime, the emission spectrum has a characteristic volcano lineshape with a narrow central transparency region surrounded by asymmetric peaks. Next, we couple the spin to a nonlinear cavity that both drives and measures it. In a sufficiently slow longitudinal field, the emission spectrum exhibits anomalous behavior, where the resonances in both the right and left sidebands lie on the same side of the central resonance. The theoretical results are compared to the experimental measurement of the emission of substitutional nitrogen P1 and nitrogen-vacancy NV^- defects in diamond.

I. INTRODUCTION

In typical magnetic resonance experiments, the system is driven and measured at the same frequency, making it difficult to detect weak response signals amid the strong driving. Another challenge appears under strong driving, where power broadening renders the spectrum featureless. In contrast, the sideband method probes the system at a frequency different from that used for driving, which enables implementing spectral filtering in the readout to eliminate the interference of the driving tone. We consider a setup that combines a strong and fast transverse drive at angular frequency ω_t with a weak and slow longitudinal drive at ω_l (throughout the paper, the letter ω is used to denote angular frequencies). We will show that when ω_l is larger than the decoherence rate $\gamma_2 = 1/T_2$, power broadening does not wash out the sideband spectra at $\omega_t \pm \omega_l$, but produces distinct features that we characterize.

In a seminal paper by Redfield [1], the response to crossed fast transverse and weak longitudinal fields was studied in spin systems [1]. Since the oscillating longitudinal field leads to the reduction of magnetic polarization, the effect was named *rotary saturation*. It was extended to optical systems [2, 3], and has potential applications in magnetic resonance imaging in medicine [4, 5]. The longitudinal field is known to affect the Rabi frequency [6–13], which is the rate of population oscillations in a transversely driven two-level system.

In this work, we present an experimental and theoretical study of the response of spin systems to crossed fields. We perform experimental measurements on two types of diamond defect: the negatively charged nitrogen-vacancy NV^- center and the substitutional nitrogen N_S

defect (also known as the P1 center or C-center). The NV center consists of the substitutional nitrogen and a neighboring vacancy in place of two carbon atoms, as shown in Fig. 1(a). The center has been extensively studied both theoretically and experimentally [14–16], and it is significant for emerging quantum technologies [17]. By contrast, the P1 center, shown in Fig. 1(b), appears when one of the carbons is exchanged with the nitrogen. This defect has a spin-1/2 and it was initially detected in electron-spin resonance experiments [18].

In the experiment, a static magnetic field B_{DC} induces Zeeman splitting of the spins. On top of this field, we apply a weak, low-frequency longitudinal field at ω_l parallel to the dc field, as well as a strong, high-frequency transverse field with angular frequency ω_t perpendicular to it. Under this two-tone driving, the spin oscillates at the sum and difference of the frequencies, acting as a frequency mixer. The oscillating spin emits radiation at central frequency ω_t and at sideband frequencies $\omega_t \pm \omega_l$, which we then measure as the emission spectrum. We show that the sideband spectrum exhibits a more complex response than the central resonance, resolving system details more clearly, with promising applications in quantum sensing.

We complement our experimental measurements with a theoretical analysis of the sideband response. Specifically, we solve the dynamical equations of motion nonperturbatively in the strong transverse field, while treating the weak longitudinal field within linear response. This approach enables us to characterize the sideband spectrum across a range of regimes as the longitudinal frequency ω_l and transverse amplitude B_t are varied. When ω_l is smaller than the decoherence rate $1/T_2$, the spectrum is power-broadened and featureless. As ω_l exceeds $1/T_2$, distinct spectral regimes emerge, exhibiting rich structure absent in the power-broadened central resonance under strong driving. At intermediate transverse field amplitudes, the sideband reveals Rabi resonances
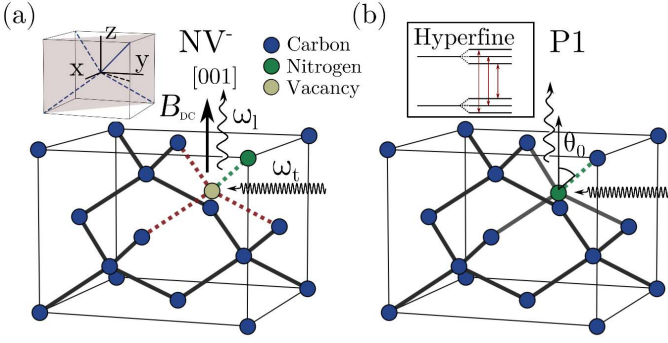
FIG. 1. NV center (a) and P1 center in diamond (b). Both centers are subjected to DC magnetic field in the [001] direction, drawn as the z-axis in the figures. This field sets the quantization axis. The slow radio frequency (RF) field (ω_l) is applied parallel to this axis, while the fast microwave field (ω_t) is perpendicular. Both centers have C_{3v}-symmetry.

that occur when the longitudinal field matches the Rabi frequency of the oscillating spin [19–21]. At very high amplitudes, a new spectral structure emerges: an asymmetric volcano lineshape with a narrow central dip, which we term the *volcano transparency*.

In our analysis, we demonstrate that, for a broad class of linear theories, the right and left sidebands should be identical, apart from an overall inversion in the ω_t–B_{DC} plane. For instance, if the right sideband spectrum is blue-shifted relative to the frequency of the cavity used to drive the system, then the left sideband spectrum must necessarily be red-shifted. This, however, is not observed experimentally. Instead, both sidebands are simultaneously blue-shifted, a phenomenon we refer to as the *sideband anomaly*. This anomaly serves as a sensitive indicator of nonlinearity in the system dynamics [22]. To illustrate this theoretically, we demonstrate that the sideband anomaly can occur in systems with Kerr nonlinearity. However, we note that Kerr nonlinearity is relatively weak in our system, and the source of the observed sideband anomaly remains unidentified.

Our paper is organized as follows. We first describe the experiment in Sec. II and introduce its theoretical description in Sec. III. In Section IV we study the spin response at the dual driving by the strong and fast transverse magnetic field and weak and slow longitudinal field. In Section V, we show that sideband symmetry is guaranteed in the linear model. In Section VI we extend the model by adding a cavity with Kerr nonlinearity, demonstrating how it shifts the spectrum, where the shift strongly depends on the ratio of the longitudinal frequency and the cavity decay rate. We find that, if the longitudinal driving is slow, the sidebands get more blueshifted than the central spectral line, and the right and left sidebands have different shifts if the cavity nonlinearity is strongly excited.
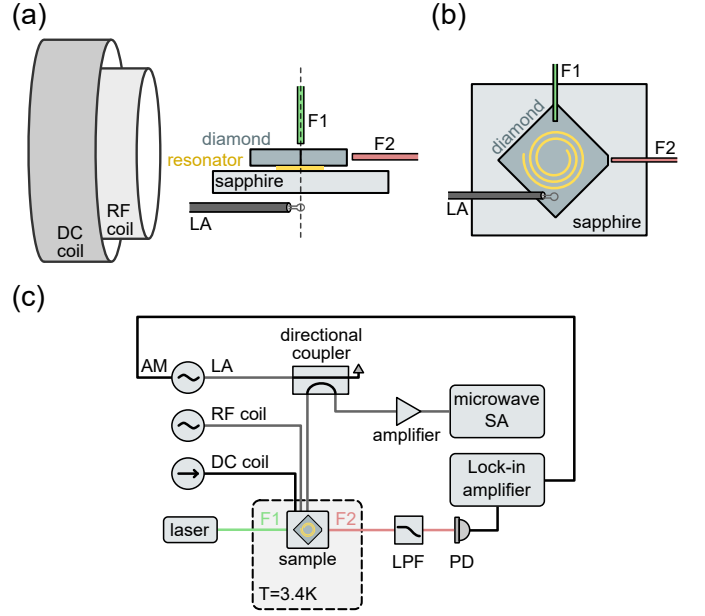
FIG. 2. (a) A sketch of the experimental setup with solenoids. (b) Top-down view of the central part of the setup. (c) Electrical and optical diagram with components described in Section II A. Black and gray lines label electrical connections, and red and green lines label optical connections.

II. THE EXPERIMENT

A. Experimental setup

Figure 2 shows the experimental layout inside the cryostat at a temperature of about 3.4 K. A [110] diamond wafer, with NV-defect concentration of $1.23 \times 10^{17} \text{cm}^{-3}$, is glued to a sapphire wafer. This wafer supports a niobium superconducting spiral resonator having frequency of $\omega_c/(2\pi) = 3.772$ GHz [23, 24], and cavity width $\gamma_c \approx 8.5$ MHz determined by fitting data to the Lorentzian function. A superconducting DC solenoid (see inset of Fig. 2 a) generates the static magnetic field, while an RF solenoid, with its axis parallel to the DC coil, provides the longitudinal drive at an angular frequency which we denote ω_l. The diamond crystal direction [001] is aligned to be nearly parallel to the static magnetic field. A loop antenna (LA) that is placed beneath the spiral resonator is employed for applying transverse driving in the microwave (MW) band, whose frequency we denote as ω_t. The role of the spiral resonator is twofold; it serves as a bandpass filter that passes frequencies close to the fundamental mode, but it also amplifies the signal from the loop antenna and from the defects.

The static field B_{DC} affects the Zeeman splitting of the defects. Although both centers have four possible orientations, applying the field along a $\langle 100 \rangle$ direction, which corresponds to angle $\theta_0 = \arccos\left(1/\sqrt{3}\right)$ relative to $\langle 111 \rangle$ bonds, causes identical response for all four orientations,

see Fig. 1.

Two multi-mode optical fibers, F1 and F2 in Fig. 2(a), are coupled to the diamond sample. Laser light at 532 nm (which is delivered to the sample by fiber F1) gives rise to optically induced spin polarization [25, 26]. The experimental setup allows implementing both methods of optical detection of magnetic resonance (ODMR) and cavity-based detection of magnetic resonance (CDMR). The photoluminescence (PL) emitted from the diamond, which is delivered by the multi-mode fiber F2, is probed using a long pass filter (LPF) and a photo detector (PD). The PD signal is measured using a lock-in amplifier (LIA). The MW signal generator, which is employed for applying transverse driving with the LA, is amplitude modulated (AM) using a low-frequency signal generated by the LIA.

The scheme of the sideband spectroscopy setup is shown in the upper part of Fig. 2(b). A directional coupler (DC) is employed for delivering incoming and outgoing LA signals. The incoming signal, which has the frequency ω_{t}, is generated by an MW function generator. An amplifier and a spectrum analyzer (SA) are used to probe the signal outgoing from the LA. An RF signal generator having frequency ω_{l} is employed for applying longitudinal driving to the RF solenoid. The defect's nonlinear response mixes transverse and longitudinal driving tones, producing the sideband peaks at frequencies $\omega_{\text{t}} \pm n\omega_{\text{l}}$, where n is an integer. We record the sideband amplitudes with SA and, throughout the paper, we focus only on the first right and left sidebands with $n = \pm 1$.

B. Measurements on P1 centers

Figure 3 presents the measurements on the P1 center. The transverse field is amplified by the spiral resonator at frequency $\omega_{\text{c}} / (2\pi) = 3.772$ GHz (discussed in more detail in Sec. II A). The resonator also amplifies the radiation emitted from the spin, enhancing the sideband signal. We resolve the hyperfine splitting induced by the interaction of the electron spin with the spin-1 nitrogen nucleus. This results in three volcano-shaped transparencies in the top row, which correspond to the three hyperfine transitions displayed schematically in Fig. 1(b) (see Appendix D for more details). While the defect's signature is weak in the central response, it emerges as a well-defined lineshape in the sideband spectrum. The peaks surrounding the central transparency are asymmetric (one is higher than the other), and this asymmetry is reversed between the left and right sidebands. In Sec. IV, we show theoretically how this spectral line emerges through the competition between Rabi resonances and power broadening.

The bottom row of Fig. 3 displays measurements performed at various transverse frequencies ω_{t}. The black line marks the cavity frequency. One expects the positions of the resonances in the right and left sidebands to be shifted in opposite directions relative to the cavity frequency. Instead, both sideband signals are strongest at a blue shift from the cavity frequency. We call this phenomenon the *sideband anomaly*.

C. Measurements on NV centers

In Figure 4, we show measurements on NV centers. The horizontal axis is the transverse driving frequency, ω_{t}, and the vertical axis is the RF coil voltage, which controls the strength of the longitudinal drive B_{l}. The top row displays the left-sideband signal, while the bottom row shows the right sideband. Each column contains both sidebands for a specific longitudinal frequency, ω_{l}. The signals are more pronounced with increasing longitudinal driving. Such behavior is expected when the driving is weak and justifies our later analysis, where we treat the longitudinal drive in linear response. By contrast, for strong longitudinal drive, the sideband signal is expected to become non-monotonic and follow a more complicated dependence involving Bessel functions [27].

The NV data confirm the sideband anomaly seen in P1-center measurements. A vertical black line marks the cavity frequency, and in all cases, both sidebands lie to its right. In Section V, we demonstrate that a purely linear system would place the left and right sidebands on opposite sides of the cavity frequency (indicated by the black lines in the figure).

Furthermore, as ω_{l} increases, the left and right sidebands show asymmetric behavior. As shown in Sec. VI, Kerr nonlinearity gives rise to similar behavior. This illustrates that nonlinearity can indeed cause the sideband anomaly. However, in the current experiment, Kerr nonlinearity is far too small to explain the observed anomaly, and its origin remains unexplained.

III. THEORETICAL MODEL

We now introduce the theoretical spin-cavity model used to describe the experimental setup of the preceding section. The spin is placed in a constant magnetic field $\mathbf{B}_{\text{DC}} = B_{\text{DC}}\hat{z}$, leading to a Zeeman splitting ω_{s}. The spin is driven by a weak and slowly oscillating longitudinal (parallel to $\hat{z}$) field. At the same time, the cavity is driven by a strong and fast oscillating field. Due to the spin-cavity interaction, the fast cavity oscillations are transferred to the spin, which therefore feels the effects of both drives. Then, as a result of frequency mixing, the spin emits radiation at the sum and difference of the two driving frequencies. The emitted radiation is amplified by the cavity. The resulting spectrum, which is a function of two frequencies, reveals a rich structure that we wish to explore.

We introduce the Hamiltonian:
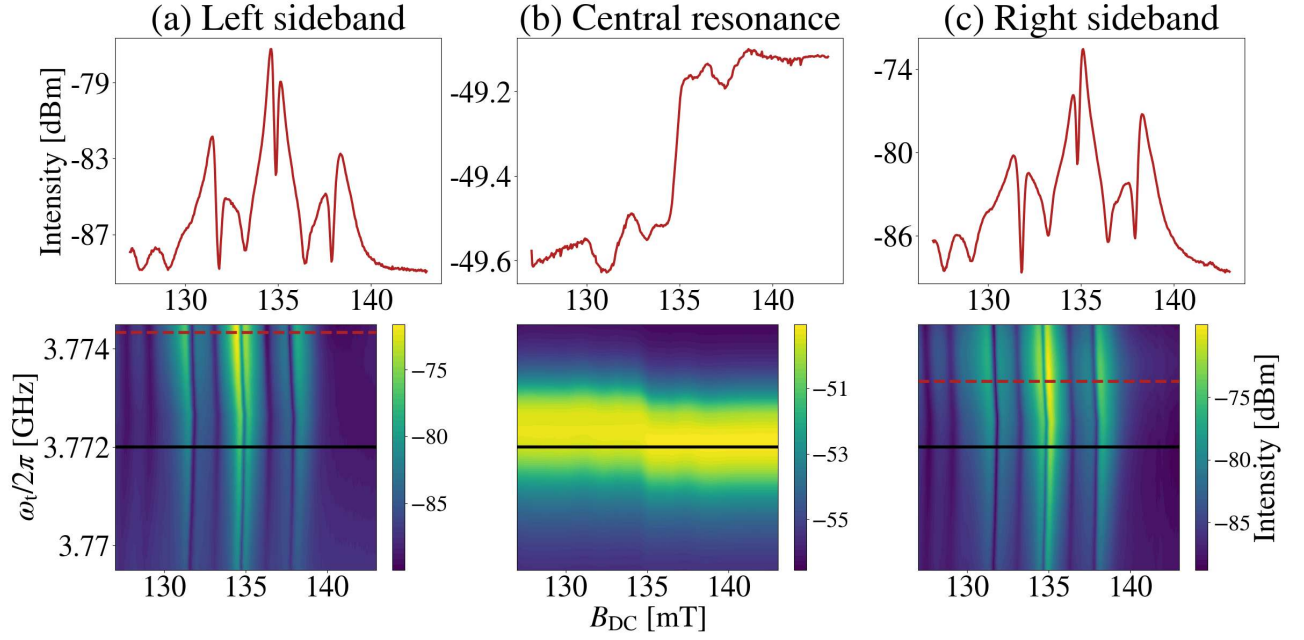
$$H = H_{\text{s}} + H_{\text{c}} + H_{\text{int}} \ . \tag{1}$$

FIG. 3. P1 sidebands, spectrum analyzer power measurement; intensity is measured in dBm units. (a) Left sideband, $\omega_\mathrm{t} - \omega_\mathrm{l}$, (b) central peak at ω_t, and (c) right sideband, $\omega_\mathrm{t} + \omega_\mathrm{l}$. The horizontal axis corresponds to the static magnetic field magnitude B_DC, and the vertical axis corresponds to the microwave driving frequency $\omega_\mathrm{t}/(2\pi)$. The RF drive frequency is set to $1\,\mathrm{MHz}$. The overlaid black lines in the lower figures mark the cavity frequency, which is also the frequency at which the upper lineshapes are extracted. Red dashed lines mark the approximate positions of the sideband resonances. The three volcanoes correspond to three different hyperfine transitions.
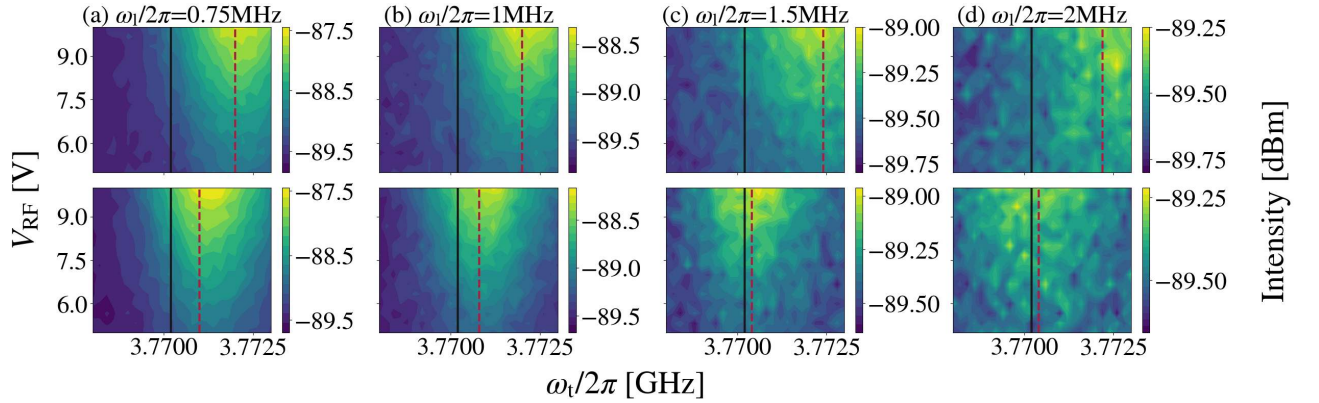
FIG. 4. The sideband measurements of the NV center as a function of the longitudinal drive strength B_l (corresponding to the voltage on the RF coil V_RF) and the transverse driving frequency ω_t for different longitudinal driving frequencies ω_l. The top row represents the left sideband data (at the frequency $\omega_\mathrm{t} - \omega_\mathrm{l}$), and the bottom row are the right sideband data (at the frequency $\omega_\mathrm{t} + \omega_\mathrm{l}$). The black vertical line is the cavity frequency ω_c as obtained from the experimental measurements. The red dashed lines show the frequency ω_t where the maximal signal, averaged over all B_l values, is observed. The sideband anomaly occurs for all of the longitudinal frequencies, but the distance between the sideband resonances increases with the increasing ω_l (which also occurs with the Kerr nonlinearity, see Sec. VI).

The spin part of the Hamiltonian is

$$H_\mathrm{s} = \frac{\omega_\mathrm{s} + B_\mathrm{l}\cos{(\omega_\mathrm{l}t)}}{2}\sigma_\mathrm{z}\,, \tag{2}$$

where σ_z is Pauli matrix. The cavity is driven at fre-

quency ω_t and it has a Kerr nonlinearity,

$$H_\mathrm{c} = \omega_\mathrm{c}a^\dagger a + \frac{K_\mathrm{c}}{4}a^\dagger a^\dagger aa + \frac{g_\mathrm{P}}{2}\left(a^\dagger e^{-i\omega_\mathrm{t}t} + ae^{i\omega_\mathrm{t}t}\right)\,, \tag{3}$$

where a is the cavity annihilation operator. The spin couples to the cavity through a Jaynes-Cummings inter-

action,

$$H_{\text{int}} = \Omega \left(a^\dagger \sigma_- + a \sigma_+ + a^\dagger \sigma_+ + a \sigma_- \right) . \qquad (4)$$

This interaction provides the feedback mechanism between the spin and cavity as it transfers energy between them. Due to the form of the interaction, the cavity drive at frequency ω_{t} is transferred to the spins as a field that is transverse to $\hat{z}$.

We can simplify the Hamiltonian by working in the rotating frame. The unitary operator that transforms the system into this frame is

$$P(t) = e^{i\omega_{\text{t}}\left(a^\dagger a - \frac{1}{2}(1-\sigma_{\text{z}})\right)t} . \qquad (5)$$

The Hamiltonian that evolves states and operators in the new frame is

$$H'(t) = P(t)H(t)P^\dagger(t) - iP(t)(\partial_t P^\dagger(t)) , \qquad (6)$$

while the time-dependent observable $A'(t)$ in the rotating frame is related to the observable A in the original frame through

$$A'(t) = P(t)AP^\dagger(t) . \qquad (7)$$

The third and fourth terms in the expression for H_{int} are rotating fast in the direction opposite to the frame, and they will be neglected in the equations of motion. The Hamiltonian is then, up to constant terms,

$$\begin{aligned} H' = {} & \Delta_{\text{c}}a^\dagger a + K_{\text{c}}a^\dagger a^\dagger aa + \frac{g_{\text{P}}}{2}\left(a + a^\dagger\right) \\ & + \frac{\Delta_{\text{s}} + B_{\text{l}}\cos(\omega_{\text{l}}t)}{2}\sigma_{\text{z}} + \Omega(a^\dagger\sigma_- + a\sigma_+). \end{aligned} \qquad (8)$$

Here, we introduced two parameters,

$$\Delta_{\text{c}} = \omega_{\text{c}} - \omega_{\text{t}}, \qquad (9)$$
$$\Delta_{\text{s}} = \omega_{\text{s}} - \omega_{\text{t}}, \qquad (10)$$

which quantify the detuning of the transverse drive from the cavity and the spin, respectively. We study the emission spectrum as function of these two parameters.

In addition to unitary evolution, the system experiences dissipation, which we model by the following relaxation parameters: γ_{c} for the cavity, γ_2 for the spin decoherence rate, and γ_1 for the spin dissipation rate, which tends to relax it to the equilibrium spin polarization $\sigma_{\text{z}}^{\text{eq}}$. In experiments that use optical spin polarization, the effective dissipation parameters can be very different from the intrinsic dissipation parameters of the system [24].

We write the equations of motion for the expectation values of σ_{z}, σ_+, and $a^\dagger$:

$$i\frac{d\langle\sigma_{\text{z}}\rangle}{dt} = 2\Omega\left(\langle a\rangle\langle\sigma_+\rangle - \langle a^\dagger\rangle\langle\sigma_-\rangle\right) - i\gamma_1\left(\langle\sigma_{\text{z}}\rangle - \sigma_{\text{z}}^{\text{eq}}\right), \qquad (11a)$$

$$i\frac{d\langle\sigma_+\rangle}{dt} = -(\Delta_{\text{s}} + B_{\text{l}}\cos(\omega_{\text{l}}t) + i\gamma_2)\langle\sigma_+\rangle + \Omega\langle a^\dagger\rangle\langle\sigma_{\text{z}}\rangle, \qquad (11b)$$

$$i\frac{d\langle a^\dagger\rangle}{dt} = -(\Delta_{\text{c}} + i\gamma_{\text{c}})\langle a^\dagger\rangle - K_{\text{c}}|\langle a^\dagger\rangle|^2\langle a^\dagger\rangle - N_{\text{S}}\Omega\langle\sigma_+\rangle - \frac{g_{\text{P}}}{2}. \qquad (11c)$$

The corresponding equations for σ_- and a can be obtained from the above by complex conjugation, by using $\langle\sigma_{\text{z}}\rangle = \langle\sigma_{\text{z}}\rangle^*$, $\langle\sigma_-\rangle = \langle\sigma_+\rangle^*$ and $\langle a\rangle = \langle a^\dagger\rangle^*$. In these equations, we used the mean-field approximation $\langle AB\rangle = \langle A\rangle\langle B\rangle$, where A and B are spin or resonator operators.

Note that in the last equation we introduced a new parameter, N_{S}, representing the number of spins that are simultaneously coupled to the cavity. In contrast, the second equation that describes the evolution of the spin operator σ_+ lacks this factor. This reflects the following asymmetry: each spin senses the cavity individually, while the cavity is driven collectively by all spins. In reality, the strength of the driving is different for each spin, and the consequences of this are discussed in the Supplementary Material [28].

In what follows, we will study the steady-state response of the system. If the longitudinal amplitude B_{l} is sufficiently small, we can expand all variables to linear order as

$$\langle O(t)\rangle \approx \langle O\rangle^{(0)} + \langle O\rangle^{(1)}e^{i\omega_{\text{l}}t} + \langle O\rangle^{(-1)}e^{-i\omega_{\text{l}}t}, \qquad (12)$$

where O represents any of the five operators of the model. Note that the equations are written in the rotating reference frame. If we were to rotate the operators back to the laboratory frame, the transverse spin operators and cavity operators would actually be oscillating at these three frequencies: the central frequency ω_{t}, the left sideband frequency $\omega_{\text{t}} - \omega_{\text{l}}$, and the right sideband frequency $\omega_{\text{t}} + \omega_{\text{l}}$. As we show in the Supplementary Material [28], the sideband emission spectrum is given by $\langle a\rangle^{(\pm 1)}$, up to overall factors.

IV. SIDEBANDS OF A DRIVEN SPIN

We now turn to a theoretical computation of the sideband response. To set the stage for the full two-dimensional response in the $\Delta_{\text{s}} - \Delta_{\text{c}}$ plane, we begin by working with fixed Δ_c and analyzing the steady-state features as a function of Δ_{s} only. If the spin-cavity feedback is not strong, we can treat the cavity, which acts as a nonlinear band-pass filter, as a source for spin transverse driving having amplitude B_{t}. For given Δ_{c}, γ_{c}, and K_{c} we determine the steady-state amplitude of this field $|\langle a^\dagger\rangle|^2$, by finding the positive solution [29] to

$$(\Delta_{\text{c}} + i\gamma_{\text{c}})\langle a^\dagger\rangle + K_{\text{c}}|\langle a^\dagger\rangle|^2\langle a^\dagger\rangle + \frac{g_{\text{P}}}{2} = 0 \qquad (13)$$

which corresponds to setting the left-hand side of Eq. (11c) to zero and neglecting the feedback of the spin.

The analysis presented in this section, in one form or another, has appeared elsewhere in the literature [2, 3]. However, for completeness, we derive the main result and

examine each regime in detail, in particular, characterizing the regimes relevant to the experiment. Nonlinear response to a strong longitudinal field underpins Landau–Zener interferometry [30, 31]. An oscillating longitudinal field can be treated as a phase modulation of the transverse drive [3, 32–34], yielding a characteristic Bessel-function dependence on the ratio of longitudinal amplitude to frequency [35]. In that framework, the transverse drive effectively contains infinitely many tones at frequencies $\omega_t + n\omega_l$, where n is an integer, and one typically applies a rotating-wave approximation (RWA) that retains only the $k\omega_l$ tone of interest while discarding $n \neq k$ tones. That approximation fails when B_t becomes arbitrarily large, but in the linear regime in B_l we can obtain the full solution in B_t by truncating the Floquet sectors to $k = 0, \pm 1$ only.

If we write the effective transverse field as $B_t = \Omega \langle a^\dagger \rangle$. We can reduce the number of equations to three,

$$i\frac{d\langle \sigma_+ \rangle}{dt} = -\left(\Delta_s + B_l \cos\left(\omega_l t\right) + i\gamma_2\right)\langle \sigma_+ \rangle + B_t \langle \sigma_z \rangle, \quad (14)$$

$$i\frac{d\langle \sigma_z \rangle}{dt} = 2\left(B_t^* \langle \sigma_+ \rangle - B_t \langle \sigma_- \rangle\right) - i\gamma_1\left(\langle \sigma_z \rangle - \sigma_z^{eq}\right), \quad (15)$$

where the equation for $\langle \sigma_- \rangle$ is the complex conjugate of the first equation. When cavity parameters are fixed, emission intensity is determined by $\langle \sigma_+ \rangle^{(\pm 1)}$ expectation values, since they are proportional to the cavity expectation values as shown in the Supplementary Material [28]. We continue the analysis by focusing on the reduced system of equations before going back to the original system to analyze the full two-dimensional spectrum.

The unitary part of the evolution in the reduced system of equations (14) and (15) can be seen to come from the simpler Hamiltonian,

$$H_s^{eff} = \left(\Delta_s + B_l \cos\left(\omega_l t\right)\right)\frac{\sigma_z}{2} + \left(B_t^* \sigma_+ + B_t \sigma_-\right). \quad (16)$$

We are concerned with the limit where the longitudinal field is treated in the linear response regime.

First, we focus on emission at the right sideband frequency $\omega_t + \omega_l$. The intensity of the emission spectrum is then proportional to the square of the absolute value of $\langle \sigma_+ \rangle^{(1)}$, as shown in the Supplementary Material [28]. The full solution for the right sideband, exact in B_t and expanded to linear order in B_l, is:

$$\langle \sigma_+ \rangle^{(1)} = \frac{-B_l B_t \sigma_z^{eq}}{2\left(\Delta_s - \omega_l + i\gamma_2\right)\left(\Delta_s^2 + \gamma_2^2 + 4\frac{\gamma_2}{\gamma_1}|B_t|^2\right)}\left[\Delta_s - i\gamma_2 - \frac{4|B_t|^2 \Delta_s\left(\omega_l - 2i\gamma_2\right)}{\left(\omega_l - i\gamma_1\right)\left(\Delta_s^2 - \left(\omega_l - i\gamma_2\right)^2\right) + 4|B_t|^2\left(\omega_l - i\gamma_2\right)}\right], \quad (17)$$

with the derivation given in Appendix A. In what follows, we restrict our attention to situations in which $\omega_l > \gamma_2 \gg \gamma_1$, although the expression (17) is more generally applicable.

The sideband spectrum depends strongly on the transverse drive amplitude B_t. To understand how the spectrum evolves, we begin with the weak-driving limit, when $B_t \ll 1$. Starting from Eq. (17), the linear response in B_t is easily read-off to be

$$\langle \sigma_+ \rangle^{(1)} = \frac{-B_l B_t \sigma_z^{eq}}{2\left(\Delta_s - \omega_l + i\gamma_2\right)\left(\Delta_s + i\gamma_2\right)} + \mathcal{O}(B_t^2). \quad (18)$$

The spectrum has two resonances, at $\Delta_s = 0$ and $\Delta_s = \omega_l$, as seen in Fig. 5(a). These arise from the two processes shown in Fig. 6(b): the resonance condition is met when the level splitting of the spin, ω_s, matches either the transverse field frequency, ω_t, or the sum of frequencies, $\omega_t + \omega_l$.

If we increase the transverse driving the spectrum changes qualitatively. The first effect comes from power broadening, arising from the factor $4\left(\gamma_2/\gamma_1\right)|B_t|^2$ in Eq. (17). This factor becomes important at $|B_t| \approx \frac{1}{2}\sqrt{\gamma_1 \gamma_2}$ and it simultaneously broadens and suppresses the resonance at $\Delta_s = 0$, as shown in Fig. 5(b).

The effects of increasing the driving further are most easily understood from the approximate expression,

$$\langle \sigma_+ \rangle^{(1)} \approx \frac{-B_l B_t \sigma_z^{eq} \Delta_s\left(\Delta_s + \omega_l\right)}{2(\Delta_s^2 + 4\frac{\gamma_2}{\gamma_1}|B_t|^2)(\Delta_s^2 + 4|B_t|^2 - \omega_l^2)}, \quad (19)$$

which is obtained from Eq. (17) by ignoring the decay rates γ_1 and γ_2, but not their ratio γ_2/γ_1. This expression can be justified in the aforementioned limit $\omega_l > \gamma_2 \gg \gamma_1$, with the caveat that the width of some resonances may need to be regulated by the decay rates. From this expression, we can extract two regimes, depending on the relative magnitude of $|B_t|$ and ω_l:

Rabi regime: When $\sqrt{\gamma_1 \gamma_2} \ll 2|B_t| \ll \omega_l$, Eq. (19) contains two sharp resonances at

$$\Delta_s = \pm\sqrt{\omega_l^2 - 4|B_t|^2}. \quad (20)$$

These resonances, shown in Fig. 5(d) are reached when the longitudinal driving ω_l matches the generalized Rabi frequency $\sqrt{\Delta_s^2 + 4|B_t|^2}$. The width of these resonances is controlled by relaxation rates that appear in the exact expression (17). The two resonances are asymmetric due to the factor of $(\Delta_s + \omega_l)$ in the numerator, which suppresses the resonance with the negative sign.

Volcano regime: When $|B_t| \gg \omega_l/2$, the condition (20) can no longer be satisfied. Then, Eq. (19) no longer contains any sharp resonances. Instead, a volcano-shaped
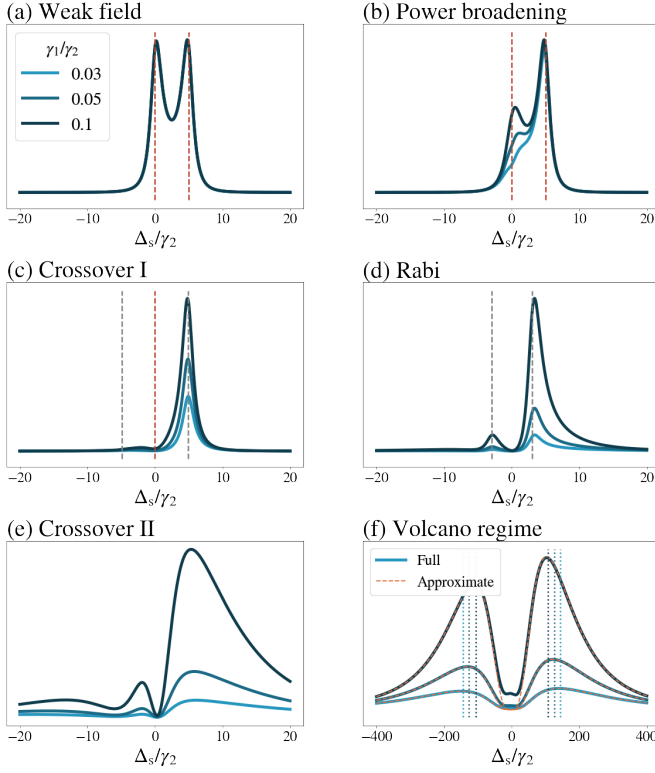
FIG. 5. The square of the absolute value of $\langle\sigma_+\rangle^{(1)}$ computed in the $\omega_l \gg \gamma_2 \gg \gamma_1$ limit as B_t is gradually increased. Throughout the figure, we keep values $\omega_l = 5$, and γ_1 is varied in each plot with values given in the legend in (a). B_t goes through values: 0.01, 0.1, 0.5, 2, 3, and 30 from (a) to (f), given in units of γ_2. The red dashed lines show the positions of $\Delta_s = 0$ and $\Delta_s = \omega_l$ resonances, while the gray dashed lines show the positions of the Rabi resonances. In the (f) plot the vertical lines are drawn in the positions of the peaks, i.e. $\pm 2|B_t|\sqrt[4]{\frac{\gamma_2}{\gamma_1}}$. Note that this last plot is drawn on a much wider scale than the other plots. The intensity (y-axis) varies significantly between the plots.

spectrum emerges, as shown in Fig. 5(f), reflecting the interplay between broad resonances centered at $\Delta_s = 0$ and the factor $\Delta_s(\Delta_s + \omega_l)$ in the numerator, which creates a transparency region near $\Delta_s = 0$. The width of the volcano is of order $2\sqrt{\gamma_2/\gamma_1}|B_t|$, while the width of the central transparency region is $2|B_t|$. As in the Rabi regime, the factor of $(\Delta_s + \omega_l)$ gives rise to asymmetry between the two peaks of the volcano. The location of the peaks of the volcano can be found from the local maxima of Eq. (19). This leads to the quintic equation from which the peak positions can be estimated, and in the limit $\omega_l \ll 2|B_t|$ they are

$$\Delta_{\max} \approx \pm 2|B_t|\sqrt[4]{\frac{\gamma_2}{\gamma_1}} - \frac{\omega_l}{8}\left(1 + \sqrt{\frac{\gamma_1}{\gamma_2}}\right) + \mathcal{O}\left(\frac{\omega_l}{|B_t|^2}\right),$$
(21)

where $\Delta_{\max}$ is the detuning at which two broad peaks reach their maximum intensity.
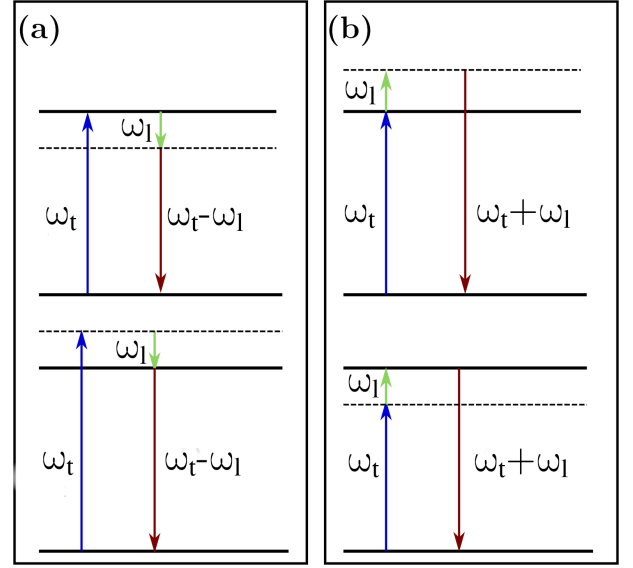
In addition, the spectrum displays crossovers at the in-

terface between the different regimes. At the crossover between weak-field and Rabi regimes [Fig. 5(c)], for $\sqrt{\gamma_1\gamma_2} \ll 2|B_t| \lesssim \gamma_2$, only the right Rabi resonance is visible. On the other hand, at the crossover between the Rabi and volcano regimes [Fig. 5(e)], for $2|B_t| \approx \omega_l$, the Rabi peaks are not sharp, but they have not been sufficiently broadened for the volcano structure to emerge. We call these crossovers I and II, respectively. The crossover II between the Rabi and the volcano regime is illustrated through the analysis of the motion of complex poles of the response function in App. B.

Figure 7 shows the different regimes in the B_t-ω_l plane. Here, we also show the spectrum in the slow longitudinal field limit $\omega_l < \gamma_2$, which is generically seen to only contain a single peak regardless of the value of B_t (except for certain fine-tuned parameters, where a richer structure can be obtained). The width of this peak tends to increase with B_t due to power broadening.

This broadening, which comes from the B_t–dependent resonance that multiplies brackets in expression (17) is a common obstacle in spectroscopy. It also appears in the central frequency response, as it can be seen from Eq. (A1), where it leads to a featureless spectrum. However, as we showed, in the sideband response, when ω_l is larger than γ_2, the spectrum develops many interesting features that are not limited by power broadening. In the other limit, if we let ω_l tend to 0, we recover the central frequency power-broadened response. When ω_l is very small but finite, most of the changes to the spectrum will still be washed out by this broadening.

Thus far, we have focused exclusively on the right sideband response. We now turn our attention to the left sideband, whose spectrum is given by the absolute value of $\langle\sigma_+\rangle^{(-1)}$. In the reduced model that we use in this
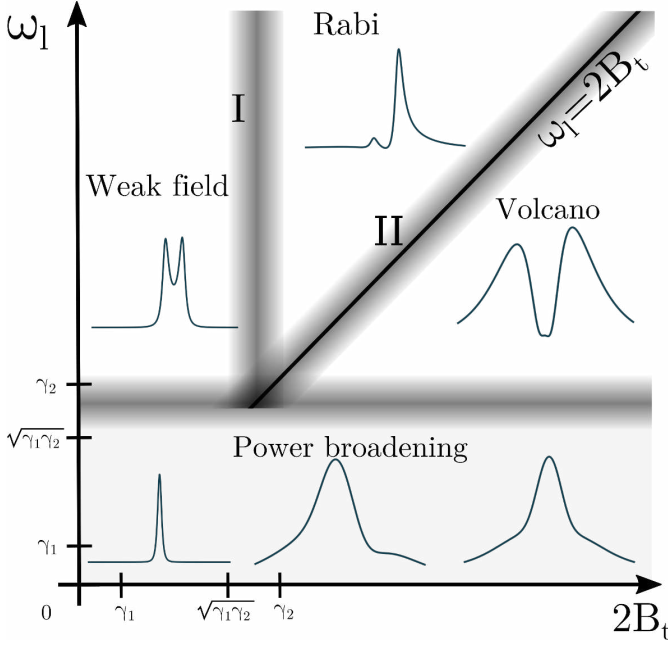

FIG. 6. Diagram of the processes that determine the linear response in B_t for (a) the left sideband, and (b) the right sideband.

FIG. 7. Different regimes of the sideband response. When $\omega_l > \gamma_2$, as B_t is increased we encounter three different regimes separated by crossover regions I and II that are shaded in the figure. The crossover II between the Rabi and the volcano regimes lies around the $\omega_l = 2B_t$ solid line. In the slow field limit ($\omega_l < \gamma_2$), the spectrum evolves smoothly without a clear separation between different regimes.

section, $\langle\sigma_+\rangle^{(-1)}$ is simply obtained by replacing ω_l with $-\omega_l$ in the expression for $\langle\sigma_+\rangle^{(1)}$ in Eq. (17). This replacement is equivalent to the transformation that consists of complex conjugation combined with the replacement of Δ_s by $-\Delta_s$. Since the spectrum only depends on the absolute value, the complex conjugation can be ignored. Hence, the left sideband spectrum is the mirror image of the right sideband spectrum, under the reflection $\Delta_s \to -\Delta_s$.

V. SPIN-CAVITY SIDEBANDS

We return to the original problem of a coupled spin-cavity system [see Sec. III], with two external drives: the spin is driven by the longitudinal field at frequency ω_l and the cavity is driven at frequency ω_t. The cavity transfers oscillations to the spin at the latter frequency through an effective magnetic field $B_t = \Omega\langle a^\dagger\rangle^{(0)}$. This field is not treated as an external parameter, as in Sec. IV, but it is determined by a single-mode driven nonlinear cavity with natural frequency ω_c. Since the spin sees two drivings, an external driving at frequency ω_l and an effective cavity driving at frequency ω_t, it can act as a frequency-mixer to produce radiation at the sum and the difference of these two frequencies. This sideband radiation, in turn, drives the cavity at $\omega_t \pm \omega_l$, and we can read out the sideband response of the spin from the cavity oscillations.
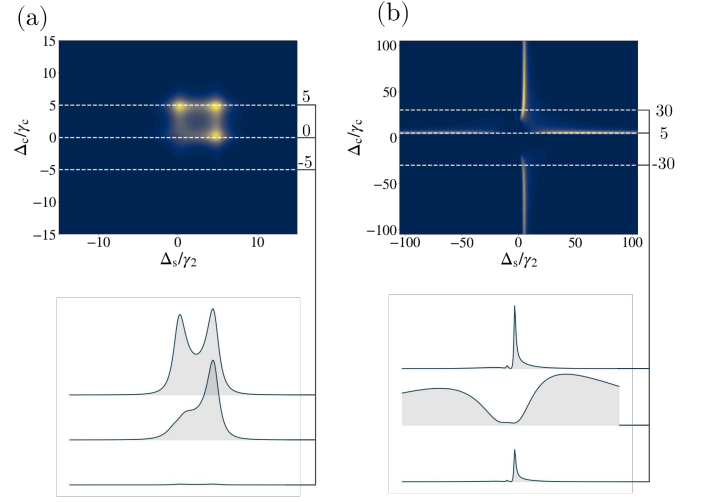

FIG. 8. 2D right sideband response given by $|\langle a^\dagger\rangle^{(1)}|^2$ without the cavity nonlinearity and the spin feedback. The strength of the cavity driving is weak in (a) where g_P is 0.1, and strong in (b), where $g_P = 100.0$. The slices along which the one-dimensional response is shown are indicated by the horizontal dashed lines. They are at the positions $\Delta_c = 0$, $\pm\omega_l$ in (a). The signal is amplified when $\Delta_c = \omega_l$ for the right sideband and this fact is reflected in the plots. However, when $\Delta_c = 0$ the spin driving is the strongest and near the linear response regime (a) we see the signal at this point. The strong field leads to power broadening and this is the reason why we see only one of two resonances. In (b) we see the transition from the volcano to the Rabi regime as Δ_c is varied. The volcano spectrum is enhanced near $\Delta_c = \omega_l$. Even though the Rabi regime is far from the amplification region, we can still see the peaks because they are much sharper than the broad volcano. The rest of the parameters of the plots are given in units of γ_2: $\omega_l = 5.0$, $\gamma_1 = 0.01$, $\gamma_c = 1.0$, and $\Omega = 0.01$.

The simplified description that we have given ignores the higher-order spin-cavity feedback effects. In actuality, the effective cavity driving at ω_t is renormalized by the spin oscillations themselves. However, the effect of this feedback on the sideband spectrum is negligible if the spin-cavity coupling strength is weak. In addition to this, we will assume at first that the cavity is linear. We use this as a basis from which we will later show how making the cavity nonlinear brings about novel effects.

A. The Right Sideband

We now study the right sideband spectral intensity function in the two-dimensional $\Delta_s - \Delta_c$ plane. In other words, in Sec. IV we presented the Δ_s-dependence of the response by fixing the cavity parameters, and now we want to study the Δ_c-dependence as well. In the Supplementary Material [28] we show that the intensity of the right sideband is determined by the $|\langle a^\dagger\rangle^{(1)}|^2$ expectation value. Within the limits mentioned earlier, in which the Kerr nonlinearity and feedback effects are neglected,

the steady state solution for the cavity equation (Eq. 11c) reduces to the damped Lorentzian oscillator solution, $\langle a^\dagger \rangle^{(0)} = \frac{-g_P}{2(\Delta_c + i\gamma_c)}$. Therefore, the effective transverse field that each spin feels is

$$B_t = \frac{-g_P \Omega}{2(\Delta_c + i\gamma_c)} \qquad (22)$$

The amplitude of the field is highest when the external driving is resonant with the cavity ($\Delta_c = \omega_c - \omega_t = 0$) and its value is $\frac{g_P \Omega}{2\gamma_c}$. As the external driving is detuned from the cavity, the amplitude falls off with the width set by the decay rate γ_c. The right sideband steady state solution for the cavity is then

$$\langle a^\dagger \rangle^{(1)} = -\frac{N_S \Omega}{\Delta_c - \omega_l + i\gamma_c} \langle \sigma_+ \rangle^{(1)} (B_t) \Bigg|_{B_t = \frac{-g_P \Omega}{2(\Delta_c + i\gamma_c)}} , \qquad (23)$$

with the derivation given in Appendix C.

Equation (23) reflects the twofold role of the cavity on the sideband response. First, the cavity provides an effective transverse drive to the spins whose amplitude is given in Eq. (22). This drive is strongest when the cavity is at resonance with the transverse frequency ω_t. Second, the cavity acts as an antenna that measures the response itself. This gives rise to the amplification factor in front of Eq. (23), which is maximal when the cavity is at resonance with the sideband frequency $\omega_t + \omega_l$. While Eq. (23) ignores feedback effects, we have checked explicitly that it captures the full solution to the mean field equations (C1) to an excellent approximation whenever the cavity-spin coupling is small.

When the cavity is weakly driven ($g_P \ll 1$) we obtain from the linear response solution in Eq. (18),

$$\frac{-g_P N_S \Omega^2 \sigma_z^{eq}}{4 (\Delta_s - \omega_l + i\gamma_2)(\Delta_s + i\gamma_2)(\Delta_c + i\gamma_c)(\Delta_c - \omega_l + i\gamma_c)} . \qquad (24)$$

This response shows four resonances. The two resonances at $\Delta_s = 0$ and $\Delta_s = \omega_l$ were discussed in Sec. IV. The resonance at $\Delta_c = 0$ comes from the fact that near the linear response regime, the spectral intensity is proportional to the magnitude of B_t, which assumes its maximum value near $\Delta_c = 0$. The last resonance occurs when $\Delta_c = \omega_l$, and it describes the amplification of the signal by the cavity.

If the cavity driving strength g_P is increased, the effective magnetic field felt by the spin increases, and power broadening suppresses the $\Delta_s = 0$ resonance. Since the magnetic field is highest near the $\Delta_c = 0$ resonance we expect this suppression to occur first near this resonance. This scenario is shown in Fig. 8(a). Out of the four resonances in the $\Delta_s - \Delta_c$ plane, the first one to be suppressed is at $\Delta_s = \Delta_c = 0$.

After an additional increase in cavity driving strength we obtain the spectrum shown in Fig. 8(b). This figure demonstrates the transition between the Rabi and the volcano regimes, which can be seen for a fixed set of

parameters. Near $\Delta_c = \omega_l$ the effective field amplitude (22) is large ($|B_t| \gg \omega_l$), corresponding to the volcano regime. Although the spectral weight of the volcano is spread out, the signal is amplified by the cavity and it is therefore clearly visible in the spectrum. On the other hand, for large Δ_c the amplification of the sideband radiation is much weaker, and one would expect not to see significant response. However, when $\omega_l \gg 2|B_t|$ we enter the Rabi regime, in which the resonances are very sharp. This leads to visible peaks even though the amplification is weak. Which of these two features, volcano and Rabi, is more visible depends on the relative sizes of γ_2 and γ_c: γ_2 sets the width of the Rabi resonances, while γ_c sets the width of the amplification region.

B. The Sideband Symmetry

In Sec. IV we showed that the left sideband response can be obtained from the right sideband by replacing Δ_s with $-\Delta_s$, but keeping B_t constant. A natural question to ask is whether this symmetry extends to the full two-dimensional spectrum. In App. C we show that the symmetry condition can be generalized: the left sideband is obtained from the right sideband by simultaneously replacing Δ_s with $-\Delta_s$ and Δ_c with $-\Delta_c$. This can be seen as a composition of two reflections in the $\Delta_s - \Delta_c$ plane or, equivalently, as a π-angle rotation of the plane. The symmetry is present even when the spin-cavity feedback is not ignored. One consequence of the symmetry is that the left sideband is most strongly amplified near $\Delta_c = -\omega_l$. The relation between the left and the right sideband spectra is illustrated in Fig. 9(a).

This symmetry relation is clearly violated in the experimentally obtained spectra shown in the bottom row of Fig. 3. The general symmetry-based principle excludes a large class of linear models and points to a nonlinear origin of the asymmetry. Although the exact details of the experimental conditions in the complex diamond-defect setup are not known, we illustrate here how Hamiltonian nonlinearity can give rise to this counterintuitive response. By introducing Kerr nonlinearity to the cavity subsystem, we break the symmetry relation. This nonlinearity enables the cavity to mix frequencies in an asymmetric way between the left and the right sidebands. The breaking of the symmetry relation between sidebands is shown in Fig. 9(b). We will next analyze the effects arising from such cavity nonlinearity.

VI. CAVITY NONLINEARITY AND THE SIDEBAND ANOMALY

Nonlinearity of the resonator gives rise to an amplitude-dependent shift of its resonant frequency. As an example, the Duffing resonator with a cubic nonlinear term in the equations of motion exhibits a blue shift for positive nonlinearity coefficient and a red shift for
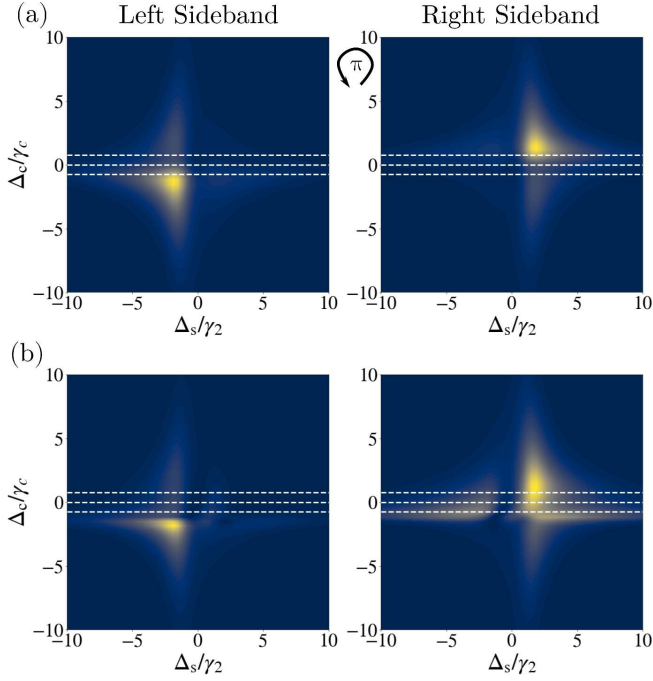
FIG. 9. Comparison between the 2D-spectra of the theoretically computed left and the right sideband. (a) In the absence of nonlinearity, when $\eta = 0$, the right sideband spectrum is obtained by π-rotation ($\Delta_c \rightarrow -\Delta_c$, and $\Delta_s \rightarrow -\Delta_s$) of the left sideband spectrum. (b) When Kerr nonlinearity is added ($\eta = 1$), the symmetry between sidebands is broken. The parameters in units of γ_2 are $\omega_l = 1.5$, $\gamma_1 = 0.01$, $\gamma_c = 2.0$, $g_P = 200.0$, $\Omega = 0.01$, $N_S = 1$, and $\sigma_z^{eq} = -1$.

negative coefficient. The Kerr nonlinearity of the cavity similarly gives rise to the cubic term in the optical Bloch equations. However, the nonlinearity can also mix frequencies and consequently modify the emission spectrum.

We show that if the resonator is driven to its nonlinear regime, the symmetry between the two sidebands is broken. We demonstrate our results with the example of the Kerr nonlinearity. First, we recall that the nonlinearity leads to the blue-shifted tilted central spectral line in the response (when the Kerr coefficient K_c is positive). We show that the influence on the sidebands is more complicated. The magnitude of the blueshift is a non-monotonic function of the longitudinal frequency and the spectral response can exhibit many complicated features. This hypersensitivity of the nonlinear response to the physical parameters points to its usefulness as a gauge of the internal dynamics of quantum systems.

The cavity is a dynamical system that both drives and measures the spins. The effects of the Kerr nonlinearity on the response are mediated through the spin-cavity feedback and become particularly visible in the sidebands. Throughout the section, we treat the nonlinearity and the spin-cavity feedback perturbatively. The perturbative solution restricts the response to be outside of the bistability region, which requires a strongly ex-

cited nonlinearity. This is the region with the two stable steady-state solutions for the Duffing resonator.

The Kerr nonlinearity with $K_c > 0$ blueshifts the cavity frequency. This can be seen in Fig. 13(c), where the spectral line is slanted to the left. As shown in App. C 2, parameter

$$\eta = \frac{g_P^2 K_c}{4\gamma_c^3}, \tag{25}$$

determines the strength of the Kerr nonlinearity. To the cubic order in η, and away from the spin resonance where the spin-cavity feedback becomes prominent, the position of the maximum of the central resonance is shifted to

$$\Delta_{c,\,res}^{(0)}|_{\Delta_s \rightarrow \infty} = -\eta\gamma_c + \mathcal{O}\left(\eta^3\right). \tag{26}$$

This shift of the resonant detuning to the left corresponds to the blue shift of the cavity frequency. As η is varied in panel (c) of Fig. 13, the maximum of the resonance closely follows this simple approximate result. It is worth noting that a further increase of η would lead the cavity to the optical bistability region.

The effect of the Kerr nonlinearity on sidebands is subtler, and it is treated in detail in App. C 3. However, the most direct effect is the shift of the spectral lines. We focus on the case when $K_c > 0$, which leads to the blue shift of the spectrum. The results can be straightforwardly generalized to the case of the negative Kerr coefficient ($K_c < 0$), though this requires higher-order terms to stabilize the Hamiltonian. As it is shown in Appendix C, the resonances that govern the amplification of the sideband signals appear. The positions of the resonance centers are to cubic order in η,

$$\Delta_{c,\,res}^{(\pm 1)} = \pm\omega_l - 2\eta\frac{\gamma_c}{1 + \left(\frac{\omega_l}{\gamma_c}\right)^2}$$
$$\mp\frac{7}{2}\eta^2\frac{\omega_l}{\left(1 + \left(\frac{\omega_l}{\gamma_c}\right)^2\right)^3} + \mathcal{O}\left(\eta^3\right). \tag{27}$$

The positions of the central resonance and the two sidebands as functions of the longitudinal frequency ω_l are shown in Fig. 10(a).

The first term in Eq. (27) exists in the absence of the Kerr nonlinearity ($\eta = 0$). It is a simple condition $\Delta_c = \omega_c - \omega_t = \pm\omega_l$ for the sideband light to hit the cavity resonance. The second term creates the blue shift when the longitudinal frequency is small compared to the cavity width γ_c. Importantly, it shifts the right and the left sidebands in the same direction. When $\omega_l \ll \gamma_c$ this shift is dominant and it comes with a non-trivial factor of 2. This factor is a consequence of the frequency mixing that occurs due to the nonlinear cavity term $K_c a^\dagger a^\dagger a$ from Eq. (11c). As ω_l is increased significantly beyond the cavity width γ_c, this effect becomes less significant since the off-resonant sidebands cannot excite the cavity
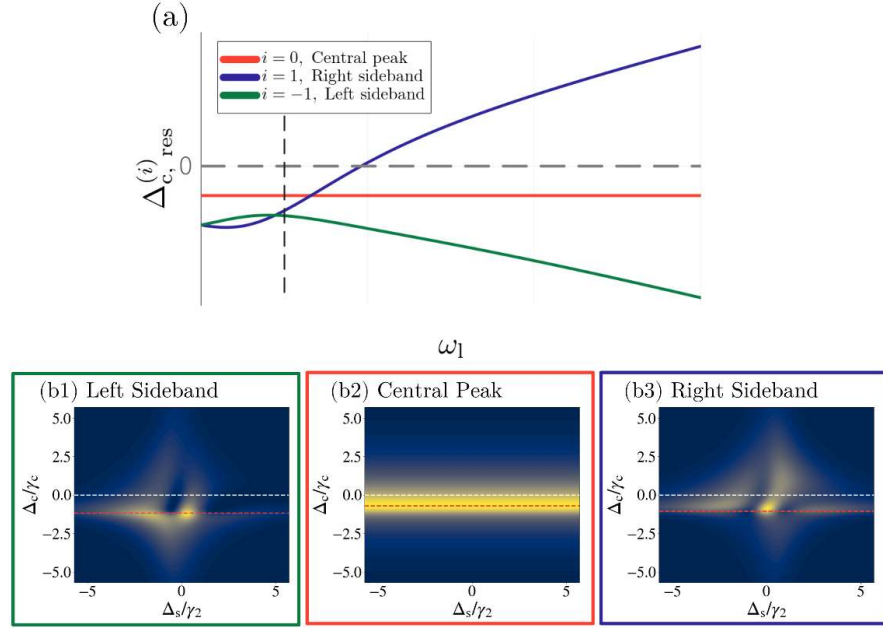
FIG. 10. The positions of the central resonance, $\Delta_{\text{c, res}}^{(0)}$, and the sideband resonances, $\Delta_{\text{c, res}}^{(\pm 1)}$, depending on the frequency of the longitudinal field ω_l are shown in (a). The strength of the Kerr nonlinearity is $\eta = 0.7$, and that is enough to lead to an anomalous behavior when ω_l is comparable to γ_c. The 2D spectra for the central line and the sidebands (b1-3) are drawn when $\omega_l = 0.5\gamma_c$. In this region, both of the sidebands are shifted to the left of the central resonance. The rest of the parameters of the plots are $g_P = 50.0$, $\Omega = 0.01$, $N_S = 1$, $\sigma_z^{\text{eq}} = -1.0$, $\gamma_1 = 0.01$, and $\gamma_c = 1.0$.

nonlinearity strongly. In the limit when $\omega_l \gg \gamma_c$ the position of the resonance can be primarily understood as a simple resonant amplification of sideband radiation if the sideband frequency matches the bare cavity frequency ω_c. The intermediate region is resolved through an interplay of *the resonant sideband amplification* when the sideband photons hit the cavity resonance and *the excitation of the Kerr nonlinearity*, which leads to frequency mixing.

It can be read out from expression (27) that when $\omega_l \ll \gamma_c$ the shift of the resonance of both of the sidebands is twice the shift of the central resonance (Eq. (26)). The right sideband is to the left of the resonance, and the *sideband anomaly* always occurs at very slow longitudinal fields. However, when ω_l is sufficiently small the sideband signals are indiscernible because of the broadening effects. Therefore, we look at the condition for the anomaly at a finite ω_l. We define the nonlinearity strength $\eta_{\text{anom}}\left(\omega_l/\gamma_c\right)$ as the condition for the onset of the anomaly,

$$\Delta_{\text{c, res}}^{(1)}\left[\eta_{\text{anom}}\left(\frac{\omega_l}{\gamma_c}\right)\right] = \Delta_{\text{c, res}}^{(0)}\left[\eta_{\text{anom}}\left(\frac{\omega_l}{\gamma_c}\right)\right]. \quad (28)$$

The solution of the equation for $\eta_{\text{anom}} = \frac{g_P^2}{4\gamma_c^3}K_c^{\text{anom}}$ gives the anomaly Kerr strength K_c^{anom} for the onset of the sideband anomaly,

$$K_c^{\text{anom}} = \frac{4}{7g_P^2}\left[\frac{\left(\omega_l^2 - \gamma_c^2\right)\left(\omega_l^2 + \gamma_c^2\right)^2}{\omega_l\gamma_c^2}\right.$$
$$\left. + \sqrt{\frac{\left(\omega_l^2 - \gamma_c^2\right)^2\left(\omega_l^2 + \gamma_c^2\right)^4}{\omega_l^2\gamma_c^4} + 14\left(\omega_l^2 + \gamma_c^2\right)^3} \right] + \mathcal{O}\left(\eta^3\right). \quad (29)$$

In Figure 10(a), the nonlinearity strength η is large enough that the order of the right and the left sidebands becomes inverted at low ω_l. This effect comes from the quadratic term in Eq. (27). One should be careful when considering these analytic results; the nonlinearity strength becomes large enough to render the approximate results qualitative. With this cautionary remark, we write the expression for the distance between the sidebands,

$$\Delta_{\text{c, res}}^{(1)} - \Delta_{\text{c, res}}^{(-1)} = 2\omega_l\left(1 - \frac{7g_P^4 K_c^2}{32\left(\omega_l^2 + \gamma_c^2\right)^3}\right) + \mathcal{O}\left(\eta^3\right). \quad (30)$$

When the term in the brackets vanishes, the order of the left and the right sideband is inverted. This happens at the inversion Kerr strength,

$$K_c^{\text{inv}} = \frac{4}{g_P^2}\sqrt{\frac{2\left(\omega_l^2 + \gamma_c^2\right)^3}{7}} + \mathcal{O}\left(\eta^3\right). \quad (31)$$
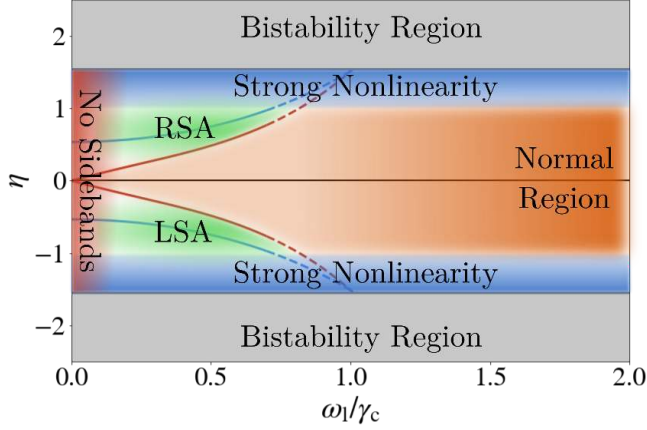
FIG. 11. The regions of the right-sideband anomaly (RSA) and the left-sideband anomaly (LSA) shown in the diagram with the nonlinearity strength η on the y-axis and the normalized longitudinal frequency ω_l/γ_c on the x-axis. The line separating two anomalous regions from the region without the anomaly (normal region) is calculated in Eq. (29) and drawn in red. Note that there is no sharp transition here, and the shifts close to the line and in the normal region can still be very large. The blue line going through anomalous regions separates parameters for which the order of the right and the left sideband is inverted and those for which it is not. As $|\eta|$ is increased, the cavity is very nonlinear and one may see double resonances and higher-order nonlinearities, among other phenomena. An additional increase leads to the appearance of two solutions, which define the bistability region. In very slow longitudinal fields, the sidebands become invisible due to broadening (the red area).

The conclusions of the section are summarized in Fig. 11. The figure sketches different regimes as a function of the cavity nonlinearity strength η and the normalized frequency of the longitudinal drive ω_l/γ_c. The results were generalized to the case of a negative Kerr coefficient ($\eta < 0$). The figure is mirror-symmetric with respect to the η-axis. While we restricted the prior analysis to $\eta > 0$, none of the equations rely on that assumption. The difference is that when $\eta < 0$ the cavity frequency is red-shifted and not blue-shifted. The anomalous behavior here is that the left sideband in Fig. 10(a) is to the right of the central resonance. We call this the *left-sideband anomaly* to differentiate it from the case of a positive Kerr coefficient where we call the effect the *right-sideband anomaly*.

The red and blue lines in Fig. 11 represent the conditions (29) and (31), respectively. The lines are drawn as dashed for high $|\eta|$ to indicate that the approximation of small $|\eta|$ used in this section starts to break down. In the region of strong nonlinearity (the blue area), the spectrum would be significantly altered even before the onset of bistability. Not only do the higher-order terms in η become important, but the structure of the spectrum is not well-described by simple resonance conditions. One would have to return to the full analysis of dynamical

equations, some of which is presented in App. C. If the cavity is driven to the nonlinear regime by strong driving g_P, the higher-order nonlinearities might also become excited and should be included in the Hamiltonian. The region of small ω_l is drawn in red and easily matches the condition for the anomaly in Eq. (29). However, this region is not experimentally accessible since for small ω_l it becomes impossible to distinguish between the central resonance at ω_t and the sidebands at $\omega_t \pm \omega_l$.

VII. OUTLOOK

Throughout the paper, we treated dissipation in an *ad hoc* way, which is justified in certain limits [36]. However, more systematic treatment through a Lindblad equation as in Ref. [13] (or alternatively a non-Markovian quantum master equation) might uncover novel details. This relies on a better microscopic understanding of the dissipation in diamond defects. The analysis in the dressed-atom picture should give an intuitive description near the Rabi regime [13], as well as provide us with a proper extension of the theory with the full quantum treatment of electromagnetic radiation [37, 38].

We modeled the cavity nonlinearity as a Kerr nonlinearity due to its relevance for many quantum resonators in solid-state physics. However, we believe that the sideband sensitivity to cavity nonlinearities is more general, and these details remain to be characterized.

VIII. ACKNOWLEDGMENTS

IX. AUTHOR CONTRIBUTION STATEMENTS

L.A. conducted the theoretical analysis and wrote the manuscript. S.H. and S.M. performed the experiments. D.P. contributed to the theorical work, and E.B. assisted with the experiment.

Appendix A: Driven spin model

The steady-state solution for the central frequency does not have corrections in linear response,

$$
\begin{aligned}
\langle \sigma_z \rangle^{(0)} &= \frac{\left(\Delta_s^2 + \gamma_2^2\right) \sigma_z^{eq}}{\Delta_s^2 + \gamma_2^2 + 4\frac{\gamma_2}{\gamma_1}|B_t|^2}, \\
\langle \sigma_+ \rangle^{(0)} &= \frac{B_t}{\Delta_s + i\gamma_2}\langle \sigma_z \rangle^{(0)} = \frac{\left(\Delta_s - i\gamma_2\right) B_t \sigma_z^{eq}}{\Delta_s^2 + \gamma_2^2 + 4\frac{\gamma_2}{\gamma_1}|B_t|^2}.
\end{aligned} \tag{A1}
$$

After enough time passes, the spin will settle to oscillate at $\pm\omega_\mathrm{l}$ frequencies in the rotating frame. We can perform calculations for one of the sideband,s and the other can be obtained by changing ω_l to $-\omega_\mathrm{l}$. Picking up the terms that oscillate at ω_l we get the following system of equations:

$$
\begin{aligned}
i\frac{d\langle\sigma_+\rangle^{(1)}}{dt} &= -\left(\Delta_\mathrm{s} - \omega_\mathrm{l} + i\gamma_2\right)\langle\sigma_+\rangle^{(1)} \\
&\quad + B_\mathrm{t}\langle\sigma_\mathrm{z}\rangle^{(1)} - \frac{B_\mathrm{l}}{2}\langle\sigma_+\rangle^{(0)}, \\
i\frac{d\langle\sigma_-\rangle^{(1)}}{dt} &= \left(\Delta_\mathrm{s} + \omega_\mathrm{l} - i\gamma_2\right)\langle\sigma_-\rangle^{(1)} \\
&\quad - B_\mathrm{t}^*\langle\sigma_\mathrm{z}\rangle^{(1)} + \frac{B_\mathrm{l}}{2}\langle\sigma_-\rangle^{(0)}, \\
i\frac{d\langle\sigma_\mathrm{z}\rangle^{(1)}}{dt} &= \left(\omega_\mathrm{l} - i\gamma_1\right)\langle\sigma_\mathrm{z}\rangle^{(1)} \\
&\quad + 2\left(B_\mathrm{t}^*\langle\sigma_+\rangle^{(1)} - B_\mathrm{t}\langle\sigma_-\rangle^{(1)}\right).
\end{aligned}
\tag{A2}
$$

The steady-state solution of the system of equations has two contributions,

$$
\langle\sigma_+\rangle^{(1)} = \frac{1}{\Delta_\mathrm{s} - \omega_\mathrm{l} + i\gamma_2}\left(-\frac{B_\mathrm{l}}{2}\langle\sigma_+\rangle^{(0)} + B_\mathrm{t}\langle\sigma_\mathrm{z}\rangle^{(1)}\right).
\tag{A3}
$$

The first term in the equation contains two resonances that correspond to two different processes in the linear response regime, where one of the resonances becomes power-broadened (shown in Fig. 5). The other term comes from the fact that the ground and excited state populations start oscillating with ω_l frequency. The solution is given in the main part of the paper.

Appendix B: Response function poles

In this appendix, we present an alternative description of the transition between the Rabi and the volcano regimes. If we make an analytic continuation of Δ_s to the complex plane, we can track the motion of poles of the response function in the complex plane. There are four poles in the approximate response, Eq. (19), two Rabi poles that are at $\pm\sqrt{\omega_\mathrm{l}^2 - 4|B_\mathrm{t}|^2}$, and two poles from the power-broadened part, $\pm 2i\sqrt{\frac{\gamma_2}{\gamma_1}}|B_\mathrm{t}|$, that always lie on the imaginary axis. The actual positions of the poles are slightly shifted relative to these values, due to the decay rates appearing in the exact expression, Eq. (17).

As shown in Fig. 12, the transition from the Rabi to the volcano regime can be seen as movement of the Rabi resonances in the complex plane away from the real axis as ω_l is decreased. In the Rabi regime, $2|B_\mathrm{t}|/\omega_\mathrm{l} \ll 1$, the resonances (red dots near the real axis in Fig. 12(a)) are responsible for most of the weight of the spectrum and they are visible as sharp peaks in the spectrum. They never intersect the real axis, because they always have an imaginary part set by decay rates. As can be seen from

Eq. (19), the response has zeros at $\Delta_\mathrm{s} = 0$ and $\Delta_\mathrm{s} = -\omega_\mathrm{l}$. Since the resonance with the negative real part is close to the zeros it is suppressed relative the other resonance.

As the ratio of transverse driving to longitudinal frequency $|B_\mathrm{t}|/\omega_\mathrm{l}$ is increased, both resonances move towards the origin, $\Delta_\mathrm{s} = 0$, leading to the crossover II region [Fig. 12(b)]. As $|B_\mathrm{t}|/\omega_\mathrm{l}$ is further increased, the resonances start moving away from each other, mainly along the imaginary axis: now the Rabi condition, (20), is satisfied but for imaginary frequencies. In the volcano regime (shown in 12(c)), the imaginary Rabi resonances create a broad peak, and the zeros (blue dots in the figure) create the central transparency region. In addition, the power-broadening resonances that lie further away on the imaginary axis provide weight to the tails of the spectrum and set the overall width of the volcano.

Appendix C: Driven spin-cavity model

The system of equations for the five operators of the coupled spin-cavity system is:

$$
\begin{aligned}
i\frac{d\sigma_+^i}{dt} &= -(\Delta_\mathrm{s} + B_\mathrm{l}\cos(\omega_\mathrm{l}t) + i\gamma_2)\sigma_+^i + \Omega a^\dagger\sigma_\mathrm{z}^i + \mathcal{F}_+^i, \\
i\frac{d\sigma_-^i}{dt} &= (\Delta_\mathrm{s} + B_\mathrm{l}\cos(\omega_\mathrm{l}t) - i\gamma_2)\sigma_-^i - \Omega a\sigma_\mathrm{z}^i + \mathcal{F}_-^i, \\
i\frac{d\sigma_\mathrm{z}^i}{dt} &= 2\Omega\left(a\sigma_+^i - a^\dagger\sigma_-^i\right) - i\gamma_1\left(\sigma_\mathrm{z}^i - \sigma_\mathrm{z}^\mathrm{eq}\right) + \mathcal{F}_\mathrm{z}^i, \\
i\frac{da^\dagger}{dt} &= -(\Delta_\mathrm{c} + i\gamma_c)a^\dagger - K_c a^\dagger a^\dagger a - \sum_{i=1}^{N_\mathrm{S}}\Omega\sigma_+^i - \frac{g_\mathrm{P}}{2} + \mathcal{F}_a^\dagger, \\
i\frac{da}{dt} &= (\Delta_\mathrm{c} - i\gamma_c)a + K_c a^\dagger a a + \sum_{i=1}^{N_\mathrm{S}}\Omega\sigma_-^i + \frac{g_\mathrm{P}}{2} + \mathcal{F}_a,
\end{aligned}
\tag{C1}
$$

where we added the Langevin forces ($\mathcal{F}_i$) to the equations, with the effect that the Lie algebra structure is preserved. The quantum correlations between the cavity and the spin are neglected ($\langle AB\rangle \approx \langle A\rangle\langle B\rangle$). It is clear that every spin within this approximation is equivalent and we can write the equations for an average spin operator components ($\sigma_\alpha = \frac{1}{N_\mathrm{S}}\sum_{i=1}^{N_\mathrm{S}}\sigma_\alpha^i$). The system of equations for expectation values can be written in terms of dimensionless variables and parameters defined in the following way:

$$
\begin{aligned}
&\tilde{\Delta}_\mathrm{c} = \frac{\Delta_\mathrm{c}}{\gamma_c}, \quad \tilde{\Delta}_\mathrm{s} = \frac{\Delta_\mathrm{s}}{\gamma_2}, \quad \tilde{\gamma}_1 = \frac{\gamma_1}{\gamma_2}, \quad \tilde{\gamma}_\mathrm{c} = \frac{\gamma_\mathrm{c}}{\gamma_2}; \\
&\eta = \frac{g_\mathrm{P}^2 K_\mathrm{c}}{4\gamma_\mathrm{c}^3}; \quad \nu = \frac{N_\mathrm{S}\Omega^2\sigma_\mathrm{z}^\mathrm{eq}}{\gamma_2\gamma_\mathrm{c}}, \quad \xi = \frac{g_\mathrm{P}^2\Omega^2}{\gamma_1\gamma_2\gamma_\mathrm{c}^2}; \\
&A = \frac{\langle a^\dagger\rangle}{\frac{g_\mathrm{P}}{2\gamma_\mathrm{c}}}, \quad \tilde{\sigma}_\mathrm{z} = \frac{\langle\sigma_\mathrm{z}\rangle}{\sigma_\mathrm{z}^\mathrm{eq}}, \quad \tilde{\sigma}_\pm = \frac{\langle\sigma_\pm\rangle}{\frac{g_\mathrm{P}\Omega\sigma_\mathrm{z}^\mathrm{eq}}{2\gamma_2\gamma_\mathrm{c}}}; \\
&\tilde{B}_\mathrm{l} = \frac{B_\mathrm{l}}{\gamma_2}, \quad \tilde{\omega}_\mathrm{l} = \frac{\omega_\mathrm{l}}{\gamma_2}.
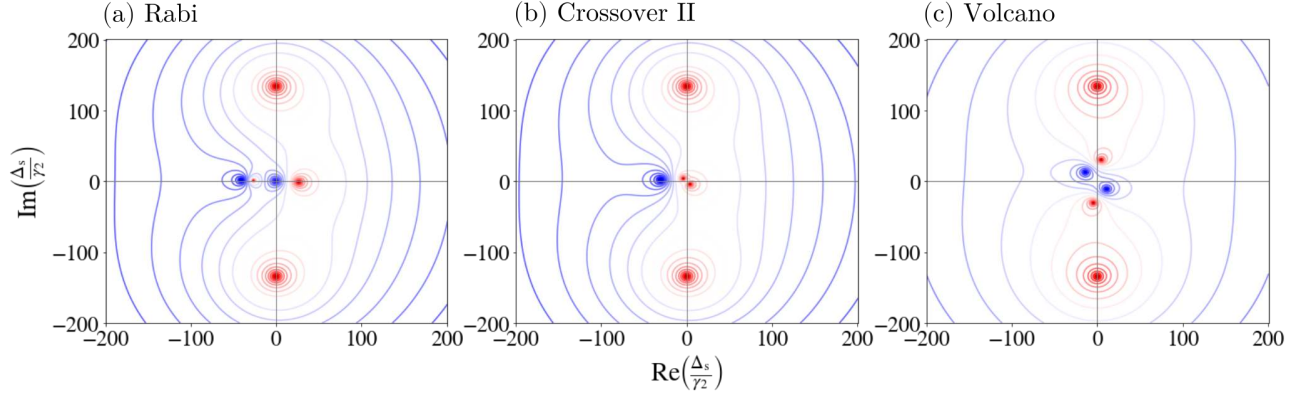\end{aligned}
\tag{C2}
$$

FIG. 12. Logarithmic intensity plot of poles associated with resonances (red dots) and zeros (blue dots) as they move through the complex frequency plane. The parameters are: $\gamma_1 = 0.05$, $|B_t| = 15.0$, and ω_l goes through values 40.0, 30.0, 3.0 from a) to c). Note that in the crossover region in b), where $\omega_l = 2B_t$ the two resonances hide the zero at the origin.

The system of equations with these new variables and parameters is

$$i\frac{d\tilde{\sigma}_+}{d\tilde{t}} = -\left(\tilde{\Delta}_s + \tilde{B}_l \cos\left(\tilde{\omega}_l \tilde{t}\right) + i\right)\tilde{\sigma}_+ + A\tilde{\sigma}_z, \quad (C3)$$

$$i\frac{1}{\tilde{\gamma}_1}\frac{d\tilde{\sigma}_z}{d\tilde{t}} = \frac{\xi}{2}\left(A^*\tilde{\sigma}_+ - A\tilde{\sigma}_-\right) - i\left(\tilde{\sigma}_z - 1\right), \quad (C4)$$

$$i\frac{1}{\tilde{\gamma}_c}\frac{dA}{d\tilde{t}} = -\left(\tilde{\Delta}_c + i\right)A - \eta|A|^2 A - \nu\tilde{\sigma}_+ - 1, \quad (C5)$$

where time is measured in units of $T_2 = \frac{1}{\gamma_2}$.

1. Steady-state sideband symmetry

In the absence of cavity nonlinearity ($\eta = 0$) there is a symmetry that connects the left and the right sideband. To study the sidebands we are going to write the steady state equations for the $+\omega_l$ Fourier component,

$$\tilde{\sigma}_+^{(1)} = \frac{-A^{(0)}\tilde{\sigma}_z^{(1)} - A^{(1)}\tilde{\sigma}_z^{(0)} + \frac{\tilde{B}_l}{2}\tilde{\sigma}_+^{(0)}}{\left(\tilde{\omega}_l - \tilde{\Delta}_s - i\right)},$$

$$\tilde{\sigma}_-^{(1)} = \frac{A^{*(0)}\tilde{\sigma}_z^{(1)} + A^{*(1)}\tilde{\sigma}_z^{(0)} - \frac{\tilde{B}_l}{2}\tilde{\sigma}_-^{(0)}}{\left(\tilde{\omega}_l + \tilde{\Delta}_s - i\right)},$$

$$\tilde{\sigma}_z^{(1)} = -\frac{\frac{\xi}{2}\left(A^{*(0)}\tilde{\sigma}_+^{(1)} - A^{(0)}\tilde{\sigma}_-^{(1)} + A^{*(1)}\tilde{\sigma}_+^{(0)} - A^{(1)}\tilde{\sigma}_-^{(0)}\right)}{\left(\frac{\tilde{\omega}_l}{\tilde{\gamma}_1} - i\right)},$$

$$A^{(1)} = \frac{\nu\tilde{\sigma}_+^{(1)}}{\left(\frac{\tilde{\omega}_l}{\tilde{\gamma}_c} - \tilde{\Delta}_c - i\right)},$$

$$A^{*(1)} = -\frac{\nu\tilde{\sigma}_-^{(1)}}{\left(\frac{\tilde{\omega}_l}{\tilde{\gamma}_c} + \tilde{\Delta}_c - i\right)}.$$

$$(C6)$$

Index in brackets specifies the Fourier component of the variables, 0 standing for the central frequency and ± 1 for the right and left sideband frequencies $\pm\omega_l$. If we reverse the signs of the detuning parameters ($\Delta_s \to -\Delta_s$ and $\Delta_c \to -\Delta_c$) and change the signs of the variables we can move from one sideband to the other. Transformations

$$\left(\tilde{\sigma}_i^{(0)}\left(-\Delta_s, -\Delta_c\right)\right)^* = -\tilde{\sigma}_i^{(0)}\left(\Delta_s, \Delta_c\right),$$

$$\left(A^{(0)}\left(-\Delta_s, -\Delta_c\right)\right)^* = A^{(0)}\left(\Delta_s, \Delta_c\right),$$

$$\left(A^{*(0)}\left(-\Delta_s, -\Delta_c\right)\right)^* = A^{*(0)}\left(\Delta_s, \Delta_c\right),$$

$$\left(\tilde{\sigma}_i^{(-1)}\left(-\Delta_s, -\Delta_c\right)\right)^* = \tilde{\sigma}_i^{(1)}\left(\Delta_s, \Delta_c\right),$$

$$\left(A^{(-1)}\left(-\Delta_s, -\Delta_c\right)\right)^* = -A^{(1)}\left(\Delta_s, \Delta_c\right),$$

$$\left(A^{*(-1)}\left(-\Delta_s, -\Delta_c\right)\right)^* = -A^{*(1)}\left(\Delta_s, \Delta_c\right),$$

$$(C7)$$

allow us to find the left sideband from the right sideband. If we are looking at the absolute expectation values of the operators, the transformation reduces to switching the signs of detunings. Turning on the cavity nonlinearity by making $\eta \neq 0$ is one possible way to break this symmetry, which leads to a different response for the left and the right sideband.

2. The central resonance

We perform the analysis in the dimensionless system of units which elucidates a clear separation between different effects. The frequencies and the rates are expressed in units of the decoherence rate γ_2 and the cavity width

γ_c,

$$\tilde{\Delta}_c = \frac{\Delta_c}{\gamma_c}, \ \tilde{\Delta}_s = \frac{\Delta_s}{\gamma_2}, \ \tilde{\gamma}_1 = \frac{\gamma_1}{\gamma_2},$$

$$\tilde{\gamma}_c = \frac{\gamma_c}{\gamma_2}, \ \tilde{B}_l = \frac{B_l}{\gamma_2}, \ \tilde{\omega}_l = \frac{\omega_l}{\gamma_2}, \ \tilde{t} = \gamma_2 t. \quad \text{(C8)}$$

The rescaled variables $\tilde{\sigma}_i$ and A correspond to the spin and the cavity, respectively, where

$$A = \frac{\langle a^\dagger \rangle}{\frac{g_P}{2\gamma_c}}, \ \tilde{\sigma}_z = \frac{\langle \sigma_z \rangle}{\sigma_z^{eq}}, \ \tilde{\sigma}_\pm = \frac{\langle \sigma_\pm \rangle}{\frac{g_P \Omega \sigma_z^{eq}}{2\gamma_2 \gamma_c}}. \quad \text{(C9)}$$

The system of equations with new parameters is:

$$i\frac{d\tilde{\sigma}_+}{d\tilde{t}} = -\left(\tilde{\Delta}_s + \tilde{B}_l \cos\left(\tilde{\omega}_l \tilde{t}\right) + i\right)\tilde{\sigma}_+ + A\tilde{\sigma}_z, \quad \text{(C10a)}$$

$$i\frac{1}{\tilde{\gamma}_1}\frac{d\tilde{\sigma}_z}{d\tilde{t}} = \frac{\xi}{2}\left(A^*\tilde{\sigma}_+ - A\tilde{\sigma}_-\right) - i\left(\tilde{\sigma}_z - 1\right), \quad \text{(C10b)}$$

$$i\frac{1}{\tilde{\gamma}_c}\frac{dA}{d\tilde{t}} = -\left(\tilde{\Delta}_c + i\right)A - \eta|A|^2 A - \nu\tilde{\sigma}_+ - 1. \quad \text{(C10c)}$$

The dimensionless parameters η, ν, and ξ set the strengths of different effects,

$$\eta = \frac{g_P^2 K_c}{4\gamma_c^3}, \ \nu = \frac{N_S \Omega^2 \sigma_z^{eq}}{\gamma_2 \gamma_c}, \ \xi = \frac{g_P^2 \Omega^2}{\gamma_1 \gamma_2 \gamma_c^2}. \quad \text{(C11)}$$

The parameter η determines the amplitude of *the cavity (Kerr) nonlinearity*, while ν determines the strength of the *the spin-cavity feedback*. Parameter ξ determines the scale of the power broadening.

We first review the effect of the nonlinearities on the central resonance of the cavity at angular frequency ω_t and proceed to discuss the results for the nonlinear response at sideband frequencies $\omega_t \pm \omega_l$.

The central resonance is obtained by looking at the zero-frequency component of equations (C10). When a linear cavity ($\eta = 0$) is uncoupled from the spin ($\nu = 0$) it settles to a steady state where the number of photons in the cavity is determined by how strongly it is driven (set by g_P and Δ_c) and how fast it is losing photons (γ_c). The nonlinearities have the effect of changing the shape of the spectral line and renormalizing the resonant frequency of the cavity. The central-resonance steady state of the cavity is the solution of the polynomial equation,

$$A^{(0)} = \frac{-1}{\tilde{\Delta}_c + i + \eta|A^{(0)}|^2 + \frac{\nu(\tilde{\Delta}_s - i)}{1 + \tilde{\Delta}_s^2 + \xi|A^{(0)}|^2}}. \quad \text{(C12)}$$

If both the spin and the Kerr nonlinearity are combined, we need to solve for the roots of the quintic equation, obtained by taking a modulus of Eq. (C12). The numerical solution is displayed in Fig. 13(a) where the central resonance intensity is plotted in the $\tilde{\Delta}_s - \tilde{\Delta}_c$ plane.

The spin-cavity feedback changes spectral properties of the cavity near the spin resonance with the appearance of the characteristic S-shape in the dependence of the spectral intensity on the spin detuning $\tilde{\Delta}_s$. The parameter ν
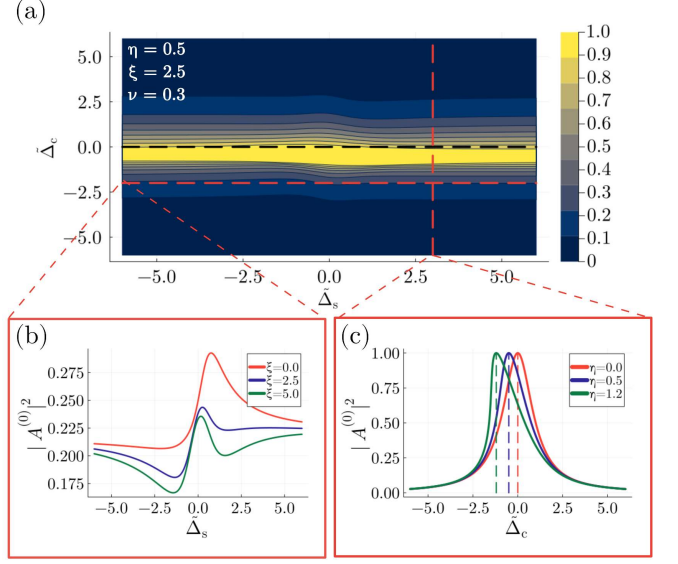

FIG. 13. The effect of both nonlinearities on the central resonance is presented in panel (a) as a two-dimensional plot in the $\tilde{\Delta}_s - \tilde{\Delta}_c$ plane for parameters shown in the plot. The S-shaped spectral line as a function of spin detuning $\tilde{\Delta}_s$ is shown in panel (b) at $\tilde{\Delta}_c = -2.0$ for different values of ξ. In (c), the spin-cavity feedback is ignored ($\nu = 0$), and $\tilde{\Delta}_s = 3.0$. The maximum of the resonance is shown to closely follow an approximate result $-\eta$ for different values of η.

determining the strength of this effect is proportional to the number of spins N_S interacting with the cavity. If a lot of spins interact with the cavity, they visibly alter the spectrum near $\tilde{\Delta}_s = 0$. The dependence of the S-shaped response on the parameter ξ is shown in Fig. 13(b). As ξ is increased, due to the increasing power of the drive, the spins effectively decouple from the cavity, since the sharp resonance near $\tilde{\Delta}_s$ is washed out.

Without nonlinearities, the cavity is a simple Lorentzian,

$$|A^{(0)}|^2 = \frac{1}{1 + \tilde{\Delta}_c^2} \Rightarrow B_t = \Omega|\langle a^{\dagger(0)}\rangle| = \frac{g_P^2}{4\left(\Delta_c^2 + \gamma_c^2\right)}, \quad \text{(C13)}$$

where $\Omega|\langle a^{\dagger(0)}\rangle|$ acts as an effective magnetic field, as shown by the system of equations in (C1). Nonlinearities may induce instabilities, which appear in Eq. (C12) when the quintic polynomial for $|A^{(0)}|^2$ acquires multiple positive roots. Although we study the cavity beyond the linear regime, we will not address the instability region.

Since the spin nonlinearity is localized near the spin resonance ($\tilde{\Delta}_s = 0$), far away from this resonance ($\tilde{\Delta}_s \gg 1$) there is only a Kerr nonlinearity and the central frequency solution is approximately given as

$$|A^{(0)}|^2 \rightarrow \frac{1}{\left(\tilde{\Delta}_c + \eta|A^{(0)}|^2\right)^2 + 1}, \quad \text{when } \tilde{\Delta}_s \rightarrow \infty.$$

$$\quad \text{(C14)}$$

The physically relevant solution is the real root of this cubic equation and there is only one real root for any $\tilde{\Delta}_c$ below $\eta \approx 1.54$. The position of the peak is the solution of:

$$\tilde{\Delta}_c + \eta |A^{(0)}|^2 = 0, \tag{C15}$$

To cubic order in η the position of the center is shifted to

$$\tilde{\Delta}_{c,\,\text{res}}^{(0)}|_{\tilde{\Delta}_s \to \infty} = -\eta + \mathcal{O}\left(\eta^3\right), \tag{C16}$$

On the other hand, without the Kerr nonlinearity ($\eta = 0$), the central frequency response is a solution to another cubic equation,

$$|A^{(0)}|^2 = \left| \frac{-1}{\tilde{\Delta}_c + i + \frac{\nu(\tilde{\Delta}_s - i)}{1 + \tilde{\Delta}_s^2 + \xi |A^{(0)}|^2}} \right|^2, \quad \text{as } \eta \to 0. \tag{C17}$$

When the spin's feedback into the cavity is weak, the solution linear in ν remains a good approximation,

$$|A^{(0)}|^2 \approx \frac{1}{1 + \tilde{\Delta}_c^2} \left(1 - \frac{2\nu \left(\tilde{\Delta}_c \tilde{\Delta}_s - 1 \right)}{\left(1 + \tilde{\Delta}_c^2 \right) \left(1 + \tilde{\Delta}_s^2 \right) + \xi} \right) + \mathcal{O}\left(\nu^2\right). \tag{C18}$$

If both of these are combined, we need to solve for the roots of the quintic equation. The results are presented in Fig. 13.

3. Sidebands

Assuming ν and η are small, we start the analysis of the sideband response, including the cavity nonlinearity. We show that the sideband spectral lines exhibit large sensitivity to the nonlinear effects, where a dramatic change of the spectrum results even from a moderately strong nonlinearity. Arguably, the most peculiar effect, which we call *the sideband anomaly*, is the possibility that both of the sidebands emerge on the same side of the central resonance.

We look at the cavity steady-state expectation value component that oscillates at the right sideband frequency ($\omega_t + \omega_l$). To the first order in the longitudinal field amplitude, the steady state, obtained from Eq. (C10c), is given by

$$A^{(1)} = \frac{\nu \tilde{\sigma}_+^{(1)} + 2\eta |A^{(0)}|^2 A^{(1)} + \eta \left(A^{(0)} \right)^2 A^{*(1)}}{\left(\frac{\tilde{\omega}_l}{\tilde{\gamma}_c} - \tilde{\Delta}_c - i \right)}, \tag{C19}$$

where the absolute value $|A^{(1)}|$ determines the cavity amplitude at the right sideband frequency $\omega_t + \omega_l$.

The expression in Eq. (C19) encapsulates many effects. Before we turn to the analysis of the second term in the numerator, *i.e.* $2\eta |A^{(0)}|^2 A^{(1)}$, we discuss the meaning of other terms. We assume that the spin-cavity feedback is weak ($\nu \ll 1$).

The term in the denominator is a resonance that occurs when the sideband frequency hits the cavity resonance ($\Delta_c = \omega_l$). The first term in the numerator, $\nu \tilde{\sigma}_+^{(1)}$, represents the spin that drives the cavity at the right-sideband frequency. The expectation value of the spin operator $\tilde{\sigma}_+^{(1)}$ at the right sideband frequency is

$$\tilde{\sigma}_+^{(1)} = \frac{\tilde{B}_l \tilde{\sigma}_+^{(0)} - A^{(0)} \tilde{\sigma}_z^{(1)} - A^{(1)} \tilde{\sigma}_z^{(0)}}{\tilde{\omega}_l - \tilde{\Delta}_s - i}. \tag{C20}$$

One of the effects of the Kerr nonlinearity is felt in the fact that the central resonance $A^{(0)}$ is modified by the Kerr nonlinearity, as shown in Appendix C. Furthermore, the term $-A^{(1)} \tilde{\sigma}_z^{(0)}$ indicates that the cavity now drives the spin at the sideband frequency. However, when the spin-cavity feedback is negligible this term can be ignored.

A more impactful consequence of the Kerr nonlinearity comes from the last term in the numerator of Eq. (C19). It connects the right sideband amplitude $A^{(1)}$ equation with its conjugate. In other words, it "mixes" the right and the left sideband solution. This term does not affect the positions of the sideband resonances, but only their detailed shape.

4. The sideband anomaly

To find the steady-state solutions for the sidebands, we need to pick up all the terms in the system of equations in Eq. (C1) that oscillate at frequency ω_l. The cavity equations for the right sideband are:

$$\begin{aligned}
&\left(\frac{\tilde{\omega}_l}{\tilde{\gamma}_c} - \tilde{\Delta}_c - i \right) A^{(1)} - 2\eta |A^{(0)}|^2 A^{(1)} \\
&- \eta \left(A^{(0)} \right)^2 A^{*(1)} - \nu \tilde{\sigma}_+^{(1)} = 0, \\
&\left(\frac{\tilde{\omega}_l}{\tilde{\gamma}_c} + \tilde{\Delta}_c - i \right) A^{*(1)} + 2\eta |A^{(0)}|^2 A^{*(1)} \\
&+ \eta \left(A^{*(0)} \right)^2 A^{(1)} + \nu \tilde{\sigma}_-^{(1)} = 0.
\end{aligned} \tag{C21}$$

The previous two equations can be combined into the expression

$$\begin{aligned}
A^{(1)} = &-\frac{\tilde{\Delta}_c - z_-}{\left(\tilde{\Delta}_c - z_+ \right) \left(\tilde{\Delta}_c - z_- \right) - \eta^2 |A^{(0)}|^4} \\
&\times \left(\nu \tilde{\sigma}_+^{(1)} - \frac{\eta \left(A^{(0)} \right)^2}{\tilde{\Delta}_c - z_-} \nu \tilde{\sigma}_-^{(1)} \right),
\end{aligned} \tag{C22}$$

where we introduced the notation for the complex frequencies,

$$z_\pm = \pm \frac{\tilde{\omega}_l}{\tilde{\gamma}_c} - 2\eta|A^{(0)}|^2 \mp i. \qquad \text{(C23)}$$

The resonance that multiplies the rest of the expression that we denote by $\mathcal{R}$ reduces to

$$\mathcal{R} \underset{\eta \to 0}{\to} \frac{1}{\tilde{\Delta}_c \mp \frac{\tilde{\omega}_l}{\tilde{\gamma}_c} \pm i} = \frac{\gamma_c}{\Delta_c \mp \omega_l \pm i\gamma_c}, \qquad \text{(C24)}$$

in the limit $\eta \to 0$. The expression describes an amplification of the sideband radiation when the outgoing light hits the cavity resonantly.

As η is increased, the existing resonance is shifted and a new resonance appears. Since we are working inside the stability region, the expression is evaluated for small η. $\mathcal{R}$ can be written as

$$\mathcal{R} = -\frac{\tilde{\Delta}_c - z_-}{\left(\tilde{\Delta}_c - \tilde{\Delta}_{c,\,+}\right)\left(\tilde{\Delta}_c - \tilde{\Delta}_{c,\,-}\right)},$$

$$\tilde{\Delta}_{c,\,\pm} = \pm \left(\frac{\tilde{\omega}_l}{\tilde{\gamma}_c} - i\right)\sqrt{1 + \frac{\eta^2|A^{(0)}|^4}{\left(\frac{\tilde{\omega}_l}{\tilde{\gamma}_c} - i\right)^2}} - 2\eta|A^{(0)}|^2,$$

$$\text{(C25)}$$

and for small η, one of the resonances is dominant,

$$\mathcal{R} \approx -\left(1 - \frac{\frac{\eta^2|A^{(0)}|^4}{2\left(\frac{\tilde{\omega}_l}{\tilde{\gamma}_c} - i\right)}}{\tilde{\Delta}_c - z_- + \frac{\eta^2|A^{(0)}|^4}{2\left(\frac{\tilde{\omega}_l}{\tilde{\gamma}_c} - i\right)}}\right) \frac{1}{\tilde{\Delta}_c - z_+ - \frac{\eta^2|A^{(0)}|^4}{2\left(\frac{\tilde{\omega}_l}{\tilde{\gamma}_c} - i\right)}}. \qquad \text{(C26)}$$

The center of the resonance is the solution of the equation,

$$\tilde{\Delta}_c - \frac{\tilde{\omega}_l}{\tilde{\gamma}_c} - 2\eta|A^{(0)}|^2 - \frac{\eta^2|A^{(0)}|^4 \frac{\tilde{\omega}_l}{\tilde{\gamma}_c}}{2\left(1 + \left(\frac{\tilde{\omega}_l}{\tilde{\gamma}_c}\right)^2\right)} = 0. \qquad \text{(C27)}$$

Since $A^{(0)}$ is a function of both $\tilde{\Delta}_c$ and η, this is a polynomial equation whose real root is the center of the resonance. By performing a similar analysis for the left-sideband solution, we write the general result as

$$\tilde{\Delta}_{c,\,\text{res}}^{(\pm1)} = \pm \frac{\tilde{\omega}_l}{\tilde{\gamma}_c} - 2\eta \frac{1}{1 + \left(\frac{\tilde{\omega}_l}{\tilde{\gamma}_c}\right)^2} \mp \frac{7}{2}\eta^2 \frac{\frac{\tilde{\omega}_l}{\tilde{\gamma}_c}}{\left(1 + \left(\frac{\tilde{\omega}_l}{\tilde{\gamma}_c}\right)^2\right)^3} + \mathcal{O}\left(\eta^3\right). \qquad \text{(C28)}$$

Appendix D: The experiment with P1 and NV centers in diamond

We present experimental measurements of the sideband-emission spectrum of the P1 center. We first discuss the discovery of the volcano transparency flanked by asymmetric peaks as seen in Fig. 3. We also show that the cavity-based experiment displays a left sideband anomaly both in the P1 and in the NV center.
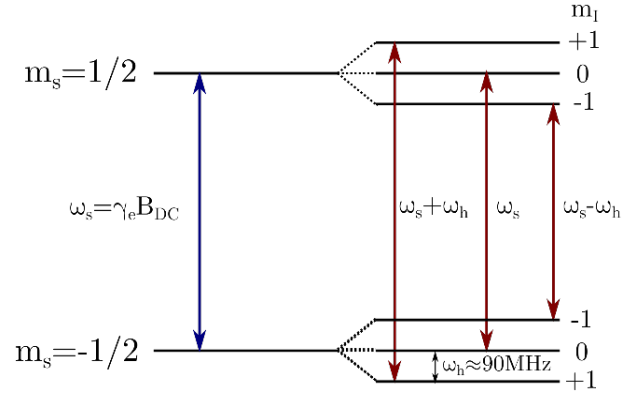

FIG. 14. Diagram of the hyperfine structure of the P1 center in diamond. The external static field B_{DC} sets the Zeeman splitting ω_s. The interaction with the nucleus introduces additional structure to the energy-level diagram with the hyperfine splitting ω_h. m_s is the spin quantum number and m_I is the nuclear spin number. The allowed transitions are marked with the red arrows in the diagram.

1. Substitutional nitrogen (P1) defect

In P1 or the substitutional nitrogen defect, a carbon atom is substituted by nitrogen. The unpaired electron forms the defect with one of the four possible neighboring carbon atoms. The spin of the defect lies within a relatively large diamond band gap [39] and interacts with the nitrogen spin-1 nucleus which leads to a hyperfine splitting. The effective Hamiltonian for the isolated spin is

$$\begin{aligned} H_{\text{P1}} = \gamma_e B_{\text{DC}} \left(S_z \cos\theta + S_x \sin\theta\right) \\ + A_\parallel S_z I_z + A_\perp \left(S_x I_x + S_y I_y\right), \end{aligned} \qquad \text{(D1)}$$

where $A_\parallel$ and $A_\perp$ are parameters that give the strength of the hyperfine coupling parallel and perpendicular to the hyperfine axis, respectively [40]. Here, S_i and I_i are spin-1/2 and spin-1 operators, respectively, the z-axis is aligned with the defect, and θ is the angle between the DC field and the defect axis. If the DC magnetic field is applied along one of the cubic axes of the crystal, then it makes an equal angle $\theta_0 = \arccos\left(1/\sqrt{3}\right)$ with respect to all four possible orientations of the defect [see Fig. 1(b)]. In that case, the response is uniform for all defects.

The DC magnetic field sets the scale of the energy splitting between the hyperfine triplets, $\omega_s = \gamma_e B_{\text{DC}}$. The strong high-frequency magnetic field acts perpendicular to the DC field and the low-frequency field acts parallel to it. We move to the frame rotating with the transverse frequency ω_t about the axis of $\mathbf{B}_{\text{DC}}$. The Hamiltonian in the rotating-wave approximation and large ω_s compared to the hyperfine terms is

$$\tilde{H}_{\text{P1}} = \left(\Delta_s + B_l \cos\left(\omega_l t\right)\right) S_{z'} + B_t S_{x'} + \omega_h S_{z'} I_{z'}, \qquad \text{(D2)}$$

where the primed axes are aligned with the DC field, $\Delta_s = \omega_s - \omega_t$ is the detuning of the spin from the trans-

verse drive. The frequency $\omega_{\mathrm{h}} = \sqrt{A_\parallel^2 \cos^2 \theta + A_\perp^2 \sin^2 \theta}$ sets the scale of the hyperfine splitting within a triplet. For the specific symmetric angle θ_0 this frequency is the same for all four possible directions, $\omega_{\mathrm{h}} = \sqrt{A_\parallel^2/3 + (2A_\perp^2)/3}$. The three transitions allowed by selection rules have frequencies ω_{s}, and $\omega_{\mathrm{s}} \pm \omega_{\mathrm{h}}$, as shown in Fig. 14.

The defect Hamiltonian effectively splits into three driven non-interacting spin subspaces. The six-dimensional Hilbert space is written as the block-diagonal Hamiltonian,

$$\tilde{H}_{\mathrm{P1}} = \bigoplus_{n \in \{0, \pm 1\}} H_{\mathrm{s}}^{\mathrm{eff}}(\Delta_{\mathrm{s}} + n\omega_{\mathrm{h}}). \qquad (D3)$$

Each block is the Hamiltonian $H_{\mathrm{s}}^{\mathrm{eff}}$ from Eq. (16) with spin energies ω_{s}, $\omega_{\mathrm{s}} + \omega_{\mathrm{h}}$, and $\omega_{\mathrm{s}} - \omega_{\mathrm{h}}$. Although these three transitions are independent, the transverse driving field can excite them simultaneously. The intensity of the emitted light is the square of the sum of electromagnetic fields emitted from the defect. Since this field is proportional to the σ_+ operator, we write

$$\mathcal{I} \propto \left| \sum_{n \in \{0, \pm 1\}} \langle \sigma_+ (\Delta_{\mathrm{s}} + n\omega_{\mathrm{h}}) \rangle \right|^2 . \qquad (D4)$$

This allows for the interference between fields that arise from different hyperfine transitions.

Experimentally, we find three volcano-like lineshapes as predicted by theory [see Fig. 3]. However, one of the volcanoes in each sideband has the opposite asymmetry. We argue that this occurs due to the interference effect described by Eq. (D4). We consider a phenomenological model where the longitudinal field causes the target equilibrium polarization in Eq. (14) to be time-dependent,

$$\sigma_{\mathrm{z}}^{\mathrm{eq}}(t) = \frac{\mathrm{Tr}\left(\sigma_{\mathrm{z}} e^{-\beta \tilde{H}_{\mathrm{P1}}(t)}\right)}{\mathrm{Tr}\left(e^{-\beta \tilde{H}_{\mathrm{P1}}(t)}\right)}, \qquad (D5)$$

where $\beta = 1/k_B T$ is an effective inverse temperature. The details of the model are discussed in Appendix D 3.

For the data in Fig. 3, the optical laser discussed in Sec. II A is used for cooling, the microwave input power is -40 dBm, and the RF peak-to-peak amplitude is 10 V (24 dBm). The electron-spin resonance at frequency $\omega_{\mathrm{s}}/(2\pi)$ is split due to interaction with the nuclear spin into three resonances. The splitting extracted from the measurement is $\omega_{\mathrm{h}}/(2\pi) \approx 90$ MHz. The splitting is significantly better resolved in the sidebands compared to the main peak data [see the top row of Fig. 3].

As we see in the experimental data, both sidebands lie to the right of the central resonance frequency $\omega_{\mathrm{c}}/(2\pi) \approx 3.772$ GHz. This corresponds to a right-sideband anomaly.

As we discussed in Sec. V B, this is prohibited in the simple linear spin-cavity model. Therefore, we proposed

introducing nonlinearity to break the symmetry between the right and the left sideband. In Sec. VI we demonstrated a mechanism by which Kerr nonlinearity can lead to this behavior. However, the experiments were performed outside of the region where the cavity nonlinearity is significantly excited, and this anomalous behavior remains to be explained. We now present the sideband data for the NV center that further explores the anomaly.

2. Nitrogen-vacancy (NV$^-$) defect

In an NV$^-$ defect, the nitrogen that is in place of carbon couples to the vacancy at one of the four possible neighboring positions [see Fig. 1 (a)]. Nitrogen provides two electrons and three carbons contribute each with one electron. The sixth electron that makes the defect negatively charged comes from the environment (possibly from the substitutional nitrogen) [15, 41]. The ground state is a spin triplet since the two holes at the defect prefer to form a spatially antisymmetric state to lower their Coulomb energy. The triplet is further split by the dipole-dipole spin interaction, where the spin-0 projection is lower in energy [for details see [14]]. The splitting of the two other levels can be adjusted by the DC magnetic field.

When the defect is driven by two crossed fields and the transverse field is tuned close to the resonance between states with spin projection $S_z = \pm 1$, then the $S_z = 0$ state can be neglected, and we can effectively treat the defect as a single doubly-driven spin-1/2 system.

The measurements of the NV center are presented in Fig. 4. We show the left and the right sideband spectra for different longitudinal frequencies ω_{l}. The optical laser for OISP is on and the microwave input power is -60 dBm. The measurements are performed for various longitudinal peak-to-peak amplitudes (V_{RF} in the figure) and transverse driving frequencies ω_{t}. All of the sideband resonances lie on the right side of the main peak, which means that they exhibit a right-sideband anomaly, as was found for the P1 centers. As ω_{l} is increased the distance between the right and the left sideband increases. We obtained the same result in the theoretical calculation with Kerr nonlinearity in Sec. VI.

As the longitudinal frequency is increased, the sideband signal becomes weaker and harder to discern from noise. As the RF amplitude increases (which corresponds to increasing B_{l}) the signal becomes stronger. In the experiment, the RF field remains in the linear regime such that higher-order sidebands are not observed.

3. Volcano transparency in P1 centers

The volcano asymmetry for one of the hyperfine transitions in the experimental data in Fig. 3 is opposite to what is expected from theory. Therefore, we propose a modification to the Bloch equations [see Eq. (14)] in

which we treat the equilibrium polarization as a time-dependent quantity. Since the Hamiltonian oscillates with a slow longitudinal frequency ω_l, we consider relaxation with a constant rate towards a time-dependent polarization, $\sigma_z^{eq}(t)$, given by the instantaneous thermal equilibrium of the Hamiltonian at time t, see Eq. (D5).

We do not provide the microscopic basis for the phenomenological model of Eq. (D5). This is in part because we do not understand well the relaxation processes in diamond defects with the OISP technique even in the absence of the longitudinal field. The model that we use cannot be derived microscopically in the form of the Lindblad equation, which uses the secular approximation. It is desirable to derive the Bloch equations from the master equation in Linbdlad form since the evolution is guaranteed to be trace-preserving and completely positive. The Lindblad equation generalizations beyond the secular approximation (which excludes the oscillating terms) were proposed recently [42–45], as well as generalizations for driven [46], and Floquet systems [47, 48]. Alternatively, one can look at the Bloch-Redfield equation [49], although this equation breaks positivity. While the Markovian property may be broken with time-dependent rates, for sufficiently small oscillations around the constant rates, this property still holds [50, 51].

With this caveat, we now look at how Bloch equations get modified if Eq. (D5) is assumed. In the presence of the optical laser and driving, T is assumed to be an effective temperature parameter and not the ambient temperature.

4. Oscillating equilibrium

If we assume the time-dependence of the equilibrium polarization as in Eq. (D5), $\sigma_z^{eq}(t)$ is to linear order in B_l

$$\sigma_z^{eq}(t) = \sigma_{z,0}^{eq} + B_l\left(\sigma_{z,1}^{eq}e^{i\omega_l t} + \sigma_{z,-1}^{eq}e^{-i\omega_l t}\right) + \mathcal{O}\left(B_l^2\right). \tag{D6}$$

If this expression is inserted into the Bloch equations the right sideband solution is modified according to

$$\langle\sigma_+\rangle^{(1)} \rightarrow \langle\sigma_+\rangle^{(1)} + \langle\sigma_+\rangle_{corr}^{(1)}, \tag{D7}$$

$$\langle\sigma_+\rangle_{corr}^{(1)} = \frac{-i\gamma_1 B_t\left(\Delta_s + \omega_l - i\gamma_2\right)\sigma_{z,1}^{eq}}{(\omega_l - i\gamma_1)(\Delta_s^2 - (\omega_l - i\gamma_2)^2) + 4|B_t|^2(\omega_l - i\gamma_2)}.$$

The P1 right-sideband spectrum with three hyperfine transitions is calculated with the modified expression as

$$\langle\sigma_+\rangle_{P1}^{(1)} = \sum_{k=\{0,\pm1\}} \langle\sigma_+\rangle^{(1)}\left(\Delta_s + k\omega_h\right), \tag{D8}$$

where ω_h is the hyperfine splitting as seen in Fig. 14. The P1 spectra calculated using this expression are shown in Fig. 15. The modified Bloch equations lead to the inversion of asymmetry of one of the volcanoes in the same manner as in the experimentally obtained spectra in Fig. 3.

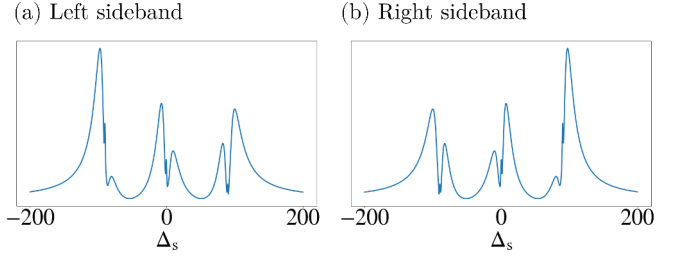(a) Left sideband   (b) Right sideband

FIG. 15. The analytically obtained P1 spectra. The asymmetry of one of the volcanoes is modified because of the interference between the different hyperfine emission lineshapes. The rightmost volcano of the left sideband has the asymmetry opposite to the other two volcanoes, and the same holds for the leftmost volcano of the right sideband. The plots were calculated using Eqs. (D7) and (D8). The parameters used in the plot are $B_t = 0.75$, $\omega_l = 1.5$, $\gamma_1 = 0.03$, $\omega_h = 90$, and $T = 1000$, all in units of γ_2.

Lastly, we present the calculation of $\sigma_z^{eq}(t)$. The exponential of the Hamiltonian can be expanded in the basis of Pauli matrices as

$$e^{-\beta|H|\hat{\mathbf{h}}\cdot\boldsymbol{\sigma}} = \cosh\left(\beta|H|\right)\mathbb{1} - \sinh\left(\beta|H|\right)\hat{\mathbf{h}}\cdot\boldsymbol{\sigma}, \tag{D9}$$

where $|H|$ is the instantaneous eigenvalue of the Hamiltonian, and $\hat{\mathbf{h}}$ is the unit vector in the Pauli basis,

$$|H|(t) = \frac{1}{2}\sqrt{\left(\Delta_s + B_l\cos\left(\omega_l t\right)\right)^2 + 4|B_t|^2}, \tag{D10}$$

$$\hat{\mathbf{h}}(t) = \frac{H_i(t)}{|H|(t)}. \tag{D11}$$

Using the properties of the Pauli matrices, we write Eq. (D5) as a function of the previous two parameters,

$$\sigma_z^{eq}(t) = -\tanh\left(\beta|H|(t)\right)\hat{\mathbf{h}}_z, \tag{D12}$$

where $\hat{\mathbf{h}}_z = \left(\Delta_s + B_l\cos\left(\omega_l t\right)\right)/(2|H|)$. We expand $\sigma_z^{eq}(t)$ to linear order in B_l to obtain

$$\sigma_z^{eq}(t) = -\frac{\Delta_s}{\Omega_R}\tanh\left(\frac{\beta\Omega_R}{2}\right) - \frac{B_l}{\Omega_R}\cos\left(\omega_l t\right)$$
$$\times\left(\frac{4|B_t|^2}{\Omega_R^2}\tanh\left(\frac{\beta\Omega_R}{2}\right) + \frac{\beta\Delta_s^2}{2\Omega_R\cosh^2\left(\frac{\beta\Omega_R}{2}\right)}\right), \tag{D13}$$

where $\Omega_R = \sqrt{\Delta_s^2 + 4|B_t^2|}$ is the generalized Rabi frequency. In the experiments where Ω_R is in the MHz range, the thermal energy is much higher than Ω_R, except for very low effective temperatures. The approximate expression in this limit is

$$\sigma_z^{eq}(t) \underset{\frac{\beta}{\Omega_R}\ll1}{\sim} -\frac{1}{2k_BT}\left(\Delta_s + B_l\cos\left(\omega_l t\right)\right). \tag{D14}$$

[1] A. G. Redfield, Nuclear magnetic resonance saturation and rotary saturation in solids, Phys. Rev. **98**, 1787 (1955).

[2] Y. Prior and E. L. Hahn, Optical rotary saturation, Phys. Rev. Lett. **39**, 1329 (1977).

[3] Y. Prior, J. A. Kash, and E. L. Hahn, Optical rotary saturation in a gas, Phys. Rev. A **18**, 2603 (1978).

[4] T. Witzel, F.-H. Lin, B. R. Rosen, and L. L. Wald, Stimulus-induced rotary saturation (sirs): A potential method for the detection of neuronal currents with mri, NeuroImage **42**, 1357 (2008).

[5] H. Ueda, H. Seki, Y. Ito, T. Oida, Y. Taniguchi, and T. Kobayashi, Dynamics of magnetization under stimulus-induced rotary saturation sequence, Journal of Magnetic Resonance **295**, 38 (2018).

[6] A. P. Saiko and R. Fedaruk, Multiplication of qubits in a doubly resonant bichromatic field, JETP Letters **91**, 681 (2010).

[7] A. P. Saiko, R. Fedaruk, A. Kolasa, and S. A. Markevich, Dissipative dynamics of qubits driven by a bichromatic field in the dispersive regime, Physica Scripta **85**, 045301 (2012).

[8] A. P. Saiko, R. Fedaruk, and S. A. Markevich, Relaxation, decoherence, and steady-state population inversion in qubits doubly dressed by microwave and radiofrequency fields, Journal of Physics B: Atomic, Molecular and Optical Physics **47**, 155502 (2014).

[9] R. Glenn, M. E. Limes, B. Pankovich, B. Saam, and M. E. Raikh, Magnetic resonance in slowly modulated longitudinal field: Modified shape of the rabi oscillations, Phys. Rev. B **87**, 155128 (2013).

[10] Y. Yan, Z. Lü, J. Luo, and H. Zheng, Effects of counter-rotating couplings of the rabi model with frequency modulation, Phys. Rev. A **96**, 033802 (2017).

[11] F. Forster, M. Mühlbacher, R. Blattmann, D. Schuh, W. Wegscheider, S. Ludwig, and S. Kohler, Landau-zener interference at bichromatic driving, Phys. Rev. B **92**, 245422 (2015).

[12] Y. S. Greenberg, E. Il'ichev, and A. Izmalkov, Low-frequency rabi spectroscopy for a dissipative two-level system, Europhysics Letters **72**, 880 (2005).

[13] Y. S. Greenberg, Low-frequency rabi spectroscopy of dissipative two-level systems: Dressed-state approach, Phys. Rev. B **76**, 104520 (2007).

[14] J. R. Maze, A. Gali, E. Togan, Y. Chu, A. Trifonov, E. Kaxiras, and M. D. Lukin, New Journal of Physics **13**, 025025 (2011).

[15] M. W. Doherty, N. B. Manson, P. Delaney, F. Jelezko, J. Wrachtrup, and L. C. Hollenberg, The nitrogen-vacancy colour centre in diamond, Physics Reports **528**, 1 (2013), the nitrogen-vacancy colour centre in diamond.

[16] G. Balasubramanian, P. Neumann, D. Twitchen, M. Markham, R. Kolesov, N. Mizuochi, J. Isoya, J. Achard, J. Beck, J. Tissler, V. Jacques, P. R. Hemmer, F. Jelezko, and J. Wrachtrup, Ultralong spin coherence time in isotopically engineered diamond, Nature Materials **8**, 383 (2009).

[17] E. Togan, Y. Chu, A. S. Trifonov, L. Jiang, J. Maze, L. Childress, M. V. G. Dutt, A. S. Sørensen, P. R. Hemmer, A. S. Zibrov, and M. D. Lukin, Quantum entanglement between an optical photon and a solid-state spin qubit, Nature **466**, 730 (2010).

[18] W. V. Smith, P. P. Sorokin, I. L. Gelles, and G. J. Lasher, Electron-spin resonance of nitrogen donors in diamond, Phys. Rev. **115**, 1546 (1959).

[19] L. S. Bishop, J. M. Chow, J. Koch, A. A. Houck, M. H. Devoret, E. Thuneberg, S. M. Girvin, and R. J. Schoelkopf, Nonlinear response of the vacuum rabi resonance, Nature Physics **5**, 105 (2009).

[20] J. Li, M. P. Silveri, K. S. Kumar, J.-M. Pirkkalainen, A. Vepsäläinen, W. C. Chien, J. Tuorila, M. A. Sillanpää, P. J. Hakonen, E. V. Thuneberg, and G. S. Paraoanu, Motional averaging in a superconducting qubit, Nature Communications **4**, 1420 (2013).

[21] S. Rohr, E. Dupont-Ferrier, B. Pigeau, P. Verlot, V. Jacques, and O. Arcizet, Synchronizing the dynamics of a single nitrogen vacancy spin qubit on a parametrically coupled radio-frequency field through microwave dressing, Phys. Rev. Lett. **112**, 010502 (2014).

[22] R. Levi, S. Masis, and E. Buks, Instability in the hartmann-hahn double resonance, Phys. Rev. A **102**, 053516 (2020).

[23] N. Maleeva, M. Fistul, A. Karpov, A. Zhuravel, A. Averkin, P. Jung, and A. Ustinov, Electrodynamics of a ring-shaped spiral resonator, Journal of Applied Physics **115**, 064910 (2014).

[24] N. Alfasi, S. Masis, R. Winik, D. Farfurnik, O. Shtempluck, N. Bar-Gill, and E. Buks, Exploring the nonlinear regime of light-matter interaction using electronic spins in diamond, Phys. Rev. A **97**, 063808 (2018).

[25] L. Robledo, H. Bernien, T. van der Sar, and R. Hanson, Spin dynamics in the optical cycle of single nitrogen-vacancy centres in diamond, New Journal of Physics **13**, 025013 (2011).

[26] D. Redman, S. Brown, R. Sands, and S. Rand, Spin dynamics and electronic states of n-v centers in diamond by epr and four-wave-mixing spectroscopy, Physical review letters **67**, 3420 (1991).

[27] S. N. Shevchenko, A. I. Ryzhov, and F. Nori, Low-frequency spectroscopy for quantum multilevel systems, Phys. Rev. B **98**, 195434 (2018).

[28] Supplementary Material for "Sideband Spectroscopy in the Strong Driving Regime: Volcano Transparency and Sideband Anomaly" (2025).

[29] This is the case when K_c is small, but in general, the cubic equation for $|\langle a^\dagger \rangle|^2$ can have three positive solutions (two of which are stable), leading to the bistability of the resonator.

[30] S. Shevchenko, S. Ashhab, and F. Nori, Landau-zener-stückelberg interferometry, Physics Reports **492**, 1 (2010).

[31] S. Masis, N. Alfasi, R. Levi, O. Shtempluck, and E. Buks, Multiphoton resonances in nitrogen-vacancy defects in diamond, Phys. Rev. A **100**, 013852 (2019).

[32] J. C. Camparo, Atomic stabilization of electromagnetic field strength using rabi resonances, Phys. Rev. Lett. **80**, 222 (1998).

[33] J. G. Coffer and J. C. Camparo, Atomic stabilization of field intensity using rabi resonances, Phys. Rev. A **62**, 013812 (2000).

[34] J. G. Coffer, B. Sickmiller, A. Presser, and J. C. Camparo, Line shapes of atomic-candle-type rabi resonances,

Phys. Rev. A **66**, 023806 (2002).

[35] M. Attrash, S. Masis, S. Hazanov, O. Shtempluck, and E. Buks, Frequency-mixing spectroscopy of spins in diamond, Phys. Rev. Appl. **20**, 054001 (2023).

[36] E. Geva, R. Kosloff, and J. L. Skinner, On the relaxation of a two-level system driven by a strong electromagnetic field, The Journal of Chemical Physics **102**, 8541 (1995), https://doi.org/10.1063/1.468844.

[37] C. Cohen-Tannoudji, J. Dupont-Roc, and G. Grynberg, *Photons and Atoms: Introduction to Quantum Electrodynamics* (Wiley, 1989).

[38] H. J. Carmichael and D. F. Walls, A quantum-mechanical master equation treatment of the dynamical stark effect, Journal of Physics B: Atomic and Molecular Physics **9**, 1199 (1976).

[39] A. M. Ferrari, S. Salustro, F. S. Gentile, W. C. Mackrodt, and R. Dovesi, Carbon **134**, 354 (2018).

[40] M. Simanovskaia, K. Jensen, A. Jarmola, K. Aulenbacher, N. Manson, and D. Budker, Sidebands in optically detected magnetic resonance signals of nitrogen vacancy centers in diamond, Phys. Rev. B **87**, 224106 (2013).

[41] J. H. N. Loubser and J. v. . Wyk, Electron spin resonance in the study of diamond, Reports on Progress in Physics **41**, 1201 (1978).

[42] G. McCauley, B. Cruikshank, D. I. Bondar, and K. Jacobs, Accurate lindblad-form master equation for weakly damped quantum systems across all regimes, npj Quantum Information **6**, 74 (2020).

[43] A. Trushechkin, Unified gorini-kossakowski-lindblad-sudarshan quantum master equation beyond the secular approximation, Phys. Rev. A **103**, 062226 (2021).

[44] P. P. Potts, A. A. S. Kalaee, and A. Wacker, A thermodynamically consistent markovian master equation beyond the secular approximation, New Journal of Physics **23**, 123013 (2021).

[45] D. Fernández de la Pradilla, E. Moreno, and J. Feist, Recovering an accurate lindblad equation from the bloch-redfield equation for general open quantum systems, Physical Review A **109**, 10.1103/physreva.109.062225 (2024).

[46] R. Dann, A. Levy, and R. Kosloff, Time-dependent markovian quantum master equation, Phys. Rev. A **98**, 052129 (2018).

[47] R. Alicki, D. Gelbwaser-Klimovsky, and G. Kurizki, Periodically driven quantum open systems: Tutorial (2012), arXiv:1205.4552 [quant-ph].

[48] T. Mori, Floquet states in open quantum systems, Annual Review of Condensed Matter Physics **14**, 35 (2023).

[49] C. Xu, A. Poudel, and M. G. Vavilov, Nonadiabatic dynamics of a slowly driven dissipative two-level system, Phys. Rev. A **89**, 052102 (2014).

[50] C. Addis, B. Bylicka, D. Chruściński, and S. Maniscalco, Comparative study of non-markovianity measures in exactly solvable one- and two-qubit models, Phys. Rev. A **90**, 052103 (2014).

[51] A. Rivas, S. F. Huelga, and M. B. Plenio, Entanglement and non-markovianity of quantum evolutions, Phys. Rev. Lett. **105**, 050403 (2010).